Flow in evolving fractures and porous media

Fredrik Eriksen

UNIVERSITÉ DE STRASBOURG

ÉCOLE DOCTORALE 413

Géophysique expérimentale,

Institut de Physique du Globe de Strasbourg

en cotutelle avec l'Université d'Oslo

THÈSE

présentée par :

Fredrik ERIKSEN

soutenue le : **31 janvier 2017**

pour obtenir le grade de : **Docteur de l'université de Strasbourg**

Discipline/ Spécialité : Géophysique

Écoulements dans des fractures et milieux poreux en évolution

THÈSE dirigée par :

M. TOUSSAINT Renaud	Directeur de recherches, l'Université de Strasbourg
M. MÅLØY Knut Jørgen	Professeur, the University of Oslo

RAPPORTEURS :

M. AURADOU Harold	Directeur de recherches, l'Université Paris-Sud
Mme. LINDNER Anke	Professeur, l'Université de Paris VI

AUTRES MEMBRES DU JURY :

M. SANDNES Bjørnar	Maître de conférences, the University of Swansea
Mme. JOUNIAUX Laurence	Directeur de recherches, l'Université de Strasbourg

Écoulements dans des fractures et milieux poreux en évolution

-

Flow in evolving fractures and porous media

by
Fredrik Kvalheim Eriksen

In joint supervision agreement between
University of Strasbourg
and
University of Oslo

This thesis is submitted to
the University of Strasbourg
for the degree of
Doctor in geophysics

Autumn 2016

Supervisors:

Prof. Renaud Toussaint
University of Strasbourg, France

Prof. Knut Jørgen Måløy
University of Oslo, Norway

Prof. Eirik Grude Flekkøy
University of Oslo, Norway

Jury members:

Dr. Harold Auradou
University of Paris-Sud, France

Prof. Anke Lindner
University of Paris VI, France

Dr. Bjørnar Sandnes
University of Swansea, United Kingdom

Dr. Laurence Jouniaux
University of Strasbourg, France

Résumé

Durant de nombreux processus dans la nature et l'industrie, l'écoulement de fluides transforme le milieu poreux (réservoir) qui les contient. En fonction des mécanismes impliqués, ces processus de transformation peuvent être rapides, durant quelques secondes ou moins, ou lents, d'une durée allant d'heure à des milliers d'années. Le projet de cette thèse se focalise sur les processus rapides et lents de transformation des réservoirs sous l'effet d'écoulements fluides, qui sont importants à comprendre notamment dans les domaines des transports de contaminant, d'exploitation améliorée (Enhanced Recovery) de gaz et d'hydrocarbures liquides, de séquestration de carbone, ou de mobilisation de sédiments souterrains. Sur la base d'expériences de laboratoire légères, nous étudions l'écoulement de fluides dans des fractures et milieux poreux en évolution, comment l'écoulement provoque cette transformation, et l'interaction entre la transformation et les caractéristiques de l'écoulement lui-même.

Les processus de transformation rapide des réservoirs incluent la déformation mécanique rapide et la fracturation dues aux fortes surpressions dans le fluide poral. Dans le cas où la pression de fluide est suffisamment élevée pour ouvrir des fractures dans le solide, une instabilité d'écoulement apparentée à celle de Rayleigh-Taylor s'initie alors que l'écoulement se concentre dans les fractures les plus longues, où la perméabilité et les gradients de pression sont plus grands aux extrémités, ce qui amène les fractures les plus développées à se propager au détriment des moins développées. Le mécanisme de stabilisation de ce type d'écoulement est la résistance du matériau à se déformer plus avant, qui augmente dans un réservoir confiné quand le matériau est compacté durant la déformation. Nous étudions ce phénomène en effectuant des expériences de laboratoire où nous injectons de l'air à surpression constante dans un milieu poreux saturé ou sec confiné dans une cellule de Hele-Shaw. Ce système simplifié est un analogue de roche/sol quasi-bidimensionnel (2D) confiné entre deux plaques de verre. Le système est optiquement transparent, et nous enregistrons l'écoulement et les processus de déformation à l'aide d'une caméra à haute vitesse à un taux de 1000 images par second. Le traitement d'images post-expérimental et l'analyse de la séquence d'images résultante produit de l'information sur la croissance et la forme des motifs de fracturation et d'invasion au cours du temps. Nous utilisons les résultats pour caractériser les propriétés typiques des structures émergentes, telles que leur dimension fractale, l'épaisseur de la déformation et la profondeur d'invasion des surpressions, la dynamique de croissance, les lois d'échelle en espace et en temps, ainsi que la classification des régimes d'écoulement et déformation en fonction des pressions d'injection et des conditions aux frontières. Par ailleurs, les milieux granulaires utilisés sont ensemencés de particules-traceurs qui permettent d'obtenir des informations sur les déplacements et déformation ayant

lieu dans le milieu poreux environnant au cours du temps. Cette information est quantifiée en traitant des séquences d'images par intercorrélation image-par-image, ce qui nous autorise à caractériser la déformation dans le matériau et son évolution temporelle. La force motrice de la déformation est le gradient de pression de pore à travers le solide, et nous calculons numériquement l'évolution du champ de cette pression intersticielle dans le milieu poreux. Dans le cas de deux fluides immiscibles dans un milieu poreux déformable saturé en fluide peu compressible, comme durant l'injection d'air dans un milieu saturé en eau, la surpression diminue à travers le milieu saturé, depuis la poche interne d'air comprimé vers l'extérieur moins pressurisé. Cette configuration stationnaire du champ de pression est évaluée en résolvant l'équation 2D de Laplace avec des conditions de pression fixe sur la frontière de la poche d'air et à la frontière externe. Par ailleurs, lorsqu'un même fluide compressible que celui initialement présent dans le poreux est injecté (comme dans l'aérofracturation par injection ponctuelle), la surpression imposée au centre diffuse dans le milieu poreux, avec une constante de diffusion dépendant de la perméabilité et porosité du milieu, et de la compressibilité et viscosité du fluide. Ce champ de pression est calculé en résolvant au cours du temps l'équation de diffusion avec la méthode de Crank-Nicholson. Finalement, le champ de pression atteint un état stationnaire, au bout d'un temps caractéristique évalué en comparant la solution de l'équation de diffusion à celle de l'équation de Laplace. En comparant les données de déformation obtenues et les champs de gradients de pression à travers le milieu poreux, nous développons des modèles théoriques de déformation et de dynamique de fracturation.

Dans un projet intimement relié, des émissions acoustiques émises durant les expériences d'injection d'air dans des granulaires sont enregistrées avec des accéléromètres de choc piézoélectriques. Par analyse de Fourier des signaux obtenus, l'évolution des émissions dans le domaine de fréquence est caractérisée durant différentes étapes de la déformation et la fracturation, et le processus de création des différents types de signaux, sont discutés, en liaison avec les données optiques. De plus, les évènements microsismiques causés par le réarrangement de particules dans les étapes tardives des expériences sont comptées en fonction du temps, et ce comportement est comparé à des évènements de grande échelle lors d'injections en puits. En combinaison avec des données de déformation optiques, on développe également une méthode de localisation des sources basée sur l'énergie des signaux enregistrés.

Les processus de transformation lents des réservoirs incluent l'évolution chimique de réseaux de fracture existants due aux réactions entre le fluide s'écoulant et la roche hôte, i.e. la dissolution et la précipitation. De tels processus peuvent augmenter et diminuer la perméabilité du système, et peuvent changer la contrainte dans le matériau entourant les fractures. Dans l'étude de ces processus lents, nous faisons des expériences d'écoulement à travers des carbonates fracturés. Des échantillons de craie de forme cylindrique de 3.8 cm de diamètre et 1.7 à 2.6 cm de hauteur sont fracturés en deux le long de leur axe principal, en chargeant les échantillons à travers leur diamètre dans un appareil de test d'essais brésiliens. Les échantillons fracturés sont remis en place de façon jointive et monté dans une cellule de Hassler (confinement cylindrique), et un fluide réactif est injecté à travers. Ici, nous injectons de l'eau distillée à débit constant de 0.1 ml/min à travers les échantillons

fracturés pour différentes durées. Un profil topographique local des surfaces de fracture dans les échantillons est mesuré avant et après l'écoulement réactif en utilisant un interféromètre à lumière blanche, donnant une résolution normale de l'ordre du micromètre. En analysant la topographie mesurée et en comparant les mesures avant et après, nous déterminons l'évolution de la rugosité et de l'ouverture de la fracture pour différentes durées d'écoulement, et étudions d'impact de la direction de l'écoulement sur l'évolution. Pour l'étude des contraintes environnantes nous construisons un appareil de test permettant de charger les fractures de façon parallèle et normale à la fracture durant l'écoulement, afin de mesurer l'évolution de la contrainte dans le matériau en fonction de l'orientation.

Le travail effectué durant cette thèse fait globalement partie d'avancées sur la compréhension des mécanismes fondamentaux des processus complexes impliqués dans les réservoirs en transformation sous l'effet des écoulements de fluide, et est impliqué dans le développement de techniques de localisation acoustique, qui peuvent avoir des applications industrielles.

Abstract

During many subsurface processes in nature and industry, the flow of fluids transforms the surrounding porous medium (reservoir) containing them. Depending on the involved mechanisms, these transformation processes can be fast, lasting only a couple of seconds or less, or slow, lasting from a few hours to several weeks or more. The project of this thesis focuses on both the fast and slow processes of transforming reservoirs due to fluid flow, which are important aspects in for example contaminant transport, improved oil and gas recovery, carbon storage, enhancement of water well and geothermal energy production, or subsurface sediment mobilization. Based on tabletop experiments and numerical simulations, we study the flow of fluids in evolving fractures and porous media; how the flow drives the transformation of the media, and the interplay between the transformation and the flow behavior itself.

Fast transformation processes of reservoirs include sudden mechanical deformation and fracturing due to high overpressure in the pore fluid. In cases where the fluid pressure is high enough to open fractures in the solid, a flow instability (Raleigh-Taylor) is initiated where the fluid flow concentrates into the longest fractures, where there is higher permeability and larger pressure gradients on the tips, such that the more developed fractures propagate on expense of the less developed ones. The stabilizing mechanism of this flow behavior is the resistance of the surrounding material to deform further, which increases in confined reservoirs when the material is compacted during deformation. We study this phenomen by performing lab experiments where we inject air at a constant overpressure into saturated or dry granular media confined inside Hele-Shaw cells. This simplified system is a quasi-2-dimensional rock/soil analog confined between two glass plates. The setup is optically transparent, which facilitates direct observations during experiments, and we record the flow and deformation processes with a high speed camera at a framerate of 1000 images per second. Post-experiment image processing and analysis of the resulting image sequences yield information about the growth and shape of the fracturing/invasion patterns over time. We use the results to characterize typical properties of the emerging structures, such as their fractal dimension, typical thickness and invasion depth, scaling exponents, growth dynamics, as well as flow regimes depending on injection pressure and boundary conditions.

Furthermore, we have tracer particles in the granular packing which provide information of the surrounding displacement and deformation in the porous media over time. This information is quantified by processing the image sequences with frame-to-frame image correlation software, and enables us to characterize the deformation in the material and how it evolves over time. The driving force of the deformation is the pressure gradient across the solid, and we calculate the evolution

of the pressure field in the porous medium numerically. In the immiscible case, e.g. when air is injected into a water saturated porous medium, the overpressure is dissipated across the saturated medium, from the overpressured air cluster towards the less pressurized outer boundary. This is a steady-state configuration of the pressure field, which is estimated by solving the 2D Laplace equation with fixed pressures in the air cluster and at the outlet boundary. On the other hand, in a porous medium where the same fluid is injected, the imposed pressure initially diffuses into the pore space with a diffusion constant that is calculated by knowing the porosity of the material and the viscosity of the fluid. This pressure field is calculated over time by solving the 2D diffusion equation with the Crank-Nicholson method. Eventually, the pressure field reaches steady-state, so the diffusing pressure field is compared with the corresponding Laplace solution at each timestep to determine when this happens. By comparing the obtained deformation data and gradients of pressure fields across the porous media, we develop theoretical models of the deformation and fracturing dynamics.

In a closely related project, where the work in this thesis is also involved, acoustic emissions during experiments with air injections into dry granular media are recorded with piezo-electric shock accelerometers. By fourier analysis of the obtained signals, the evolution of the emissions in the frequency domain is characterized during the different stages of deformation and fracturing, and the processes creating the various types of signals are discussed in comparison with the optical data. In addition, microseismic events caused by particle rearrangement in the later stages of the experiments are counted and fitted with real world events. In combination with the optical data of deformations, an energy based localization technique of the sources of these microseismic events is developed.

Slow transformation processes of reservoirs include chemical evolution of existing fracture networks due to reactions between the flowing fluid and host rock, i.e. dissolution and precipitation. Such processes further increase or decrease the permeability of the system, and may change the stresses in the material surrounding the fractures. In the study of such slow processes, we perform reactive flooding experiments through fractured carbonates. Chalk samples, cylinders of 3.8 cm diameter and 1.7 to 2.6 cm in length, are fractured in two pieces through their principal axis, by loading the samples across their diameter in a brazilian strength test apparatus. The fractured samples are put back together, mounted inside a Hassler cell (cylindrical confinement), and flooded with a reactive fluid. Here, we inject distilled water at constant flow rate of 0.1 ml/min through the fractured samples for various amounts of time. A local topographical profile of the fracture surfaces in the samples are measured before and after the reactive flooding by using a white light interferometer, giving a height resolution of a few microns. By analyzing the measured topography and comparing the before/after measurements, we investigate the local evolution of roughness and fracture aperture after different durations of flooding, and investigate the impact of flow direction on the changes. For the study of the surrounding stresses we are constructing a setup to load the samples parallell and normal to the fracture plane during flooding, in order to measure the evolution of stresses in the material depending on these orientations.

The work done in this thesis project is ultimately a part of further understanding

the fundamental mechanisms of complex processes involved in transforming reservoirs due to fluid flow, and is also involved in the development of acoustic localization techniques which may have industrial applications.

Acknowledgements

I have carried out the work of my thesis under a joint supervision agreement between the University of Strasbourg and the University of Oslo, which I think was a very nice arrangement combining expert knowledge of the experimental geophysics group in Strasbourg and the complex physics group in Oslo. On this note, I would like to thank my supervisors Renaud Toussaint, for giving me the opportunity to do this thesis in Strasbourg, and Knut Jørgen Måløy for welcoming me to the Oslo group on a regular basis. I appreciate our nice discussions and your valuable advice. I would also like to thank my co-supervisor Eirik Grude Flekkøy, for helpful input and comments during this work. I have enjoyed working with you all during this thesis. I thank Harold Auradou, Anke Lindner, Bjørnar Sandnes and Laurence Jouniaux for accepting to be in the jury of this thesis.

Furthermore, I thank Alain Steyer, Miloud Talib and Mihailo Jankov for technical support with experimental equipment, as well as Reidar Inge Korsnes and Anders Nermoen for helping me with experiments at the University of Stavanger and IRIS. I would also like to thank all the ITN FlowTrans people, and the people in the Oslo and Strasbourg groups, for being good friends and colleagues. It has been a great experience to cooperate with you and to be part of an international and multidisciplinary research network. Thank you Guillaume Dumazer, Renaud Toussaint and Semih Turkaya for help with the french translation.

Finally, I would like to thank my family for all their help and support, and my fiancee Marthe for all your support and patience during this work.

This project has received funding from the European Unions Seventh Framework Programme for research, technological development and demonstration under grant agreement no. 316889, ITN FlowTrans.

List of Papers

Paper 1

Invasion patterns during two-phase flow in deformable porous media
Fredrik K. Eriksen, Renaud Toussaint, Knut J. Måløy and Eirik G. Flekkøy
Frontiers in Physics, 3:81 (2015)

Paper 2

Pneumatic fractures in confined granular media
Fredrik K. Eriksen, Renaud Toussaint, Semih Turkaya, Knut J. Måløy and Eirik G. Flekkøy
Physical Review E, (Submitted Oct. 2016)

Paper 3

Pressure evolution and deformation of confined granular media during pneumatic fracturing
Fredrik K. Eriksen, Renaud Toussaint, Semih Turkaya, Knut J. Måløy and Eirik G. Flekkøy
Physical Review E (Proposed paper to be submitted)

Paper 4 (co-author)

Bridging aero-fracture evolution with the characteristics of the acoustic emissions in a porous medium
Semih Turkaya, Renaud Toussaint, Fredrik K. Eriksen, Megan Zecevic, Guillaume Daniel, Eirik G. Flekkøy and Knut J. Måløy

Frontiers in Physics, 3:70 (2015)

Paper 5 (co-author)

Localization based on estimated source energy homogeneity
Semih Turkaya, Renaud Toussaint, Fredrik K. Eriksen, Olivier Lengliné, Guillaume Daniel, Eirik G. Flekkøy and Knut J. Måløy
Review of Scientific Instruments, (2016)

Contents

Chapter 1

Résumé français du contenu scientifique

1.1 Article 1 - Pattern d'invasion en écoulement diphasique à travers un milieu poreux déformable

Dans cet article nous avons étudié les motifs d'invasion qui se forment au cours de l'injection d'air dans un milieu poreux déformable saturé par une solution liquide. Des échantillons sont préparés en répartissant une mono-couche the billes de verres á l'intérieur d'une cellule de Hele-Shaw circulaire de 40 cm de diamètre placée horizontalement et avec un interstice de 1 ou 1.4 mm. Les échantillons sont préparés en suivant 3 conditions aux bords différentes : (i) non-déformable (ND) - les billes sont fixes et forment un milieux-poreux rigide; (ii) confiné-déformable (CD) - les billes peuvent se déplacer à l'intérieur de la cellule mais ne peuvent s'en échapper grâce à un filtre placer au bord; (iii) ouvert-déformable (OD) - les billes peuvent à la fois se déplacer à l'intérieur de la cellule et de s'échapper de la cellule à son extrémité. Le milieux poreux est saturé par une solution visqueuse de glycerol-eau (80% en masse). Au cours de la manipulation, de l'air est injectée au centre de la cellule avec une surpression constante comprise entre 25 et 100 mbar, tandis qu'une caméra rapide Photron SA5 capture le processus d'invasion en vue de dessus avec une résolution de 125 images par secondes. Chaque expérience dure entre 0.9 et 9.7 s, le temps d'observation diminue lorsque la pression d'injection, ou la déforméabilité augmentent. Les motifs d'invasion ainsi que la déformation du milieu est analysée par traitement numérique des images en appliquant un seuil sur la palette de gris. La déformation est obtenue par correlation d'images (DIC).

Des motifs de déformation caractéristiques obtenus pour chaques conditions aux bords sont présenté sur la figure 1.1 avec le graph de l'épaisseur moyenne de la digitation en fonction du rayon dans le système de coordonnées axi-symmétrique. On peut observer à l'échelle de la cellule une chactéristique commune : une structure dentritique ramifiée se développant du centre vers les bords, principalement dans la direction radiale, les ramifications les plus avancées se développant au dépens des ramifications les moins avancées. Les motifs d'invasion présentent néanmoins des différences locales si on observe en détail à l'aide du graph présentant l'épaisseur moyenne de la digitation. Les motifs obtenus avec les conditions aux bords ND

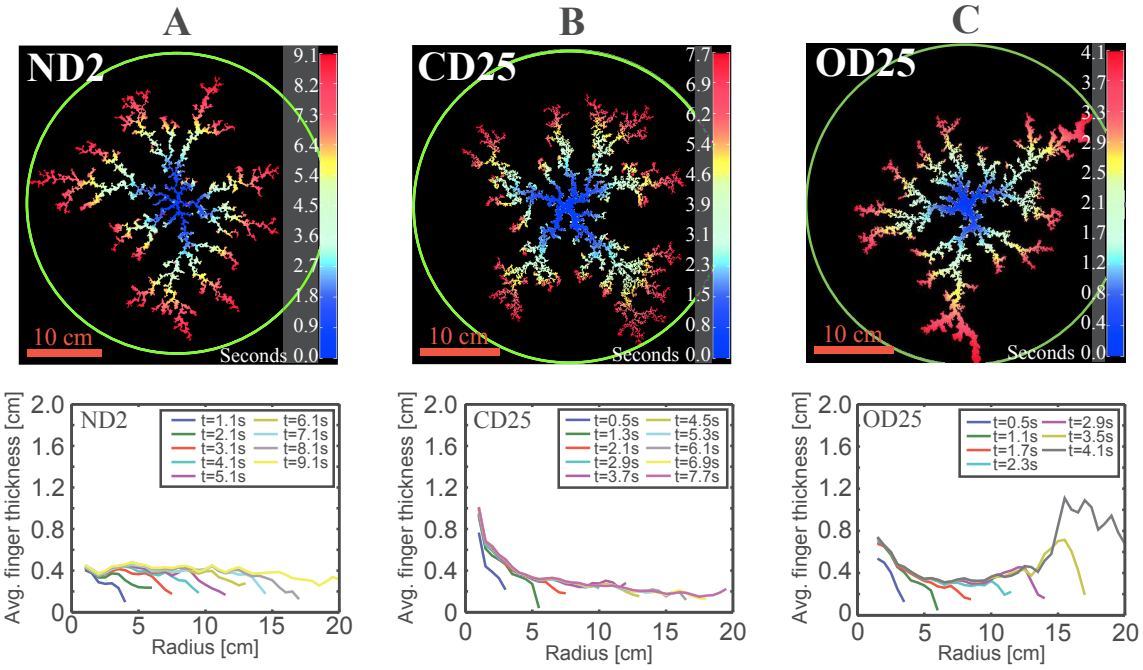

Figure 1.1: En haut : Motifs obtenus à l'instant de la rupture avec des conditions de type non-déformable (ND) (A), confiné déformable (CD) (B), et déformable ouvert (C), avec une pression d'injection de 25 hPa. L'échelle de couleurs utilisée indique l'instant où le pixel à été envahie par l'air en secondes aprés le début, allant du bleu au commencement vers le rouge foncé au moment de la rupture. Le cercle vert indique le bord de la cellule. En bas : profil de épaisseure moyenne de la digitation en fonction du rayon à différents instants correspondant aux motifs du dessus.

présentent une digitation allongée et fine, l'épaisseur des doigts apparaît approximativement indépendente de la coordonnée radiale, en dehors de la zone d'injection. Les motifs obtenus avec des conditions aux bords CD présentent au centre un faible nombre de doigts épais qui deviennent plus nombreux et plus fins à mesure que l'on s'éloigne du centre. Enfin, les conditions aux bords OD produisent une digitation raréfiée et épaisse au centre, devenant plus dense et fine avant de redevenir raréfié et épaisse proche du bord de la cellule. Les variations de l'épaisseur de la digitation dans un motif d'invasion à travers un milieu poreux déformable proviennent de la compétition entre les intéraction de surface, déterminée par les effets de capillarité, et la friction déterminée par les contraintes granulaires. Dans le matériau déformable, la pression capillaire est bien plus faible que la surpression dans le cluster d'air. Ainsi nous observerons systématiquement une invasion de pore (digitation fine) lorsque les contraintes entre les grains dominent les effets de capillarité. À l'inverse, si le déplacement des billes devient plus aisé que l'invasion d'un pore, le doigt aura la possibilité de s'élargir.

La contrainte granulaire est liée à la déformation du milieu, lorsque la quantité de grains compacté devient plus difficile à déplacer. La cartographie des déformations obtenues dans le cas de conditions aux bords de type CD et OD, avec une pression d'injection de 100 hPa, sont présentée sur la figure 1.2. Le nombre total de déplacements radiaux, aisi que les déformations volumiques sont présentée au com-

mencement, à mi-course, en fin de l'expérience et au moment de la rupture. Les déplacements radiaux dans les deux expériences sont dirigés vers l'extérieur à partir du centre d'injection, sans atteindre initialement le bord extérieur. Dans l'expérience de type CD, la zone de déplacement s'étale progressivement sans atteinde le bord extérieur de la cellule qui reste stable. Le champ de déformation volumique correspondant montre que à l'extérieu du cluster d'invasion le milieu est progressivement compacté. On observe une transition entre l'invasion par élargissement de la digitation et l'invasion de pores dans la deuxième partie de la manipulation. Dans le cas de conditions aux bords de type OD, les déplacements radiaux en dehors du cluster d'invasion augmentent en intensité dans le temps, pour finalement atteindre de bord extérieur de la où les billes quittent la cellule. La déformation volumique correspondante montre que le milieux est initialement compacté, et qu'une décompaction progressive se développe proche du bord. Dans cette expérience l'élargissement des doigts ne montre pas de transision vers un phénomène d'invasion de pores. Dans les expériences obtenues avec des pressions d'injection plus faibles la compaction initiale semble être responsable d'une transition vers une invasion de pores, alors que la décompaction extérieure provoque une seconde transition vers un élargissement des doigts. La figure 1.3 contient un cliché caractéristique des déplacements tangentiels autour de l'élargissement des doigts, ce qui montre que les billes s'éloignent perpendiculairement des doigts.

Les valeurs de dimension fractales du motif à l'instant de la rupture sont présentées sur la figure 1.4 pour les expériences réalisées avec une pressiion d'injection de 25 hPa pour chaque condition au bords. Pour chaque motif obtenus la dimension de *box-counting* D_b calculée apparaît dans une gamme de valeurs comprises entre 1.55 et 1.63. Ceci correspond aux valeurs attendues dans le cas d'une digitation visqueuse dans un milieu poreux rigide, indiquant une strucutre commune avec le présent motif d'invasion à l'échelle de la cellule. Pour les motifs obtenus avec des conditions aux bords de type ND, la dimension de masse D_m correspond à la fois à la dimension de *box-counting*, et à la dimension locale $D_L + 1$. Ces valeurs de dimensions sont approximativement indépendente de la coordonnée radiale sur les zones stabilisées suffisamment éloignées des bords de la cellule. Ceci montre que ces motifs ont une dimension fractale bien définie à l'échelle de la cellule, ce qui est cohérent avec de précédents travaux dans ce domaine [1, 2]. Les valeurs de dimension de masse pour des motifs obtenus dans un milieu déformable présentent généralement un écart avec la dimension de *box-counting* ou la dimension locale, ce qui signifie que la méthode de mesure est sensible à l'épaisseur décroissante de la digitation avec la coordonnée radiale á l'intérieur de la cellule. Cependant dans les zones stabilisées du motif obtenu avec des conditions aux bords de type CD, à des pressions d'injection comprises entre 25 et 75 hPa, la dimension de *box-counting* suivent relativement bien les valeurs de dimension locale, ce qui signifie que les zones du motifs stabilisé ont une dimension fractale bien définie, proches des valeurs obtenues avec des conditions aux bords de type ND. Pour les observations réalisées avec des conditions aux bords de type CD avec une surpression de 100 hPa, ainsi que pour toutes les observations réalisées avec des conditions aux bords de type OD, la dimension locale présente une décroissance avec la coordonnées radiale, et l'adéquation avec la dimension de *box-counting* n'est obtenue que pour un rayon intermédiaire. Ceci indique que les motifs des systèmes

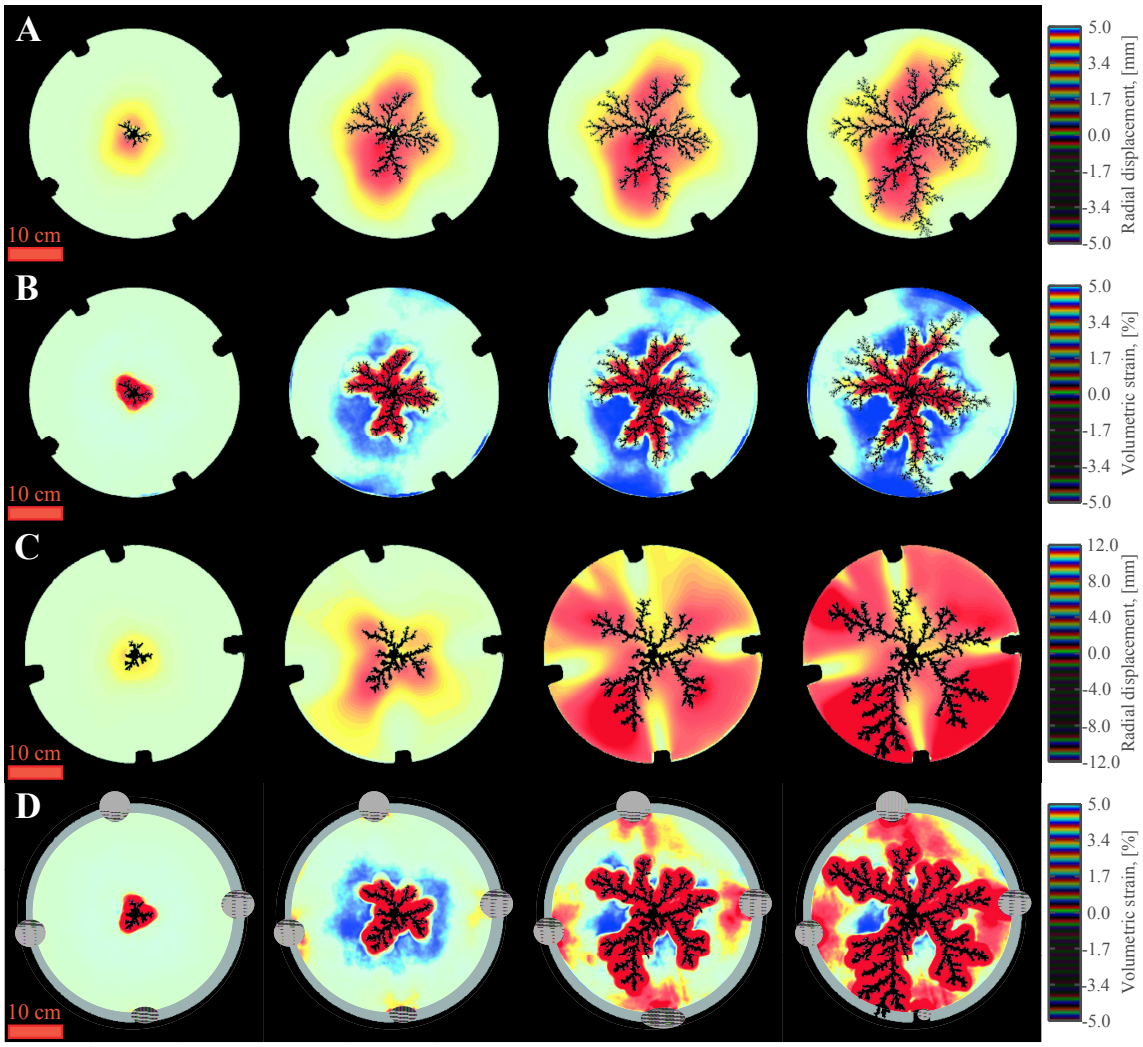

Figure 1.2: Déformation totale à différents instants au cours de l'injection : Déplacement radial (A) et déformation volumique (B) avec des conditions aux bords de type confiné déformable (CD) et une pression d'injection de 100 hPa. Déplacement radial (C) et déformation volumique (D) pour des conditions ouvert déformable avec une pression d'injection 100 hPa. Les clichés sont obtenus de gauche à droite pour les lignes (A) et (B) à 20, 54, 77 et 100% du temps de rupture, et pour les lignes (C) et (D) à 18, 43, 75, et 100% du temps de rupture. la zone grisée sur la ligne (D) correspond à la région où les effets de bords dus à la fuite des billes perturbent fortement les calculs de déformations et ont été volontairement omis.

les plus déformés n'ont pas de dimension fractale bien définie à l'échelle de la cellule, mais possède une dimension fractale définie localement, avec une transition vers une classe d'universalité lorsque la coordonnée radiale augmente. Initialement, les parties vides des digitations épaisses présentent une dimension locale de 1.7 ce qui correspond à la même dimension fractale que pour un processus d'aggrégation par diffusion (DLA), ainsi que pour un processus de digitation visqueuse. Pour des valeurs intermédiaires $D_L + 1 \approx 1.6$, ce qui est cohérent avec les valeurs obtenues avec une digitation visqueuse dans un milieu poreux. Pour les zones extérieures avec

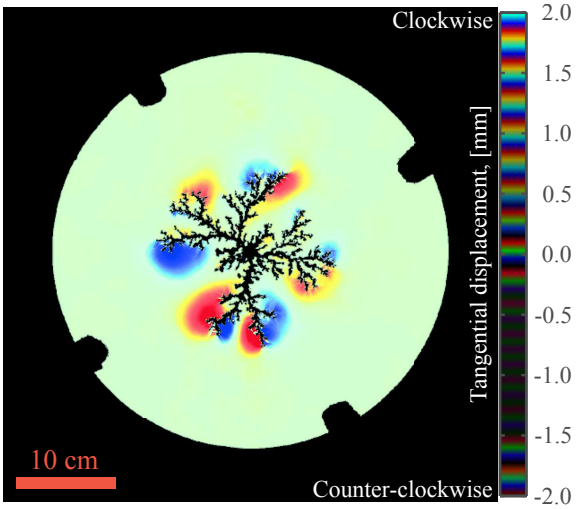

Figure 1.3: Exemple du comportement du déplacement tangentiel sur l'intervalle de temps $[448 - 488]$ ms ($[50 - 54]\%$ du temps de rupture) pour des conditions aux bords de type confiné déformable avec une pression d'injection de 100 hPa.

des conditions aux bords de type OD, $D_L + 1$ prend des valeurs proches de 1.4, ce qui à la dimension fractales 1.43 mesurée dans le cas de fractures dans une colle [3].

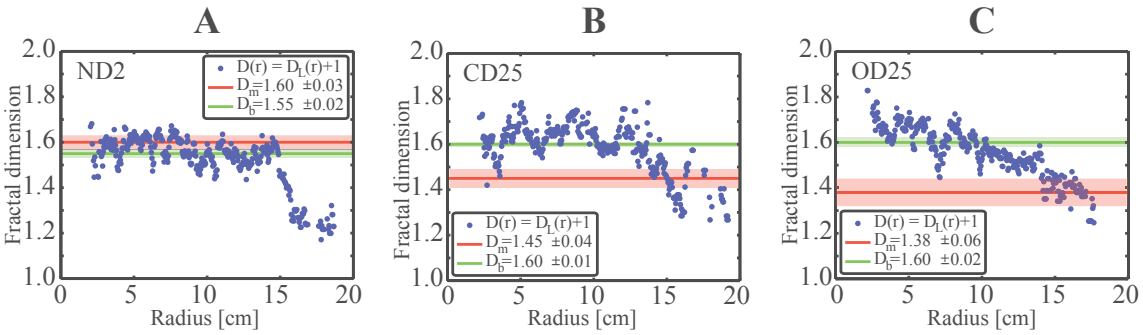

Figure 1.4: Les symboles bleus indiquent la dimension fractal locale $D_L + 1$ en fonction du rayon dans la cellule pour un motif obtenu avec des conditions aux bords non-déformables (A), confiné déformable (B), et déformables ouvertes (C) à l'instant de la rupture et pour un pression d'injection de 25 hPa. La dimension de masse D_m est indiquée en trait plein rouge, les deux bandes rouge pâle représentant l'incertitude, et la dimension de *box counting* D_b en trait pointillé vert, les deux bandes vert pâle représentant l'incertitude.

En considérent la dynamique de croissance, ont trouve que la masse N et le rayon r du motif augmente dans le temps comme :

$$N(t) = N_b(t/t_b)^{\alpha}, \text{ and } r(t) = r_b(t/t_b)^{\beta}, \tag{1.1}$$

avec N_b, r_b et t_b correspondant respectivement aux valeurs de la masse, du rayon, et du temps atteintes au moment de la rupture. Ainsi à un instant donné, la loi d'échelle pour la masse et le rayon est donnée par :

$$\frac{N(r)}{N_b(t/t_b)^{\alpha}} = \left(\frac{r}{r_b(t/t_b)^{\beta}}\right)^{D_m}. \tag{1.2}$$

La figure 1.5 montre les clichés de la loi d'échelle pour une experience en milieu défomable avec une pression d'injection de 100 hPa (CD100 et OD100), qui montre comment la masse dépend du temps et de rayon en suivant la loi de Family-Vicsek. Ce qui donne la loi d'échelle suivante pour la dimension de masse:

$$D_m = \alpha/\beta. \tag{1.3}$$

Pour une condition aux limites de type CD100 on trouve $\alpha = 1.58$ et $\beta = 1.02$, et pour OD100, $\alpha = 1.73$ et $\beta = 1.10$. En applicant les paramétres de la loi d'échelle sur ces deux dernières conditions aux bords CD100 et OD100 dans l'équation (1.3), on obtient respectivement les dimensions de masse $D_m = 1.55$ et $D_m = 1.57$, ce qui est similaire à leur dimensions de *box counting*, et cohérent avec la dimension fractale d'une digitation visqueuse en milieu poreux. En outre, nous avons découvert que l'exposant dynamique α pour la zone envahie au cours du temps augmente avec la déformabilité du milieu. Ceci implique que l'évolution de la zone envahie en fonction du temps possède une grande dépendance avec la déformabilité.

Une présentation détaillée des méthodes et résultats de cette étude se trouve dans l'article corrsepondant présenté au chaptire 4. Cet article a été publié dans la revue Frontiers in Physics en 2015.

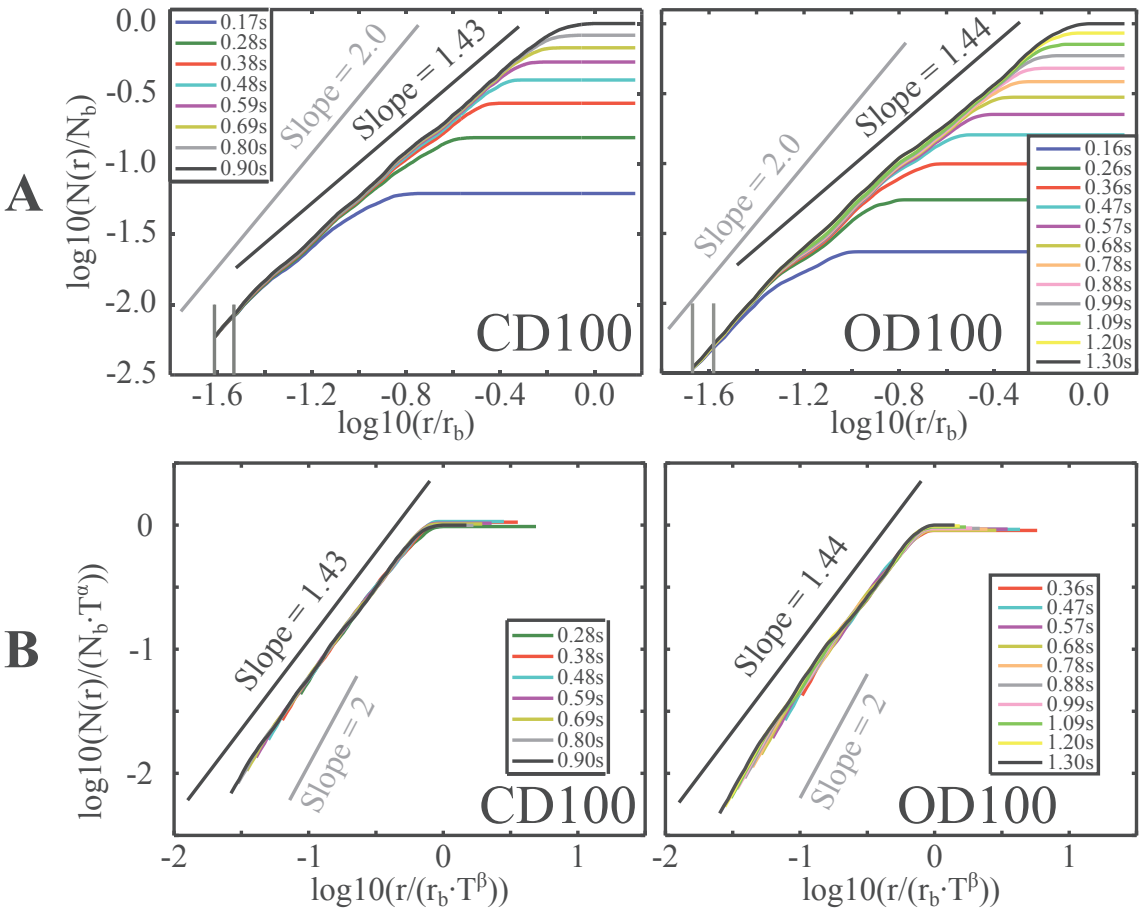

Figure 1.5: (A) Courbes de rayon-masse à différents instants pour des conditions confinées déformables à 100 hPa (à gauche), et pour des conditions déformable ouvert (à droite). Au commencement de chaque courbe la ligne grisée la plus à gauche marque une distance de 1 mm en dehors du rayon de cutoff inférieur. Le trait discontinu noir montre la dimension de masse estimée à partir de la pente pour les motifs obtenus au moment de la rupture. Le trait discontinu grisé possède une pente de 2, et est un guide pour l'oeil indiquant la dimension de l'espace occupé par une bulle vide. (B) Loi d'échelle Family-Vicsek de la même courbe de rayon-masse qu'en (A), excepté pour le plus petit des clusters d'air avec une masse totale inférieure à 10 % de la masse à l'instant de la rupture, c'est-à-dire avant que le régime d'instabilité par digitation ne commence. Sur les axes $T = (t/t_b)$ correspond au rapport du temps sur l'instant de rupture, r étant la coordonnée radiale, r_b le rayon de la cellule, $N(r)$ correspond à la masse incluse dans un rayon r, N_b est la masse totale à l'instant de la rupture, α et β sont les paramètres de la loi d'échelle. Ici, pour des conditions aux bords de type CD100 : $\alpha = 1.58$ et $\beta = 1.02$, et de type OD100 : $\alpha = 1.73$ et $\beta = 1.10$

1.2 Article 2 - Fracturation pneumatique dans des milieux granulaires confinés

Dans cette étude, nous caractérisons les canaux formés durant l'injection d'air dans un milieu granulaire sec et dense confiné dans une cellule de Hele-Shaw linéaire et horizontal. La cellule présente une séparation inter-plaques de 1 mm, et est remplie avec un ensemble de billes de polystyrène non expansé de 80 microns de diamètre (fraction solide initial de 0.44 à 0.5). Le milieu granulaire dans la cellule occupe 70 cm de long et 32 cm de large, et il est empêché de sortir de la cellule par la présence d'un filtre perméable à l'air au niveau du côté de sortie. Sur le côté de l'injection, le milieu présente initialement une interface air-solide linéaire perpendiculaire à la direction de l'écoulement moyen. Durant les expériences, de l'air est injecté coté amont à surpression constante dans la gamme de 5 - 250 kPa, forçant l'air à couler à travers le milieu vers le bord de sortie. Une caméra rapide Photron SA5 capture le processus d'invasion depuis le surplomb de la cellule à un taux de 1000 images/s. Les expériences durent typiquement entre 1 et 5 s. Les canaux d'invasion résultant sont analysés par traitement d'images, durant lequel les motifs sont binarisés en seuillant les valeurs de niveaux de gris.

En fonction de la pression d'injection (et de la contrainte solide reliée à la fraction solide), nous observons que le milieu présente soit un comportement analogue à un solide, ou une transition d'analogue à fluide vers un comportement analogue à solide durant l'injection d'air. Dans le régime analogue à solide, il n'y a pas de déplacements apparents de grains et l'air atteint la sortie de la cellule en s'infiltrant à travers le réseau de pores entre les grains. D'autre part, dans le régime analogue à fluide, on observe une déformation significative, où les billes sont déplacées d'une quantité correspondant à plusieurs tailles de grains, par échange de quantité de mouvement entre les molécules d'air et les grains. A une surpression suffisante, le milieu granulaire a un comportement très semblable à celui d'un liquide visqueux envahi par de l'air, car le flux ouvre des canaux vides de grains, une instabilité de type Saffman-Taylor entraînant des motifs d'invasion dendritiques [4]. Un mécanisme de stabilisation de cette instabilité est la création de chaînes de frottement et de contrainte entre les billes pendant la compaction et, en raison des conditions aux limites, on arrive toujours à un milieu au comportement de type solide à la fin d'une expérience.

Pour explorer les régimes d'écoulement, nous avons varié la surpression appliquée dans la plage de 5 kPa à 250 kPa, et pour effectuer les moyennes des résultats observables pour des expériences similaires, nous définissons six catégories de flux typiques dans cette gamme de surpressions. Les structures finales typiques sont indiquées pour chaque catégorie sur la figure 1.6. Les comportements typiques d'écoulements dans les 6 catégories sont décrits comme suit:
Catégorie 1 - Pas de déformation.
Catégorie 2 - Le milieu est d'abord compacté sans formation de canaux d'invasion.
Catégorie 3 - Un canal court est formé, où la longueur finale du canal est inférieure à la moitié de la longueur du milieu initial.
Catégorie 4 - Un canal long est formé, où la longueur finale du canal est plus de la moitié de la longueur du milieu initial.

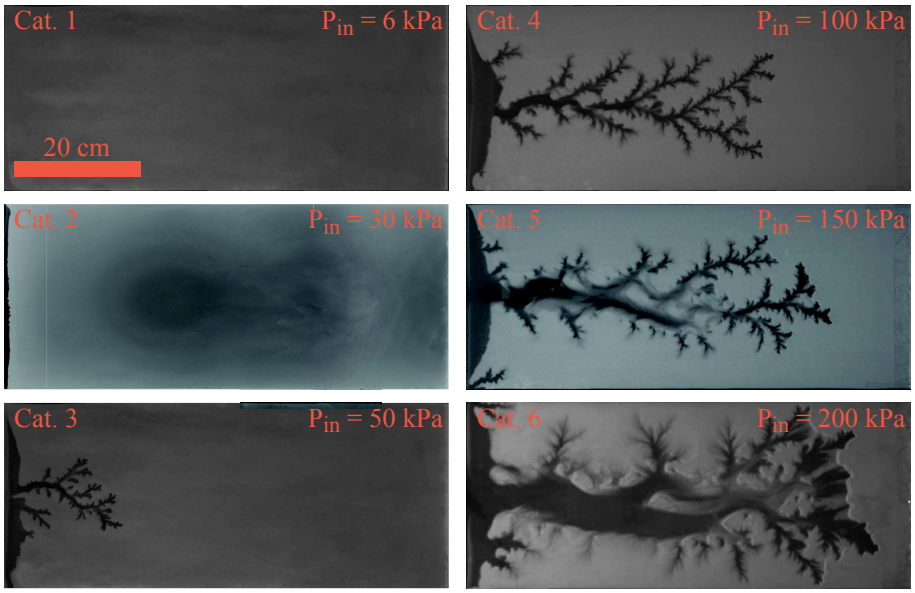

Figure 1.6: Structures finales typiques par catégorie, où le milieu granulaire est en gris et les zones vides de grains sont en noir, montrant que pour des pressions d'injection P_{in} croissantes, les doigts deviennent plus longs et plus épais.

Table 1.1: Catégories d'écoulement avec valeurs de pressions reliées ; surpression moyenne avec deux déviations standards $\overline{P_{in}} \pm 2\sigma$, et nombre d'expériences analysées N par catégorie.

Category	$\overline{P_{in}} \pm 2\sigma$ [kPa]	N
1	9 ± 5	3
2	26 ± 18	5
3	64 ± 50	5
4	110 ± 44	6
5	134 ± 43	10
6	213 ± 50	4

Catégorie 5 - Un canal long est formé avec un canal principal plus épais que les doigts en branche en raison de l'érosion à l'intérieur du canal.
Catégorie 6 - Un canal épais et long avec quelques branches est formé. De l'érosion et la fusion des canaux adjacents se passent pendant la croissance. Les gammes typiques de pression d'injection pour chaque catégorie sont indiquées dans le tableau 1.1.

La figure 1.7 montre les dimensions fractales évaluées localement $(D_L + 1)$ en fonction de la profondeur dans le milieu granulaire pour les structures finales. Les courbes montrent un comportement plus ou moins constant sur la plupart des profondeurs (la dimension haute initiale est due à une plus grande surface initiale vide de billes et la dimension inférieure finale est due à des effets de taille finie des motifs), ce qui indique que les motifs ont des dimensions fractales locales bien définies, constantes, dans la partie développée des canaux. Les modèles de catégorie 3, 4 et 5 ont des dimensions locales typiques correspondant aux dimensions globales D

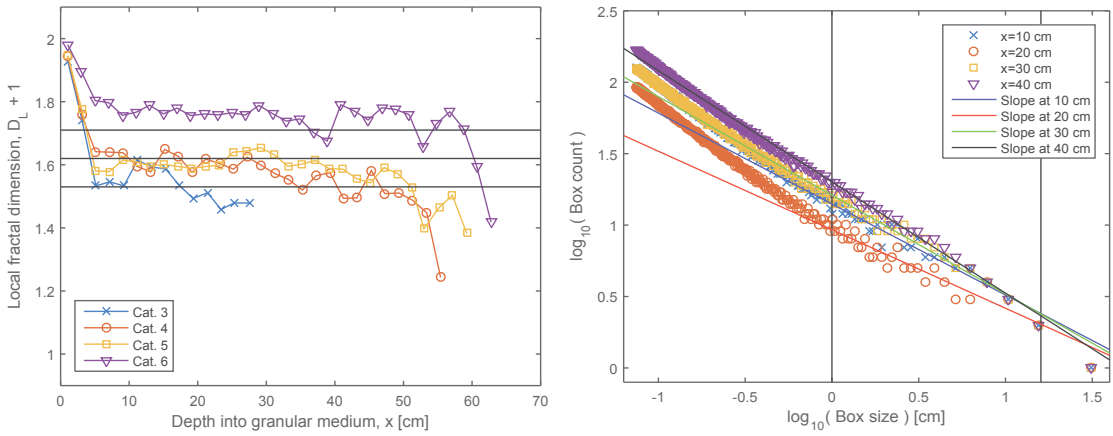

Figure 1.7: A gauche: Dimensions fractales locales ($D_L + 1$) en fonction de la profondeur dans le milieu pour les structures finales moyennées par catégorie. Nous voyons que les motifs dans toutes les catégories ont des dimensions locales plus ou moins constantes et bien définies en fonction de la profondeur. Les principales parties des motifs des catégories 3 à 5 ont des dimensions locales correspondant aux valeurs établies pour les doigts visqueux dans les milieux poreux saturés (entre les lignes en pointillés). Pour les motifs de la catégorie 6, les dimensions locales correspondent à des valeurs plus proches de la dimension fractale pour les motifs DLA et les motifs d'écoulement dans une cellule Hele-Shaw saturée (ligne continue). A droite: Exemples de pentes par comptage de boîte local à différentes profondeurs d'une même expérience.

= 1.53, 1.58, 1.60, respectively. respectivement. Ceci est dans la gamme des dimensions visibles pour les doigts visqueux dans les milieux poreux rigides, où D = 1.53 - 1.62 [1, 2, 5]. Pour les motifs de catégorie 6, la dimension locale est plus élevée, avec une valeur typique correspondant à $D = 1.76$, ce qui est plus proche des dimensions observées pour les amas d'agrégation limitée par diffusion (DLA) et les doigts visqueux dans une cellule Hele-Shaw saturée vide ($D = 1.71$) [6, 7].

Dans la figure 1.8 A) on voit que la longueur du canal croît linéairement avec le temps initialement avant de décélérer vers une longueur finale, et que la vitesse de croissance et la profondeur finale des structures d'invasion augmentent avec l'augmentation de la pression d'injection. Le taux de croissance constant initial semble être une loi d'échelle de la pression d'injection en $P_{in}^{\frac{3}{2}}$. Dans la figure 1.8 B), le graphe logarithmique de la vitesse de pointe $v(t)/(P_{in}^{3/2})$ en fonction du temps indique que lorsque la vitesse de la pointe des doigts diminue, elle suit une équation en loi de puissance du temps, $v(t) \propto t^{-\alpha}$, où $\alpha = 2.5 \pm 0.2$. Ainsi, la vitesse de croissance est constante initialement, avant de transiter vers une décroissance en loi de puissance avec le temps. Ce comportement est étudié plus en détail, la vitesse initiale constante v_0 est une l'échelle de la pression d'injection P_{in} en

$$v_0 = C \cdot P_{in}^{\frac{3}{2}}, \tag{1.4}$$

où $C \approx 10^{-\frac{3}{2}}$ cm/(s·kPa$^{\frac{3}{2}}$) est obtenu à partir de la partie initiale des courbes

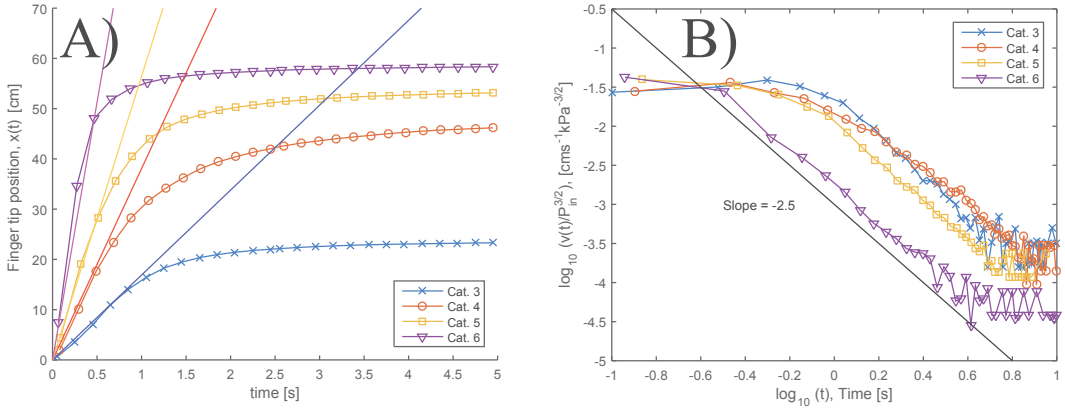

Figure 1.8: A) Position de la pointe des doigts $x(t)$ en fonction du temps, moyennée pour toutes les expériences par catégorie. Les courbes ont typiquement une croissance linéaire initiale avec le temps qui transite vers une décroissance avec le temps. Les motifs se développent plus rapidement et plus longtemps pour des pressions d'injection croissantes, et la croissance linéaire initiale est observées comme suivant une loi d'échelle proportionnelle à $P_{in}^{3/2}$ comme indiqué par les lignes en pointillés. B) Tracé bilogarithmique de la vitesse $v(t)$ de la pointe des doigts en fonction du temps, moyennée par catégorie. Les données sont regroupées suivant l'axe des ordonnées en divisant $v(t)$ par $P_{in}^{\frac{3}{2}}$, où $P_{in} = 64$, 110, 134 and 213 kPa, pour les catégories 3, 4, 5 et 6 respectivement. Le plateau constant initial correspond à la période à croissance linéaire avec le temps, qui transite ensuite vers une loi de puissance, droite de pente descendante proche de -2.5 (ligne en tirets) pour toutes les catégories, montrant que la décélération de la vitesse de croissance suit une loi de puissance avec le temps d'exposant.

cumulées $v(t)/P_{in}^{\frac{3}{2}}$ sur l'axe des ordonnées de la figure 1.8 B). En insérant la valeur de C dans l'équation (1.4), nous pouvons à la place regrouper les courbes le long de l'axe des ordonnées avec $v(t)/v_0$ résultant en unités sans dimension et normalisées pour la vitesse. Afin de regrouper les courbes le long de l'axe temporel, on définit un temps critique $t = t_c$ comme le moment où la vitesse de croissance passe d'une constante à une décroissance de la loi de puissance avec le temps. Au moment critique, la position de pointe de doigt peut être décrite comme

$$x_c = x(t_c) = v_0 \cdot t_c, \tag{1.5}$$

ce qui donne

$$t_c = \frac{x_c}{v_0} = \frac{x_c}{C \cdot P_{in}^{\frac{3}{2}}}. \tag{1.6}$$

De plus, nous vérifions si x_c peut être décrit comme une fraction typique R de x_f, la longueur finale du canal, résultant en $x_c = R \cdot x_f$, ce qui donne

$$t_c = \frac{R \cdot x_f}{C \cdot P_{in}^{\frac{3}{2}}}. \tag{1.7}$$

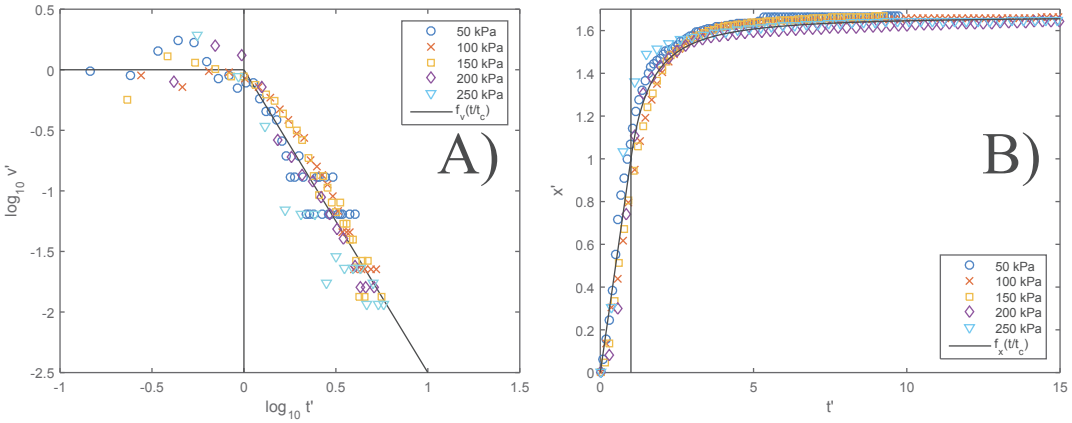

Figure 1.9: A) Tracé logarithmique des vitesses de pointe de doigts regroupées en données réduites $v' = v(t')/v_0$ en fonction de $t' = t/t_c$ pour des expériences individuelles avec diverses pressions d'injection. La ligne verticale pointillée indique la transition en $t' = 1$, et la courbe en tirets montre la fonction proposée $f_v(t')$. Rappelons que les paramètres utilisés pour le regroupement des courbes sont donnés par la pression d'injection, comme $v_0 = C \cdot P_{in}^{\frac{3}{2}}$ et $t_c = ((\alpha - 1)/\alpha) \cdot (x_f/v_0(P_{in}))$, où $C = 10^{-\frac{3}{2}}$ cm/(s·kPa$^{\frac{3}{2}}$) et $\alpha = -2.5$. B) Les positions de pointe de doigt regroupées en données réduites $x' = x(t')/v_0 \cdot t_c$ en fonction de $t' = t/t_c$, pour les mêmes expériences individuelles. La ligne verticale pointillée indique la transition en $t' = 1$, et la courbe en tirets montre la fonction proposée $f_x(t')$.

En traçant $v(t^*)/v_0$ en fonction de $t^* = t \cdot (v_0/x_f) = R \cdot (t/t_c)$ dans un graphe log-log, on constate que les courbes se regroupent le long de l'axe temporel avec un point de transition correspondant à $R \approx 0.6$. Puisque nous avons maintenant les constantes C et R, on peut calculer v_0 et t_c pour les expériences individuelles en insérant les P_{in} et x_f respectifs dans les équations (1.4) et (1.7). La figure 1.9 A) montre des tracés en log-log échelonnés de $v' = v(t')/v_0$ en fonction de $t' = t/t_c$ pour les expériences individuelles avec des pressions d'injection dans la plage de 50 à 250 kPa, qui suivent la même courbe sans dimension donnée par la fonction

$$f_v(t') = \begin{cases} 1, & \text{if } t' \leq 1 \\ t'^{-\alpha}, & \text{if } t' > 1, \text{ where } \alpha = 2.5. \end{cases} \tag{1.8}$$

De la même façon, nous regroupons la position de la pointe de doigt $x' = x(t')/x_c$ et nous la représentons en fonction de $t' = t/t_c$ pour les mêmes expériences individuelles, comme le montre la figure 1.9 B). Ici, les données regroupées suivent la courbe donnée par la fonction

$$f_x(t') = \begin{cases} t', & \text{if } t' \leq 1 \\ \frac{1}{1-\alpha} t'^{1-\alpha} + \frac{\alpha}{\alpha - 1}, & \text{if } t' > 1, \end{cases} \tag{1.9}$$

Qui est trouvée en intégrant chaque partie de l'équation (1.8), en exigeant que $f_x(t' > 1) \to 1$ lorsque $t' \to 1$. De plus, $f_x(\infty) = \alpha/(\alpha - 1) = x_f/x_c = 1/R$, ce

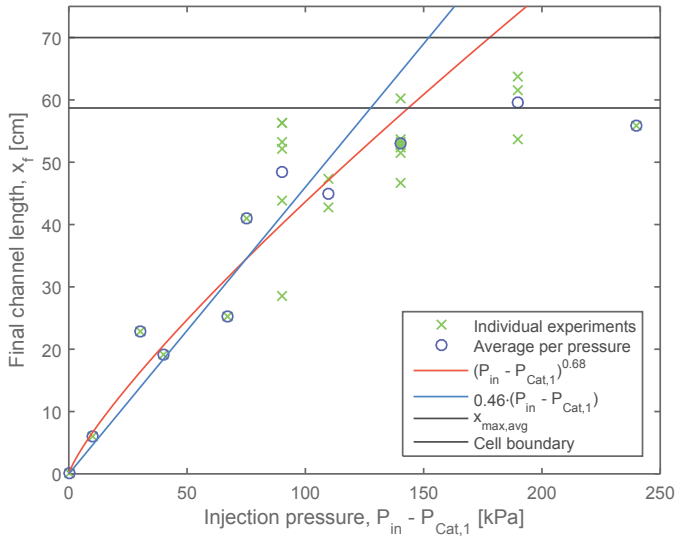

Figure 1.10: La longueur finale du canal x_f est tracée en fonction de $(P_{in} - P_{cat,1})$, où $P_{cat,1} = 9$ kPa est la pression d'injection moyenne pour la catégorie 1, où $x_f = 0$. On observe une certaine dispersion (due à la variabilité des configurations initiales de grains d'une expérience à l'autre), mais également une tendance croissante dans x_f pour des pressions d'injection P_{in} croissantes, et que la longueur de canal final pour les pressions d'injection les plus élevées est limitée par la frontière extérieure fermée. Une relation $(P_{in} - P_{cat,1})^{0.68}$ a été déterminée à partir des valeurs moyennes de x_f par pression pour $P_{in} \in [20, 150]$ kPa et suggèrent une en loi de puissance. Alternativement, le modèle linéaire $0.46 \cdot (P_{in} - P_{cat,1})$ est tout aussi efficace. La longueur maximale moyenne des canaux $x_{max,avg}$ a été trouvée en faisant la moyenne de x_f sur les expériences avec $P_{in} \geq 200$ kPa, pour indiquer l'influence de la taille finie des cellules.

qui donne $R = (\alpha - 1)/\alpha = 0.6$, ce qui correspond très bien à nos observations. En substituant α dans l'équation (1.7), on obtient

$$t_c = \frac{\alpha - 1}{\alpha} \cdot \frac{x_f}{C \cdot P_{in}^{\frac{3}{2}}}. \tag{1.10}$$

Avec les équations (1.4 - 1.10), nous proposons une description de la dynamique fondamentale du système. Puisque nous avons estimé expérimentalement α et avons l'équation (1.4) reliant la vitesse de croissance initiale à la pression d'injection, nous pouvons estimer l'évolution de la longueur de canal pendant l'invasion pour une pression d'injection donnée et une longueur de canal finale. Pour une description complète, l'étape suivante consiste à caractériser la dépendance de x_f sur P_{in} Pin de sorte que le résultat attendu d'une injection d'air puisse être estimé par la seule pression d'injection. Une brève discussion à ce sujet est présentée à la figure 1.10.

Une présentation plus détaillée des méthodes et des résultats de cette étude est donnée dans l'article connexe présenté au chapitre 5. L'article a été soumis à Physical Review E en octobre 2016.

1.3 Article 3 - Évolution de la pression et déformation des milieux granulaires confinés lors de fracturation pneumatique

Nous présentons ici une étude sur l'évolution des déformations et de la pression interstitielle dans un milieu granulaire dans les mêmes expériences que dans la section précédente. Les champs de déplacement du milieu granulaire sont obtenus à partir d'images expérimentales par corrélation d'image numérique (DIC), et l'évolution de la pression de fluide poreux est estimée numériquement en résolvant une équation de diffusion pour la surpression de la phase air. En outre, nous évaluons la solution de l'équation de Laplace pour le champ de pression à chaque instant pour vérifier si, quand et où le champ de pression diffusante peut être approché par l'équation de Laplace.

Typiquement, le processus de déformation pendant les expériences peut être séparé en 3 étapes; La mobilisation initiale des grains, la formation des canaux et la compaction autour, et l'étape en instabilités de glissement dans un milieu compacté. Parce que le système devient bloqué en raison des conditions aux limites, peu d'activité a lieu après 5 s. En comparant la différence entre la pression de pore diffusante et pression solution de Laplace, nous avons constaté que les deux solutions sont pratiquement égales après 0.8 - 1 s. La partie gauche de la figure 1.11 montre des instantanés de l'amplitude de la vitesse granulaire pendant des fenêtres temporelles de 10 ms pour une expérience avec une pression d'injection de 200 kPa. Les instantanés sont centrés sur $t = 100$, 200, 300, 400, 500 et 600 ms, montrant des déplacements typiques pendant les étapes initiales de mobilisation et de chenalisation. Le premier instantané, à $t = 100$ ms se trouve dans la dernière partie de l'étape de mobilisation initiale. Il n'y a toujours pas de canal formé, juste une interface légèrement incurvée air-solide avec une zone de grains mobilisés devant elle, couvrant environ la moitié de la cellule. Le déplacement se fait principalement dans le sens de l'écoulement, et est plus rapide le long du centre de la cellule et plus proche de l'interface air-solide. Le reste des instantanés, $t = 200 - 600$ ms, sont pris au cours de l'étape d'instabilité et de compaction. Au cours de cette étape, les doigts s'ouvrent et forment un canal d'invasion croissant dans le temps. La zone initialement grande et étalée de grains mobilisés devant l'interface air-solide se rétrécit en taille et amplitude au fil du temps, en se concentrant autour des pointes des plus longs doigts. Les déplacements sont les plus importants près et à l'avant des doigts les plus longs, et les mouvements derrière l'extrémité des doigts les plus longs sont très modérés. La partie droite de la figure 1.11 montre les valeurs absolues du gradient de pression $|\nabla P|$, à la fois pour les champs de pression diffusante et de pression laplacienne, aux mêmes instants que ceux décrits ci-dessus. Au cours de la croissance du canal (avant même que la pression diffusante converge vers la solution de Laplace), la pression diffusante est similaire à la pression de Laplace en ce qui concerne l'écrantage des gradients de pression derrière les pointes de doigt les plus longues, et sur la présence des gradients de pression les plus élevés devant les plus longs doigts. De plus, au cours de l'expansion rapide des canaux, l'amplitude des gradients de pression dans le champ de pression diffusante semble être jusqu'à

1.5 - 2 fois supérieure à ceux de la solution de Laplace dans la région entourant les pointes de doigt les plus avancées (entre 5 et 8 cm). Nous voyons que les régions les plus déplacées du milieu coïncident bien avec les gradients de pression les plus élevés, tandis que $|\nabla P|$ et $|\vec{v}_g|$ tendent vers 0 derrière les plus longs doigts.

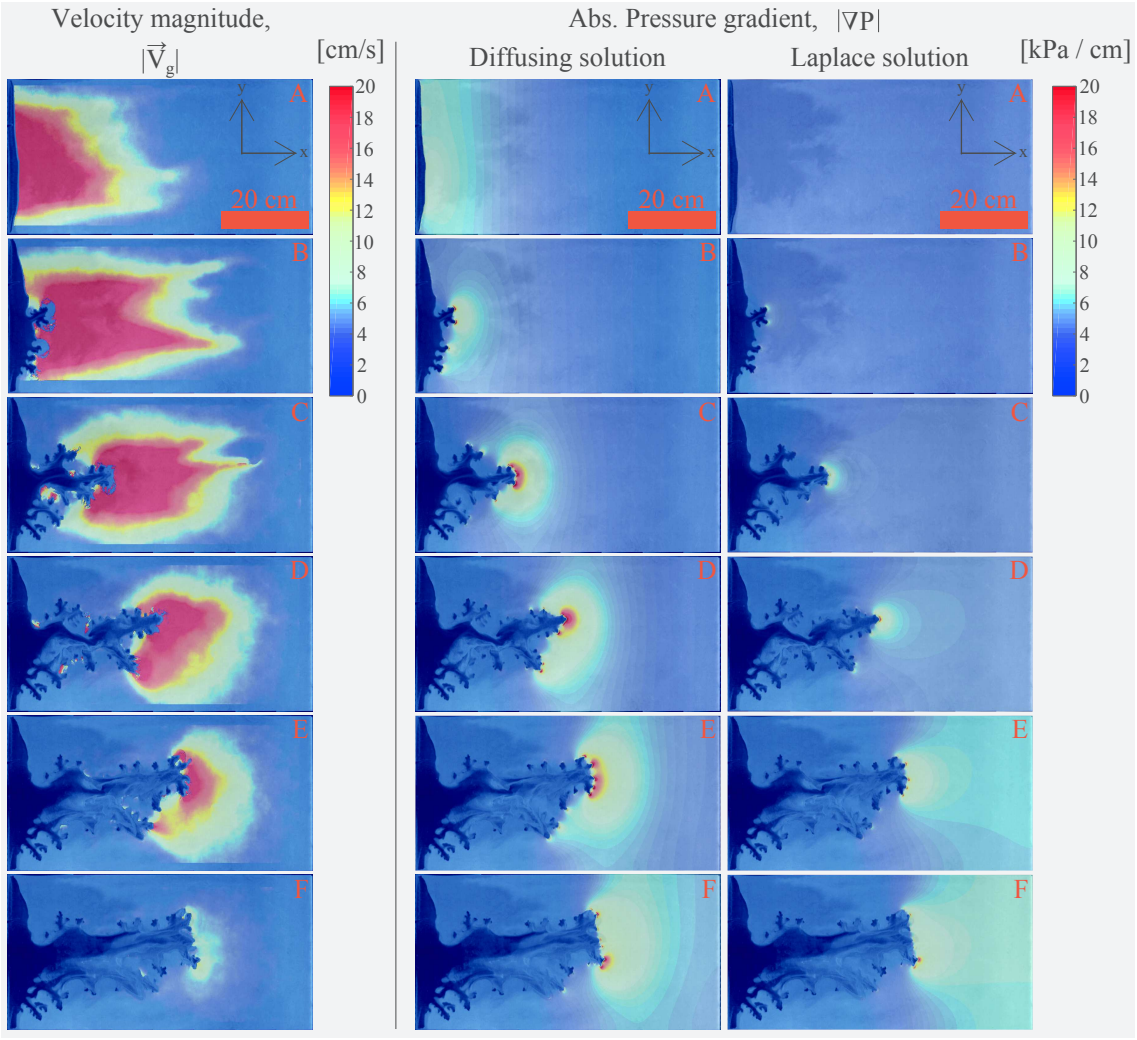

Figure 1.11: Gauche : Magnitude de vitesse moyenne $|\vec{v}_g|$ durant des fenêtres en temps de largeur $\Delta t = 10$ ms, centrées sur $t = 100$, 200, 300, 400, 500 et 600 ms pour les instantanés A-F respectivement. La pression d'injection est de $P_{in} = 200$ kPa. La zone de grains mobiles croît initialement jusqu'à l'échelle de la cellule, puis ensuite se focalise sur le doigt le plus avancé lorsque le milieu se compacte. Les grains derrière le canal le plus avancé ne sont pas significativement déplacés (Noter que nous avons retiré les données dans le canal, cependant du bruit provenant du mécanisme d'érosion dans le canal apparaît en C - E). Droite : valeur absolue du gradient de pression pour les deux solutions de pression dans les instantanés A-F. La différence principale entre les champs diffusant et Laplacien est que la pression diffusante présente des gradients plus forts autour de l'interface air-solide et des extrémités de doigts, alors qu'elle présente des gradients moins forts autour de l'interface de sortie. A partir de 'instantané F, les gradients commencent à sembler similaires en magnitude autour des canaux. Dans les deux solutions, le gradient de pression est écranté derrière les doigts les plus avancés, et les magnitudes les plus élevées sont présentes autour des doigts les plus longs.

La direction de la force motrice (opposée au gradient de pression) se trouve bien en corrélation avec la direction du déplacement granulaire. Pour les déplacements au-dessus du seuil de bruit de 0.1 pixel, nous montrons, en évaluant le coefficient de corrélation normalisé pour les directions, que les grains se déplacent plus ou moins toujours dans la direction opposée au gradient de pression. De plus, on trouve la zone de compaction à partir des champs de déplacement total en tant que zone où les billes ont été déplacées de plus d'un dixième de pixel (70 µm), c'est-à-dire comme zone où les billes qui été déplacées par rapport à la configuration initiale. La zone de compaction croît dans la direction de l'entrée vers la sortie, et dans toutes nos expériences, elle atteint la limite de sortie peu de temps après le début de l'injection, typiquement après $t = 170$ à 250 ms.

L'amplitude de la vitesse dans la région en avant des canaux en développement est trouvée comme présentant une relation linéaire par rapport au gradient de pression moyen, dispersée mais assez claire. Le coefficient α des fits linéaires

$$|\vec{v}_g| = \alpha|\nabla P| + c \tag{1.11}$$

décrivant la croissance moyenne de la vitesse due à une croissance de ∇P est représentés en fonction du temps pour les expériences à pression d'injection $P_{in} =$ 150, 200 and 250 kPa dans le graphe de gauche de la figure 1.12. Pour regrouper les données le long de l'axe des temps, on utilise le temps normalisé $t' = t/t_c$ où t_c est le temps auquel la zone compactée atteint le bord de sortie dans les expériences respectives. Nous observons pour toutes les expériences que pour les temps précédant celui où la zone compacte atteint la sortie, α augmente linéairement avec le temps. Ensuite, après que le front de compaction ait atteint le bord de sortie, α semble présenter une décroissance exponentielle avec le temps. L'insert dans la figure de gauche sur la figure 1.12 montre qu'il y a une seuil de transition en gradient de pression ∇P_c tel que $|\vec{v}_g| = 0$ si $\nabla P < \nabla P_c$, i.e. aucun mouvement de grains n'est observé en dessous de ce seuil. Le gradient seuil est lié à l'équation(1.11) en écrivant $|\vec{v}_g| = \alpha(\nabla P - \nabla P_c)$, où $\nabla P_c = -c/\alpha$. Les seuils ∇P_c ne viennent pas des forces exercées par l'air, mais de la contrainte solide le long des plaques, qui dépendent des contraintes solides normales et des configurations de grains, ainsi que des contrainte dans le plan. C'est donc essentiellement une manifestation de la contrainte solide transmise dans les contacts entre les grains et entre grains et plaques, que nous ne modélisons pas ici, mais que nous mesurons indirectement globalement à travers ∇P_c. Les forces déplaçant les grains dans le milieu granulaire sont reliées au gradient de pression intersticielle $-\nabla P$, ainsi que les contraintes solides normales et de cisaillement entre billes et plaques. Nous ne résolvons pas directement les contraintes solides à partir des expériences, mais si la force motrice principale ressentie est due à l'échange de quantité de mouvement avec l'air, $-\nabla P$, ceci suggère une rhéologie de type non-Newtoniennes pour le milieu granulaire entre les plaques. Supposant une rhéologie de type Bingham où

$$\vec{v}_g = -\frac{h^2}{\mu_B}(\nabla P - \nabla P_c), \tag{1.12}$$

et où h est l'écart entre plaques, la pâte granulaire a une viscosité de Bingham effective $\mu_B \propto 1/\alpha$. Si la force principale ressentie par le milieu est due à $-\nabla P$,

nos résultats suggèrent une décroissance en $\mu_B \propto t^{-1}$ avant que la zone compactée atteigne le bord de sortie, et une viscosité de Bingham effective croissant exponentiellement en temps $\mu_B \propto e^{\beta t}$ après que la zone compactée ait atteint le bord de sortie. Le seuil ∇P_c évolue durant les expériences comme montré dans la figure de droite sur la figure 1.12 pour les expériences avec pressions d'injection $P_{in} = 150$, 200 et 250 kPa. Une fois de plus, les données ont été regroupées le long de l'axe en temps en normalisant par le temps auquel la zone compactée atteint le bord externe. Nous observons que les seuils moyens ∇P_c diminuent de façon similaire lorsque avant que la zone compacté atteigne le bord, décroissant à partir de ∇P_c entre 10 et 15 kPa/cm initially, intialement, jusqu'à un minimum autour de 1 - 2 kPa/cm autour du temps auquel la zone compactée atteint le bord. Après cet instant, les seuils commencent à augmenter, d'autant plus rapidement que la pression d'injection est élevée. Ceci dépend probablement de la pression d'injection et de la vitesse de croissance du canal d'invasion, i.e. du taux de compaction et des forces disponibles pour compacter le milieu plus encore. Lorsque l'augmentation de ∇P_c ralentit (autour de t/t_c vers 2.5 - 3), les seuils approchent le gradient de pression dans la zone entourant les doigts les plus longs. En conséquence, le milieu devient progressivement similaire à un solide avec une partie mobile se réduisant aux alentours des doigts les plus longs puis disparaissant, et on transite vers le régime compacté.

Une présentation plus détaillée des méthodes et résultats dans cette étude est donnée dans l'article relié présenté au chapitre 6. L'article est un manuscrit proposé pour être soumis à Physical Review E dans un futur proche (2017).

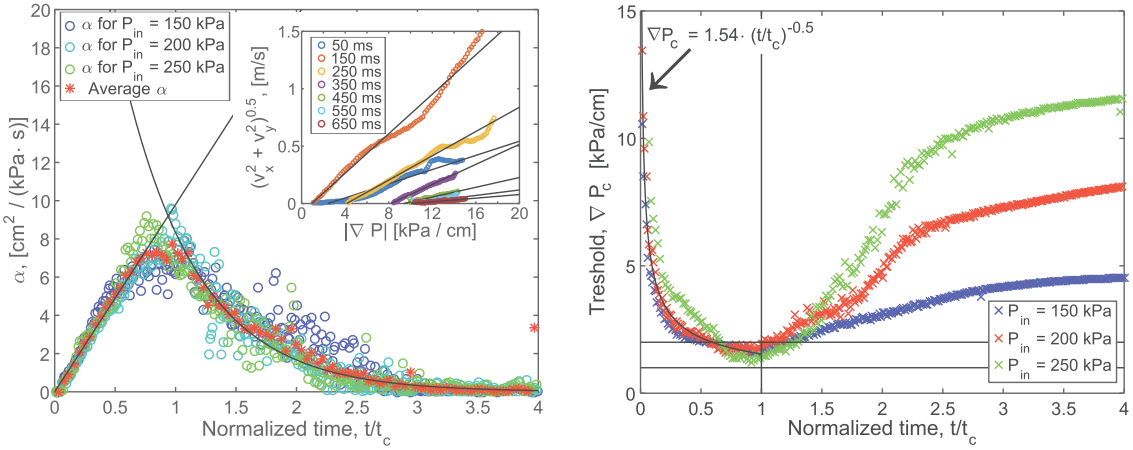

Figure 1.12: Gauche : évolution du paramètre de fit linéaire α avec le temps, décrivant la relation moyenne $|\vec{v}_g| \approx \alpha \cdot |\nabla P| + c$ entre l'amplitude de la vitesse granulaire $|\vec{v}_g|$ et la norme du gradient de pression $|\nabla P|$. Les figures pour α proviennent d'expériences où la pression d'injection vaut $P_{in} = 150$, 200 et 250 kPa, où les données ont été regroupées le long de l'axe en temps en normalisant par t_c, temps où la zone compactée atteint le bord de sortie. Avant cet instant ($t < t_c$), α augmente linéairement avec le temps (relation linéaire $\alpha = 9.8 \cdot (t/t_c)$), alors que pour $t > t_c$, α présente une décroissance exponentielle avec le temps (fit exponentiel $\alpha = 41.68 \cdot e^{-1.61(t/t_c)}$). Dans l'insert : Exemples de fits linéaires de la norme de la vitesse moyenne en fonction du gradient de pression. Noter qu'au cours du temps, apparaît un décalage depuis l'axe des ordonnées, correspondant au seuil $\nabla P_c = -c/\alpha$. Pour les expériences avec pressions d'injection $P_{in} = 150$, 200 et 250 kPa, la valeur de t_c est respectivement 240, 250 et 170 ms. Droite : Evolution des seuils ∇P_c en fonction du temps normalisé t/t_c pour les expériences avec $P_{in} = 150$, 200 et 250 kPa. Pour $t/t_c \leq 1$, les seuils décroissent depuis 10 - 15 kPa/cm initialement jusqu'autour de 1 à 2 kPa/cm (indiqués par les lignes horizontales). Après que la zone compactée ait atteint le bord de sortie, pour $t/t_c = 1$, ∇P_c commence à augmenter en temps, plus rapidement pour des pressions d'injection croissantes. Ensuite, pour t/t_c autour de 2.5 3, l'augmentation du seuil avec le temps ralentit. Après cet instant, ∇P_c approche les valeurs de gradient de pression de pore $|\nabla P|$ dans la zone entourant les doigts les plus longs.

1.4 Article 4 - L'évolution de l'aero-fractures et les caractéristiques des émissions acoustiques dans un milieu poreux

Dans cet article, les émissions acoustiques (issues du même type d'expérience présentée dans l'article 2 et 3) sont enregistrées et analysées simultanément aux données optiques. Les émissions acoustiques sont enregistrées en utilisant des capteurs piézoélectriques et des accéléromètres. Tous les capteurs sont attachés sur la plaque du bas de la cellule de Hele-Shaw. Durant les expériences, les interactions entre la partie solide et la partie fluide (l'air) dans la cellule génèrent des émissions acoustiques qui sont transmises par les plaques en verre et enregistrées par les différents capteurs. Les différents événements acoustiques sont caractérisés et comparés dans le domaine de Fourier. Finalement, on a défini deux différents types d'événements, le type 1 et le type 2. Le type 1 correspond à des événements qui ont les caractéristiques suivantes: ils sont émergents, c'est à dire non impulsifs, ils sont dominés par les basses fréquences et ils durent plus longtemps que le type 2. Les événements de type 1 sont générés durant la formation des canaux et la compaction du milieu poreux. Au contraire, les évènements de type 2 ont une fréquence moyenne plus haute, ils sont impulsifs et de courte durée. Ils commencent à apparaitre vers la fin de la formation des canaux pendant le réarrangement des grains. Par ailleurs, on a remarqué que la fréquence moyenne du signal (dans une fenêtre temporelle d'environ 5 ms) évolue pendant la formation des canaux. Le nombre cumulatifs des événements de type 2 suit une loi "d'Omori modifiée" de la même manière que les aftershocks après un tremblement de terre. Cet article a été publié dans Frontiers in Physics en Septembre 2015 et a été ajouté dans le chapitre final de cette thèse.

1.5 Article 5 - Localisation basée sur l'homogénéité d'énergie estimée de la source

Dans cet article on propose une nouvelle méthode de localisation de la source d'un signal basée sur l'énergie de la source. La méthode est développée et testée avec des données synthétiques et expérimentales. Une bille en acier est lancée sur des points marqués sur une plaque en verre (ou en plexiglass selon les expériences). La distance entre la position estimée et la position réelle a été enregistrée pour plusieurs points. La nouvelle méthode de localisation a été comparée avec les méthodes préexistantes. On a conclu que la méthode proposée est polyvalente et qu'elle donne de meilleurs résultats que les autres méthodes. La méthode utilise les signaux arrivant à plusieurs capteurs (4 dans le cas présent) et calcule l'énergie de la source grâce à une grille couvrant tout l'espace où peut être positionnée cette source. Sur la grille, le meilleur ajustement (best fit) des positions estimées par tous les capteurs montre la position finale estimée de la source. La qualité de l'estimation avec cette méthode a été comparée pour différentes fréquences d'échantillonnage, pour des plaques dispersives ou non dispersives et avec ou non des ondes réfléchies sur les côtés des plaques (plaques infinie ou finie). Il est possible d'adapter cette méthode

en 3D dans le cadre d'un futur projet. Cet article a été publié in Review of Scientific Instruments en Septembre 2016 et a été ajouté dans le chapitre final de cette thèse.

Chapter 2

Introduction

This thesis is article based, so the text is intended to wrap up the work and results covered in the papers, making it easier to read the work as a whole. This first chapter gives a general introduction to the topic of flow in transforming porous media in the field of experimental geophysics and physics. The problem is put into context, and various challenges and motivations for studying such processes are introduced. Chapter 2 introduces basic concepts and analysis methods. Then, the work of this thesis is presented in separate chapters for each paper, including the main questions, methods and results. In the final chapter, future perspectives are discussed. The thesis also has an appendix including the scientific articles where I contributed as a co-author with experiments and discussions.

2.1 Context and motivation

During many subsurface processes in nature and industry, the flow of fluids transforms the surrounding porous medium containing them (reservoir), e.g. when fluids flow at a high rate between the grains of soil or chemically react with the solid within pore networks in rocks. Depending on the involved mechanisms, these transformation processes can be fast, lasting only a couple of seconds or less, or slow, lasting from a few hours to several weeks or more. Fast transformation processes of reservoirs include sudden mechanical deformation, fracturing and channel formation due to sufficient overpressure or flow rates in the pore fluid. Slow transformation processes of reservoirs include chemical evolution of existing fractures or pore networks due to reactions between the flowing fluid and host medium, i.e. dissolution and precipitation. Reservoir transformation processes further increase or decrease the permeability of the system, which influences the flow of pore fluids and may change the stresses in the material surrounding the deformations. Thus regardless of rate, reservoir transformations due to fluid flow change the boundary conditions of the flow which itself is causing the changes on the host medium. These are cases where the deformations and fluid flow are coupled processes, which makes a system very challenging to fully understand. Even as separate problems, fluid flow in porous media and deformation of granular media are complicated processes, for example granular materials may have a behavior that resemble solid-, liquid-, or gas-like materials depending on the flow regime. This is one of the special properties of granular

materials [8]. In addition, the rheology of dense granular fluids is very complex and is still an open research topic [9]. Another example is immiscible flow in porous media, i.e. flow involving at least two fluids that cannot mix, where one fluid is displacing the other. This adds interfacial forces to the system, which influences the flow path taken by the fluids.

Since flow and deformations in porous media often occur in nature and industry, this is a heavily researched topic in many fields of earth sciences. In some cases, for example, the research is focused on understanding and preventing dangerous situations due to high pressures and deformations, while in other cases it is studied for situations where such processes are desirable to induce in a controlled manner. In physics, a motivation for studying this topic is to increase the fundamental understanding of these complex systems, and in geology further knowledge of such processes help to explain active natural systems or structures formed in soil and rocks. Furthermore, increased knowledge of the fast transformation processes may have applications in earth science and industry where multiphase flow and solid deformation occur; Several processes in engineering, industry and earth sciences involve pneumatic (gas) or hydraulic (liquid) fracturing of the soil, which occurs when fluids in the ground are driven to high enough pressures to deform, fracture and generate porosity in the surrounding soil or rock. For example in environmental engineering, pneumatic or hydraulic fracturing is done to enhance the removal of hazardous contaminants in the vadose zone (soil remediation) [10, 11], for soil stabilization injection to ensure a solid foundation for structures [12], or in packer tests for project planning, risk assessment and safe construction of dams and tunnels [13]. In industry, hydraulic fracturing is done to enhance oil and gas recovery [14–16], CO_2 sequestration [17], water well- and geothermal energy production [18–20]. Related natural processes such as subsurface sediment mobilization are studied in earth sciences, where sand injectites, mud diapirs and mud volcanoes are formed due to pore-fluid overpressure [21–26]. For example, the Lusi mud volcano in Indonesia is the biggest and most damaging mud volcano in the world [27], having displaced 40 000 people from their homes, and has been active since May 2006. There is an ongoing debate about how it was triggered, i.e. whether it formed naturally by an earthquake or geothermal process [28–31], or that it is a man-made consequence of a nearby drilling operation by a company probing for natural gas [32]. The evolution of faults and fractures at crustal scale can also be affected by fluid flow [33–35] as well as the rheology of fluid saturated faults [36–38].

2.2 Experimental study of flow in complex systems

There are many methods and challenges in researching flow of fluids in complex systems such as granular materials. However, real-world systems are difficult to analyze; obviously we can not directly see what is going on in the soil during such processes, and we cannot completely recreate such systems at the lab scale. In experimental geophysics and complex matters physics, this topic is widely studied in experiments where a complex system is decomposed into simpler analog models

such that one can observe and investigate isolated fundamental processes which play a role in the bigger picture. A widely used tool for simplified flow experiments is the Hele-Shaw cell, which is a thin cell made up of two glass plates separated by a very small gap (usually 0.1 - 1 mm) compared to their surface area. In a Hele-Shaw cell, the geometry of the problem is reduced from 3-D to quasi-2-D, the cell orientation can be used to effectively adjust or remove the influence of gravity, and perhaps most importantly one can directly see what is going on during experiments. In such a simplified system, a sample can be prepared to represent a transparent quasi-2-dimensional rock/soil analog. Experimental data can be captured in the form of time-lapse image sequences, such that post-experiment image processing and analysis yield information about the growth and shape of the flow patterns over time, as well as eventual deformation fields in the host medium. Similarly, numerical models may be created and validated in 2-D before expanding to the more complicated 3-D case.

In early research on the flow of two immiscible fluids in Hele-Shaw cells, it was found that the invasion by a less viscous fluid into a more viscous fluid results in a displacement instability where viscous fingering patterns form [4]. This means that the invading fluid displaces the more viscous one in separated finger-like intrusions, while leaving the fluid inbetween the fingers less or not displaced. Following an increased interest in this phenomenon, two-phase flow have been widely studied in quasi-2-dimensional porous media confined in thin cells with radial and linear geometries [2, 39–50]. In horizontal cells containing rigid disordered porous media, the unstable invasion patterns during drainage are found to be fractal and either form an invasion percolation cluster [51] in the capillary fingering regime [52, 53], or long thin fingers resembling Diffusion Limited Aggregation (DLA) patterns in the viscous fingering regime [1, 54]. The flow regime depends on the ratio between the driving and stabilizing forces involved in flow and pore-invasion. In systems where air is injected with high enough overpressure into dry dense granular media in thin cells, granular fingering patterns (channels empty of particles) emerge as a result of pneumatic fracturing [55–59]. This granular fingering instability is also observed in liquid saturated dense porous media where the same fluid is injected [60]. The patterns formed during fluid injection into a granular medium, and evolution of the fluid-solid interface, have been found to resemble viscous fingering [57]. The decompaction, fluidization regimes, and coupling between air and granular flow have been studied for air injection at different overpressures in cells with open outer boundary [56, 58]. A similar confined system, where the granular medium cannot leave the cell, was studied in numerical simulations in [59, 61]. During air injection at different overpressures they found that fractures grow faster, longer, as well as coarsen with increasing injection pressure. Further, by varying the interstitial fluid viscosity, two flow regimes were identified; one with finely dispersing bubbles and large scale collective motion of particles, the other one with build-up of a compaction front and fracturing. These flow regimes depend on whether the medium is primarily deformed by the imposed pressure gradient in the fluid, or interactions through particle contacts. This in turn depends on the diffusivity of the interstitial fluid pressure in the granular medium. The main difference between the viscous- and granular fingering instabilities is the absence of interfacial tension in the granular case [58]. However,

both instabilities are driven by the pressure gradient across the defending medium, which is largest on the longest finger tips. Therefore, more advanced fingers grow on expense of the less advanced ones. Another notable difference between air injection into a dry granular medium and a liquid saturated one is that the overpressure initially diffuses into the packing in the dry case (compressible flow), while it is already a steady-state Laplace field over the defending liquid in the saturated case (incompressible flow).

Moreover, combinations of immiscible and granular flow in thin cells have been studied, during air injection into liquid saturated granular media and suspensions. The characteristics of emerging patterns and behavior of the media depend on injection rate and the competition between mobilized friction and surface forces [5, 40, 43, 51, 62–71]. For example, one observes flow regimes such as two phase flow in rigid porous media [40, 51, 69–71], capillary fracturing [63], stick-slip bubbles and labyrinth patterns [5, 43, 62–68]. In the opposite case, during liquid injection into dry granular media [42], the flow behavior goes from stable invasion towards granular fingering for increasing flow rate and viscosity of the invading fluid. At intermediate conditions, fractures open up inside the invaded region. The same trend is shown in numerical studies for gas injection into granular media containing the same gas [59]. Granular fingering instabilities have also been studied in closed vertical cells, where gravity drives the flow as heavier beads fall down from a granular layer at the top of a lighter fluid layer [45, 47, 48, 72–74]. When the beads detach at the front, they form fingers of falling granular material surrounding finger-like bubbles of rising fluid. These fingers are found to coarsen over time until they reach a typical wavelength depending on the interstitial fluid and bead size.

The motivation for investigating fundamental properties of flow in porous media in table-top experiments is to develop theoretical models describing the mechanisms of deformation, dynamic evolution and structure of flow patterns on pore- and sample scale, as well as how these phenomena scale with e.g. size, time and driving forces. Later on, such models can be considered when investigating more complex systems such as in 3-D geometry and natural phenomena.

2.3 The focus of this thesis

Based on table-top experiments and numerical simulations, we study the fast processes of fluid flow in deforming granular media and evolving fractures. Air is injected at constant overpressure into saturated or dry granular media confined inside Hele-Shaw cells. We vary boundary conditions, injection pressure and initial saturating fluid of the medium. In addition, we present a sub-project focused on slow processes with experiments on reactive flow in fractured calcite samples. The rest of this section presents a summary of the specific experiments we performed.

We present an exploratory study where we experiment with the combination of two-phase and granular flows by performing air injection into saturated monolayers of beads. Here, we study the formation of viscous fingering and fracturing patterns that occur when air at constant overpressure invades a radial Hele-Shaw cell containing a liquid-saturated deformable porous medium, i.e. during the flow of two non-miscible fluids in a confined granular medium at high enough rate to de-

form it. The sample is created by preparing monolayers of glass beads in cells with various boundary conditions, ranging from a rigid disordered porous medium to a deformable granular medium with either a semi-permeable or a free outer boundary. By injecting air at constant overpressure into a deformable saturated monolayer of beads, we have a system where particles may be displaced by a viscous pressure gradient and/or interfacial forces between the two fluids. Since it is a single layer of beads without imposed confining pressure, granular stress is expected to depend on the boundary condition and number of particles in contact ahead of the flow, rather than build-up of normal stress against the plates. As a result of competition between viscous and capillary forces, and build-up/relaxation of friction during flow, we observe transitions between finger opening and pore invasion in the viscous fingering regime, for example during initial compaction or outer decompaction during flow in the open cell. The resulting patterns are characterized in terms of growth rate, average finger thickness as function of radius and time, and fractal properties. Based on experiments with various injection pressures, we identify and compare typical pattern characteristics when there is no deformation, compaction, and/or decompaction of the porous medium. We show that the patterns formed have characteristic features depending on the boundary conditions. The study is part of fundamental research on pattern morphology in various deforming systems, which is important for increased understanding of flow in any deformable porous medium.

Next, we present an experimental study on flow regimes and pattern formation during air injection into confined granular media. In this experiment, we inject air at constant overpressure into a dry dense granular medium inside a linear Hele-Shaw cell, where air escapes at the outlet while beads cannot. As opposed to similar experiments with open outer boundary conditions [56,58,60], after the flow compacts the medium there is no decompaction. Due to the confined nature of the experiment, it is thought to be a laboratory analog to pneumatic and hydraulic fracturing of tight rock reservoirs where the free boundary at the surface is very distant from the injection zone, i.e. in a situation where fracture propagation stops long before reaching a free surface, such that the surrounding medium is not decompacted. We thus observe the material behavior (at high enough overpressure to displace beads) to have a transition from fluid-like to solid-like during experiments, and that eventual invasion patterns initially expand like viscous fingering in the fluid-like regime, crossing over to stick-slip propagation of the tips as the medium becomes more solid-like, until it reaches a final structure when the compacted medium has reached a completely solid-like behavior. What is less obvious, is how the flow patterns in this system change with the injection pressure. By varying the imposed overpressure, we identify and describe the different flow regimes. The motivation of this setup is to study the granular fingering instability in compacting granular media. We characterize typical properties of the emerging structures, such as their fractal dimension, typical thickness and invasion depth, growth dynamics, as well as flow regimes depending on injection pressure.

Then, with the same experimental setup as above, we present a study where we focus on characterizing the deformations and the evolution of the pressure in the medium surrounding the channel growth. Displacement fields are found experimen-

tally with a Digital Image Correlation technique, while we calculate the evolution of the pressure field in the porous medium numerically. Two solutions of the pressure field are evaluated; A steady-state configuration of the pressure field, which is estimated by solving the 2D Laplace equation with fixed pressures in the air cluster and at the outlet boundary. The other one is a solution where the imposed pressure initially diffuses into the pore space with a diffusion constant based on the porosity of the material and the viscosity of the fluid. This pressure field is calculated over time by solving the 2D diffusion equation with the Crank-Nicholson method. The two solutions for the pressure are compared to check if, when and where the diffusing pressure field satisfies the Laplace solution. By investigating the obtained deformation data and pressure gradients across the granular medium, we discuss the deformations, growth dynamics and rheology.

Finally, we present preliminary results in a chapter about a sub-project studying slow transformation processes, where we perform reactive flooding experiments in fractured carbonate reservoir rock. Here, calcite core samples (cylinders of 3.8 cm diameter and 1.7 to 2.6 cm in length) are fractured into two pieces through their principal axis by loading them across their diameter until failure. After being fractured, the pieces are put back together and mounted inside a Hassler cell (cylindrical confinement). During the experiments the system is flooded with a reactive fluid at a constant flow rate parallel to the fracture plane. Here, we inject distilled water at a constant flow rate of 0.1 ml/min through the fractured samples in experiments of various durations. A local topographical profile of the fracture surfaces is measured before and after the reactive flooding by using a white light interferometer, which in principle has a height resolution down to a few nanometers. With this data we compare the initial and final profiles to investigate the evolution of surface roughness and fracture aperture for different durations of flooding, and investigate the impact of flow direction on the changes.

In a closely related project, where the work in this thesis also contributes, acoustic emissions during experiments with air injections into dry granular media are recorded with piezo-electric shock accelerometers. Scientific papers discussing the results are shown in the appendix of this thesis. In Fourier analysis of the obtained signals, the evolution of the emissions is characterized in the frequency domain during the different stages of deformation and fracturing, and the processes creating the various types of signals are discussed in comparison with the optical data. Here, it is shown that different stages of the invasion process can be identified acoustically in terms of characteristic frequencies and distinct microseismic events. In addition, microseismic events caused by particle rearrangement in the later stages of the experiments are counted and fitted with characteristics of real world seismic events [75]. In combination with the optical data of deformations, an energy based localization technique for the sources of these microseismic events is developed [76].

The work done in this thesis project is ultimately a part of further understanding the mechanisms of complex processes involved in transforming reservoirs due to fluid flow, and is also partly involved in the development of acoustic localization techniques which may have industrial applications.

Chapter 3

Basic concepts and methods

3.1 Flow in porous media

Porous materials can be divided into two parts, the solid part forming the porous matrix, and the pore-space which is the interstitial space where fluids can be present. If the pore-space is interconnected, the porous material is permeable, i.e. the pores are connected and fluids are able to flow through the material using these pathways. In a granular medium, like soil, the space between grain contacts is connecting the whole pore-space making it very permeable. Porosity is the ratio of the volume of the pore-space to the total volume of a porous sample and is given by

$$\phi = \frac{V_{pores}}{V_{tot}} = 1 - \rho_s, \tag{3.1}$$

where ρ_s is the solid fraction. The porosity is a measure of how porous a solid is, and is a dimensionless number between 0 and 1. Permeability describes the ability of fluid flow through a porous medium and is often related to the porosity. In granular media, the average permeability in a sample is given by the Kozeny-Carman relation [59, 62, 75] (in this case for a packing of spherical beads)

$$\kappa = \frac{a^2\phi^3}{180(1-\phi)^2}, \tag{3.2}$$

where a is the bead diameter.

Fluid flow is driven by pressure, viscous and external forces as described in the Navier-Stokes fluid equations of motion:

$$\rho\left(\frac{\partial\vec{v}}{\partial t} + \vec{v}\cdot\nabla\vec{v}\right) = -\nabla P + \mu\nabla^2\vec{v} + \vec{F}. \tag{3.3}$$

Equation (3.3) states that the acceleration of a fluid element with density ρ is driven in the direction of the pressure force $-\nabla P$, viscous force $\mu\nabla^2\vec{v}$, and external forces $\vec{F}$ such as gravity. However, the Navier-Stokes equations require sufficient boundary conditions to be solved. In porous media, the boundary conditions are very complex and is practically impossible to define precisely. However, it gives a view on the forces involved. Instead, rather than considering the fluid flow on pore scale, it is common and useful for flow at small enough Reynolds number to average

the flow in porous media on sample scale by using the phenomenological Darcy law. This law relates the volume flux per unit area, or Darcy velocity, $\vec{v} = \frac{Q}{A}$ to the permeability, viscosity, pressure gradient and gravity as

$$\vec{v} = -\frac{\kappa}{\mu}(\nabla P - \rho\vec{g}). \tag{3.4}$$

In cases where gravity can be neglected, as for a horizontal Hele-Shaw cell, the Darcy velocity is found by

$$v = -\frac{\kappa}{\mu}\nabla P. \tag{3.5}$$

In immiscible two-phase flow in porous media, e.g. when gas invades a porous medium saturated with a liquid, capillary and interfacial forces are added to the problem. Capillary forces originate from the adhesive forces between a fluid and a solid surface, and interface tension comes from the cohesive forces between the molecules of a liquid. Wettability is a measure on the tendency of a fluid droplet to smear out on a smooth solid surface in the presence of a second fluid. It is measured in terms of contact angle θ, i.e. the angle between the solid surface inside the droplet and the tangent of the fluid-fluid interface at the triple point between the two fluids and the solid. Normally in a porous medium with two fluids present, one fluid has stronger contact forces with the solid than the other. The fluid with stronger contact forces is said to be wetting, with $\theta \in [0°, 90°]$, while the other is said to be non-wetting, with $\theta \in (90°, 180°]$. In two-phase flow where the non-wetting fluid is displacing the wetting one, called drainage, the invading fluid meets capillary thresholds it must overcome to displace the defending fluid out of narrow pore-necks. The narrower the pore-neck, the higher is the pressure threshold, which is given by the Young-Laplace equation as

$$P_{cap} = \gamma\left(\frac{1}{R_1} + \frac{1}{R_2}\right)\cos\theta, \tag{3.6}$$

where γ is the interfacial tension and R_1 and R_2 are the vertical and horizontal sizes of a given pore-neck. Since fluid flow tend to follow the path of least resistance, the pore geometry at the fluid-fluid interface influence the flow path taken by the invading fluid.

The flow regime during drainage of a horizontal porous medium depends on the ratio between the driving and stabilizing forces involved in flow and pore-invasion, described by the dimensionless capillary number Ca [40, 41]. The capillary number is the ratio of viscous pressure drop over capillary pressure drop at the characteristic pore scale, and can be found by

$$Ca = \frac{\mu v a^2}{\gamma\kappa}, \tag{3.7}$$

where v is the Darcy velocity. For low capillary numbers ($Ca \ll 1$) capillary fingering dominates and for higher capillary numbers ($Ca \to 1$) there is a crossover to viscous fingering. In the capillary fingering regime, the invading fluid displaces the defending fluid pore-by-pore with slow build-up and relaxation of the invading fluid pressure

fluctuating around the capillary threshold values. In the viscous fingering regime, a viscous pressure gradient across the defending fluid leads to a flow instability where more advanced parts of the invading cluster grow on expense of less advanced ones in finger like intrusions. The instability is explained by the pressure field in the defending liquid; The defending liquid can be considered incompressible ($\partial\rho/\partial t = 0$), and for incompressible flow in porous media we can combine the continuity equation

$$\frac{\partial \phi \rho}{\partial t} + \nabla \cdot (\rho \vec{v}) = 0 \;\Rightarrow\; \nabla \cdot \vec{v} = 0 \tag{3.8}$$

and the Darcy law in eq. (3.5) to get the Laplace equation $\nabla^2 P = 0$ for the pressure in the defending liquid. Since the pressure can be assumed uniform in the invading gas cluster, the driving force ∇P is effectively screened behind the longest fingers [1]. In a horizontal Hele-Shaw cell the pressure field is given by the 2-D Laplace equation

$$\frac{\partial^2 P}{\partial x^2} + \frac{\partial^2 P}{\partial y^2} = 0. \tag{3.9}$$

A fingering instability similar to viscous fingers occurs during fluid injection at sufficient overpressure into a dense granular medium saturated with the same fluid, i.e. branched channels empty of grains open up even in the absence of surface tension. In this situation, the invading air displaces grains by momentum exchange and open up pathways of increased local permeability. These channels expand quickly in the flow direction, and are screening the pressure gradient from the less advanced ones, inhibiting their growth. For compressible gas flow in a dry dense granular medium, the gas pressure P evolves in the medium according to the equation [59,77]

$$\frac{\partial P}{\partial t} = D\nabla^2 P - \vec{v}_g \cdot \nabla P - \frac{P}{\phi} \nabla \cdot \vec{v}_g, \tag{3.10}$$

where $\vec{v}_g$ is the local granular velocity and D is a diffusion constant. If the terms involving the granular velocity are negligible, equation (3.10) reduces to the diffusion equation for the pressure between the grains, which in 2-D is given by

$$\frac{\partial P}{\partial t} = D\nabla^2 P = D\left(\frac{\partial^2 P}{\partial x^2} + \frac{\partial^2 P}{\partial y^2}\right). \tag{3.11}$$

The diffusion constant D can be approximated for granular media as [75]

$$D = \frac{\kappa P_0}{\phi \mu} = \frac{a^2 \phi^2 P_0}{180(1-\phi)^2 \mu}, \tag{3.12}$$

assuming an ideal gas, which is valid for conditions without strong density variations, i.e. in a system where the pressure is not varying by orders of magnitude. Here, P_0 is the atmospheric pressure, and it is assumed the Carman-Kozeny expression (3.2) is valid for the permeability κ [59, 75]. In a rigid 1-dimensional porous medium, the analytical solution for the 1-D diffusing pressure is

$$P(x,t) = P_{in}\left(1 - \frac{x}{L}\right) - \sum_{n=1}^{\infty} \frac{2P_{in}}{\pi n} \sin\left(\frac{n\pi x}{L}\right) e^{-\frac{n^2\pi^2}{L^2}Dt}, \tag{3.13}$$

where L is the system length. Equation (3.13) shows that for increasing time t, the diffusing pressure goes towards the steady-state Laplace solution $P(x) = P_{in}\left(1 - \frac{x}{L}\right)$.

3.2 Pattern formation and analysis

Many structures formed in different processes in nature appear as similar patterns, which is sometimes explained by their common growth dynamics. For example, the flow patterns formed in our experiments result in structures similar to other natural patterns occuring in Laplacian growth systems, e.g. DLA clusters, viscous fingers in empty Hele-Shaw cells, manganese dendrites, or lightning bolts as shown in figure 3.1. In such systems, ramified structures expand at a rate proportional to the gradient of a Laplacian ($\nabla^2\phi = 0$) potential field, such that $v \propto \nabla\phi$. This type of patterns is in the DLA universality class, where a fractal dimension of $D = 1.71$ is expected [2,40]. However, the fractal dimensions found for viscous fingering patterns in porous Hele-Shaw cells usually have values of $D \in [1.53 - 1.62]$ [1, 2, 5]. It has been established that flow in porous media is better described by another Laplacian model, the Dielectric Breakdown Model (DBM), where the interfacial growth rate is proportional to the potential gradient of a power η higher than 1, i.e. $v \propto (\nabla\phi)^\eta$, where $\eta = 2$ for viscous fingers in porous media [2, 40]. A feature of pattern growth which is typical for Laplacian growth systems is that there is an active growth zone on the tips of a frozen structure due to screening of the potential gradient by the most advanced parts of the structure.

By looking closely at the patterns in figure 3.1, we notice that they have self-similar features over a range of scales, e.g. a smaller branch resemble the whole larger pattern. Another good example of self-similarity over a limited range of scales is the fern shown in figure 3.2. A common method to characterize the self-similar feature of a pattern is to analyze its fractal dimension, which is a spatial scaling exponent. In other words, if the fractal dimension of a pattern exists, it reveals information about how the pattern fills the space it occupies. There are different ways to estimate the fractal dimension of a pattern [78, 79]. Presented here are three methods we used for studying invasion patterns contained in binary images.

For a radially growing fractal pattern, its area N (mass) scales with its size r (radius) according to a power-law relationship referred to as the mass-radius relation,

$$N(r) \propto r^{D_m}, \tag{3.14}$$

where the exponent D_m is the fractal mass-dimension of the pattern. In binary images, the mass-radius relation of a radial pattern can be obtained by evaluating the area (number of white pixels) contained within a given radius from the origin of the pattern, and plot the result as function of radius in a log-log plot. The mass dimension D_m is then found as the slope of a linear fit where $\log_{10}(N(r)) \sim D_m \log_{10}(r)$.

The fractal box-counting dimension D_b is found by dividing the image into boxes, i.e. dividing the image into equal squares of sides s, and count the number N of squares that contain a part of the pattern as function of box size s. For a fractal,

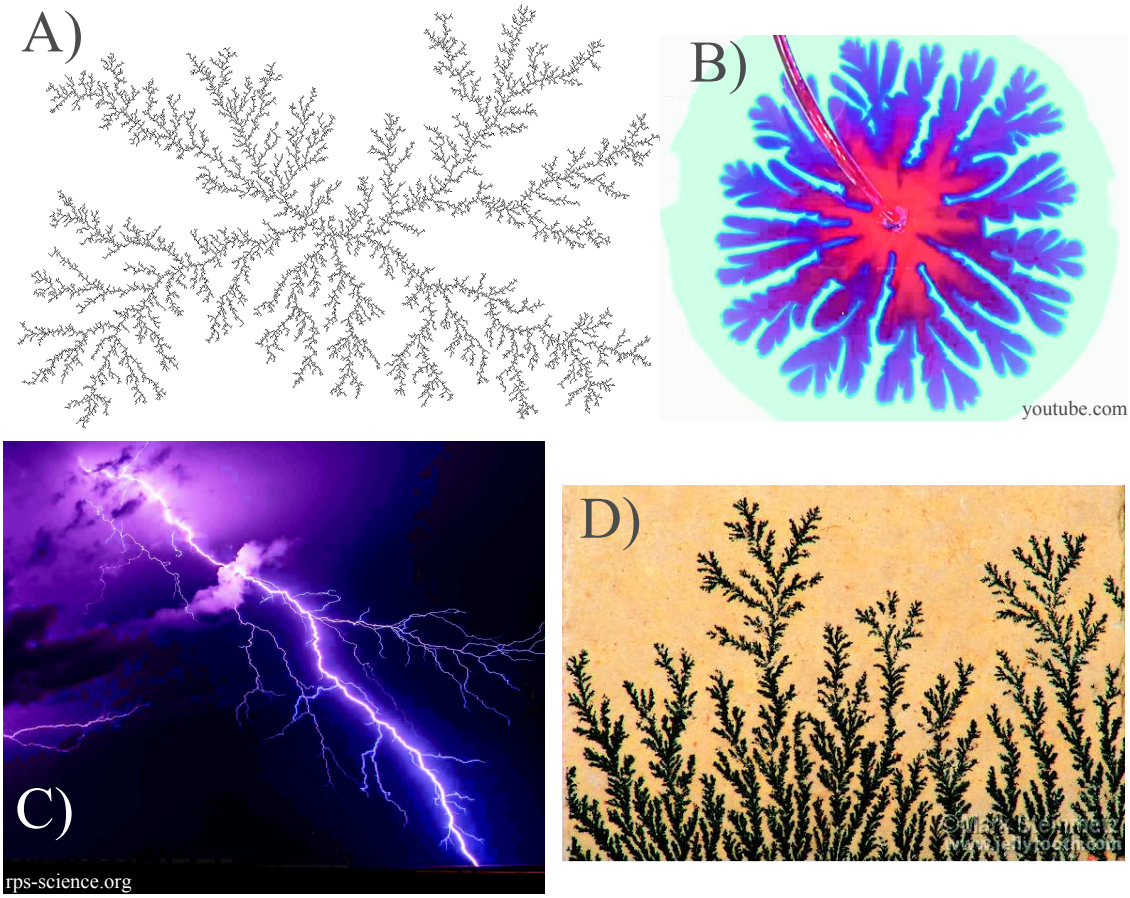

Figure 3.1: Dendritic patterns in different systems: A) Radial DLA simulation B) Viscous fingers in a radial Hele-Shaw cell, C) Lightning bolt, and D) Manganese dendrites.

the relationship between the number of boxes covering the pattern and their size follow a power law

$$N(s) \propto s^{-D_b}, \tag{3.15}$$

such that the box-counting dimension D_b is found from slope of the linear fit $\log_{10}(N(s)) \sim -D_b \log_{10}(s)$ [2, 5, 78, 79].

The equations (3.14) and (3.15) give globally defined fractal dimensions with values between 1 and 2. Local fractal dimensions can be estimated to check how well defined these global fractal dimensions are. For a radial pattern, a local fractal dimension $D_L(r)$ is estimated as function of radius by intersecting the pattern with a concentric ring at each radius and do 1-dimensional box counts along the rings; At each radius r, the ring is divided into equal arc segments and the number N of arc segments that intersect the pattern is counted as function of arc length l as the arc length is decreased. Similarly for linear patterns, a local fractal dimension $D_L(x)$ is estimated as function of depth along the structures; At each depth x, the structure is intersected with a perpendicular line, and 1-dimensional box counts are done along that line, i.e. the line is divided into segments of equal length l and the number N of line segments that intersect the pattern is counted as function of

Figure 3.2: It is easy to see the self-similarity of this fern. Look at the tiniest leaves of the fern: They are organized in a pattern that looks like a fern. These tiny "ferns" are organized on branches that look like small ferns. These fern looking branches are arranged on the stem of the fern in the familiar pattern.

segment length l as it is decreased. In both cases, for a fractal there are locally defined power laws (for given x or r)

$$N(l) \propto l^{-D_L}, \tag{3.16}$$

and we find the local fractal dimensions $D_L(x)$ or $D_L(r)$ at given x or r from slopes of the linear fit $\log_{10}(N(l)) \sim -D_L \log_{10}(l)$. For a perfect fractal, D_L is constant over depth or radius.

The locally obtained fractal dimensions has values between 0 and 1. Therefore, in order to compare D_L with D_m and D_b it is necessary to use Mandelbrot's rule of thumb for intersecting fractal sets [78, 80]. It states that the codimension of an intersected set equals the sum of the codimensions of the individual intersecting sets, here given by

$$\begin{aligned} E_2 - D_L &= (E_2 - E_1) + (E_2 - D) \\ &\Downarrow \\ D &= D_L + 1, \end{aligned} \tag{3.17}$$

where D is the global fractal dimension of the pattern, $E_1 = 1$ is the dimension of the ring or line intersecting it, and $E_2 = 2$ is the dimension of the image plane containing the sets.

3.3 Image processing

3.3.1 Binary images: Extracting patterns to analyze

The experimental image data in this thesis are sequences of grayscale images. These images are processed in Matlab to segment out the patterns into binary images, i.e. images with either black or white pixels, where the white pixels (value=1) represent the pattern and the black pixels (value=0) represent the background, or the bead-filled region. After obtaining binary images of the patterns, we can quantify for example the pattern radius or length, mass (number of white pixels), and fractal dimensions as explained in section 3.2

For the images from experiments presented in chapter 4, pattern segmentation is done by first subtracting the grayscale values of each image in the sequence with the initial image to remove most of the background. Then, a suitable threshold value is defined such that all pixel values less than the threshold are set to 0 while the rest, being a part of the pattern are set to 1. In the deformable experiments, deformations cause speckle fluctuations in the difference images, so an additional step of removing noise must be done where small clusters of white pixels not connected to the main cluster are set to 0. Figure 3.3 shows an example of pattern segmentation in a deformed medium.

For the granular media presented in chapters 5 and 6, we obtain binary image sequences from the raw data by thresholding each frame with the initial image as reference, such that pixels having a value less than 30 % of the corresponding initial value becomes white and the rest remain black (in these experiments, the patterns are darker than the medium).

3.3.2 Digital Image Correlation: Obtaining displacement fields

Frame-to-frame granular displacement fields are obtained with Ncorr, an open-source Matlab based Digital Image Correlation (DIC) software [81,82]. The basic principle of Ncorr is to cross-correlate subwindows of one image with an image taken at a later time to obtain displacement vectors $\vec{U}(x,y) = u(x,y)\vec{i} + v(x,y)\vec{j}$ located at (x,y) positions in the first image, thus indicating the displacement of the subwindows between the images. In brief steps, the Ncorr algorithm works as follows:

1. A subwindow at a selected position in the first image is cross-correlated with the succeeding image by calculating the normalized cross-correlation in Fourier space. This yields the displacement with integer pixel accuracy, i.e. the initial guess.

2. To estimate the displacement with sub-pixel accuracy, a quintic B-spline interpolation of the graymap in the vicinity of the initial guess is calculated. This

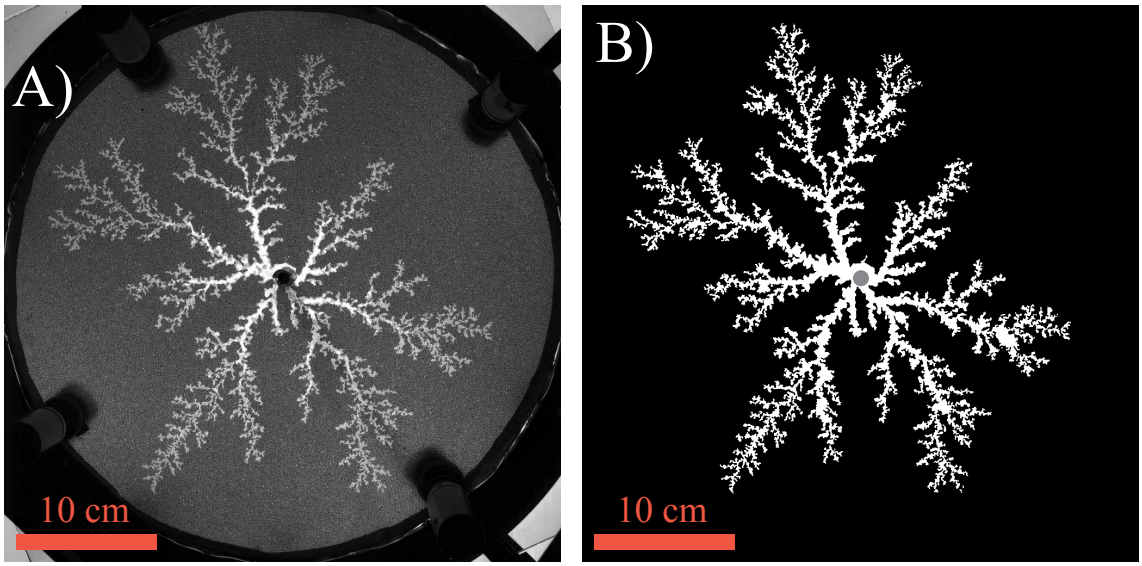

Figure 3.3: The raw data breakthrough image of the confined deformable experiment with 75 hPa injection pressure (A), and the resulting binary image after segmentation of the air cluster (B), where the active pixels belonging to the cluster is shown in white and the inactive background pixels are shown in black. The dark injection region where it is difficult to separate saturated and invaded parts is indicated in gray, and is excluded from our analysis.

permits the approximate graylevel to be evaluated at non-integer coordinates in this area.

3. In the interpolated area, the subwindow is iteratively translated and deformed in small steps towards a best fit, done by minimizing a cost-function. This gives the displacement with sub-pixel accuracy.

4. The full image displacement field is found by the Reliability Guided DIC method; The remaining subwindows are analyzed in queue, one after the other, by using solved displacements of a nearest neighbor as initial guess. Thus, only steps 2 - 3 are repeated for the remaining subwindows. The queue of subwindows is updated at each iteration, such that the algorithm always analyzes the one with the best correlation at the initial guess.

Furthermore, Green-Lagrangian strains are calculated from spatial derivatives of the incremental displacement field as

$$\begin{aligned} E_{xx} &= \frac{1}{2}\left(2\frac{\partial u}{\partial x} + \left(\frac{\partial u}{\partial x}\right)^2 + \left(\frac{\partial v}{\partial x}\right)^2\right) \\ E_{yy} &= \frac{1}{2}\left(2\frac{\partial v}{\partial y} + \left(\frac{\partial u}{\partial y}\right)^2 + \left(\frac{\partial v}{\partial y}\right)^2\right) \\ E_{xy} &= \frac{1}{2}\left(\frac{\partial u}{\partial y} + \frac{\partial v}{\partial x} + \frac{\partial u}{\partial x}\frac{\partial u}{\partial y} + \frac{\partial v}{\partial x}\frac{\partial v}{\partial y}\right), \end{aligned} \tag{3.18}$$

which for small deformations are similar to small strains: $E_{xx} = \varepsilon_{xx} = \partial u/\partial x$, $E_{yy} = \varepsilon_{yy} = \partial v/\partial y$, and $E_{xy} = \gamma_{xy} = 0.5 \cdot (\partial u/\partial y + \partial v/\partial x)$, i.e. when the quadratic terms can be neglected. Ncorr also includes an algorithm for obtaining the total Lagrangian displacement from the incremental displacement fields. See the article by the developers of Ncorr [81], or the web page [82], for an in-depth explanation of the software.

Chapter 4

Invasion patterns during two-phase flow in deformable porous media

4.1 Motivation

Viscous fingering patterns in rigid porous media have been found to be self-similar fractal structures over a range of scales, where they have a characteristic branched appearance. However, how do the characteristic features of a viscous fingering pattern change when the flow can deform the medium it invades? And how does the growth dynamics depend on this? By asking these questions we got motivated to investigate experimentally the invasion of air at constant and maintained overpressure into liquid-saturated deformable porous media. We designed the experimental setup so that we could vary the boundary conditions of the porous medium and the injection pressure, obtaining different degrees of deformations. From the experimental results we characterize the invasion patterns in terms of their spatial properties and growth dynamics, investigate spatial and dynamic scaling exponents, discuss what is common and different between the various boundary conditions, and investigate the typical deformations surrounding the growing structures. In this section, we present our methods and main results in this study before including the scientific article containing all details of the work and discussion of results.

4.2 Methodology

4.2.1 Experimental setup

The experiments were performed within the confines of a radial and horizontal Hele-Shaw cell. A sketch of the experimental setup is shown in figure 4.1. The radial cell has a diameter of 40 cm and is made out of two 1 cm thick circular glass plates separated by a gap of 1.0 - 1.4 mm depending on boundary condition. The cell plates are clamped together and metal spacers are used to maintain the cell gap. Through the center of the bottom plate is an injection hole of 10 mm diameter. The rim of the cell is always open to fluids, and is the cell outlet. The invading air is supplied from a

pressurized air source, connected to the cell inlet hole via a pressure regulator used to control the injection overpressure and a valve used to start/stop the flow. We create the porous medium by placing a monolayer of 1 mm spherical glass beads inside the cell. The porous medium is prepared with either a non-deformable, confined deformable or open deformable boundary condition, which are presented in the next paragraph. After the monolayer of beads is placed inside the cell, the pore space is saturated with a viscous water-glycerol solution (80 % glycerol by mass) which is wetting the beads and cell plates. The saturating liquid is colored black, giving contrast for image processing purposes. The cell is positioned on top of a custom made lightbox which gives uniform and flicker-free illumination from below. Looking down from directly above the cell is a Photron SA5 high speed camera, which during experiments captures grayscale images with a spatial resolution of 1024×1024 pixels at a framerate of 125 images/s (1 pixel $\approx$ 0.4 mm in the cell). The camera is connected to a computer with the camera software (Photron FASTCAM Viewer) which is used to control it and download the experimental images. The experimental procedure is as follows: First, the overpressure of the invading air is set with the pressure regulator while the inlet valve to the cell is closed. The experiment starts when the inlet valve is opened, allowing air to invade the cell at a constant and maintained overpressure, making the growing air cluster drain the medium radially outwards until it breaks through at the rim. When the air breaks through at the rim, the experiment is finished. As mentioned, the whole invasion process is recorded with the high speed camera. Binary images of the patterns and displacement maps of the media are found from the experimental images as discussed in section 3.3.

4.2.2 Three cases of boundary conditions

The porous medium with the non-deformable (ND) boundary condition is rigid, single-layered and disordered. This boundary condition is used for having a reference to viscous fingering without deformation. The medium is prepared on the bottom disk before assembling the cell. First, the top surface of the bottom disk is coated with an adhesive transparent plastic film (clear contact paper). Then, beads are poured onto the adhesive surface such that they attach at random positions. The process is continued until no more beads are able to hit the bottom disk surface, i.e. when the longest distance between beads in the monolayer is shorter than a bead diameter. After removing beads on top of the monolayer by tilting the cell plate, the top disk (also adhesive) is put onto the resulting monolayer and clamped together with the bottom disk. The disk separation therefore equals the bead diameter of 1.0 mm. The saturating liquid is injected into the porous medium through the cell inlet with a syringe.

The porous medium with the confined deformable (CD) boundary condition is a random close packed monolayer of beads which can be displaced within the cell volume, but are prevented to leave the cell by a semi-permeable boundary. This sample type is prepared partially before and after assembling the cell. First, the rim of the bottom disk is fitted with a semi-permeable belt made of foam rubber, which is permeable to fluids and impermeable to beads. Next, the top disk is placed onto the bottom disk and they are clamped together, with the cell gap maintained by 1.4

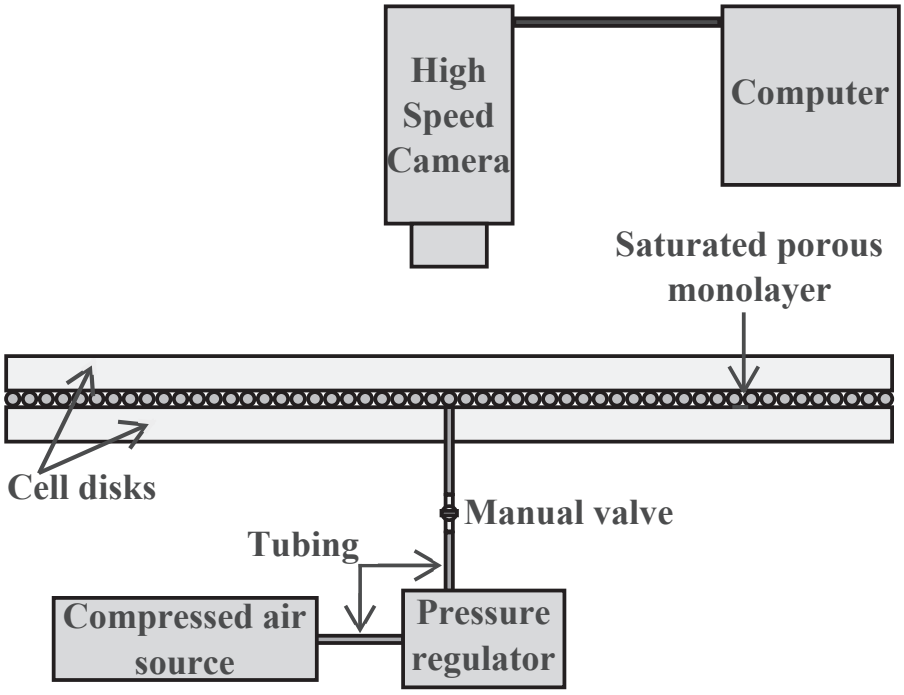

Figure 4.1: Sketch of the experimental setup for the two-phase flow experiments: The horizontal cell consists of two transparent disks of 40 cm in diameter, clamped together (not shown) but separated by a small gap. The gap is big enough to accommodate a saturated porous monolayer of 1.0 mm beads. This sketch represents the non-deformable system, however the setup is the same for the other boundary conditions as well. A compressed air source is connected to an injection hole in the center of the bottom disk, and a pressure regulator is used to adjust the constant injection pressure between 25 and 100 hPa. During air injection, the high speed camera situated directly above the cell captures the invasion at a framerate of 125 frames per second.

mm thick spacers between the disks at the clamp positions. The cell gap ensures the possibility of bead displacement as well as keeping the bead packing approximately single-layered. The gap above the beads (0.4 mm) is still smaller than the large interparticle nearest distance in the system (1 mm), and we observed no significant invasion occurring over several bead lengths in the gap above the beads. Finally, beads are injected into the cell through the central injection hole until they form a monolayer that fills the confined volume. To avoid deformation when injecting the saturating liquid, we introduce the liquid by gravity stabilized imbibition (stable invasion of wetting liquid), i.e. the cell is slightly tilted ($\approx 7°$) and the liquid is slowly injected through the rim at the lowest point. During this procedure, the cell outlet is sealed with a rubber belt.

The porous medium with the open deformable (OD) boundary condition is prepared in the same way as the CD one, but with a temporary semi-permeable boundary at the rim which is removed before experiments. This means that the open deformable porous medium is a deformable monolayer where the beads can be displaced and also pushed out of the cell at the open perimeter. Thus, we have satu-

rated porous media with three cases of boundary conditions; on one side of the scale we have the non-deformable boundary condition where nothing is deformed in the medium, on the other end of the scale we have the open deformable boundary condition where most of or all of the medium is deformed, and somewhere in between we have the confined deformable medium.

4.3 Main results

A total of 41 experiments were performed. Most of them were trial and error experiments while developing the methods, but we ended up with 10 experiments considered successful and good to analyze. Of these experiments, 2 are in the ND medium with an injection pressure of 25 hPa (hPa = mbar), 4 are in the CD medium with the injection pressures 25, 50, 75 and 100 hPa, and 4 are in the OD medium also with the injection pressures 25, 50, 75 and 100 hPa. The experiments lasted between 0.9 and 9.7 s, typically with shorter times for increasing injection pressure and deformability.

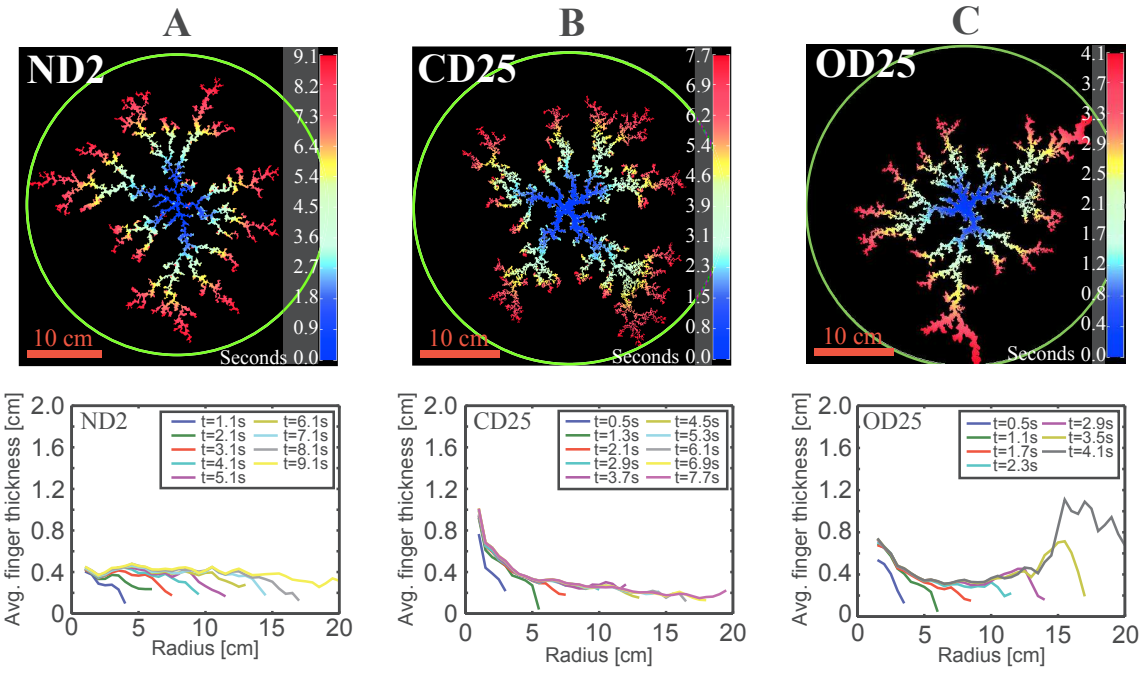

Figure 4.2: Top: Breakthrough patterns for the non-deformable experiment (A), confined deformable experiment (B), and open deformable experiment (C) with an injection pressure of 25 hPa. The color code indicates the time a pixel is invaded by air in seconds after start, where blue is at the start and dark red is at breakthrough. The green circles indicate the cell rim. Bottom: Average finger thickness as function of radius plotted at several snapshots for the patterns above.

Typical patterns from each boundary condition are shown in figure 4.2 together with plots of their average finger thickness as function of radius. We see that they have common features on cell scale, i.e. a branching dendritic structure that spreads out from the center, mainly in the radial direction, where more advanced fingers grow

on expense of the less advanced ones. This behavior is expected since the invasion flow follows Darcy's law in eq. (3.5) with the pressure field given by the Laplace equation (3.9) outside the air cluster of constant pressure, such that the pressure gradient is screened inside the longest fingers. However, if we look more in detail together with the average finger thickness plots, we see that the patterns are different locally; The ND patterns have long thin fingers, and the thickness of the fingers is more or less constant with radius outside the injection center. The CD patterns typically feature centrally few and thick fingers that cross over to thinner and more numerous fingers with increasing radius. Finally, the OD patterns have centrally few and thick fingers which crosses over to more numerous and thinner fingers at intermediate radii, which then crosses back to few thick fingers near the cell outlet. Variations in the finger thickness of invasion patterns in the deformable porous media is due to the competition between interface forces depending on capillary thresholds and friction depending on granular stress. For the deformable media, we find the typical capillary threshold to be $p_{cap} \approx 225$ Pa. When considering that $p_{cap} \ll 25$ hPa, the lowest injection pressure applied, the overpressure in the air cluster is always larger than the capillary thresholds. Therefore, we will always see pore invasions (thin fingers) if the granular stress overcomes the capillary thresholds. In the opposite case, when it is easier to move beads than invade a pore, the finger opens up and becomes thicker.

The granular stress is related to the deformation of the medium, where more compacted beads are harder to displace. Deformation maps for the CD and OD experiments with an injection pressure of 100 hPa are shown in figure 4.3. Accumulated radial displacements and volumetric strains are shown at an early stage, around mid-experiment, at a later stage and at breakthrough. Radial displacements in both experiments is directed outwards from the injection center, and do not reach all the way to the rim initially. In the CD experiment, the displaced area grows towards a final extent and magnitude, which goes to zero near the rim. The corresponding volumetric strain shows that the medium is increasingly compacted with time outside the invasion cluster. Finger opening is observed in regions where the volumetric strain exceeds 0.05. Thus, there is a crossover from finger opening to pore invasion in the latter half of the experiment. In the OD experiment, the radial displacements increase in magnitude outside the growing cluster with time, and eventually reach the rim where beads leave the cell. The corresponding volumetric strains shows that the medium is initially compacted and with time there is increasing decompaction near the rim. In this particular experiment the finger opening did not cross over to pore invasions, but for the experiments with lower injection pressures the initial compaction is thought to cause a crossover to pore invasions while the outer decompaction causes the crossover back to finger opening. Figure 4.4 shows a typical snapshot of tangential displacements surrounding opening fingers, which shows that beads are displaced perpendicularly away from the fingers.

Obtained fractal dimensions of the breakthrough patterns are shown in figure 4.5 for experiments with 25 hPa injection pressure in each boundary condition. For all breakthrough patterns (also in the experiments not shown) the box dimensions are found to be in the range of $D_b = 1.55$ to 1.63 , which is consistent with viscous fingers in rigid porous media, reflecting that the patterns have a common structure

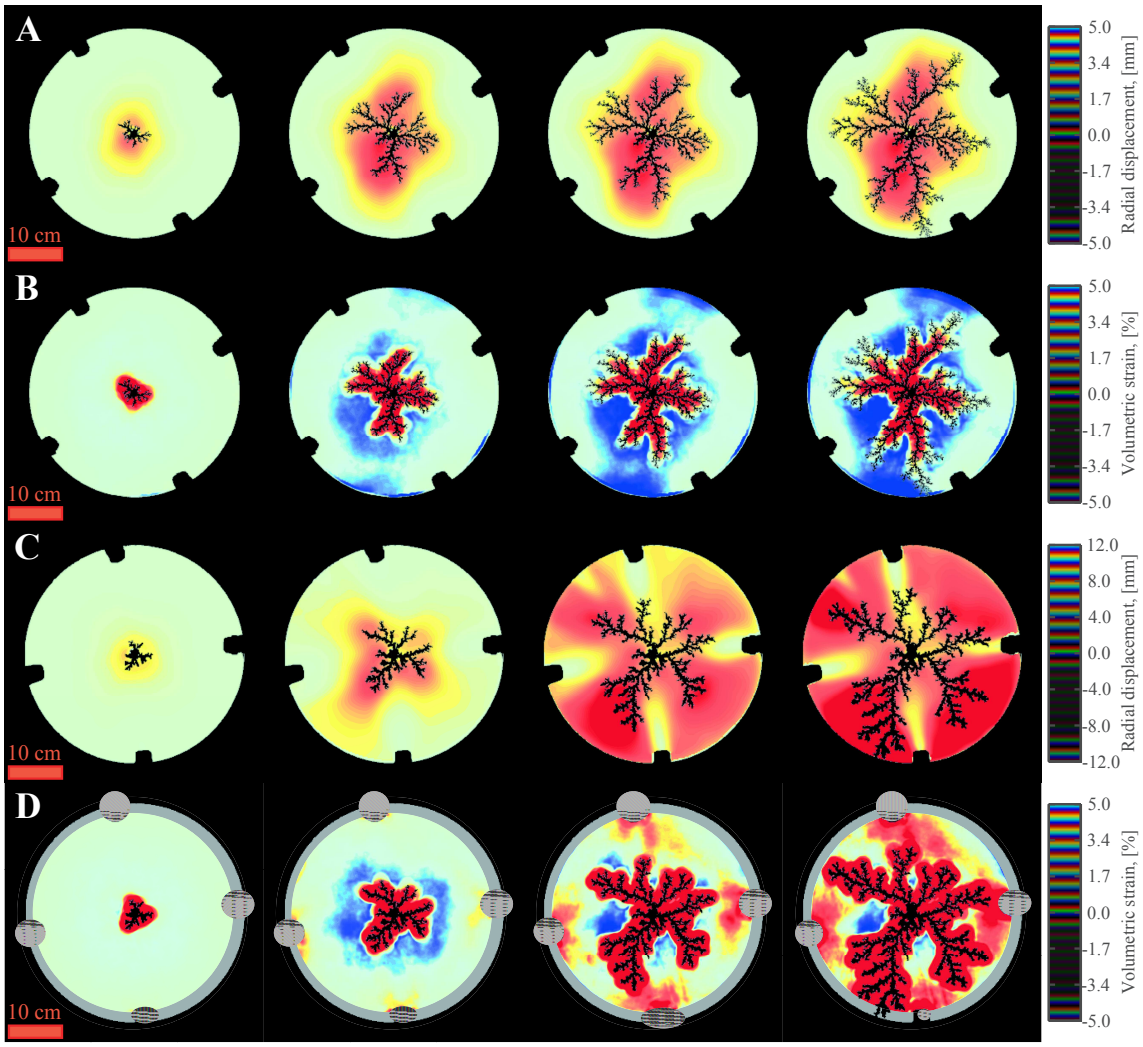

Figure 4.3: Visualization of accumulated deformation at different snapshots during experiments: Radial displacements A) and volumetric strains B) in the confined deformable experiment with 100 hPa injection pressure. The radial displacements C) and volumetric strains D) are for the open deformable experiment with 100 hPa injection pressure. Time is increasing from left to right, where the snapshots in A) and B) are taken at 176, 488, 696, and 904 ms (i.e., 20, 54, 77, and 100 % of the breakthrough time). The snapshots in C) and D) are taken at 232, 544, 960, and 1272 ms (i.e., 18, 43, 75, and 100 % of the breakthrough time). For the radial displacements (A,C), red color means that displacements are directed outwards and blue means inwards. For the volumetric strains (B,D), red color means decompaction and blue means compaction. The gray area in D) indicate omitted data where boundary effects of beads leaving the cell influence the strain calculations.

on cell scale. For the ND patterns, the mass dimensions D_m correspond well to both the box dimensions and the local dimensions $(D_L + 1)$, which are more or less constant as function of radius in the developed parts. This indicates that they have well defined fractal dimensions on cell scale consistent with earlier work on the topic [1, 2]. Mass dimensions for the patterns in the deformable systems generally

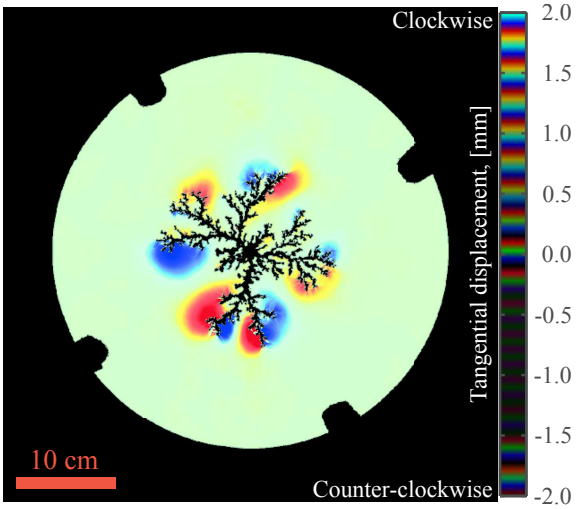

Figure 4.4: Example of tangential displacement behavior taken from the interval of 448 - 488ms (50 - 54% of breakthrough time) for the confined deformable experiment with 100 hPa injection pressure. Blue color means counter-clockwise displacements and red means clockwise displacements.

do not correspond well with the box or local dimensions, probably due to finite size effects, i.e. the less developed outer parts contribute to a decrease in the mass-radius slope. However, in the developed parts of the patterns in CD with injection pressures from 25 to 75 hPa, the box dimensions correspond fairly well to the local dimensions indicating that the developed parts of these patterns have a well defined fractal dimension similar to ND. For the CD experiment with 100 hPa overpressure and all OD experiments the local dimensions are found to decrease with radius and only correspond to the box dimensions at an intermediate range. This indicates that the patterns in the most deformed systems do not have a well defined fractal dimension on cell scale, but have locally defined fractal dimensions and transitions of universality class with radius; Initially, the empty region of thick fingers have local dimensions corresponding to 1.7 which is the fractal dimension for DLA patterns and viscous fingering patterns in empty cells. At an intermediate range $(D_L + 1) \approx 1.6$, which is consistent with viscous fingers in rigid porous media. For the outer parts in the OD systems, $(D_L + 1)$ approaches 1.4, which is similar to the fractal dimension of 1.43 measured for fractures in a paste [3].

When looking at the growth dynamics, we found that the mass N and radius r of the patterns grow with time as

$$N(t) = N_b(t/t_b)^\alpha, \text{ and } r(t) = r_b(t/t_b)^\beta, \tag{4.1}$$

where N_b, r_b and t_b are breakthrough values of mass, radius and time respectively. Thus at a given time during an experiment, the scaled mass-radius relationship from eq. (3.14) is given by

$$\frac{N(r)}{N_b(t/t_b)^\alpha} = \left(\frac{r}{r_b(t/t_b)^\beta}\right)^{D_m}. \tag{4.2}$$

Figure 4.6 shows snapshots of the scaled mass-radius relations in the deformable

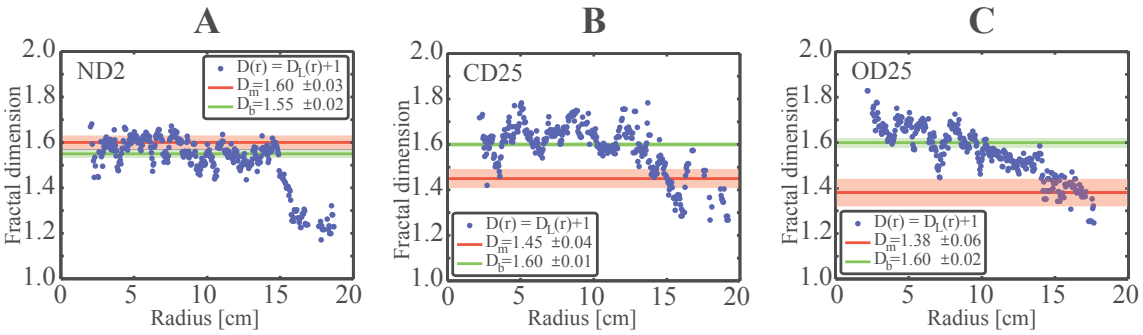

Figure 4.5: The blue dots represent local fractal dimensions plotted as $(D_L + 1)$ as function of radius for the non-deformable breakthrough pattern (A), confined deformable breakthrough pattern (B), and open deformable breakthrough pattern (C) for 25 hPa injection pressure. The estimated mass dimensions D_m are indicated as solid red lines with uncertainties shown as light red bands, and the box dimensions D_b are indicated as dotted green lines with uncertainties shown as light green bands.

experiments with 100 hPa injection pressure (CD100 and OD100), which shows that the mass dependence on time and radius can be collapsed onto a master curve according to a Family-Vicsek relationship. This gives the scaling law for the mass dimension

$$D_m = \alpha/\beta. \tag{4.3}$$

For CD100, $\alpha = 1.58$ and $\beta = 1.02$, and for OD100, $\alpha = 1.73$ and $\beta = 1.10$. When inserting the scaling exponents for CD100 and OD100 into eq. (4.3), we get the mass dimensions $D_m = 1.55$ and 1.57 respectively, which is similar to their respective box dimensions and consistent with fractal dimensions for viscous fingers in rigid porous media. Furthermore, we found that the dynamic scaling exponent α for the invaded area over time increases with deformability of the medium, implying that the invaded area changes at a faster rate with deformability since $dN(t)/dt \sim t^{\alpha-1}$.

A more detailed presentation of the methods and results in this study is given in the related article over the following pages. This article was published in Frontiers in Physics in 2015.

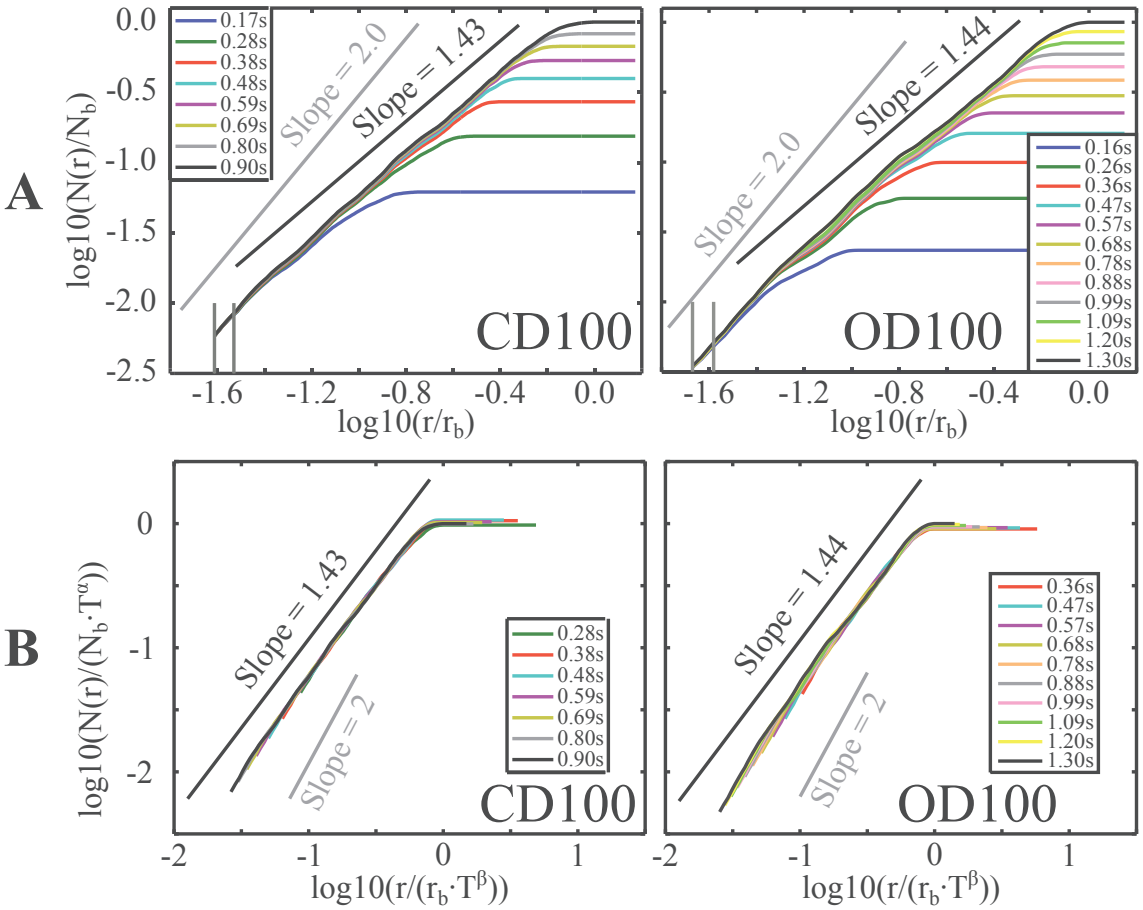

Figure 4.6: (A) Examples of mass-radius relations at several snapshots for the confined deformable experiment at 100 hPa (left) and an open deformable experiment at 100 hPa (right). At the start of the curves, the leftmost gray vertical lines mark the lower radius cutoff, which is just outside the injection region, and the gray vertical lines to the right mark a distance of 1 mm outside the lower cutoff. The black dashed lines show the estimated mass dimensions from the slopes for the breakthrough patterns. The gray dashed lines has slope of 2 to indicate the space filling dimension of an emptied bubble. (B) Family-Vicsek scaling of the same mass-radius relations as above, except for the smallest clusters with a total mass < 10 % of the breakthrough mass (before the fingering instability begins). On the axes, $T = (t/t_b)$ is the ratio of time over breakthrough time, r is radius, r_b is breakthrough radius, $N(r)$ is mass within radius r, N_b is total mass at breakthrough, and α and β are scaling exponents. Here, for CD100: $\alpha = 1.58$ and $\beta = 1.02$, and for OD100: $\alpha = 1.73$ and $\beta = 1.10$.

PAPER 1

frontiers in Physics

ORIGINAL RESEARCH
published: 02 October 2015
doi: 10.3389/fphy.2015.00081

Invasion patterns during two-phase flow in deformable porous media

Fredrik K. Eriksen[1,2]*, *Renaud Toussaint*[1], *Knut J. Måløy*[2] and *Eirik G. Flekkøy*[2]

[1] *Institut de Physique du Globe de Strasbourg, Université de Strasbourg/EOST, Centre National de la Recherche Scientifique, Strasbourg, France,* [2] *Department of Physics, University of Oslo, Oslo, Norway*

We study the formation of viscous fingering and fracturing patterns that occur when air at constant overpressure invades a circular Hele-Shaw cell containing a liquid-saturated deformable porous medium—i.e., during the flow of two non-miscible fluids in a confined granular medium at high enough rate to deform it. The resulting patterns are characterized in terms of growth rate, average finger thickness as function of radius and time, and fractal properties. Based on experiments with various injection pressures, we identify and compare typical pattern characteristics when there is no deformation, compaction, and/or decompaction of the porous medium. This is achieved by preparing monolayers of glass beads in cells with various boundary conditions, ranging from a rigid disordered porous medium to a deformable granular medium with either a semi-permeable or a free outer boundary. We show that the patterns formed have characteristic features depending on the boundary conditions. For example, the average finger thickness is found to be constant with radius in the non-deformable (ND) system, while in the deformable ones there is a larger initial thickness decreasing to the ND value. Then, depending on whether the outer boundary is semi-permeable or free there is a further decrease or increase in the average finger thickness. When estimated from the flow patterns, the box-counting fractal dimensions are not found to change significantly with boundary conditions, but by using a method to locally estimate fractal dimensions, we see a transition in behavior with radius for patterns in deformable systems; In the deformable system with a free boundary, it seems to be a transition in universality class as the local fractal dimensions decrease toward the outer rim, where fingers are opening up like fractures in a paste.

Keywords: two-phase flow, drainage, deforming porous media, viscous fingering, fracturing

OPEN ACCESS

Edited by:
Antonio F. Miguel, University of Evora, Portugal

Reviewed by:
Sujata Tarafdar, Jadavpur University, India
Christopher William MacMinn, University of Oxford, UK

***Correspondence:**
Fredrik K. Eriksen, Institut de Physique du Globe de Strasbourg, 5 Rue René Descartes, 67084 Strasbourg Cedex, France
eriksen@unistra.fr

Specialty section:
This article was submitted to Interdisciplinary Physics, a section of the journal Frontiers in Physics

Received: *03 June 2015*
Accepted: *18 September 2015*
Published: *02 October 2015*

Citation:
Eriksen FK, Toussaint R, Måløy KJ and Flekkøy EG (2015) Invasion patterns during two-phase flow in deformable porous media. Front. Phys. 3:81. doi: 10.3389/fphy.2015.00081

Introduction

Multi-phase flow in porous and granular materials are complex processes in nature and industry, and the understanding of the involved mechanisms is an ongoing challenge. In early research on the flow of two immiscible fluids in thin cells (Hele-Shaw cells), it was found that the invasion by a less viscous fluid into a more viscous fluid results in a displacement instability where viscous fingering patterns form [1]. This means that the invading fluid displaces the more viscous one in separated finger-like intrusions, while leaving the fluid inbetween the fingers less or not displaced. Following an increased interest in this phenomenon, two-phase flow have been widely studied in quasi-2-dimensional porous media confined in thin cells with circular and rectangular geometries [2–14]. In horizontal cells containing rigid disordered porous media,

the unstable invasion patterns during drainage are found to be fractal and either form an invasion percolation cluster [15] in the capillary fingering regime [16, 17], or long thin fingers resembling DLA patterns in the viscous fingering regime [18, 19]. The flow regime during drainage of a horizontal porous medium is dependent on the ratio between the driving and stabilizing forces involved in flow and pore-invasion, usually described by the dimensionless capillary number Ca [3, 5]. The capillary number is the ratio of viscous pressure drop over capillary pressure drop at the characteristic pore scale, and can be found by

$$Ca = \frac{\mu v a^2}{\gamma \kappa}, \tag{1}$$

where μ is the viscosity of the saturating fluid, v is a characteristic velocity (flux/injection cross section), a is the bead diameter, γ is the interface tension between the invading and defending fluid and κ is the permeability of the porous medium. For low capillary numbers ($Ca \ll 1$) capillary fingering dominates and for higher capillary numbers ($Ca \rightarrow 1$) there is a crossover to viscous fingering. The stabilizing mechanism is provided by a network of capillary pressure thresholds situated at the pore-necks along the fluid-fluid interface. The capillary thresholds arise from the surface tension γ between the immiscible fluids and is described by

$$p_{cap} = \frac{\gamma}{R_1} + \frac{\gamma}{R_2}, \tag{2}$$

where R_1 and R_2 are the smallest possible radii of curvature for the interface meniscus in the vertical and horizontal directions. In a perfect wetting situation, the radii are half the height of the pore-neck and half the width of the pore-neck. The capillary pressure thresholds at each pore is thus determined by the pore geometry. The consequence of Equation (2) is that the pressure difference dP between the invading and saturating fluids has to overcome a certain threshold before a given pore is invaded, i.e., $dP > p_{cap}$. At low enough capillary numbers, at very low constant injection flow, we will see pore-by-pore invasions where the fluid takes the path of least resistance (larger pores have lower thresholds), leaving some pores trapped and/or never invaded. At higher capillary numbers, flow may be driven on a sample scale by a viscous pressure gradient over the saturating fluid. The filtration velocity (interstitial fluid velocity times the porosity) v through a porous medium with permeability κ is described by Darcy's law as

$$v = -\frac{\kappa}{\mu}\nabla P \approx \frac{\kappa}{\mu}\frac{\Delta P}{r}, \tag{3}$$

where μ is the viscosity of the saturating fluid, ΔP is the pressure difference between the invading fluid and the cell outlet, and r is the distance from the invading fluid to the cell outlet. At high enough capillary numbers, since the pressure can be considered constant within the invading fluid cluster [19], Equation (3) shows that the parts of the cluster that are closer to the outside of the cell flow faster than less advanced parts. In addition, the pressure distribution is given by the Laplace equation ($\nabla^2 P = 0$) such that the longest fingers are "screening" the pressure gradient from the less advanced fingers [19]. Due to this instability and the geometry of the pore-space, an invasion bubble will become perturbed early and we will see the onset of viscous fingers from the most advanced parts of the interface, growing on expense of the less advanced parts. In addition, the flow path of fingers is influenced by random capillary thresholds at the interface.

In similar systems where air is injected with high enough overpressure into dry and dense deformable porous media in thin cells, granular fingering patterns emerge as a result of hydraulic fracturing of the dense packing [20–24]. This granular fingering is also observed in liquid saturated dense porous media where the same fluid is injected [25]. An interesting observation in these cases is that despite the absence of surface tension, the granular fingering patterns resemble viscous fingering. This fingering formation is driven by momentum exchange between the flowing fluid and particles, and becomes unstable like viscous fingers when the fluid-solid interface is perturbed. The stabilizing mechanism during granular fingering was found to be particle-particle and particle-plate friction, which builds up in stress-chains during compaction of the multi-layered packing and prevents further particle displacement.

Moreover, combinations of two-phase and granular flow in thin cells have been studied. In e.g., [26–28] it was found that a range of different patterns emerge when air is injected in granular suspensions in thin cells. Invasion patterns such as frictional fingering, viscous fingering, fluidized fronts and stick-slip bubbles were observed depending on bead fraction and injection rate. The resulting patterns depend on whether the invading fluid overcomes frictional or capillary thresholds first, i.e., bead displacement occurs when the capillary threshold is highest and pore-invasion when the frictional threshold is highest. Experiments with air injection into saturated deformable porous media placed under a confining pressure was studied in Holtzman et al. [29]. For a given interface tension γ and friction coefficient μ_f, the crossover from fingering to fracturing during constant flow rates was found to depend only on the confining pressure P_c and particle size d, and that fracturing tends to occur if the particle size is below a critical value $d_c = (\gamma/\mu_f){P_c}^{-1}$. In other words, opening of pore-necks and fracturing was observed when capillary forces could overcome frictional thresholds and rearrange particles. Flow induced deformation in a monolayer of deformable porous media has also been studied in the absence of surface tension, during fluid injection into a soft granular media saturated with the same fluid [30]. During injection, the beads were observed to be displaced radially outwards due to the pressure gradient in the flow, and an empty cavity formed around the injection center. In these experiments, no fingers emerged and the central cavity stabilized at a certain size since the beads were confined within the cell.

In this paper we present an exploratory study where we further experiment with the combination of two-phase and granular flows by performing air injection into saturated monolayers of beads. It is part of fundamental research on pattern morphology in various deforming systems, which is important for increased understanding of flow in any deformable porous medium.

By injecting air at a constant overpressure into a deformable saturated monolayer, we have a system where particles may be displaced by a viscous pressure gradient and/or capillary forces between the two fluids. Since it is a single layer of beads without imposed confining pressure, granular stress is expected to depend on the boundary condition and number of particles in contact ahead of the flow, rather than build-up of normal stress against the plates. The outer boundary can be set to either allow or prevent decompaction of the medium. As a result of competition between viscous and capillary forces, and build-up/relaxation of friction during flow, we expect to see transitions between finger opening and pore invasion in the viscous fingering regime, for example during initial compaction or outer decompaction. We aim to characterize these flow patterns and porous media deformations, depending on imposed boundary conditions and injection pressure.

Increased knowledge of the mentioned processes may have applications in earth science and industry where multiphase flow and solid deformation occur. Examples are oil and gas production [31–33], carbon sequestration [34], enhancement of water well- and geothermal energy production [35–37]. There may also be applications in natural flow, especially in the field of subsurface sediment mobilization, where formations like sand injectites, mud diapirs, and mud volcanoes occur due to pore-fluid overpressure [38–43].

Materials and Methods

Three different types of porous media samples are created by preparing them with the different boundary conditions referred to as non-deformable (ND), confined deformable (CD), or open deformable (OD). These three sample types are presented after a brief introduction to the general experimental setup which is common for all the experiments.

Experimental Setup

In general, the porous samples are created by forming a single layer of 1.0 mm diameter glass beads between the transparent plates of a horizontal and circular Hele-Shaw cell. The bead size has a tolerance of ±10%, but beads are sifted, resulting in a distribution between 1.0 and 1.1 mm. The diameter of the cell is 40 cm, and the 10 mm thick plates are clamped together with a vertical plate separation of 1.0 mm in the ND case and 1.4 mm in the deformable cases. This setup results in obtained volume fractions of 32.7 ± 0.9% beads in the ND cell, and 29.4 ± 1.8% beads in the cell for the deformable systems. If we only consider the volume occupied by the monolayers, the deformable systems have $\sim 10^5$ beads with a volume fraction that is 68.2 ± 4.2% of η_{hcp}, where $\eta_{hcp} = 60.5\%$ is the volume fraction of the densest possible bead configuration in the cell if the plate separation is 1.0 mm (i.e., a hexagonal close packing with $\sim 1.45 \cdot 10^5$ beads). The ND systems have $\sim 8 \cdot 10^4$ beads and a volume fraction that is 54.2 ± 1.4% of η_{hcp}. The reason for the different monolayer volume fractions arise from the different filling procedures for the ND and CD/OD systems, which are described in the next section. The fluid inlet to the sample is a 10 mm diameter hole in the center of the bottom disk, and the outlet is the open perimeter along the rim of the cell. After a sample is prepared, its pore-space is saturated with a viscous water-glycerol solution consisting of 20% water and 80% glycerol by mass, with a viscosity of 0.045 Pa·s. The saturating fluid is wetting the beads as well as the cell disks. **Figure 1** shows a cross-sectional illustration of the experimental setup.

The experimental procedure is also common for all the sample types; the air overpressure to be applied at the cell inlet is pre-set with a pressure regulator situated between a pressurized air reservoir and the cell inlet. The experiment starts when the inlet valve is opened, allowing air to invade the sample with a maintained and constant overpressure. As the overpressure is kept constant at a pressure in the range from 25 to 100 hPa (hPa = mbar), the air cluster will grow and drain the sample radially outwards until it breaks through at the rim. Breakthrough of the air cluster was seen in all our experiments and marks the end of the experiment. The cell is illuminated by flicker free white light from below, and a Photron SA5 high-speed camera positioned above the cell captures optical data at a framerate of 125 frames per second (fps) during the experiment.

Three Cases of Boundary Conditions

The porous matrix of a ND sample is rigid, single-layered and disordered. This sample type is prepared on the bottom disk before assembling the cell; first, the top surface of the bottom disk is coated with an adhesive, thin and transparent plastic film. Then, beads are poured onto the adhesive surface, which will cause them to attach at random positions on the bottom disk. The process is continued until no more beads are able to hit the bottom disk surface, i.e., when the longest distance between

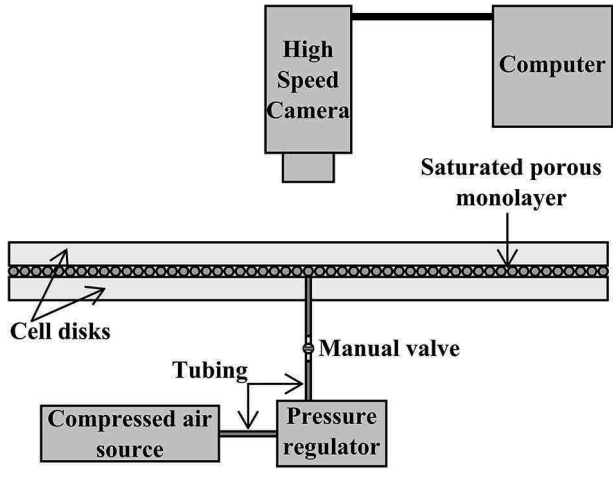

FIGURE 1 | Sketch of the experimental setup for the two-phase flow experiments: The horizontal cell consists of **two** transparent disks of 40 cm in diameter, clamped together (not shown) but separated by a small gap. The gap is big enough to accommodate a saturated porous monolayer of 1.0 mm beads. This sketch represents the non-deformable system, however the setup is the same for the other boundary conditions as well. A compressed air source is connected to an injection hole in the center of the bottom disk, and a pressure regulator is used to adjust the constant injection pressure between 25 and 100 hPa. During air injection, the high speed camera situated directly above the cell captures the invasion at a framerate of 125 frames per second.

beads in the monolayer is shorter than a bead diameter. Pores that are slightly smaller than a bead can occur, so this filling procedure generates a rather loose packed random layer. After removing excess beads of a beginning second layer, the top disk, also adhesive, is put onto the resulting monolayer and clamped together with the bottom disk. The disk separation therefore equals the bead diameter of 1.0 mm.

The porous matrix of a CD sample is a random close packed monolayer of beads which can be displaced within the cell volume, but are prevented to leave the cell by a semi-permeable border. This sample type is prepared partially before and after assembling the cell. First, the rim of the bottom disk is fitted with a semi-permeable belt made of foam rubber (it can be seen in **Figure 2A**). This belt, which is permeable to fluids and impermeable to beads, is 5 mm wide. Next, the top disk is placed onto the bottom disk and they are clamped together. The disk separation is controlled with 1.4 mm thick spacers between the disks at the clamp positions, and ensures the possibility of bead displacement as well as keeping the bead packing approximately single-layered. The gap above the beads (0.4 mm) is still smaller than the large interparticle nearest distance in the system (1 mm), and we observed no significant invasion occurring over several bead lengths in the gap above the beads. When clamped between the plates, the semi-permeable belt with an elastic stiffness of 1.5 kPa is imposed a 47% compressive strain, and has an estimated permeability of 10^{-5} cm^2. Finally, beads are injected into the cell through the central injection hole until they form a monolayer that fills the confined volume. Since the beads may rearrange during the filling procedure, this method results in a more close packed random layer than achieved with the ND method.

The OD sample is prepared in the same way as the CD sample, but with a temporary semi-permeable border at the rim which is removed before experiments. This means that the OD porous matrix is a deformable monolayer where the beads can be displaced and also pushed out of the cell at the open perimeter. Thus, on one side of the scale we have the ND boundary condition where nothing is deformed in the porous medium, and on the other end of the scale we have the OD boundary condition where most of or all of the sample is deformed. Somewhere in between we have the CD boundary condition.

Performed Experiments

Ten experiments are considered in this study. They lasted between 0.9 and 9.7 s, where two of them were ND, four were CD and four were OD. The two ND experiments, used as reference for no deformation, were both injected with an air overpressure of 25 hPa and are labeled ND1 and ND2. Patterns in this system will appear similar for higher injection pressures since we already are in the viscous fingering regime. The CD experiments are referred to as CD25, CD50, CD75, and CD100 since the injection pressures were set as 25, 50, 75, and 100 hPa, respectively. The injection pressures in the OD experiments were selected in the same way, so these experiments are referred to as OD25, OD50, OD75, and OD100. Approximate capillary numbers Ca were calculated for each experiment, based on the equation

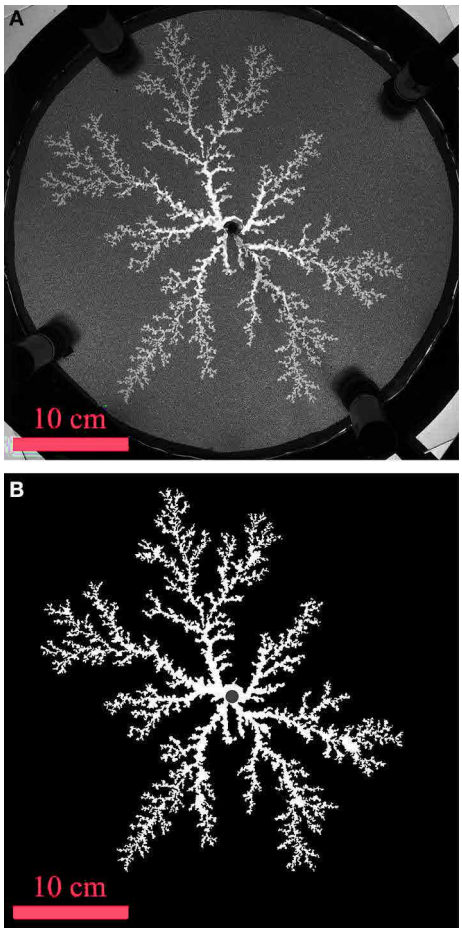

FIGURE 2 | The raw data breakthrough image of the confined deformable experiment with 75 hPa injection pressure (A), and the resulting binary image after segmentation of the air cluster (B), where the active pixels belonging to the cluster is shown in white and the inactive background pixels are shown in black. The dark injection region where it is difficult to separate saturated and invaded parts is indicated in gray, and is excluded from our analysis. In the raw data image we can also see the 0.5 cm thick semi-permeable belt surrounding the porous medium.

$$Ca = \frac{\Delta P a^2}{\gamma R}, \tag{4}$$

which is obtained by combining Equations (1) and (3), where $a = 1$ mm is the typical pore size, $\gamma = 65.7$ μN/mm is the interfacial tension between the fluids, $R = 20$ cm is the cell radius and ΔP is the imposed overpressure. The approximate capillary numbers are found to be $Ca = 0.2$, 0.4, 0.6, and 0.8 for $\Delta P = 25$, 50, 75, and 100 hPa, respectively, and independent of boundary conditions. These capillary numbers confirm that the displacement flow in all our experiments is dominated by viscous forces (viscous fingering regime), as seen in e.g., Løvoll et al. [3] for $Ca = 0.22$. A characteristic permeability for the systems is estimated with the Kozeny-Carman relation [27],

$$\kappa = \frac{a^2 \phi^3}{180(1-\phi)^2}, \tag{5}$$

where a is the bead diameter and ϕ is the porosity. For the ND system with a porosity of 0.673, we get $\kappa = 1.22{\cdot}10^{-4}$ cm^2, and for the deformable systems with a porosity of 0.706 we get $\kappa = 2.26{\cdot}10^{-4}$ cm^2 (initially, before deformation). In the CD system, the permeability of the outer belt is one order of magnitude lower than the initial permeability of the porous medium, however we observed no significant influence on the flow regime due to that. For a characteristic filtration velocity, the pressure drop along a distance L is given by $\Delta P = \mu v L/\kappa$. Even if κ is smaller in the belt than in the cell, its extent L along the flow is much smaller than the radius of the cell. Thus, the characteristic pressure drop, which scales like L/κ, is much larger in the cell than in the belt—explaining why it does not seem to significantly affect the pattern.

The raw data from each experiment is a sequence of grayscale images with a spatial resolution of 1024 × 1024 pixels, where the side of one pixel corresponds to 0.4 mm. The framerate yields high temporal resolution with a snapshot every 8 ms, and each image contains information about the instantaneous configuration of the air cluster and the porous medium. A raw data snapshot is shown in **Figure 2A**.

Flow Pattern Analysis

The raw images are transformed into binary images of the air clusters, i.e., every pixel being a part of the air cluster, defined as having an intensity value above a certain threshold, is given the pixel-value "1" (white) while all the other pixels are assigned the pixel-value "0" (black). An example is shown in **Figure 2B**. In the images of ND experiments, beads have been removed by subtracting the graymap field of the initial image from the graymap field of the current image - a process called image subtraction technique (as e.g., in Løvoll et al. [3], Niebling et al. [12]). Later on, trapped liquid clusters within fingers are replaced by white pixels, considering them as parts of the finger. In the images of deformable experiments, beads have been removed by deleting small white clusters not connected to the large white pattern. A dark central region of 10 mm in diameter is caused by shadow from the injection tubing, so image data here is not considered (the air cluster cannot be distinguished from the liquid). There are different features of the flow patterns that we want to analyze, such as their shape, growth, and fractal dimension. This information is obtained from the binary images with various image processing methods.

To get a visual overview of the shape and growth of a flow pattern over time we create a figure of the breakthrough pattern where colors indicate the time when a pixel was invaded by air. Such a figure is made by summing together all the binary images in the sequence (obtained as explained above), creating a matrix where the elements indicate the number of timesteps during which the considered pixel has been invaded: A value more than 1 means that invasion occurred earlier than breakthrough, 1 is at breakthrough and 0 means that this pixel is never invaded. This matrix is then converted to a figure where colors represent the time of invasion at each pixel of the air cluster, and shown in **Figure 3** for each of the experiments.

In addition to a visual characterization of the patterns, we obtain some quantities to describe the growth of the clusters over time. To investigate the growth of the clusters we plot the radius of the most advanced finger and the radial variation of finger thicknesses as function of time. The longest finger radius as function of time is found by assigning values to the pixels in the binary patterns according to their distance from the injection center, and then record the highest value of each image in the sequence. For the investigation of radial finger thickness variation we look at the average finger thickness as a function of radius from the injection center. This is found by counting the number of active pixels within a small window (plus minus one pixel) around each integer radius, giving the total sum of finger widths per radius. These values are then divided by the corresponding number of fingers per radius (the number of active pixel-segments at each radius), giving the average finger thickness per radius.

Fractal analysis is a commonly used method to describe a two-phase flow pattern since its fractal dimension, when it exists, reveals information about how the pattern fills the space it occupies. There are different ways to estimate the fractal dimension of a pattern [44, 45]. We will look at the mass- and box fractal dimensions, and compare them with local fractal dimensions of intersections at different radii. The mass-radius relation of a pattern is found by counting the number of active pixels (mass) contained within each radius from the injection center. If the log-log plot of the mass-radius relation is linear, such that it follows a power law

$$N(r) \propto r^{D_m}, \tag{6}$$

the fractal mass-dimension D_m of the pattern is found as the slope of the plot. Figure A1 in the Supplementary Material shows the mass-radius relations for the breakthrough patterns from each experiment. The fractal box-dimension of a pattern is estimated by counting the number of squares needed to cover the pattern as a function of the side length of the square. As boxes we use grids of equal squares, where the pattern center is always in the center of a square. Starting with a square larger than the image size, a box count is performed before decreasing the box size. This is repeated until the smallest square covering the entire pattern is found. Then, the smallest box covering the entire pattern is divided into equal but increasingly smaller squares for each box count. The procedure of subsequent box size decreasing and counting is continued until the lower size limit of one pixel is reached. For a fractal, the number of boxes N as function of side length l follows a power law

$$N(l) \propto l^{-D_b}, \tag{7}$$

The value of the fractal box-counting dimension D_b is found as the opposite of the slope of the number of boxes as function of side length in a log-log plot. The slope is fitted between the lower box size cutoff at 1 mm (typical pore size), and the upper cutoff at the largest box size where at least one box does not cover the pattern. Figure A2 in the Supplementary Material shows these plots for each experiment. Finally, a local fractal dimension D_L is estimated as function of radius by intersecting the pattern with a one pixel thick, concentric ring at each radius and do

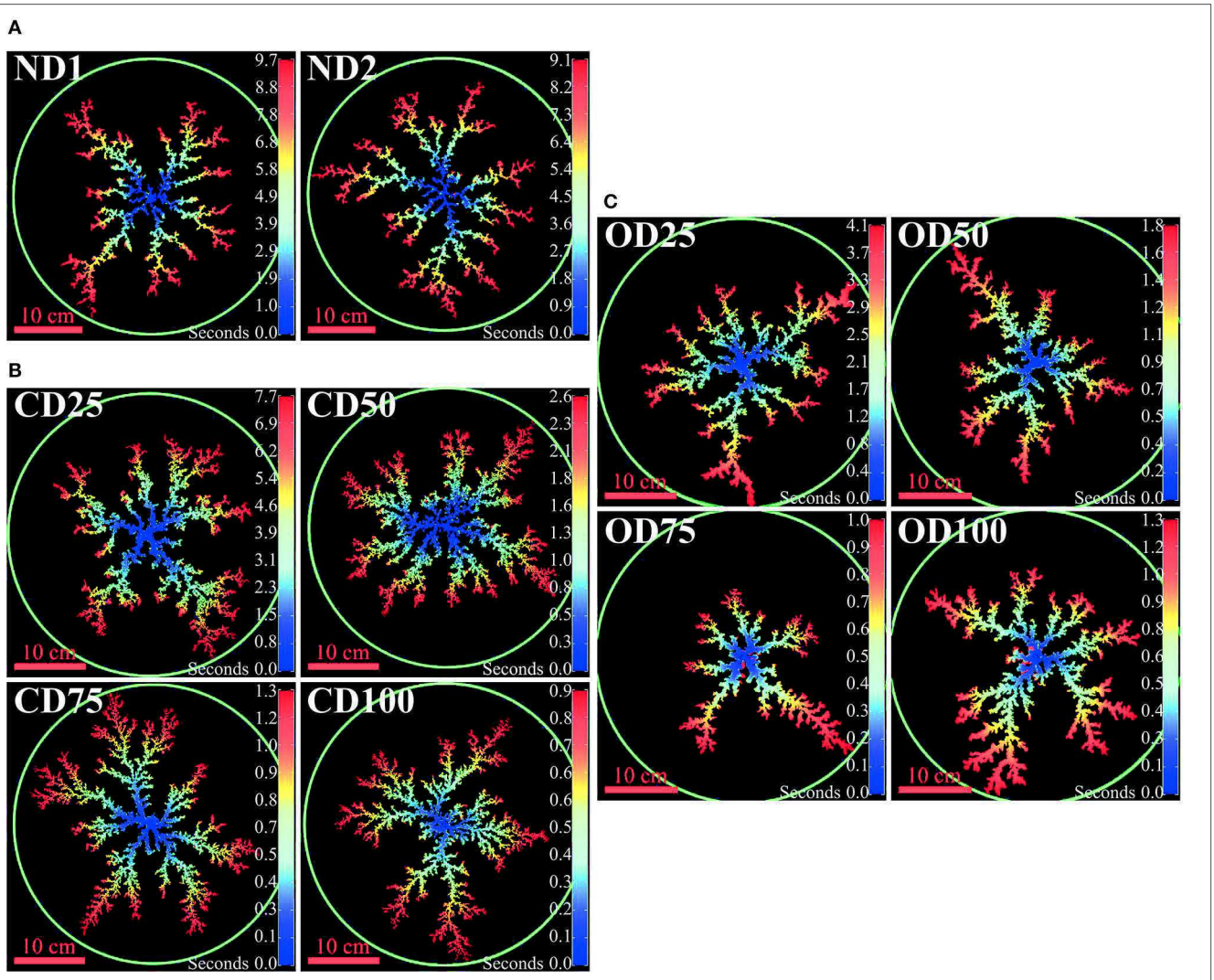

FIGURE 3 | Breakthrough patterns for the non-deformable experiments (A), confined deformable experiments (B), and open deformable experiments (C). Both ND experiments have an injection pressure of 25 hPa, while for the CD and OD experiments the number in the experiment name (top left corners) gives the injection pressure in hPa. The color code indicates the time of air invasion in seconds after start, where blue is at the start and dark red is at breakthrough. The green circles indicate the cell rims.

1-dimensional box counts along the rings. At each radius, the ring is divided into equal arc segments and the number of arc segments that intersect the pattern are counted as function of arc length as the arc length is decreased. The number of arc segments intersecting the pattern is plotted in a log-log plot as a function of arc length, and we find the local fractal dimension as the opposite of the value of the slope as shown in **Figure 4**. The local dimension slopes have one upper and one lower cutoff length at each radius. The upper cutoff length is approximately the separation distance between fingers along the ring, and the lower cutoff length is approximately the average thickness of the fingers. We set the lower cutoff constant as the average finger thickness for the ND patterns, which is found to be approximately 0.4 cm (see Section Pattern Characteristics). The upper cutoff length is set at each radius as the maximum arc length where at least one of the arc segments does not intersect the pattern and is not counted. It is assumed that the flow patterns have an isotropic pattern morphology such that the local fractal dimensions are independent on the angular offset of the arcsegment cuts. In order to compare D_L with D_m and D_b we use Mandelbrot's rule of thumb for intersecting fractal sets [46, 47]. It states that the codimension of a set of intersection points equals the sum of codimensions of the individual intersecting sets. In our case, in the image plane (with dimension $E = 2$), the intersecting sets are the air cluster of codimension 2-D and a ring of codimension 2-1. This gives

$$\begin{aligned} (2 - D) \; + (2 - 1) &= 2 - D_L \\ \Downarrow & \\ D &= D_L + 1, \end{aligned} \tag{8}$$

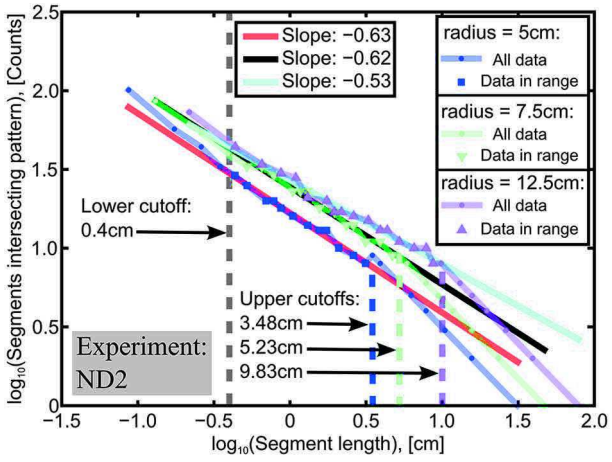

FIGURE 4 | Results of 1-dimensional box counts of the ND2 pattern along a radius of 5, 7.5, and 12.5cm. The slopes that are used to determine the local fractal dimension are fitted to the data points in the range between the lower cutoff of 0.4cm (average finger width) and the upper cutoffs where the pattern appears space filling (indicated by arrows). We see that the upper cutoff, which is approximately the separation between fingers, increase for increasing radius. Local dimension as function of radius is found as the negative value of such slopes, estimated at each pixel radius (approximately every 0.04 cm) outside the injection region. However, at radii where there are <10 data points between cutoffs, the local dimensions are not included for analysis.

where D is the fractal dimension of the pattern and D_L is the local fractal dimension. In a physical view, if the mass within a circle of thickness dr is given by $dr{\cdot}\alpha(2\pi r)^{D_L}$ where α is a constant pre-factor, the total mass inside a radius R is given by

$$N(R) = \alpha \cdot (2\pi)^{D_L} \int_0^R r^{D_L} dr = \frac{\alpha \cdot (2\pi)^{D_L}}{(D_L + 1)} \cdot R^{D_L+1} \propto R^{D_L+1}, \tag{9}$$

if D_L is independent of r. For a perfect fractal cluster $N(R) \sim R^D$, so if $D_L(r)$ is constant we have a perfect fractal with fractal dimension $D = D_L + 1$.

Deformation Analysis

We quantify the deformation of a porous medium by processing the sequence of raw images with a Digital Image Correlation (DIC) software called Ncorr, which by cross-correlation of subsequent frames estimates both direction and magnitude of bead displacements. Closer discussions of this DIC algorithm is found in Blaber et al. [48], Hariral et al. [49]. A qualitative assessment of deformations in the different sample types is done by comparing figures representing the porous media where values of radial displacement components at each pixel is represented by a color code. In addition, areas of compaction or decompaction are identified in figures where the volumetric strains ε_v are represented at each pixel. The volumetric strains are found by Vable [50]

$$\varepsilon_v = \varepsilon_{xx} + \varepsilon_{yy}, \tag{10}$$

assuming that $\varepsilon_{zz} = 0$ in the direction normal to the plates, corresponding to the fixed character of the side plates. The strains ε_{xx} and ε_{yy} at a pixel are estimated from the gradients of the displacement fields around that pixel. In order to reduce noise, least-squares fits are made to the displacement fields within an approximate 2 mm radius around the evaluated pixel, and the slopes of the fits are considered as the displacement gradients.

Results

Pattern Characteristics

The flow patterns from all ten experiments are shown in **Figure 3**, where the color of a pixel indicates the time taken from experiment start until the area of the pixel became invaded by air (For readers who wants a closer look, a larger image is included in the Supplementary Material). In **Figure 3A**, we see that the flow patterns in ND media have long and thin fingers, and the thickness of the fingers appears constant at all radii outside the injection center. The flow patterns in CD media are shown in **Figure 3B**, and they typically feature centrally few and thick fingers that cross over to thinner and more numerous fingers with increasing radius. For the flow patterns in OD media, shown in **Figure 3C**, we see centrally few and thick fingers that cross over to more numerous and thinner fingers at intermediate radii, which then cross back to few thick fingers near the cell outlet. The intermediate region where the fingers are thinner seems to decrease in length for increasing injection pressure. In all the systems the growth of fingers is mainly in the radial direction, favored on the finger tips, and more advanced fingers grow on expense of less advanced fingers.

Figure 5 shows plots of the longest finger radius as function of time for all the experiments, as well as breakthrough times as function of overpressure. The experiments and their breakthrough times are also listed in **Table 1**.

Both the ND experiments were performed with a constant injection pressure of 25 hPa, and we see that the time required to reach breakthrough of the air cluster is similar for both experiments. In the CD experiments we see that the time until breakthrough decreases for increasing injection pressure. This is also seen in the OD boundary condition, except for OD100 which breaks through slower than OD75. The patterns seem to grow with a roughly constant rate over time with some deviations, e.g., a faster growth rate initially for the CD25 and CD50 cases, and OD75 with an increasing growth rate in the second half of the experiment.

In **Figure 6**, plots of the average finger thickness as function of radius are shown in several snapshots during the experiments. For both the ND experiments in **Figure 6A** we see that, over time, the average finger thickness approaches a limiting curve with a more or less constant value around 0.4 cm. For the CD experiments in **Figure 6B** we again see the average finger thickness approach a limiting curve over time, but in this system there is a continuous decrease in average finger thickness with increasing radius. For the CD25, CD75, and CD100 breakthrough patterns the average finger thickness starts at 1.0–1.5 cm near the injection center and quickly decreases to the ND value of 0.4 cm. The CD50 breakthrough pattern already has

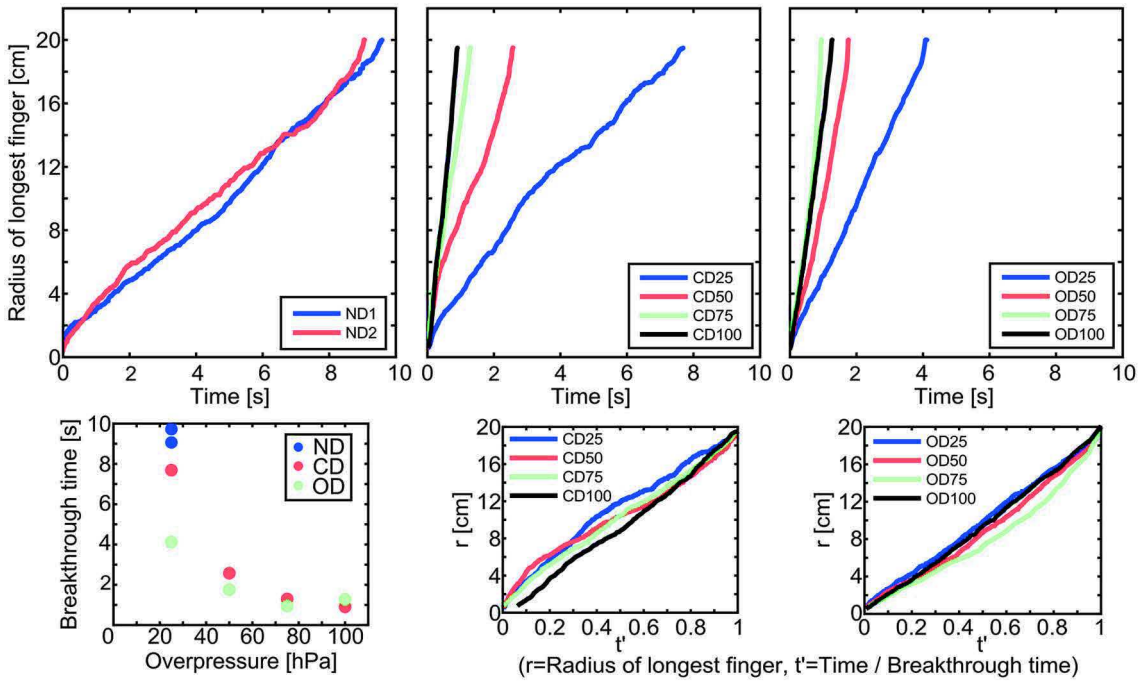

FIGURE 5 | Radius of longest finger as function of time for all the experiments, grouped by boundary condition. From top left to top right: non-deformable, confined deformable, and open deformable. The injection pressure in both ND experiments is 25 hPa, while the number in the experiment names for the CD and OD experiments gives the injection pressure in hPa. In the bottom plots below the deformable experiments, time is divided by breakthrough time to compare the shape of the curves, and the bottom left plot shows the breakthrough times as function of overpressure for all the experiments.

TABLE 1 | Breakthrough times for the experiments.

ND experiment	Breakthrough time [s]	CD experiment	Breakthrough time [s]	OD experiment	Breakthrough time [s]
ND1	9.7	CD25	7.7	OD25	4.1
ND2	9.1	CD50	2.6	OD50	1.8
		CD75	1.3	OD75	1.0
		CD100	0.9	OD100	1.3

an average finger thickness of 0.4 cm initially. However, for all the patterns, when the average finger thickness has decreased to 0.4 cm it will continue to decrease slowly toward 0.2 cm over the remaining radial length of the sample. In the plots for the OD experiments in **Figure 6C**, we also see that the average finger thickness approach a limiting curve over time. In this system, the limiting curves have initially larger average finger thicknesses which decrease and approach the ND constant value of 0.4 cm with increasing radius. Then, after remaining at a thickness of around 0.4 cm over an intermediate range, the average finger thickness increases again when approaching the cell rim. The intermediate range where the average finger thickness is similar to the ND flow patterns seems to decrease in size for increasing injection pressure.

The different fractal dimensions found for the breakthrough patterns are shown in **Figure 7**; **Table 2**.

Having used Equation (8), the local dimensions are plotted as $D_L(r) + 1$, and the mass dimensions D_m and box dimensions D_b are indicated as lines with uncertainties. The uncertainty intervals for the fractal dimensions are determined as the difference between the steepest and least steep slope that can be fit within a 95% confidence interval around the best fits in the log-log plots. In **Figure 7A**, we see that the ND1 and ND2 mass dimensions are virtually equal to their corresponding box dimensions since they have overlapping uncertainty intervals. The mass and box dimensions also correspond well with the local fractal dimensions according to Mandelbrot's rule of thumb, since $D_L(r) + 1$ fluctuates around the corresponding D_m and D_b values. A sharp decrease in local dimensions is seen close to the rim, and is due to finite size effects of the clusters. In **Figure 7B** we see the fractal dimensions found for the CD patterns. Except for the CD50 pattern where the mass dimension is equal to the box dimension within the uncertainties, the mass dimensions are significantly lower than the obtained box dimensions. The box dimensions correspond better to the local dimensions than the mass dimensions do. As for the ND patterns the CD25 and CD50

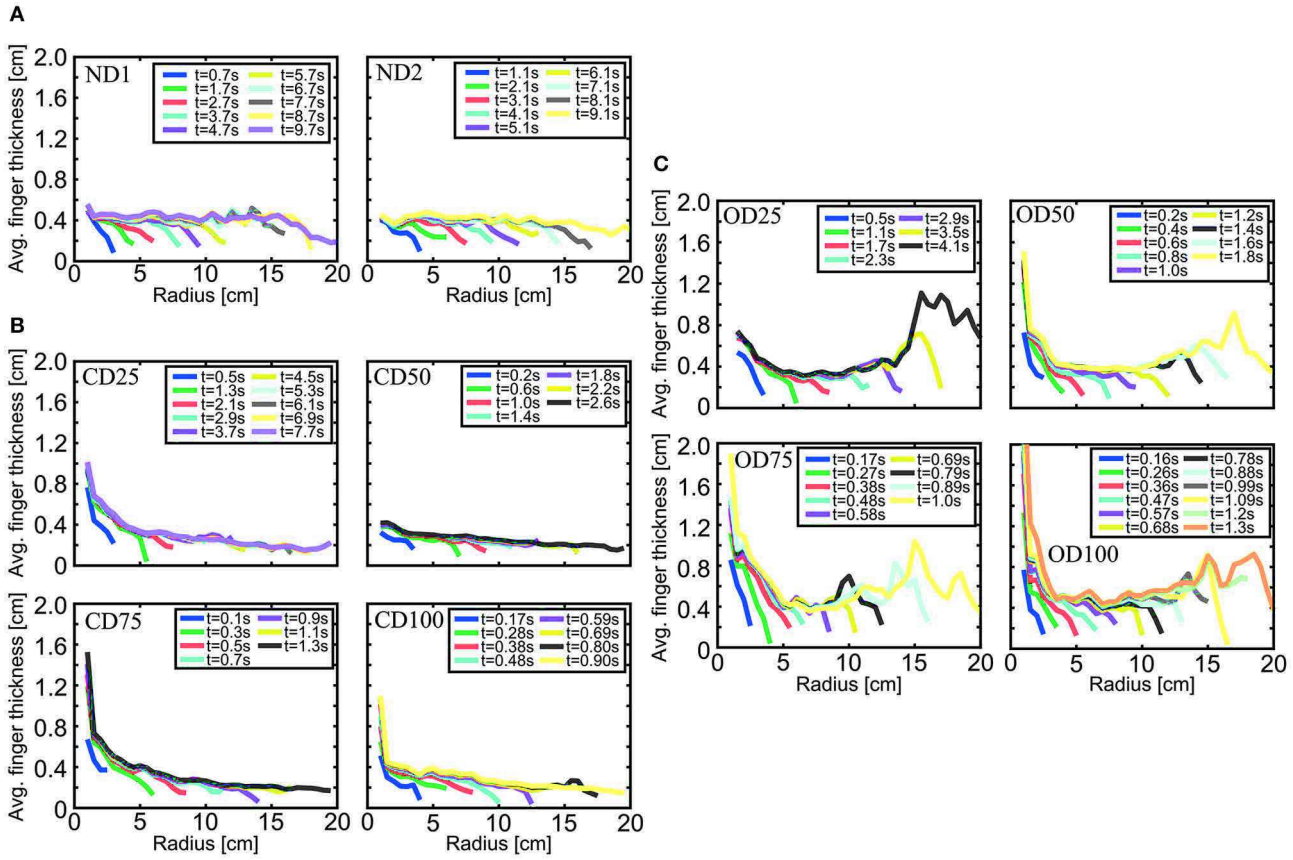

FIGURE 6 | Average finger thickness as function of radius plotted at several snapshots for the non-deformable experiments (A), confined deformable experiments (B), and open deformable experiments (C). The injection pressure in both ND experiments is 25 hPa, while the number in the experiment names for the CD and OD experiments gives the injection pressure in hPa.

local dimensions fluctuate around the box dimension values, before the outer finite size effects make the local dimensions decrease. For the higher injection pressures, CD75 and CD100, we see an inner region with higher local dimensions, before the local dimensions approach values fluctuating around the corresponding box dimensions, and finally decrease due to the finite size effects. The obtained dimensions for the OD breakthrough patterns are plotted in **Figure 7C**. All of the patterns show a decreasing trend in local dimensions for increasing radius. The mass dimensions are significantly lower than the obtained box dimensions, and the box dimensions seem to best correspond to the local dimensions for intermediate radii. Inner regions show higher local dimensions, with $D_L(r) + 1$ starting on 1.8–1.9, indicating emptier inner structures.

Figure 8A shows examples of mass-radius relations at several snapshots of growing clusters in each boundary condition. For the boundary conditions probed, the mass-radius relations are seen to grow toward a limiting curve over time. The flat regions seen at larger radii are outside the current pattern, and they give the total mass at that time. We check whether the mass dependence on time and radius can be collapsed onto a master curve according to a Family-Vicsek relationship [51]. Indeed, such a relationship is common in many growth phenomena, as e.g., in rough interface evolution during two-phase flow in Hele-Shaw cells [52], interface depinning models [53], fracture front growth [54] and thermal roughening of dipolar chains [55, 56]. **Figure 8B** shows Family-Vicsek scaling of the same mass-radius relations as in **Figure 8A**, and show how they scale over time. We have assumed that the total mass N and longest finger r of a pattern scales with time as

$$N(t) = N_b \cdot (t/t_b)^{\alpha} \quad , \quad r(t) = r_b \cdot (t/t_b)^{\beta}, \tag{11}$$

where N_b, r_b, and t_b are breakthrough values of mass, radius and time, respectively. It is a reasonable assumption once the fingering instability is established, i.e., after the patterns had grown to a mass of around 10% of N_b. The plots are shown in Figure A3 in the Supplementary Material. Since, in addition, the mass-radius relation is assumed to follow Equation (6), the scaled mass-radius relation should be on the form

$$\frac{N(r,t)}{N_b \cdot (t/t_b)^{\alpha}} = \left(\frac{r}{r_b \cdot (t/t_b)^{\beta}} \right)^{D_m}, \tag{12}$$

where D_m is the mass dimension of the pattern. We find the scaling exponent α from the slope of the log-log plot of $(N(t)/N_b)$

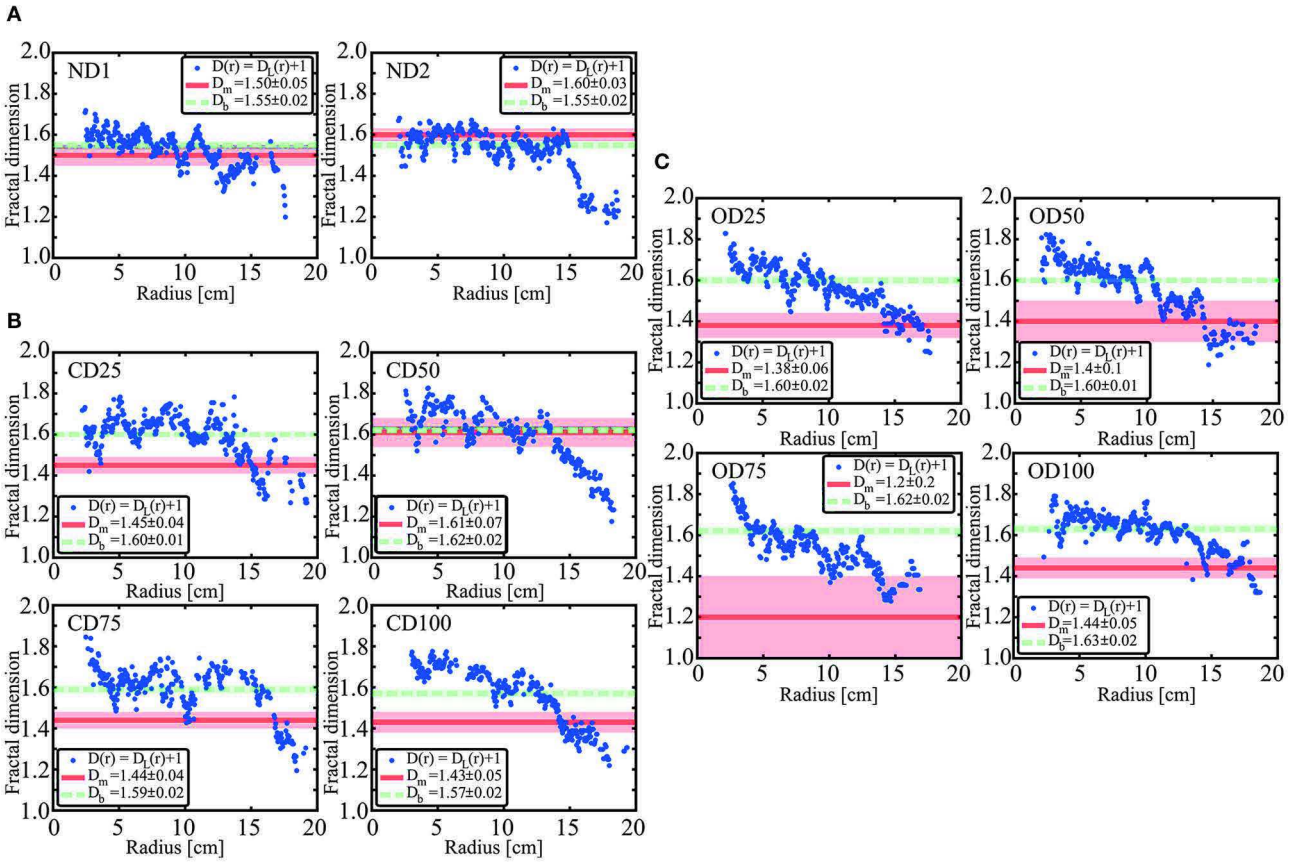

FIGURE 7 | The blue dots represent local fractal dimensions plotted as ($D_L + 1$) as function of radius for the non-deformable breakthrough patterns (A), confined deformable breakthrough patterns (B), and open deformable breakthrough patterns (C). The estimated mass dimensions D_m are indicated as solid red lines with uncertainties shown as light red bands, and the box dimensions D_b are indicated as dotted green lines with uncertainties shown as light green bands. Overlaps of the D_m and D_b uncertainties are colored gray. The injection pressure in both ND experiments is 25 hPa, while the number in the experiment names for the CD and OD experiments gives the injection pressure in hPa.

TABLE 2 | The fractal mass dimensions D_m and box dimensions D_b for the breakthrough patterns.

	ND1	ND2	CD25	CD50	CD75	CD100	OD25	OD50	OD75	OD100
D_m	1.50 ± 0.05	1.60 ± 0.03	1.45 ± 0.04	1.61 ± 0.07	1.44 ± 0.04	1.43 ± 0.05	1.38 ± 0.06	1.40 ± 0.10	1.20 ± 0.20	1.44 ± 0.05
D_b	1.55 ± 0.02	1.55 ± 0.02	1.60 ± 0.01	1.62 ± 0.02	1.59 ± 0.02	1.57 ± 0.02	1.60 ± 0.02	1.60 ± 0.01	1.62 ± 0.02	1.63 ± 0.02

as function of (t/t_b), and the scaling exponent β from the slope of the log-log plot of $(r(t)/r_b)$ as function of (t/t_b), following Equation (11). The estimated values for α and β are presented in **Table 3**, and the corresponding plots are shown in Figure A3 in the Supplementary Material.

For the ND boundary condition we see that the scaled curves collapse fairly well on top of each other, except for an inner part which has a slightly lower mass-radius slope. The slopes are however limited to the estimated mass dimension. For both the deformable boundary conditions we see that the scaled curves collapse well on top of each other and along the estimated mass dimensions. Although, there are inner parts with slopes close to 2 falling down from the collapsed curves. This effect is most obvious in the OD plots.

Deformations

Deformation of the porous media is illustrated in **Figure 9** for selected snapshots of the confined and OD experiments with an injection pressure of 100 hPa. The radial displacements and volumetric strains are shown at an early stage, around mid-experiment, at a later stage and at breakthrough. Radial displacement of beads in the CD boundary condition, seen in **Figure 9A**, are directed outwards from the injection center. In the initial stage, the displacements do not reach all the way to the rim of the cell, but over time the displaced area grows toward a final size and magnitude, which goes toward zero near the rim. The corresponding volumetric strains are shown in **Figure 9B**, and show that the porous medium is increasingly compacted with time outside the invasion cluster.

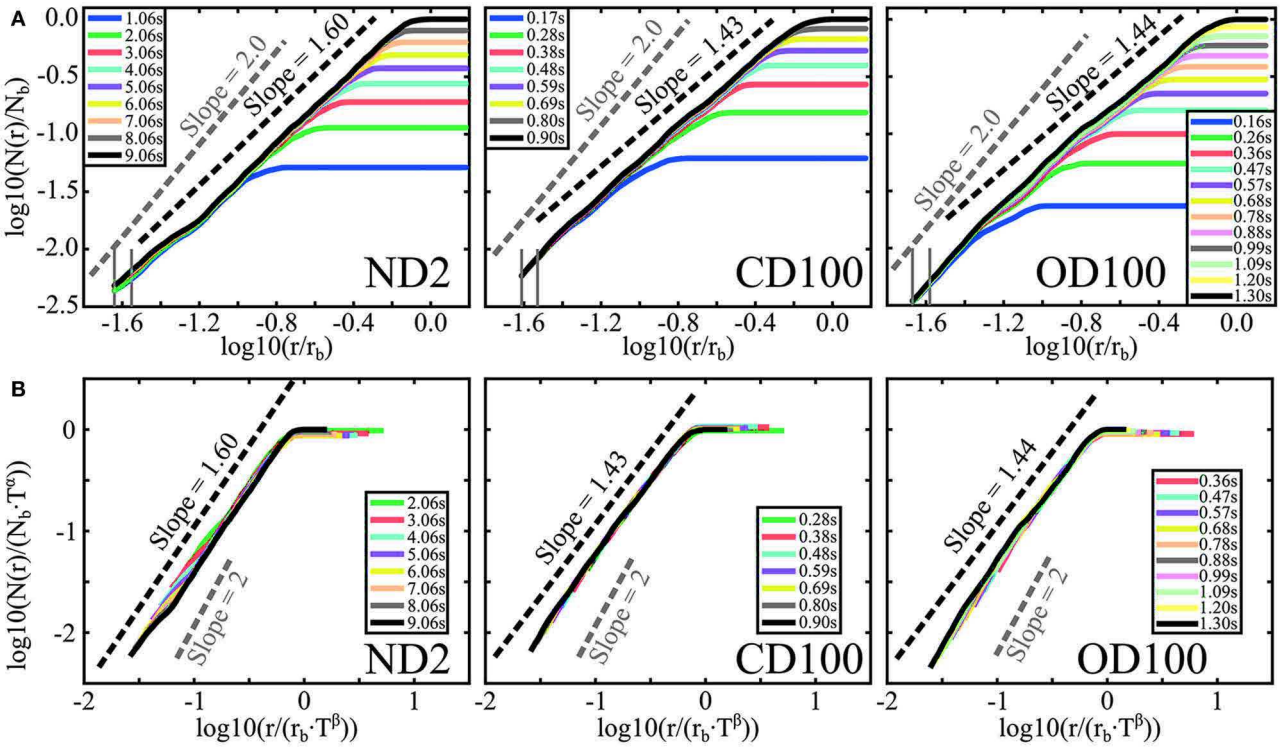

FIGURE 8 | (A) Examples of mass-radius relations at several snapshots for a non-deformable experiment at 25 hPa (left), a confined deformable experiment at 100 hPa (middle), and an open deformable experiment at 100 hPa (right). At the start of the curves, the leftmost gray vertical lines mark the lower radius cutoff, which is just outside the injection region, and the gray vertical lines to the right mark a distance of 1 mm outside the lower cutoff. The black dotted lines show the estimated mass dimensions for the breakthrough patterns. The gray dotted lines has slopes of 2 to indicate the space filling dimension of an emptied bubble. **(B)** Family-Vicsek scaling of the same mass-radius relations as above, except for the smallest clusters with a total mass <10% of the breakthrough mass. On the axes, $T = (t/t_b)$ is the ratio of time over breakthrough time, r is radius, r_b is breakthrough radius, $N(r)$ is mass within radius r, N_b is total mass at breakthrough, and α and β are scaling exponents. Here, for ND2: $\alpha = 1.45$ and $\beta = 0.80$, for CD100: $\alpha = 1.58$ and $\beta = 1.02$, and for OD100: $\alpha = 1.73$ and $\beta = 1.10$.

Finger opening, i.e., parts of the air cluster empty of beads, is observed in regions where the volumetric strain exceeds 0.05. Thus, there is a crossover from finger opening to pore invasion in the latter half of the experiment. Radial displacements at different snapshots for the OD100 experiment are shown in **Figure 9C**. We see a similar behavior as in the CD case initially, where the inner beads are displaced radially outwards from the injection center while the outer beads are not yet displaced. With time, the radial displacements increase in magnitude outside the growing cluster and eventually reach out to the rim where beads leave the cell. The corresponding volumetric strains for the OD snapshots are shown in **Figure 9D**. Initially, there is compaction outside the growing air cluster, and with time there is increasing decompaction of the outer portion of the medium. Again, finger opening is observed in regions with volumetric strain above 0.05 and we see that it goes on until breakthrough in this experiment.

The tangential displacements were found to look similar for both boundary conditions, and is illustrated for a 40 ms interval in **Figure 10**. The displacements are directed away from the sides of the fingers, and are higher in magnitude for larger fingers. Outside the air cluster, where radial displacement dominates, tangential displacement magnitudes are small.

TABLE 3 | The scaling exponents α and β found for the experiments ND2, CD100, and OD100.

	α	β	$D_m = \alpha/\beta$
ND2	1.45 ± 0.18	0.80 ± 0.17	1.81 ± 0.35
CD100	1.58 ± 0.12	1.02 ± 0.13	1.55 ± 0.25
OD100	1.73 ± 0.10	1.10 ± 0.04	1.57 ± 0.14

Discussion

When we examine the flow patterns in **Figure 3**, we find that they have both common features across boundary conditions and typical characteristics depending on the boundary conditions. In common, they all have the dendritic branching structure that spreads out from the center, similar to DLA [18], where longer fingers grow on expense of less advanced fingers. This behavior is expected for viscous fingering in a porous medium since the invasion flow follows Darcy's law (3), with the pressure distribution given by the Laplace equation outside the air cluster (of constant pressure) such that the pressure gradient is screened inside the longest fingers [19]. We do observe in **Figures 6**, **8** that spatial properties of the structures grow toward limiting curves

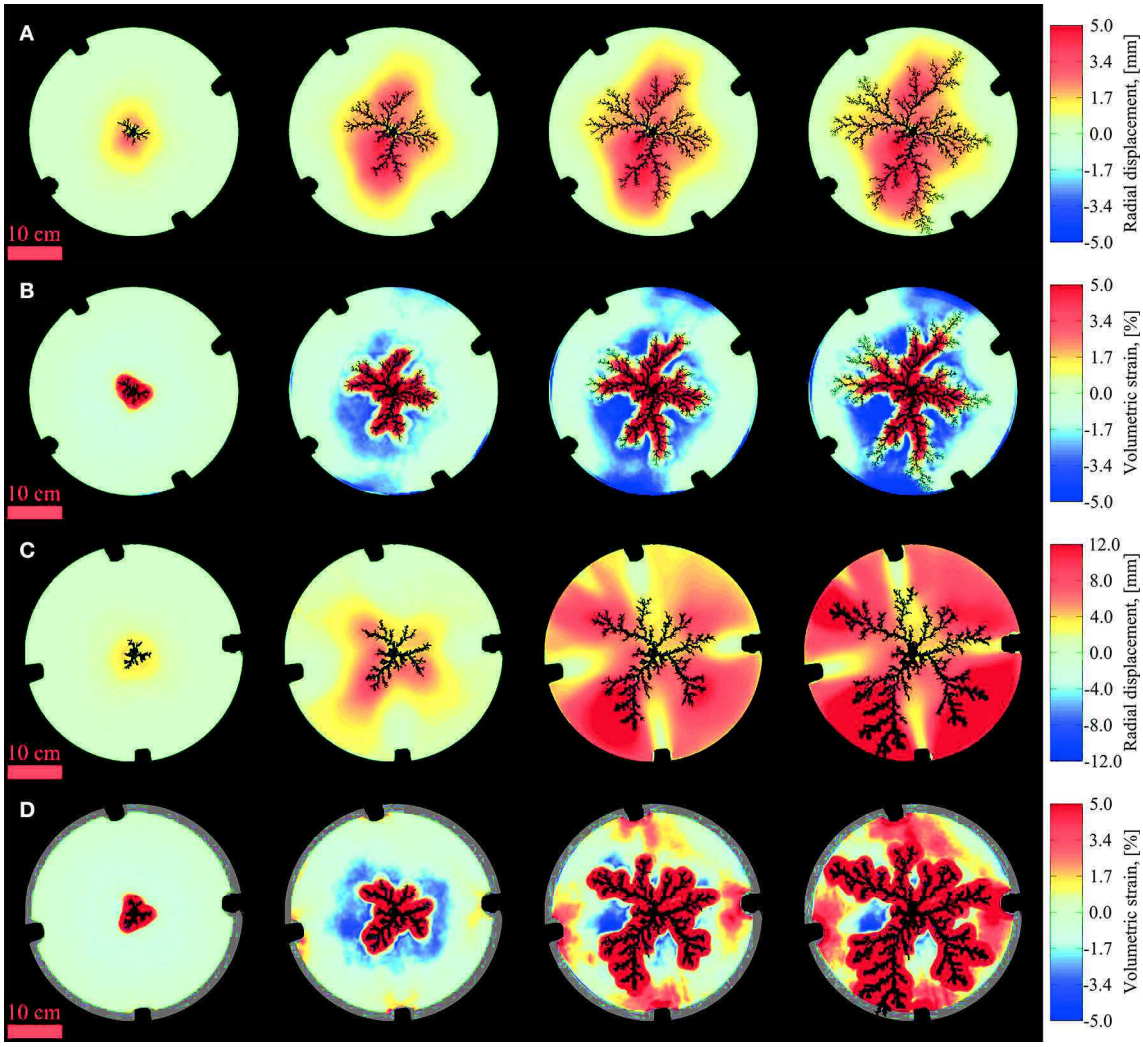

FIGURE 9 | Visualization of accumulated deformation at different snapshots during experiments: Radial displacements **(A)** and volumetric strains **(B)** in the confined deformable experiment with 100 hPa injection pressure. The radial displacements **(C)** and volumetric strains **(D)** are for the open deformable experiment with 100 hPa injection pressure. Time is increasing from left to right, where the snapshots in **(A,B)** are taken at 176, 488, 696, and 904 ms (i.e., 20, 54, 77, and 100% of the breakthrough time). The snapshots in **(C,D)** are taken at 232, 544, 960, and 1272 ms (i.e., 18, 43, 75, and 100% of the breakthrough time). For the radial displacements **(A,C)**, red color means that displacements are directed outwards and blue means inwards. For the volumetric strains **(B,D)**, red color means decompaction and blue means compaction. The air clusters and areas outside of the cell are shown in black, and the black bumps at the cell rim are due to the clamps. The gray areas in **(D)** indicate omitted data where boundary effects of beads leaving the cell influence the strain calculations.

over time, and in **Figure 7** that the local fractal dimensions show a sudden decrease at the outermost radii, i.e., the active growth zone. This confirms that growth dynamics of the patterns follow a behavior where an outer active growth zone surrounds an internally developed and frozen pattern, as described in similar linear systems [3, 4]. The fundamental similarity in the growth dynamics of the structures is reflected by their similar global appearance across boundary conditions. This is also indicated by the fractal box dimensions, which are all observed in the range from 1.55 to 1.63, consistent with earlier observed values of e.g., 1.53 [4] and 1.62 [19] for viscous fingers in ND porous media. The breakthrough times, shown in **Figure 5**, are generally observed to decrease with increased deformability and injection pressure, while the growth rates generally seem to have a linear trend with some fluctuations.

Typically, as seen in **Figures 3A**, **6A**, invasion patterns in the ND system has long thin fingers with approximately the same finger thickness at all radii. In the deformable systems, typical invasion patterns have initially an air bubble emptied of grains, as observed in Johnsen et al. [21]. The empty bubble seems larger for higher injection pressure and deformability, but in all cases it branches rather quickly into few and thick fingers. In the CD system (**Figures 3B**, **6B**) the few thick fingers cross over to increasingly numerous and thinner fingers with radius, while in the OD system (**Figures 3C**, **6C**), typical invasion patterns goes from the few thick fingers into more numerous and thinner

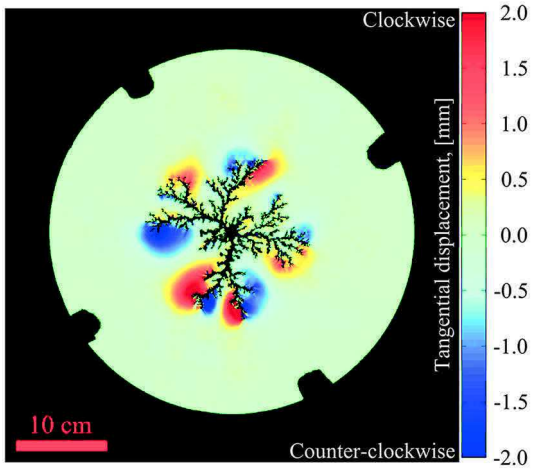

FIGURE 10 | Example of tangential displacement behavior taken from the interval of 448–488 ms (50–54% of breakthrough time) for the confined deformable experiment with 100 hPa injection pressure. Blue color means counter-clockwise displacements and red means clockwise displacements. The air cluster and area outside of the cell are shown in black, and the black bumps at the cell rim are due to the clamps.

fingers before crossing back to few and thick fingers close to the rim. The key difference between the deformable systems is visualized in **Figures 9B,D**. The porous medium in the CD system is increasingly compacted as the cluster grows, while the porous medium in the OD system is centrally compacted and then decompacted near the rim as the cluster grows. Inside the longest finger radius, displacements are observed to be directed out from the side of fingertips as in **Figure 10**, while outside the invasion cluster, radial displacements dominate.

The radial displacements outside the invasion cluster are driven by a viscous pressure gradient, as in the experiments by MacMinn et al. [30] where a saturated granular material is injected with the same fluid. We assume that radial displacement occurs outside the invasion cluster when

$$\Delta p > \sigma_g, \tag{13}$$

where Δp is the viscous pressure drop across a bead and σ_g is the granular stress opposing bead displacement. In the OD boundary condition, decompaction at the rim is believed to initiate when the pressure drop across the outer layer of beads overcome the pressure necessary to move one bead out of the cell, $\Delta p > \sigma_b$.

The displacements away from fingertips correspond to opening of fractures by capillary forces, as e.g., discussed in Holtzman et al. [29]. A typical capillary threshold in our deformable systems is found from Equation (2) as

$$p_{cap} = \gamma \left(\frac{2}{a} + \frac{2}{b} \right), \tag{14}$$

where a is the typical bead size and b is the plate separation, giving $p_{cap} = 225.26$ Pa. Since the lowest injection pressure in our experiments is 2500 Pa, we can always expect pore invasions if fracturing does not occur. However, if

$$p_{cap} > \sigma_g \text{ and } \Delta p_\perp > \sigma_g, \tag{15}$$

where $\Delta p_\perp$ is the pressure drop perpendicular to fingers across beads, fracturing is assumed to occur. Limiting mechanisms for fracturing can then be an increase in σ_g due to compaction and accumulated friction, or a decrease in $\Delta p_\perp$ due to pressure screening from the longest fingers.

In the CD system fracturing occurs initially, but since the granular stress increase as the medium compacts over time, we observe a crossover from fracturing to pore invasions. In the OD system, fracturing occurs initially and may cross over to pore invasions in the intermediate compacted region due to compaction and accumulated friction. Later on, when the fingers approach the open rim, the medium decompacts and friction is relaxed such that fracturing re-initiates. This results in a new instability as fingers are sensitive to the proximity of the open rim, and we observe 1–2 fingers grow to breakthrough on expense of the others. The outer fingers appear similar to fractures in a paste [57]. During the outer fracturing instability for the higher injection pressures, we also see an increased number of branches on the longest fingers. This could be a consequence of outer decompaction of the media, in the sense that the pore sizes increase along the fingers and become more easily invaded.

The local fractal dimensions in **Figure 7A** are more or less constant inside the frozen region, and correspond well to the global mass- and box dimensions by Mandelbrot's rule of thumb (8). Thus, the ND patterns have fairly well defined fractal dimensions on a global scale, between 1.5 and 1.6, consistent with earlier observed values. The local fractal dimensions in **Figure 7B**, for the CD experiments, are observed to be approximately constant in the frozen part of the patterns, similar to the ND case for the lower injection pressures (CD25, CD50). However, for higher injection pressures we see slightly higher local dimensions initially, influenced by the central emptied structures and thick fingers. The local dimensions for the structures in the OD system, **Figure 7C**, are more or less decreasing with radius. In addition, mass dimensions for the deformable patterns generally do not correspond well with the local dimensions due to finite size effects. In other words, the less developed outer parts contribute to a decrease in the mass-radius slope. For the CD100 and OD experiments the box dimension only corresponds with a part of the local dimensions. This indicates that the patterns in the most deformable systems does not have a well-defined global fractal dimension, but have locally defined fractal dimensions and transitions of universality class with radius. The initial emptied and thick finger regions seem to have local dimensions corresponding to around 1.7 which is the measured fractal dimension for invasion patterns in empty cells and DLA [58, 59]. In an intermediate region, the local dimensions correspond well to the measured box dimensions around 1.6, indicating viscous fingering. For the outer parts in the OD system, the local dimensions decrease toward 1.4, which is similar to the measured box dimension of 1.43 for fractures in a paste [57].

After pattern growth develops into viscous fingering, the mass-radius relations as function of time are found to scale according to a Family-Vicsek scaling relation, where $N(t) = N_b \cdot (t/t_b)^{\alpha}$ and $r(t) = r_b \cdot (t/t_b)^{\beta}$. The dynamic scaling exponents α for the invaded area over time $N(t) \sim t^{\alpha}$ are observed to increase with the deformability of the porous media. When considering that

$$\frac{dN(t)}{dt} \sim t^{\alpha-1}, \tag{16}$$

we see that higher values of α imply that the invaded area changes at a faster rate. To the knowledge of the authors, a dynamic scaling exponent for invasion area over time for two-phase flow in deformable porous media is not discussed in earlier papers. Thus, we present a new measured exponent which calls for theoretical evaluation and comparison with theoretical models. When mass dimensions of the patterns in the deformable systems are estimated from the scaling law, $D_m = \alpha/\beta$, we get the values 1.55 ± 0.25 for CD100 and 1.57 ± 0.14 for OD100, which is similar to the respective box dimensions as well as observed fractal dimensions of patterns in ND systems.

Acknowledgments

This project has received funding from the European Union's Seventh Framework Programme for research, technological development and demonstration under grant agreement no. 316889, ITN FlowTrans. We acknowledge the support of the University of Strasbourg and the IDEX program through the award "Hope of the University of Strasbourg," and the University of Oslo. We thank Mihailo Jankov for technical support.

Supplementary Material

The Supplementary Material for this article can be found online at: http://journal.frontiersin.org/article/10.3389/fphy.2015.00081

References

1. Saffman PG, Taylor G. The penetration of a fluid into a porous medium or Hele-Shaw cell containing a more viscous liquid. *Proc R Soc Lond A Math Phys Sci.* (1958) **245**:312–29. doi: 10.1098/rspa.1958.0085
2. Lenormand R. Pattern growth and fluid displacements through porous media. *Physica A*. (1986) **140**:114–23.
3. Løvoll G, Méheust Y, Toussaint R, Schmittbuhl J, Måløy KJ. Growth activity during fingering in a porous Hele-Shaw cell. *Phys Rev E*. (2004) **70**:026301. doi: 10.1103/PhysRevE.70.026301
4. Toussaint R, Løvoll G, Méheust Y, Måløy KJ, Schmittbuhl J. Influence of pore-scale disorder on viscous fingering during drainage. *Europhys Lett.* (2005) **71**:583. doi: 10.1209/epl/i2005-10136-9
5. Toussaint R, Måløy KJ, Méheust Y, Løvoll G, Jankov M, Schäfer G, et al. Two-phase flow: structure, upscaling, and consequences for macrosopic transport properties. *Vadoze Zone J.* (2012) **11**:3. doi: 10.2136/vzj2011.0123
6. Huang H, Zhang F, Callahan P, Ayoub J. Granular fingering in fluid injection into dense granular media in a Hele-Shaw cell. *Phys Rev Lett.* (2012) **108**:258001. doi: 10.1103/PhysRevLett.108.258001
7. Kong XZ, Kinzelbach W, Stauffer F. Morphodynamics during air injection into water-saturated movable spherical granulates. *Chem Eng Sci.* (2010) **65**:4652–60. doi: 10.1016/j.ces.2010.05.007
8. Varas G, Vidal V, Géminard JC. Morphology of air invasion in an immersed granular layer. *Phys Rev E*. (2011) **83**:061302. doi: 10.1103/PhysRevE.83.061302
9. Vinningland JL, Johnsen Ø, Flekkøy EG, Toussaint R, Måløy KJ. Granular Rayleigh-Taylor instability: experiments and simulations. *Phys Rev Lett.* (2007) **99**:048001. doi: 10.1103/PhysRevLett.99.048001
10. Frette V, Feder J, Jøssang T, Meakin P. Buoyancy-driven fluid migration in porous media. *Phys Rev Lett.* (1992) **68**:3164. doi: 10.1103/PhysRevLett.68.3164
11. Völtz C, Pesch W, Rehberg I. Rayleigh-Taylor instability in a sedimenting suspension. *Phys Rev E*. (2001) **65**:011404. doi: 10.1103/PhysRevE.65.011404
12. Niebling MJ, Flekkøy EG, Måløy KJ, Toussaint R. Mixing of a granular layer falling through a fluid. *Phys Rev E*. (2010) **82**:011301. doi: 10.1103/PhysRevE.82.011301
13. Birovljev A, Furuberg L, Feder J, Jøssang T, Måløy KJ, Aharony A. Gravity invasion percolation in two dimensions: experiment and simulation. *Phys Rev Lett.* (1991) **67**:584. doi: 10.1103/PhysRevLett.67.584
14. Méheust Y, Løvoll G, Måløy KJ, Schmittbuhl J. Interface scaling in a two-dimensional porous medium under combined viscous, gravity, and capillary effects. *Phys Rev E*. (2002) **66**:051603. doi: 10.1103/PhysRevE.66.051603
15. Wilkinson D, Willemsen JF. Invasion percolation: a new form of percolation theory. *J Phys A Math Gen.* (1983) **16**:3365–76.
16. Chandler R, Koplik J, Lerman K, Willemsen JF. Capillary displacement and percolation in porous media. *J Fluid Mech.* (1982) **119**:249–67.
17. Lenormand R, Zarcone C. Capillary fingering: percolation and fractal dimension. *Transp Porous Media*. (1989) **4**:599–612.
18. Paterson L. Diffusion-Limited Aggregation and two-fluid displacements in porous media. *Phys Rev Lett.* (1984) **52**:1621–4. doi: 10.1103/PhysRevLett.52.1621
19. Måløy KJ, Feder J, Jøssang T. Viscous fingering fractals in porous media. *Phys Rev L*. (1985) **55**:2688.
20. Lemaire E, Abdelhaye YOM, Larue J, Benoit R, Levitz P, van Damme H. Pattern formation in noncohesive and cohesive granular media. *Fractals* (1993) **1**:968–76. doi: 10.1142/S0218348X93001040
21. Johnsen Ø, Toussaint R, Måløy KJ, Flekkøy EG. Pattern formation due to air injection into granular materials confined in a circular Hele-Shaw cell. *Phys Rev E*. (2006) **74**:001301. doi: 10.1103/PhysRevE.74.011301
22. Cheng X, Xu L, Patterson A, Jaeger HM, Nagel SR. Towards the zero-surface-tension limit in granular fingering instability. *Nat Phys.* (2008) **4**:234–7. doi: 10.1038/nphys834
23. Johnsen Ø, Toussaint R, Måløy KJ, Flekkøy EG, Schmittbuhl J. Coupled air/granular flow in a linear Hele-Shaw cell. *Phys Rev E*. (2008) **77**:011301. doi: 10.1103/PhysRevE.77.011301
24. Niebling MJ, Toussaint R, Flekkøy EG, Måløy KJ. Dynamic aerofracture of dense granular packings. *Phys Rev E*. (2012) **86**:061315. doi: 10.1103/PhysRevE.86.061315
25. Johnsen Ø, Chevalier C, Lindner A, Toussaint R, Clément E, Måløy KJ, et al. Decompaction and fluidization of a saturated and confined granular medium by injection of a viscous liquid or gas. *Phys Rev E*. (2008) **78**:051302. doi: 10.1103/PhysRevE.78.051302
26. Chevalier C, Lindner A, Leroux M, Clément E. Morphodynamics during air injection into a confined granular suspension. *J NonNewton Fluid Mech.* (2009) **158**:63–72. doi: 10.1016/j.jnnfm.2008.07.007
27. Sandnes B, Flekkøy EG, Knudsen HA, Måløy KJ, See H. Patterns and flow in frictional fluid dynamics. *Nat Commun.* (2011) **2**:288. doi: 10.1038/ncomms1289
28. Eriksen JA, Marks B, Sandnes B, Toussaint R. Bubbles breaking the wall: two-dimensional stress and stability analysis. *Phys Rev E*. (2015) **91**:052204. doi: 10.1103/PhysRevE.91.052204

29. Holtzman R, Szulczewski ML, Huanes R. Capillary fracturing in granular media. *Phys Rev Lett.* (2012) **108**:264504. doi: 10.1103/PhysRevLett.108.264504
30. MacMinn CW, Dufresne ER, Wettlaufer JS. Fluid-driven deformation of a soft granular material. *Phys Rev X.* (2015) **5**:011020. doi: 10.1103/PhysRevX.5.011020
31. Montgomery CT, Smith MB. Hydraulic fracturing: history of an enduring technology. *J Pet Technol.* (2010) **62**:26–32. doi: 10.2118/1210-0026-jpt
32. Department of Energy, Hydraulic fracturing white paper (2004), EPA 816-R-04-003, Appendix A.
33. Naik GC. *Tight Gas reservoirs - An Unconventional Natural Energy Source for the Future* (2003). Available online at: http://www.pinedaleonline.com/socioeconomic/pdfs/tight_gas.pdf (Accessed 11, 2014).
34. Johnson SM, Morris JP. Hydraulic fracturing mechanisms in carbon sequestration applications. In: *43rd U.S. Rock Mechanics Symposium and 4th U.S. - Canada Rock Mechanics Symposium*. Asheville, NC: American Rock Mechanics Association (2009).
35. Williamson WH, Wooley DR. *Hydraulic Fracturing to Improve the Yield of Bores in Fractured Rock*. Canberra, ACT: Australian Government Publishing Service (1980).
36. Rummel F, Kappelmayer O. The Falkenberg geothermal frac-project: concepts and experimental results. *Hydraul Fract Geotherm Energy*. (1983) **5**:59–74. doi: 10.1007/978-94-009-6884-4_4
37. Clark L. Energy company plans to frack volcano. In: *Wired Science* (2012). Available online at: http://www.wired.com/wiredscience/2012/10/newberry-volcano-fracking (Accessed 11, 2014).
38. Hurst A, Cartwright J, Duranti D. Fluidization structures produced by upward injection of sand through a sealing lithology. In: Van Rensbergen P, Hillis RR, Maltman AJ, Morley CK, editors. *Subsurface Sediment Mobilization*. London: Geological Society (2003), Special Publications 216. pp. 123–38.
39. Løseth H, Wensaas L, Arntsen B, Hovland M. Gas and fluid injection triggering shallow mud mobilization in the Hordaland Group, North Sea. In: Van Rensbergen P, Hillis RR, Maltman AJ, Morley CK, editors. *Subsurface Sediment Mobilization.* London: Geological Society (2003), Special Publications 216. pp. 139–57.
40. Van Rensbergen P, Poort J, Kipfer R, De Batist M, Vanneste M, Klerkx J, et al. Near-surface sediment mobilization and methane venting in relation to hydrate destabilization in southern Lake Baikal, Siberia. In: Van Rensbergen P, Hillis RR, Maltman AJ, Morley CK, editors. *Subsurface Sediment Mobilization*. London: Geological Society (2003), Special Publications 216. pp. 207–21.
41. Talukder AR, Comas MC, Soto JI. Pliocene to recent mud diapirism and related mud volcanoes in the Alboran Sea (Western Mediterrenean). In: Van Rensbergen P, Hillis RR, Maltman AJ, Morley CK, editors. *Subsurface Sediment Mobilization*. London: Geological Society (2003), Special Publications 216. pp. 443–59.
42. Pralle N, Külzer M, Gudehus G. Experimental evidence on the role of gas in sediment liquefaction and mud volcanism. In: Van Rensbergen P, Hillis RR, Maltman AJ, Morley CK, editors. *Subsurface Sediment Mobilization*. London: Geological Society (2003), Special Publications 216. pp. 159–71.
43. Deville E, Battani A, Griboulard R, Guerlais S, Herbin JP, Houzay JP, et al. The origin and processes of mud volcanism: new insights from Trinidad. In: Van Rensbergen P, Hillis RR, Maltman AJ, Morley CK, editors. *Subsurface Sediment Mobilization*. London: Geological Society (2003), Special Publications 216. pp. 475–90.
44. Feder J. *Fractals*. New York, NY: Plenum Press (1988).
45. Barabási AL, Stanley HE. *Fractal Concepts in Surface Growth*. Cambridge: Cambridge University Press (1995).
46. Mandelbrot BB. The fractal geometry of nature. New York, NY: W. H. Freeman and company (1982).
47. Feder J. *Fractals*. New York, NY: Plenum Press (1988).
48. Blaber J, Adair B, Antoniou A. Ncorr: open-source 2D digital image correlation matlab software. *Exp Mech.* (2015) **55**:1105–22. doi: 10.1007/s11340-015-0009-1
49. Hariral R, Ramji M. Adaption of open source 2D DIC Software Ncorr for solid mechanics applications. In: *9th International Symposium on Advanced Science and Technology in Experimental Mechanics, New Delhi* (2014).
50. Vable M. *Mechanics of Materials, 2nd Edn*. Michigan Technological University (2014). Available online at: http://www.me.mtu.edu/~mavable/MoM2nd.htm
51. Family F, Vicsek T. Scaling of the active zone in the Eden process on percolation networks and the ballistic deposition model. *J Phys A Math Gen.* (1985) **18**:L75–81. doi: 10.1088/0305-4470/18/2/005
52. Horváth VK, Family F, Vicsek T. Dynamic scaling of the interface in two-phase viscous flows in porous media. *J Phys A Math Gen.* (1991) **24**:L25–9. doi: 10.1088/0305-4470/24/1/006
53. Makse HA, Nunes Amaral LA. Scaling behavior of driven interfaces above the depinning transition. *Europhys Lett.* (1995) **31**:379–84. doi: 10.1209/0295-5075/31/7/007
54. Tallakstad KT, Toussaint R, Santucci S, Schmittbuhl J, Måløy KJ. Local dynamics of a randomly pinned crack front during creep and forced propagation: an experimental study. *Phys Rev E.* (2011) **83**:046108. doi: 10.1103/PhysRevE.83.046108
55. Toussaint R, Helgesen G, Flekkøy EG. Dynamic roughening and fluctuations of dipolar chains. *Phys Rev Lett.* (2004) **93**:108304. doi: 10.1103/PhysRevLett.93.108304
56. Toussaint R, Flekkøy EG, Helgesen G. Memory of fluctuating Brownian dipolar chains. *Phys Rev E.* (2006) **74**:051405. doi: 10.1103/PhysRevE.74.051405
57. Lemaire E, Levitz P, Daccord G, Van Damme H. From viscous fingering to viscoelastic fracturing in colloidal fluids. *Phys Rev Lett.* (1991) **67**:2009. doi: 10.1103/PhysRevLett.67.2009
58. Sharon E, Moore MG, McCormick WD, Swinney HL. Coarsening of viscous fingering patterns. *Phys Rev Lett.* (2003) **91**:205504. doi: 10.1103/PhysRevLett.91.205504
59. Davidovitch B, Levermann A, Procaccia I. Convergent calculation of the asymptotic dimension of diffusion limited aggregates: scaling and renormalization of small clusters. *Phys Rev E.* (2000) **62**:R5919–22. doi: 10.1103/PhysRevE.62.R5919

Conflict of Interest Statement: The authors declare that the research was conducted in the absence of any commercial or financial relationships that could be construed as a potential conflict of interest.

Chapter 5

Pneumatic fractures in confined granular media

5.1 Motivation

The opening of channels during fluid injection into dense granular media saturated with the same fluid has been found to resemble viscous fingering patterns [57]. Experiments with this has been performed in open Hele-Shaw cells where the medium decompacts at the outlet for sufficient overpressures [56, 58, 60]. A closed version of the system, where the cell outlet boundary is open to fluids but closed to beads was studied numerically in [59, 61]. Following the work in the previous chapter, we were interested in characterizing typical channeling patterns and their evolution in an experimental version of the closed cell. We wanted to study typical flow behavior, pattern evolution and their characteristics for varying injection pressures. In addition, it was interesting to check how experiments in a roughly 10 times larger cell correspond with the simulations, and how the patterns differ from the ones in granular media with a free boundary. As in the previous chapter, the methods and main results in this study are presented before including the scientific article containing all details of the work and discussion of results.

5.2 Methodology

5.2.1 Experimental setup

The experimental setup is a linear Hele-Shaw cell, partially filled with Ugelstad spheres [83], i.e. dry, non-expanded polystyrene beads with a diameter of 80 µm ± 1 %. The cell is made out of two rectangular glass plates (80×40×1 cm in length, width and thickness respectively) clamped together on top of each other with an aluminum spacer controlled separation of 1 mm. A cell volume (76×32×0.1 cm) is formed between the plates by an impermeable sealing tape as shown in figure 5.1, with one of the short sides left open (outlet). Next, beads are filled into the cell by pouring them through the open side until they occupy about 90 % of the cell volume, followed by closing the open side with a semi-permeable filter (a 50 µm steel mesh) to keep beads inside the cell while allowing air to escape. The cell is then flipped

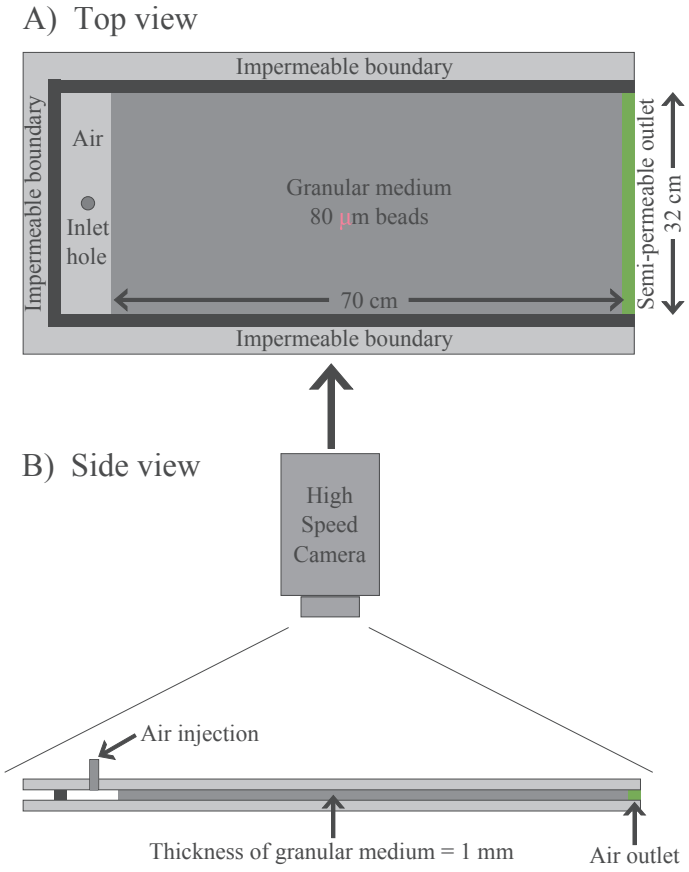

Figure 5.1: Sketch of the experimental setup. A) Top-down view of the prepared cell: The granular medium is confined inside the cell by three impermeable boundaries and an air permeable boundary on the outlet side. The granular medium is placed against the outlet boundary such that it has a linear interface against a region empty of beads on the sealed inlet side, where pressurized air can be injected. B) Side view of the setup showing the high speed camera placed above. The glass plates are clamped together with aluminum framing while the cell gap is controlled with spacers, which are not shown here.

vertically to place the granular medium against the semi-permeable outlet by using gravity, resulting in a volume packing fraction of approximately $\rho_s = 0.44 \pm 0.04$, assumed to be more or less uniform across the medium. This leaves a volume empty of beads on the sealed side of the cell, opposite to the semi-permeable outlet, with a linear air-solid interface. An inlet hole on the sealed side of the cell is connected to a pressurized air tank which lets us inject air at a constant and maintained overpressure, $P_{in} = P_{abs,in} - P_0$ (absolute pressure - atmospheric pressure), ranging from 5 to 250 kPa. This will force air to move through the granular medium, towards the semi-permeable outlet, where $P_{abs,out} = P_0 = 100$ kPa, or in terms of overpressure above the atmospheric one, $P_{out} = 0$.

During experiments, the prepared cell is positioned horizontally. A selected overpressure is set at the pressure tank outlet and verified by a Honeywell pressure sensor with an accuracy of ± 4 kPa. The tubing between the pressure tank and the cell inlet is equipped with an electronic valve such that the air injection is started

with a digital trigger signal. Positioned above, with a top-down view of the cell, a Photron SA5 high speed camera is started with the same trigger signal, recording the air invasion at a framerate of 1000 images/s and a resolution of 1024×1024 pixels (1 pixel ≈ 0.7 mm in the cell). Light from a 400 W Dedolight studio lamp provides uniform and flicker-free illumination onto the white beads of the medium. A small fraction of the beads (< 10 %) are dyed black with ink to create tracer particles that are used for tracking frame-to-frame deformations in the granular medium. The experiments are run for 10 s, but typically the fracturing and/or compaction of the granular medium takes less than 5 s. Binary patterns of invasion channels are obtained as discussed in section 3.3.1.

5.3 Main results

Depending on injection pressure (and friction related to packing fraction) we observe the granular medium to exhibit either a solid-like behavior, or a transition from fluid-like to solid-like behavior during air injection. In the solid-like regime, there is no apparent bead displacements and the air is reaching the cell outlet by seeping through the network of pores between beads. On the other hand, in the fluid-like regime we observe significant deformation, where beads are displaced by an amount corresponding to several bead sizes, by momentum exchange between air molecules and beads. At sufficient overpressure the granular medium has a behavior much like a viscous liquid being invaded by air, as the flow opens up channels empty of beads, a Saffman-Taylor like instability [4] resulting in dendritic invasion patterns. A stabilizing mechanism of this flow instability is the build-up of friction and stress chains between beads during compaction, and due to the boundary conditions we always end up with a solid-like medium towards the end of an experiment.

To explore eventual flow regimes we varied the applied overpressure within the range of 5 kPa to 250 kPa. Six typical flow behaviors were identified in this range of overpressures, and the typical final structures are shown for each category in figure 5.2. The typical flow behaviors in the 6 categories are described as follows;

Category 1 - No deformation: The porous medium appears rigid with no significant bead displacement or invasion pattern formed. Category 2 - Deformation without fingers: The medium is initially compacted during a collective displacement of beads towards the outlet side without the formation of invasion channels. Category 3 - Short thin fingers: A short dendritic invasion pattern is formed, where the final length of the channel is less than 50% of $L = 70$ cm, the initial length of the granular medium, with an average finger thickness less than 2 cm. The channel grows primarily on the longest fingers, while it is frozen in the parts more than 5 cm behind. Category 4 - Long thin fingers: A long dendritic invasion pattern is formed, where the final length of the channel is more than 50% of L, with an average finger thickness less than 2 cm. The channel grows mainly on the longest fingers, typically within 10 cm of the most advanced finger tip. Category 5 - Long thin fingers with thicker main channel: A long dendritic invasion pattern is formed with a thicker main channel than the branch fingers due to erosion inside the channel, i.e. motion of beads non-perpendicular to the channel interface, but with a major tangential component along it. The final length is more than 50% of L, with an

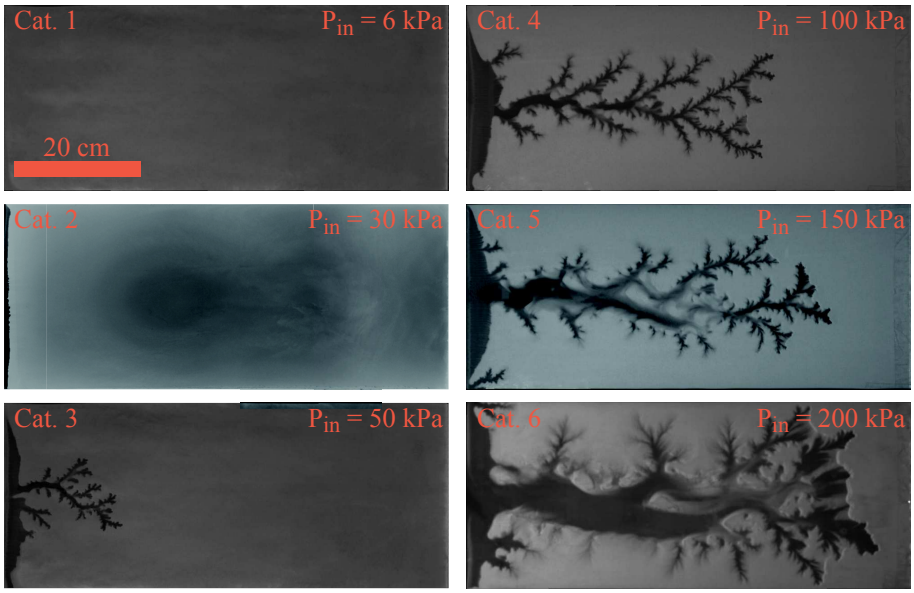

Figure 5.2: Typical final structures per category, where the granular medium is gray and areas empty of beads are black, showing that for increasing P_{in} the fingers become longer and thicker.

average finger thickness between 2 cm and 4 cm. The channel grows mainly on the longest fingers, typically within 15 cm of the most advanced finger tip, where the growth behind 10 cm is mostly due to erosion. The erosion is not persistent, and rarely occurs more than 15 cm behind the most advanced tip. Category 6 - Long dominating channel: A long and thick main channel with some dendritic branches is formed. The width of the main channel increases by erosion and with side channels and branches merging into it. The final length is more than 50% of L, with an average finger thickness more than 4 cm. The channel growth is more like fracturing, with an active growth zone spanning the entire length of the channel. Erosion and finger merging is observed to occur even at distances of 30-40 cm behind the most advanced tip. Again, erosion is not persistent and stops around the point when the channel reaches 90 % of its final length. Typical ranges of P_{in} for each category are shown in table 5.1. The pressure ranges for each category overlap, indicating diffuse boundaries between flow regimes, probably in part due to randomness in the initial bead configuration.

For categories with invasion channels (Cat. 3 to 6) we discuss the typical pattern characteristics and their growth dynamics. Figure 5.3 A) shows the average finger thickness w per category of the final structures, plotted as function of depth x into the granular medium measured from the initial boundary position. The plot shows that the patterns in categories 3 and 4 have roughly the same finger thickness, averaging around 1.4 cm and is more or less constant as function of depth. Erosion is not observed inside these channels, so a finger thickness around 1.4 cm seems typical when there is no erosion. The category 5 patterns show initially thicker fingers along the first half of the structures, here with an average thickness of 3.3 cm, which then decreases down towards the typical thickness seen for categories 3 and 4. The larger initial finger thickness is due to erosion inside the main channel, meaning that beads

Table 5.1: The flow categories with related pressure values; mean overpressure within two standard deviations $\overline{P_{in}} \pm 2\sigma$, as well as the number of experiments N analyzed per category.

Category	$\overline{P_{in}} \pm 2\sigma$ [kPa]	N
1	9 ± 5	3
2	26 ± 18	5
3	64 ± 50	5
4	110 ± 44	6
5	134 ± 43	10
6	213 ± 50	4

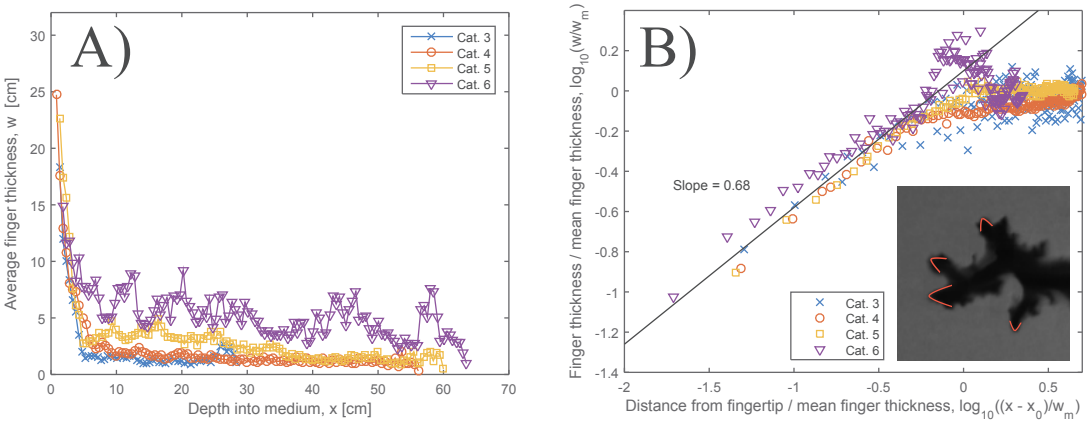

Figure 5.3: A) Average finger thickness w as function of depth x into the medium for the final structures, averaged per categories 3 - 6. We see that for the structures in Cat. 5 (erosion) and Cat. 6 (erosion and finger merging) the fingers are thicker, all the way to the finger tip for Cat. 6. In B), the finger thickness w plotted in a log-log plot as function of the distance d from the finger tip. The data shown is the average of about 50 measurements in time for each experiment, averaged again for each category. The data is collapsed by the finger thickness at the base of the tips w_b found as the average finger thickness where w has reached a more or less constant level. The average slope at different times during several experiments is $\beta = 0.68$, indicating a more rounded shape of the tips. In the inset: Snapshot of typical finger tips together with profiles corresponding to $\beta = 0.68$ (red lines).

near the channel walls are re-mobilized in the flow direction after the initial growth, making the channel grow wider. As average thicknesses here suggest, this effect typically increase the channel width by an amount of around 2 cm. The category 6 patterns typically have thick fingers throughout their entire length up to the tips, with an average of 5.3 cm. This thickness is achieved both by erosion inside the main channel, and with fingers merging together. When fingers merge and form a cluster of beads, these beads are mobilized in the flow direction. In general we see an increase in finger thickness and length for increasing pressures. We look closer on how the fingers are shaped on the tips. To get a description of the shape of finger tips, we look at how the finger thickness w grow as function of distance d from the finger tip, which is found to follow a power law within the length of the tip region [57] (where the finger thickness increase with d before it saturates):

$$w(d) \propto d^{\beta}. \tag{5.1}$$

When w is plotted as a function of d in a log-log plot, the slope β for $w(d)$ within the tip region reveal information about the shape of the tip; it has a more rounded shape for $\beta < 1$, while it has a pointy cusp-shape for $\beta > 1$. We have averaged $w(d)$ over time for each experiment, i.e. obtaining the average finger tip shape during flow in each experiment. Figure 5.3 B) shows a log-log plot of the finger thickness as function of distance from the finger tip, averaged per category. The collapsed average slopes from all experiments seem to fall along the same line with $\beta = 0.68$, indicating more rounded finger tips with the same shape in all experiments. However, a purely round profile would give $\beta = 0.5$, so the fact that we measure a bigger value means that there still is a singularity in curvature towards the tip - even if it is not a spike shape. The singularity can be shown as follows, where

$$w \sim d^{\beta} \Rightarrow d \sim w^{\frac{1}{\beta}} \Rightarrow \frac{dd}{dw} \sim w^{\frac{1}{\beta}-1}, \tag{5.2}$$

gives the slope of the front. From this we find the expression for the curvature as,

$$\kappa \sim \frac{d^2 d}{dw^2} \sim w^{\frac{1}{\beta}-2} \text{ (or } d^{1-2\beta}). \tag{5.3}$$

If $\beta > 0.5$, $\frac{1}{\beta} - 2 < 0$ and κ diverges at the tip where w (and d) $\rightarrow 0$. At the same time, if $\beta < 1$, the slope does not diverge at $d = 0$, and yields a more rounded profile. We did not observe any cusps as reported in [57] with $\beta = 1.43 \pm 0.2$, consistent with theory on fluid fingering in the zero-surface tension limit. The value of β is found to fluctuate around the estimated value $\beta = 0.68$ over time, indicating that the tip shapes does not seem to change significantly during the different stages of the experiments.

The box-counting dimensions are estimated according to eq. (3.15) and averaged per flow category. For the less developed category 3 patterns $D_b = 1.41$, while for categories 4 and 5 which have the best preserved (not damaged significantly by erosion) and developed channels, the box dimensions are $D_b = 1.54$ and $D_b = 1.53$ respectively, within the range of box dimensions found for viscous fingers in saturated porous media, i.e. D = 1.53 - 1.62 [1, 2, 5]. For category 6 patterns, we observe $D_b = 1.63$. Categories 3, 4 and 5 have interface dimensions $D_F = 1.40$, 1.52, 1.48

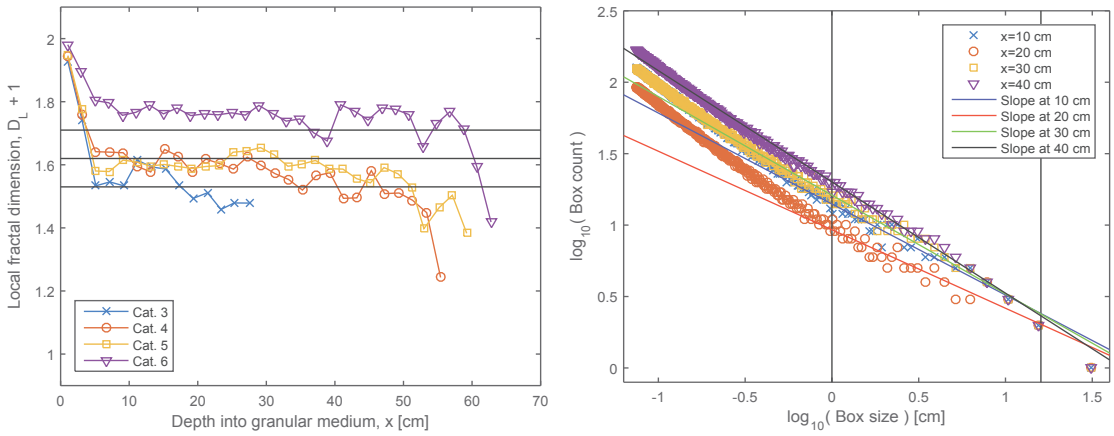

Figure 5.4: Left: Local fractal dimensions ($D_L + 1$) as function of depth into the medium for the final structures averaged per category. We see that the patterns in all categories have more or less constant and well defined local dimensions as functions of depth. The main parts of the patterns in categories 3-5 have local dimensions corresponding to established values for viscous fingers in saturated porous media (between the dashed lines). For patterns in category 6, the local dimensions correspond to values closer to the fractal dimension for DLA patterns and flow patterns in a saturated Hele-Shaw cell (solid line). Right: Examples of local box-counting slopes at different depths of the same experiment.

respectively (found by doing box-counts on binary images of the air-solid interface) which are close to their corresponding box-counting dimensions, while category 6 patterns have $D_F = 1.41$ which is about 0.2 less than the corresponding box-counting dimension. This can be interpreted in terms of finger thickness, i.e. the front becomes more similar to the structure for decreasing finger thickness. In addition, this indicates that the air-solid interface has similar roughness in all experiments. Figure 5.4 shows the local fractal dimensions $D_L + 1$ as function of depth into the granular medium for the final structures. For all flow categories, the curves show a more or less constant behavior over most of the depths (the initial high dimension is due to a larger initial area empty of beads, and the final lower dimension is due to finite size effects of the patterns), which indicates that the patterns have consistent local fractal dimensions over a range of x. The categories 3, 4 and 5 patterns have typical local dimensions corresponding to the global dimensions $D = 1.53$, 1.58, 1.60, respectively. This is within the range of dimensions seen for viscous fingers in saturated porous media ($D = 1.53$ - 1.62). For the category 6 patterns the local dimension is higher, with a typical value corresponding to $D = 1.76$, which is closer to the dimensions seen for DLA clusters and viscous fingers in an empty saturated Hele-Shaw cell ($D = 1.71$) [6,7].

Now, the growth dynamics are presented. Figure 5.5 A) shows that the channel length grows linearly with time initially before it decelerates towards a final length, and that both the growth velocity and final depth of the invasion structures increase with increasing injection pressure. The initial constant growth rate seems to scale with the injection pressure as $P_{in}^{\frac{3}{2}}$. In the simulations done by Niebling et al. [59,61]

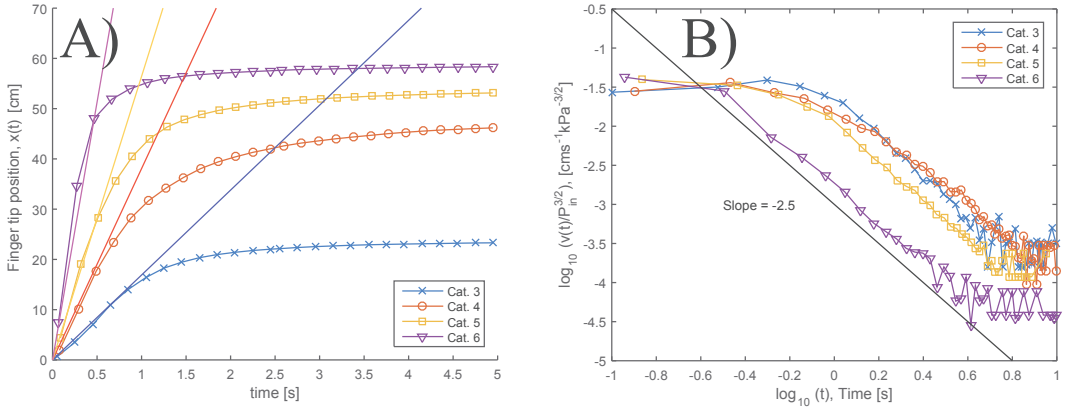

Figure 5.5: A) The finger tip position $x(t)$ as function of time, averaged for all experiments per category. The curves typically have an initial linear growth with time which crosses over to a decay with time. The patterns grow faster and longer for increasing injection pressure, and the initial linear growth is found to scale proportionally with $P_{in}^{3/2}$ as indicated by the dashed lines. B) Log-log plot of the finger tip velocity $v(t)$ as function of time, averaged per category. The data is collapsed along the ordinate axis by dividing $v(t)$ by $P_{in}^{\frac{3}{2}}$, where $P_{in} = 64$, 110, 134 and 213 kPa, for category 3, 4, 5 and 6 respectively. The initial constant plateau correspond to the period with linear growth over time, which then crosses-over to a declining slope close to -2.5 (dashed line) for all the categories. The slopes show that the decay in growth velocity follows a power law equation with time.

of a similar, but smaller system they too observe an initial linear growth velocity crossing over to decay over time. However, they observe the initial growth velocity to scale with P_{in} as $v \propto P_{in}^{1/2}$ in these simulations. In figure 5.5 B), the log-log plot of the finger tip velocity $v(t)/(P_{in}^{3/2})$ as function of time indicates that when the finger tip velocity begins to decrease, it follows a power law equation with time, $v(t) \propto t^{-\alpha}$, where $\alpha = 2.5 \pm 0.2$. Thus, the growth velocity is constant initially, before it crosses over to a power law decay with time. This behavior is investigated in more detail; The constant initial velocity v_0 is found to scale with injection pressure P_{in} as

$$v_0 = C \cdot P_{in}^{\frac{3}{2}}, \tag{5.4}$$

where $C \approx 10^{-\frac{3}{2}}$ cm/(s·kPa$^{\frac{3}{2}}$) is found from the initial part of the collapsed curves $v(t)/P_{in}^{\frac{3}{2}}$ along the ordinate axis in figure 5.5 B). By inserting the value for C into equation (5.4), we can instead collapse the curves along the ordinate axis with $v(t)/v_0$ resulting in dimensionless and normalized units for the velocity. In order to collapse the curves along the time axis, we define a critical time $t = t_c$ as the time when the growth velocity crosses over from being constant to follow a power law decay with time. At the critical time, the finger tip position can be described as

$$x_c = x(t_c) = v_0 \cdot t_c, \tag{5.5}$$

which gives

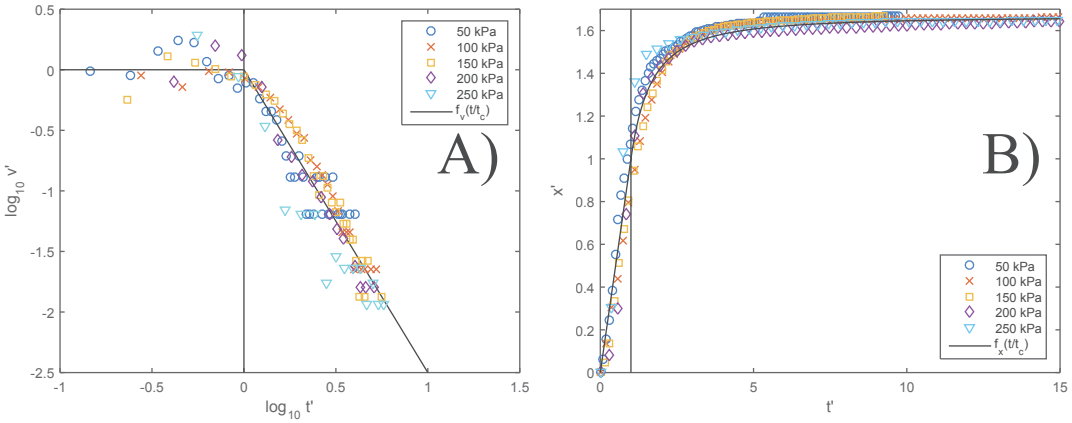

Figure 5.6: A) Log-log plot of the collapsed finger tip velocities $v' = v(t')/v_0$ as function of $t' = t/t_c$ for individual experiments with various injection pressure. The dotted vertical line indicates the cross-over at $t' = 1$, and the dashed curve shows the proposed function $f_v(t')$. Recall that the parameters used for the collapse are given by the injection pressure, as $v_0 = C \cdot P_{in}^{\frac{3}{2}}$ and $t_c = ((\alpha - 1)/\alpha) \cdot (x_f/v_0(P_{in}))$, where $C = 10^{-\frac{3}{2}}$ cm/(s·kPa$^{\frac{3}{2}}$) and $\alpha = -2.5$. B) The collapsed finger tip positions $x' = x(t')/x_c$ as function of $t' = t/t_c$, for the same individual experiments. The dotted vertical line indicates the cross-over at $t' = 1$, and the dashed curve shows the proposed function $f_x(t')$.

$$t_c = \frac{x_c}{v_0} = \frac{x_c}{C \cdot P_{in}^{\frac{3}{2}}}. \tag{5.6}$$

Further, we check if x_c can be described as a typical fraction R of x_f, the final length of the channel, such that $x_c = R \cdot x_f \propto x_f$, which gives

$$t_c = \frac{R \cdot x_f}{C \cdot P_{in}^{\frac{3}{2}}} \propto \frac{x_f}{P_{in}^{\frac{3}{2}}}. \tag{5.7}$$

By plotting $v(t^*)/v_0$ as function of $t^* = R \cdot (t/t_c) = R \cdot ((t \cdot C \cdot P_{in}^{\frac{3}{2}})/x_f)$ in a log-log plot, we found that the curves are collapsed along the time axis with a cross-over point corresponding to $R \approx 0.6$. Since we now have the constants C and R, we can calculate v_0 and t_c for individual experiments by inserting the respective P_{in} and x_f into equations (5.4) and (5.7). Figure 5.6 A) shows scaled log-log plots of $v' = v(t')/v_0$ as function of $t' = t/t_c$ for individual experiments with injection pressures in the range of 50 - 250 kPa, which follow the same dimensionless curve given by the function

$$f_v(t') = \begin{cases} 1, & \text{if } t' \leq 1 \\ t'^{-\alpha}, & \text{if } t' > 1, \text{ where } \alpha = 2.5. \end{cases} \tag{5.8}$$

Similarly, we collapse the fingertip position $x' = x(t')/x_c$ and plot it as function of $t' = t/t_c$ for the same individual experiments, shown in figure 5.6 B) (Note that the data is from single experiments, i.e. not the average values as in figure 5.5 B),

explaining the increased amount of noise). Here, the collapsed data follow the curve given by the function

$$f_x(t') = \begin{cases} t', & \text{if } t' \leq 1 \\ \frac{1}{1-\alpha} t'^{1-\alpha} + \frac{\alpha}{\alpha-1}, & \text{if } t' > 1, \end{cases} \tag{5.9}$$

which is found by integrating each part of equation (5.8), requiring that $f_x(t' > 1) \to 1$ when $t' \to 1$. Further, $f_x(\infty) = \alpha/(\alpha - 1) = x_f/x_c = 1/R$, giving $R = (\alpha - 1)/\alpha = 0.6$, which fits very well with our observations. By substituting α into equation (5.7) we get,

$$t_c = \frac{\alpha - 1}{\alpha} \cdot \frac{x_f}{C \cdot P_{in}^{\frac{3}{2}}}. \tag{5.10}$$

With equations (5.4 - 5.10) we propose a description of the fundamental dynamics of the system. Since we have experimentally estimated α and have equation (5.4) relating the initial growth velocity to injection pressure, we can estimate the evolution of the channel length during the invasion for a given injection pressure and final channel length. For a complete description, the next step is to characterize the dependency of x_f on P_{in} such that the expected result of an air injection could be estimated by the injection pressure alone. A brief discussion about this is presented in figure 5.7.

A more detailed presentation of the methods and results in this study is given in the related article over the following pages. The article was submitted to Physical Review E in October 2016.

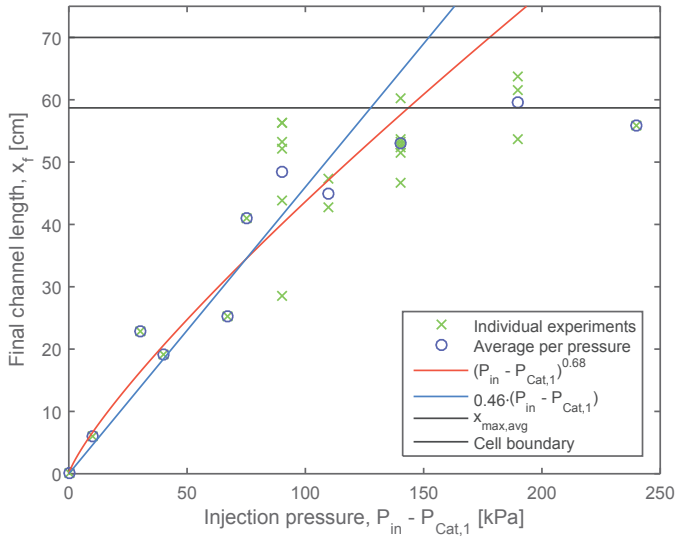

Figure 5.7: The final channel length x_f is plotted as function of $P_{in} - P_{cat,1}$, where $P_{cat,1} = 9$ kPa is the average injection pressure for category 1, where $x_f = 0$. We see that there is a rather scattered (due to randomness in the initial bead configuration from experiment to experiment), but increasing trend in x_f for increasing P_{in}, but also that the final channel length for the highest injection pressures is limited by the closed outer boundary. The fit $(P_{in} - P_{cat,1})^{0.68}$ was found from the averaged x_f per pressure for $P_{in} \in [20, 150]$ kPa and suggest a power-law relationship. Alternatively, the linear fit $0.46 \cdot (P_{in} - P_{cat,1})$ fits equally well. The average limiting line $x_{max,avg}$ was found by averaging x_f over the experiments with $P_{in} \geq 200$ kPa, to indicate the influence of the cell boundary. Hopefully, future experiments with much more repetitions could be conducted to reveal a clearer relationship between x_f and P_{in}.

PAPER 2

Pneumatic fractures in confined granular media

Fredrik K. Eriksen,* Renaud Toussaint, and Semih Turkaya
Institut de Physique du Globe de Strasbourg,
Université de Strasbourg/EOST,
Centre National de la Recherche Scientifique, Strasbourg, France

Knut J. Måløy and Eirik G. Flekkøy
Department of Physics, University of Oslo, Oslo, Norway

(Dated: March 27, 2017)

We perform experiments where air is injected at a constant overpressure P_{in}, ranging from 5 to 250 kPa, into a dry granular medium confined within a horizontal linear Hele-Shaw cell. The setup allows us to explore compacted configurations by preventing decompaction at the outer boundary, i.e. the cell outlet has a semi-permeable filter such that beads are stopped while air can pass. We study the emerging patterns and dynamic growth of channels in the granular media due to fluid flow, by analyzing images captured with a high speed camera (1000 images/s). We identify 6 typical flow regimes, depending on the imposed overpressure, ranging from no channel formation at low P_{in} around 10 kPa, to large thick channels formed by erosion and fingers merging at high P_{in} around 200 kPa. The flow regimes where channels form are characterized by typical finger thickness, final depth into the medium and growth dynamics. The shape of the finger tips during growth is studied by looking at the finger width w as function of distance d from the tip. The tip profile is found to follow $w(d) \propto d^{\beta}$, where $\beta = 0.68$ is a typical value for all experiments, also over time. This indicates a singularity in the curvature $d^2d/dw^2 \sim \kappa \sim d^{1-2\beta}$, but not of the slope $dw/dd \sim d^{\beta-1}$, i.e. more rounded tips rather than pointy cusps, as they would be for the case $\beta > 1$. For increasing P_{in}, the channels generally grow faster and deeper into the medium. We show that the channel length along the flow direction has a linear growth with time initially, followed by a power law decay of growth velocity with time as the channel approaches its final length. A closer look reveal that the initial growth velocity v_0 is found to scale with injection pressure as $v_0 \propto P_{in}^{\frac{3}{2}}$, while at a critical time t_c there is a cross-over to the behavior $v(t) \propto t^{-\alpha}$ where α is close to 2.5 for all experiments. Finally, we explore the fractal dimension of the fully developed patterns. For example for patterns resulting from intermediate P_{in} around 100-150 kPa, we find that the box-counting dimensions lie within the range $D_B \in [1.53, 1.62]$, similar to viscous fingering fractals in porous media.

PACS numbers: 83.60.Wc, 81.05.Rm, 47.20.Ma

I. INTRODUCTION

Several processes in engineering, industry and earth sciences involve pneumatic (gas) or hydraulic (liquid) fracturing of the soil, which occurs when fluids in the ground are driven to high enough pressures to deform, fracture and generate porosity in the surrounding soil or rock. For example in environmental engineering, pneumatic or hydraulic fracturing is done to enhance the removal of hazardous contaminants in the vadose zone (soil remediation) [1, 2], for soil stabilization injection to ensure a solid foundation for structures [3], or in packer tests for project planning, risk assessment and safe construction of dams and tunnels [4]. In industry, hydraulic fracturing is done to enhance oil and gas recovery [5–7], CO_2 sequestration [8], water well- and geothermal energy production [9–11]. Related natural processes such as subsurface sediment mobilization are studied in earth sciences, where sand injectites, mud diapirs and mud volcanoes are formed due to pore-fluid overpressure [12–17]. For example, the Lusi mud volcano in Indonesia is the biggest and most damaging mud volcano in the world [18], having displaced 40 000 people from their homes, and has been active since May 2006. There is an ongoing debate about how it was triggered, i.e. whether it formed naturally by an earthquake or geothermal process [19–22], or that it is a man-made consequence of a nearby drilling operation by a company probing for natural gas [23].

Fluid injections into granular media has been extensively studied in laboratory experiments and simulations, where a common method to simplify the problem is to confine the experiment within a quasi-2-dimensional geometry, i.e. a Hele-Shaw cell. In [24, 25], the decompaction, fluidization regimes, and coupling between air and granular flow was studied in dry granular media in open circular and rectangular cells during air injection at different overpressures. Similar behavior was seen for liquid saturated granular material injected with the same

* Also at Department of Physics, University of Oslo, Oslo, Norway; Correspondence: eriksen@unistra.fr

liquid [26], so it is reasonable to assume that studies of pneumatic fracturing also have qualitative relevance to hydraulic fracturing. The two cases are similar in the sense of no interface tension and viscosity difference between the invading and interstitial fluids. The differences in an experiment where a liquid is used instead of a gas are that the viscosity is higher, such that the injection pressure needed to move beads is lower, and that the compressibility is lower such that the pressure diffuses much faster. However, near the invading channels, the pressure gradients are found to be qualitiatively similar in both cases, leading to similar growth mechanisms for the channels [27]. Further, the compressibility felt in water on the scale of a $\sim$ 100 m reservoir is similar to the compressibility felt in air on the scale of a $\sim$ 1 m experiment, and therefore the effect of pressure diffusion is included when air is used in such experiments. The patterns formed during fluid injection into a granular medium, and evolution of the fluid-solid interface, have been found to resemble Diffusion Limited Aggregation patterns (DLA) and viscous fingering [28], a fingering instability that occurs when a less viscous liquid is injected into a porous medium containing a more viscous liquid with which it cannot mix [29]. As mentioned in [25], the main difference between the viscous- and granular fingering instabilities is the absence of interfacial tension in the granular case. For example, the stabilizing forces in viscous fingering are surface forces, while in granular fingering it is the build-up of friction between particles and against the confinement. However, both instabilities are driven by the pressure gradient across the defending medium, which is largest on the longest finger tips, making more advanced fingers grow on expense of the less advanced ones. A notable difference between air injection into a dry granular medium and a saturated one is that the overpressure initially diffuses into the packing in the dry case, while it is already a steady-state Laplace field over the defending liquid in the saturated case. This difference arises from the compressibility of the defending phase.

Further, during air injection into liquid saturated granular media and suspensions, the characteristics of emerging patterns and behavior of the media depend on injection rate, and the competition between mobilized friction and surface forces [30–43]. For example, one observes flow regimes such as two phase flow in rigid porous media [39–43], capillary fracturing, stick-slip bubbles and labyrinth patterns [30–38]. In the opposite case, during liquid injection into dry granular media [44], the flow behavior goes from stable invasion towards saturated granular fingers for increasing flow rate and viscosity of the invading fluid. These fingering patterns are thought to form due to the permeability contrast between the channels empty of grains and the granular medium. At intermediate conditions, fractures open up inside the invaded region. The same trend is shown in numerical studies for gas injection into granular media containing the same gas [45].

Granular fingering instabilities have also been studied in closed vertical cells, where gravity drives the flow as heavier beads fall down from a granular layer at the top of a lighter fluid layer [46–51]. When the beads detach at the front, they form fingers of falling granular material surrounding finger-like bubbles of rising fluid. These fingers are found to coarsen over time until they reach a typical wavelength depending on the interstitial fluid and bead size.

Typically, in all processes involving fluid injection into granular media, there are flow regimes where the medium has either solid-like behavior or fluid-like behavior. This is one of the special properties of granular materials, which also show gas-like behavior in some cases [52].

In this paper, we present an experimental study on flow regimes and pattern formation during air injection into confined granular media. More specifically, we inject air at constant overpressure into a dry granular medium inside a Hele-Shaw cell, where air escapes at the outlet while beads cannot. The motivation of this setup is to study the granular Saffman-Taylor instability in compacting granular media, and the coupling between compaction and flow. A similar, but smaller system has been studied in numerical simulations by Niebling et al. [45, 53]. During air injection at different overpressures they found that fractures grow faster, longer, as well as coarsen with increasing injection pressure. Here, the fracture propagation velocity is roughly constant initially and scales with the square root of the injection pressure. Further, by varying the interstitial fluid viscosity, two flow regimes were identified; one with finely dispersing bubbles and large scale collective motion of particles, the other one with build-up of a compaction front and fracturing. These flow regimes depend, respectively, on whether the particles are primarily accelerated by the imposed pressure gradient in the fluid, or interactions through particle contacts. This in turn depends on the diffusivity of the interstitial fluid pressure in the granular medium. We analyze our findings in light of these results, to investigate what is similar and what is different in our roughly 10 times larger cell with the same cell gap. As opposed to similar experiments, with open outer boundary conditions, after the flow compacts the medium there is no decompaction. We thus expect the material behavior (at high enough overpressure to displace beads) to have a transition from fluid-like to solid-like during experiments, and that eventual invasion patterns will initially resemble viscous fingering in the fluid-like regime, crossing over to stick-slip fracture propagation as the medium becomes more solid-like, until it reaches a final structure as the compacted medium has reached a completely solid-like behavior. What is less obvious, is how the flow patterns in this system change with the injection pressure. By varying the imposed overpressure, we identify and describe the different flow regimes. Due to the confined nature of the experiment, it is thought to be a laboratory analog to pneumatic and hydraulic fracturing of tight rock reservoirs where the free boundary at

the surface is very distant from the injection zone. Therefore, new insight into this problem may have industrial applications in addition to increase the understanding of flow and transformations in porous media.

It is also worth to mention a closely related project [54], where acoustic emissions recorded during the experiments are analyzed. There, it is shown that different stages of the invasion process can be identified acoustically in terms of characteristic frequencies and distinct microseismic events.

II. METHODS

A. Experimental setup

The experimental setup is a linear Hele-Shaw cell, partially filled with Ugelstad spheres [55], i.e. dry, non-expanded polystyrene beads with a diameter of 80 µm ± 1 %. The cell is made out of two rectangular glass plates (80×40×1 cm in length, width and thickness respectively) clamped together on top of each other with an aluminum spacer controlled separation of 1 mm. A cell volume (76×32×0.1 cm) is formed between the plates by an impermeable sealing tape as shown in figure 1, with one of the short sides left open (outlet). Next, beads are filled into the cell by pouring them through the open side until the packing occupy about 90 % of the cell volume, followed by closing the open side with a semi-permeable filter (a 50 µm steel mesh) to keep beads inside the cell while allowing air to escape. The cell is then flipped vertically to place the granular medium against the semi-permeable outlet by using gravity, resulting in a volume packing fraction of approximately $\rho_s = 0.44 \pm 0.04$, assumed to be more or less uniform across the medium. This leaves a volume empty of beads on the sealed side of the cell, opposite to the semi-permeable outlet, with a linear air-solid interface. An inlet hole on the sealed side of the cell is connected to a pressurized air tank which lets us inject air at a constant and maintained overpressure, $P_{in} = P_{abs,in} - P_0$ (absolute pressure - atmospheric pressure), ranging from 5 to 250 kPa. This will force air to move through the granular medium, towards the semi-permeable outlet, where $P_{abs,out} = P_0 = 100$ kPa, or in terms of overpressure above the atmospheric one, $P_{out} = 0$.

During experiments, the prepared cell is positioned horizontally. A selected overpressure is set at the pressure tank outlet and verified by a Honeywell pressure sensor with an accuracy of ±4 kPa. The tubing between the pressure tank and the cell inlet is equipped with an electronic valve such that the air injection is started with a digital trigger signal. Positioned above, with a top-down view of the cell, a Photron SA5 high speed camera is started with the same trigger signal, recording the air invasion at a framerate of 1000 images/s and a resolution of 1024×1024 pixels (1 pixel ≈ 0.7 mm in the cell). Light from a 400 W Dedolight studio lamp provides uniform and flicker-free illumination onto the white beads of the medium. A small fraction of the beads (< 10 %) are dyed black with ink to create tracer particles that are used for tracking frame-to-frame deformation in the granular medium, which is studied in another article [27] (note that in figures 2, 3 and 6, there are some darker areas creating patterns in the initial packing. This is due to a higher concentration of dyed beads, which does not have any significance on the experiments). The experiments are run for 10 s, but typically the fracturing and/or compaction of the granular medium takes less than 5 s.

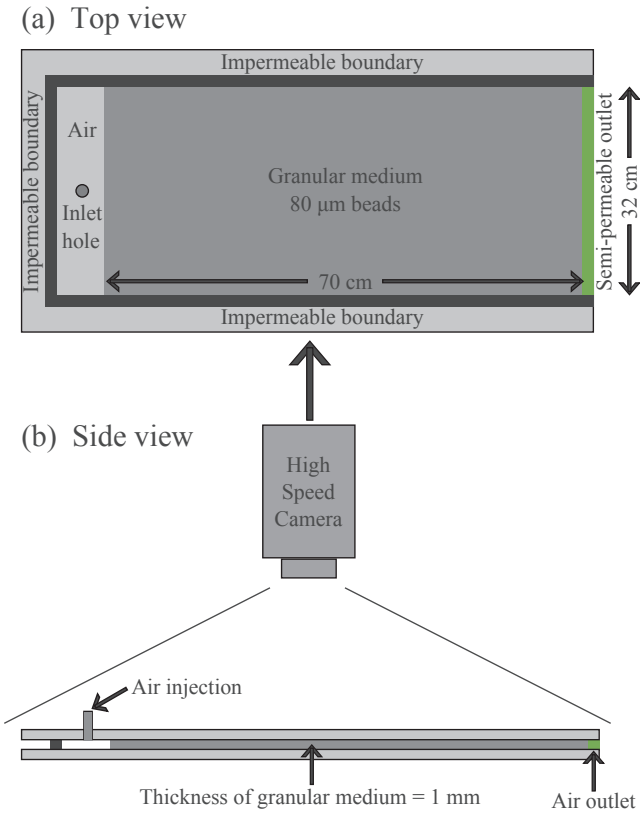

FIG. 1. Sketch of the experimental setup. (a) Top-down view of the prepared cell: The granular medium is confined inside the cell by three impermeable boundaries and an air-permeable boundary on the outlet side. The granular medium is placed against the outlet boundary such that it has a linear interface against a region empty of beads on the sealed inlet side, where pressurized air can be injected. (b) Side view of the setup showing the high speed camera placed above. The glass plates are clamped together with aluminum framing while the cell gap is controlled with spacers, which are not shown here.

B. Image processing

In analysis of the images from the high speed camera, we investigate flow regimes, characteristics and evolution of the fracturing patterns formed. We perform image

FIG. 2. Example of image processing. (a): The initial granular medium, (b): A snapshot during the experiment, (c): The resulting binary image where the pattern has been segmented. The segmentation is done by setting all pixels having 30 % less grayscale intensity in a snapshot compared to the initial image to the value 1 while the other pixels are set to the value 0.

processing with Matlab to obtain the information contained in the images. Quantitative analysis of the invasion patterns is done by converting the grayscale raw data into binary images, i.e. images with either black or white pixels, where the white pixels (value=1) represent the pattern and the black pixels (value=0) represent the background, or the bead-filled region. We obtain such binary image sequences from the raw data by thresholding each frame with the initial image, such that the pixels having a value less than 30% of the corresponding initial value becomes white and the rest remain black, as shown in figure 2 (c). In addition, once a pixel is invaded (and made white) it will remain white for the rest of the experiment to correct for mobilized beads flowing inside channels, which occurs due to erosion and fingers merging in some experiments. From the binary images we extract information such as invasion depth over time, average finger thickness as function of depth, and fractal dimensions.

III. RESULTS

Depending on injection pressure (and friction related to packing fraction) we observe the granular medium to exhibit either a solid-like behavior, or a transition from fluid-like to solid-like behavior during air injection. In the solid-like regime, there is no apparent deformation (bead displacements), and the air is reaching the cell outlet by seeping through the network of pores between beads. On the other hand, in the fluid-like regime we observe significant deformation, where beads are displaced by an amount corresponding to several bead sizes, by momentum exchange between air molecules and beads. At sufficient overpressure the granular medium has a behavior much like a viscous liquid being invaded by air, as the flow opens up channels empty of beads, a Saffman-Taylor like instability [29] resulting in dendritic invasion patterns. A stabilizing mechanism of this flow instability is the build-up of friction and stress chains between beads during compaction, so due to the boundary conditions in our experiments we always end up with a solid-like medium towards the end of an experiment.

TABLE I. The flow categories with related pressure values; mean overpressure within two standard deviations $\overline{P_{in}} \pm 2\sigma$, as well as the number of experiments N analyzed per category.

Category	$\overline{P_{in}} \pm 2\sigma$ [kPa]	N
1	9 ± 5	3
2	26 ± 18	5
3	64 ± 50	5
4	110 ± 44	6
5	134 ± 43	10
6	213 ± 50	4

A. Flow regimes

To explore the various flow regimes we have systematically varied the air injection pressure within the range of 5 kPa to 250 kPa, and we have identified 6 flow regimes occurring in this range. Typical final structures are shown for each category in figure 3, and the associated range of injection pressure is listed in table I. Videos of channels formed in categories 3 - 6 are found in the supplementary material [57–60].

We have grouped the experimental results into categories from 1 to 6, corresponding to flow regimes defined by final pattern characteristics and how the channels expand. When discussing the growth, new growth dA refers to the area added to the channel between two successive snapshots, and the active growth zone is the region of the pattern where dA is added, described in terms of extent d behind the most advanced channel tip.

- Category 1 - No deformation:
  The porous medium appears rigid (solid-like), with no significant bead displacement or invasion pattern formed.

- Category 2 - Initial compaction without fingers:
  The medium is initially compacted during a collective displacement of beads towards the outlet side, without the formation of invasion channels

- Category 3 - Short thin fingers:
  A short dendritic invasion pattern is formed, where the final length of the channel is less than 50% of $L = 70$ cm, the initial length of the granular medium, with an average finger thickness less than

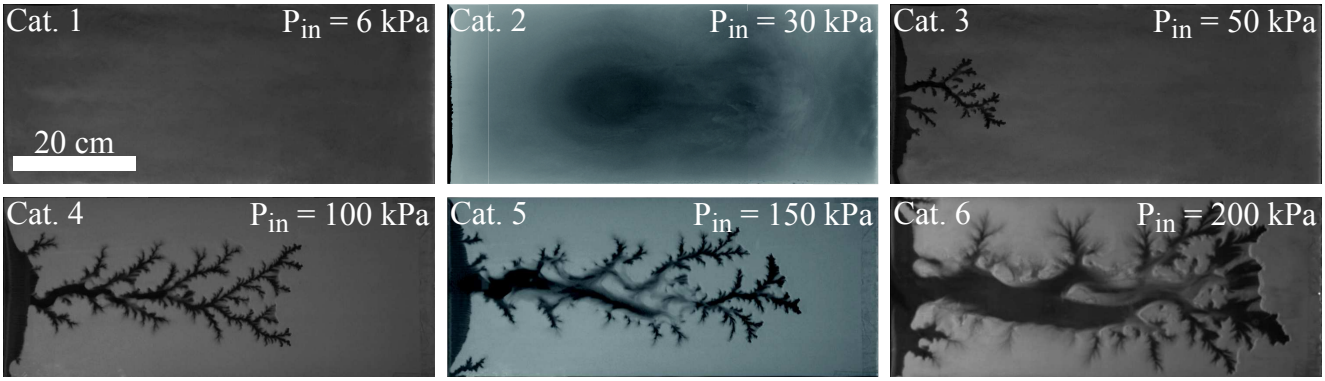

FIG. 3. Typical final structures per category, where the granular medium is gray and areas empty of beads are black, showing that for increasing P_{in} the fingers become longer and thicker. A full-size figure of the patterns shown here is found in the supplementary material [56].

2 cm. The channel growth is like fingering with an active growth zone typically within 5 cm from the most advanced tip, i.e. the channel grows primarily on the longest fingers, while it is frozen in the parts more than 5 cm behind. The new growth as function of distance behind the longest finger typically peaks halfway into the growth zone.

- Category 4 - Long thin fingers:
  A long dendritic invasion pattern is formed, where the final length of the channel is more than 50% of L, with an average finger thickness less than 2 cm. The channel growth is like fingering with an active growth zone typically within 10 cm of the most advanced finger tip. The amount of new growth as function of distance behind the longest finger typically peaks halfway into the growth zone.

- Category 5 - Long fingers with thicker main channel:
  A long dendritic invasion pattern is formed with a thicker main channel than the branch fingers, i.e. due to erosion inside the channel. The final length is more than 50% of L, with an average finger thickness between 2 cm and 4 cm. The channel growth is like fingering with an active growth zone typically within 15 cm of the most advanced finger tip. The amount of new growth is typically more spread out as function of distance behind the longest finger, where the growth between 10-15 cm behind the most advanced tip is mostly due to erosion. The erosion is not persistent, and rarely occurs more than 15 cm behind the most advanced tip.

- Category 6 - Long dominating channel:
  A long and thick main channel with some dendritic branches is formed. The width of the main channel increases by erosion (i.e. motion of beads non-perpendicular to the channel interface, but with a major tangential component along it) and with side channels and branches merging into it. The final length is more than 50% of L, with an average finger thickness more than 4 cm. The channel growth is more like fracturing, with an active growth zone spanning the entire length of the channel. Erosion and finger merging is observed to occur even at distances of 30-40 cm behind the most advanced tip. Again, erosion is not persistent and stops around the point when the channel reaches 90 % of its final length. When the erosion stops, we observe that the main channel walls and side fingers are slowly expanding perpendicularly to the average flow direction.

As one can expect, the pressure ranges for the categories overlap, indicating diffuse boundaries between flow regimes, probably due to randomness in the initial bead configuration. Table I lists the typical values of P_{in} we used for experiments within a category, and how many experiments were done. The distribution of new growth dA behind the longest fingers at different intervals is shown in figure 4 for typical experiments in the categories 3 to 6. The new growth in these plots is found by subtracting successive binary images A of the patterns pixel by pixel, i.e. $dA = A(t + \Delta t) - A(t)$, where Δt is the time between snapshots where the channels grow by 10 % increments of their final lengths (this method of selecting Δt is done in order to plot comparable distributions of dA at different times of the experiment since the growth rate decreases at later times). In the plots, the distribution of new growth over the distance d behind the most advanced finger is represented by a normalized value $n_{dA}(d)$, which is the mass of the new growth dA at the depth d, divided by the width of the cell such that $n_{dA}(d)$ is a dimensionless number $\in [0, 1]$ indicating the fraction of the cell width at position d that contains new growth. For categories 3-5 the growth typically extends in a region of 10-15 cm behind the most advanced tip, whereas for category 6 the growth extends along the whole channel length. The category 6 channels have a rapid and large volume change compared to

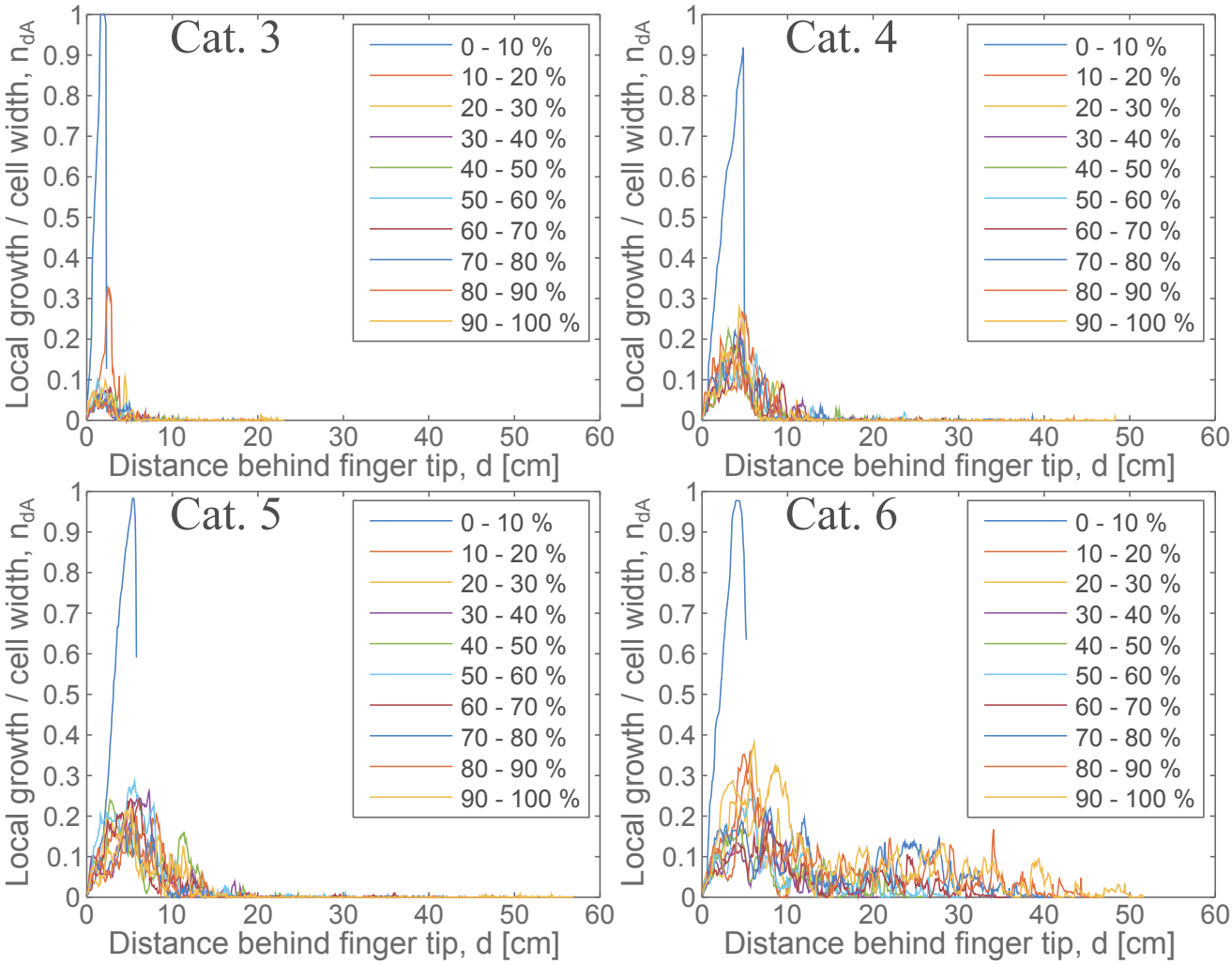

FIG. 4. Distribution of new growth over the distance behind the most advanced finger tip, at different intervals, during typical experiments in categories 3 to 6. The new growth is measured on intervals between successive snapshots where the channel length grows 10 % of the final channel length for each snapshot. The large initial new growth (0 % - 10 %) in all plots corresponds to the initial bulge that forms before the channeling instability begins. The plots indicate the depth of the active growth zone, which goes from very narrow for category 3 (the growth is focused on the most advanced tips), to the whole channel length for category 6.

the other ones, with a high air flow velocity resulting in erosion along the entire channel. In addition, the rapid expansion could let the channel pressure remain somewhat lower than P_{in} during growth, such that when it stops the pressure rises to P_{in}. If it is so, pressure gradients could form at the solid-air interface far behind the most advanced finger explaining the small growth there. The categories 4 and 5 are not fundamentally different, but since category 5 has erosion and category 4 does not, we make separate categories for the purpose of averaging results among similar experiments. The displacement of the granular medium outside the channels is similar for all categories; In front of channels and branches, beads are pushed like a piston and compacted until the system is jammed. Beads are also pushed out from the side of fingers in the active growth zone, opening up for branches.

In the rest of the paper, we focus on the categories 3 - 6, which are the flow regimes where invasion fingers are formed. For these flow regimes, we discuss the typical characteristics of the patterns formed and their growth dynamics.

B. Finger characteristics

In figure 5 we see the average finger thickness w of the final structures as function of depth x into the granular medium, measured from the initial boundary position. The average finger thickness of a pattern at a given depth into the granular medium is found by intersecting the bi-

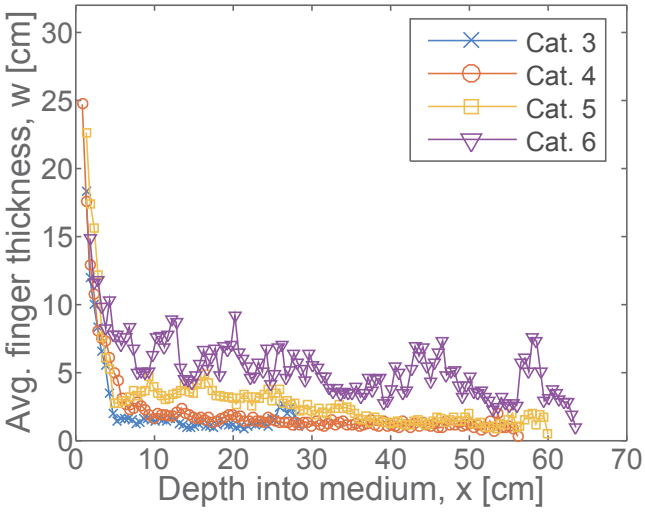

FIG. 5. Average finger thickness w as function of depth x into the medium for the final structures, averaged per categories where fingers occur (Cat. 3 - 6). We see that for the structures in Cat. 5 (erosion) and Cat. 6 (erosion and finger merging) the fingers are thicker - up to the finger tip for Cat. 6.

nary image of the pattern with a line perpendicular to the average flow direction at that depth, and count the total number of white pixels intersected. In other words, the total width of the pattern is measured followed by dividing it by the number of connected pixel groups, i.e. the number of fingers. This is done for each experiment and the results are averaged within each category. We see that the patterns in categories 3 and 4 have roughly the same thickness, averaging around 1.4 cm and is more or less constant as function of depth. We do not observe erosion inside these channels, so a finger thickness around 1.4 cm seems typical when there is no erosion. The category 5 patterns show initially thicker fingers along the first half of the structures, here with an average thickness of 3.3 cm, which then decreases down towards the typical thickness seen for categories 3 and 4. The larger initial finger thickness is due to erosion inside the main channel, meaning that beads near the channel walls are re-mobilized in the flow direction after the initial growth, making the channel grow perpendicular to it. As average thicknesses here suggest, this effect typically increase the channel width by an amount of around 2 cm. The category 6 patterns typically have thick fingers throughout their entire length up to the tips, with an average of 5.3 cm. This thickness is achieved both by erosion inside the main channel, and with fingers merging together. After fingers merge and trap clusters of beads, these beads are mobilized in the flow direction. In general we see an increase in finger thickness and length for increasing pressures. Some examples of both erosion and finger merging are shown in figure 6 for an experiment with $P_{in} = 200$ kPa.

The plot in figure 7 shows the average number of fingers N_f as function of depth x into the medium (found as

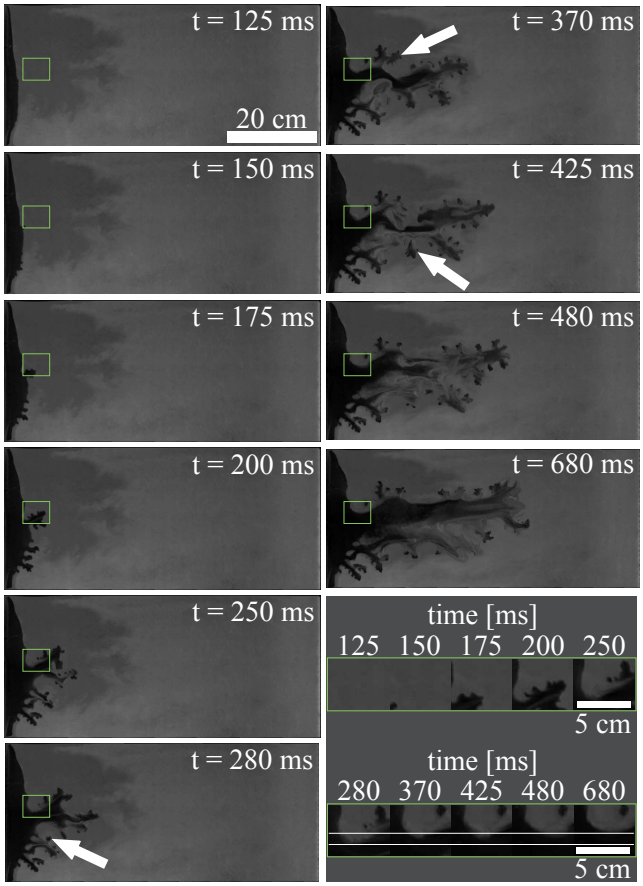

FIG. 6. Snapshots from an experiment with $P_{in} = 200$ kPa, showing examples of erosion and finger merging. The green rectangle indicates the area cut out and enlarged in the bottom right inset: Here we see erosion inside the channel as beads (gray area) are removed over time. The white arrows point at fingers that will merge into the main channel in the following snapshot, carving out trapped clusters of beads which are then mobilized in the flow direction. A full-size version of this figure is found in the supplementary material [61].

the number of connected pixel groups on vertical cross-sections, as explained for figure 5) for the final structures in each category. For patterns in the categories 3 and 4, the number of fingers increase at lower depths than for patterns in the categories 5 and 6, where there is a more pronounced initial region with fewer fingers, crossing over to more fingers during the last half of their length. This could indicate that channels with few branches form when the friction is low compared to the driving force $\propto \nabla P$, with a cross-over to the patterns branching out with more fingers as the friction is becoming comparable to the driving force due to compaction. The sudden drop in N_f at the deepest parts of the patterns is due to the finite size of the structures, where only a few of the longest fingers reach.

To get a description of the shape of finger tips, we look

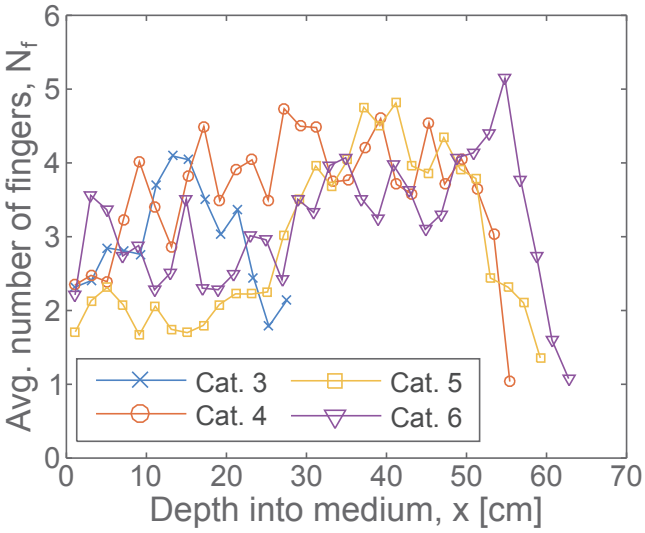

FIG. 7. The average number of fingers N_f as function of depth x into the granular medium, averaged over the final patterns in the same category. The plot indicates that for increasing injection pressure, an initial region with fewer fingers extends deeper into the medium before an increase in N_f towards the final depth. This suggests more branching of the channels as the beads become harder to displace. The sudden drop in N_f close to the tips is due to the finite size of the patterns.

at how the finger thickness w grow as function of distance d from the finger tip, which is found to follow a power law within the length of the tip region [28] (where the finger thickness increase with d before it saturates):

$$w(d) \propto d^{\beta}. \tag{1}$$

When w is plotted as a function of d in a log-log plot, the slope β for $w(d)$ within the tip region reveal information about the shape of the tip; it has a more rounded shape for $\beta < 1$, while it has a pointy cusp-shape for $\beta > 1$. We have averaged $w(d)$ over time for each experiment, i.e. obtaining the average finger tip shape during flow in each experiment. Figure 8 (a) shows a log-log plot of the finger thickness as function of distance from the finger tip, averaged per category. The collapsed average slopes from all experiments seem to fall along the same line with $\beta = 0.68$, indicating more rounded finger tips with the same shape in all experiments. However, a purely round profile would give $\beta = 0.5$, so the fact that we measure a bigger value means that there still is a singularity in curvature towards the tip - even if it is not a spike shape. The singularity can be shown as follows, where

$$w \sim d^{\beta} \Rightarrow d \sim w^{\frac{1}{\beta}} \Rightarrow \frac{dd}{dw} \sim w^{\frac{1}{\beta}-1}, \tag{2}$$

gives the slope of the front. From this we find the expression for the curvature as,

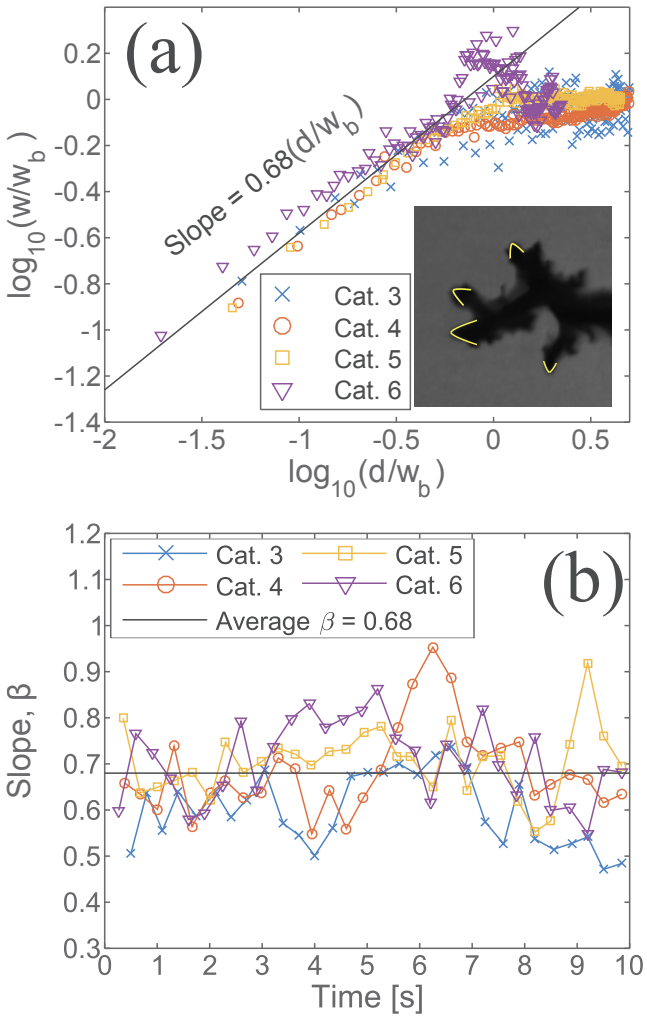

FIG. 8. (a) The finger thickness w plotted in a log-log plot as function of the distance d from the finger tip. The data shown is the average of about 50 measurements in time for each experiment, averaged again for each category. The data is collapsed by the finger thickness at the base of the tips w_b found as the average finger thickness where w has reached a more or less constant level, which seems to be a typical length scale for the tip region. The finger thickness at the base of the tips is found as. The average slope at different times during several experiments is $\beta = 0.68$, indicating a more rounded shape of the tips. In the inset: Snapshot of typical finger tips together with profiles corresponding to $\beta = 0.68$ (yellow lines). (b) The slope β averaged per category as function of time during experiments. The plot shows that the slope for the tip profile fluctuates around $\beta = 0.68$ over time during the experiments, suggesting that the tips are more rounded than cusp-like at all times.

$$\kappa \sim \frac{d^2 d}{dw^2} \sim w^{\frac{1}{\beta}-2} \text{ (or } d^{1-2\beta}). \tag{3}$$

If $\beta > 0.5$, $\frac{1}{\beta} - 2 < 0$ and κ diverges at the tip where w (and d) $\to 0$. At the same time, if $\beta < 1$, the slope

does not diverge at $d = 0$, and yields a more rounded profile.

We have not observed any cusps as reported in [28] with $\beta = 1.43 \pm 0.2$, consistent with theory on fluid fingering in the zero-surface tension limit. The evolution of β over time is plotted in figure 8 (b), which shows that for all experiments, β fluctuates around the estimated value $\beta = 0.68$ over time, indicating that the tip shapes does not seem to change significantly during the different stages of the experiments.

C. Fractal analysis

By looking at the invasion patterns, we notice that they have self-similar features, e.g. a smaller branch resemble the whole larger pattern. To characterize this feature we analyze fractal dimensions of the final patterns in three different ways. The box-counting dimension D_B is found for each final structure by covering the binary image with boxes, i.e. dividing the image into equal squares of sides s, and count the number N of squares that contain a white pixel as function of box size s. For a fractal, the relationship between the number of boxes covering the pattern and their size follow a power law

$$N(s) \propto s^{-D_B}, \tag{4}$$

such that the box-counting dimension D_B is found as the negative value of the slope of $N(s)$ in a log-log plot [30, 62–64]. By obtaining box-counting data over a range of sizes s, we estimate D_B from the slope of linear fits between an upper cutoff $s = 32$ cm (cell width) and a lower cutoff $s = 1$ cm (typical for thinner fingers). In addition, we obtain the box-counting dimension D_F of the front (air-solid interface). This is found in the same way as the box dimension, but with binary images where only pixels on the perimeter of the patterns are white. Finally, we estimate local fractal dimensions D_L as function of depth along the structures. To get the local fractal dimension at a given depth, we intersect the structure at that depth with a vertical line (perpendicular to the flow direction) and do a 1-dimensional box counting along that line, i.e. divide the line into pieces of equal length l and count the number N of line segments containing white pixels as function of l. Again, for a fractal we have the power law

$$N(l) \propto l^{-D_L}, \tag{5}$$

and we find the local fractal dimensions at given depths from slopes of linear fits between $l = 16$ cm and $l = 1$ cm. To compare D_L with D_B we use one of Mandelbrot's rules of thumb [63, 65]. It states that the codimension of an intersected set equals the sum of the codimensions of the individual intersecting sets, here given by

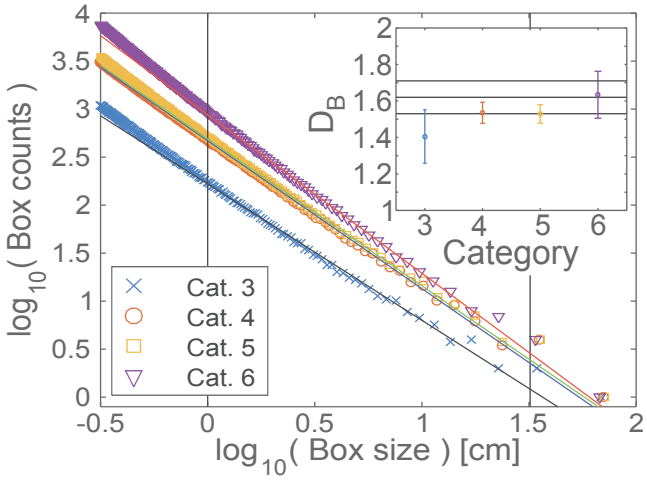

FIG. 9. Average box-counting slopes per category, the lower and upper limits are indicated with the vertical lines and mark the typical thickness of the thinnest fingers (1 cm) up to the cell width (32 cm). In the inset: Box-counting fractal dimensions D_B averaged per category, the error bars show 2 standard deviations. Patterns in categories 4 and 5 with $D_B = 1.53$ and $D_B = 1.54$ are within the range of earlier measured values for viscous fingers in saturated porous media (between the dashed lines). The less developed patterns in category 3 is below this range, with $D_B = 1.41$, and the thicker category 6 patterns are close above with $D_B = 1.63$. The solid line indicates $D_B = 1.71$ for Diffusion Limited Aggregation patterns.

$$\begin{aligned} E_2 - D_L &= (E_2 - E_1) + (E_2 - D) \\ &\Downarrow \\ D &= D_L + 1, \end{aligned} \tag{6}$$

where D is the fractal dimension of the pattern, $E_1 = 1$ is the dimension of the line intersecting it, and $E_2 = 2$ is the dimension of the image plane containing the sets.

The box-counting dimensions are averaged per flow category and plotted in figure 9. We see that the box dimension for the less developed category 3 patterns is $D_B = 1.41$. For categories 4 and 5, the box dimensions are $D_B = 1.54$ and $D_B = 1.53$ respectively. For category 6 patterns, we observe $D_B = 1.63$. Patterns in category 4 and 5 have box dimensions within the range of box dimensions found for viscous fingers in saturated porous media, i.e. D = 1.53 - 1.62 [30, 64, 66].

Figure 10 shows the results of box-counting the air-solid interface of the final structures, averaged per category. We see that categories 3, 4 and 5 have interface dimensions $D_F = 1.40, 1.52, 1.48$ respectively which are close to their corresponding box-counting dimensions, while category 6 patterns have $D_F = 1.41$ which is about 0.2 less than the corresponding box dimension. This can be interpreted in terms of finger thickness, i.e. the front becomes more similar to the structure for decreasing finger thickness.

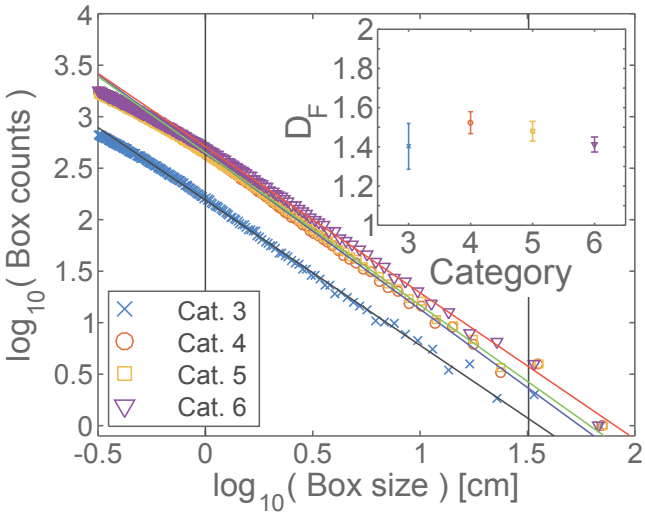

FIG. 10. Average box-counting slopes per category, the lower and upper limits are indicated with the vertical lines and mark the typical thickness of the thinnest fingers (1 cm) up to the cell width (32 cm). In the inset: Box-counting fractal dimensions D_F of the solid-air interface per category. The error bars show 2 standard deviations.

Figure 11 shows the local fractal dimensions D_L as function of depth into the granular medium. For all flow categories, the curves show a more or less constant behavior over most of the depths (the initial high dimension is due to a larger initial area empty of beads, and the final lower dimension is due to finite size effects of the patterns), which indicates that the patterns have consistent local fractal dimensions over a range of x. The categories 3, 4 and 5 patterns have typical local dimensions of 1.53, 1.58, 1.60, respectively. This is within the range of dimensions seen for viscous fingers in saturated porous media ($D = 1.53$ - 1.62), while the category 6 patterns the local dimension is higher, with a typical value of $D_L = 1.76$, which is closer to the dimensions seen for DLA clusters and viscous fingers in an empty saturated Hele-Shaw cell ($D = 1.71$).

D. Growth dynamics

In figure 12 (a), the finger tip position averaged per category is plotted as function of time, which is found by recording the maximum depth of the patterns in the binary images at each snapshot. We see that for all experiments, the channel length grows linearly with time initially before it decelerates towards a final length, and that both the growth velocity and final depth of the invasion structures increase with increasing injection pressure. The initial constant growth rate seems to scale with the injection pressure as $P_{in}^{\frac{3}{2}}$. In figure 12 (b), the finger tip positions per category is divided by $P_{in}^{\frac{3}{2}}$ to show that they fall along the same line initially. In the simulations

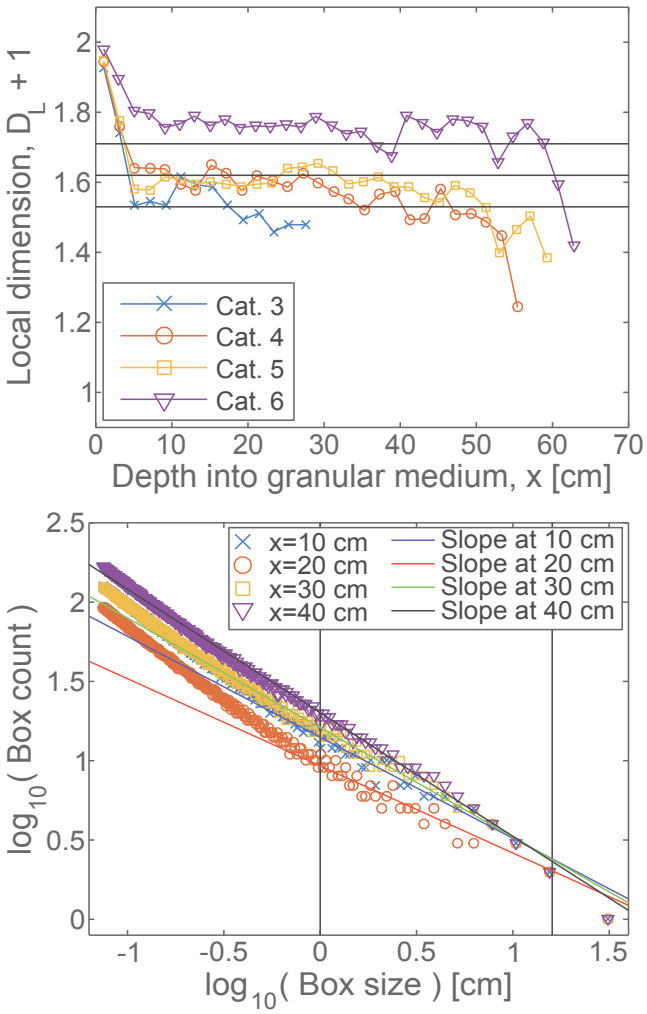

FIG. 11. Top: Local fractal dimensions ($D_L + 1$) as function of depth into the medium for the final structures averaged per category. We see that the patterns in all categories have more or less constant and well defined local dimensions as functions of depth. The main parts of the patterns in categories 3-5 have local dimensions corresponding to established values for viscous fingers in saturated porous media (between the dashed lines). For patterns in category 6, the local dimensions correspond to values closer to the fractal dimension for DLA patterns and flow patterns in a saturated Hele-Shaw cell (solid line). Bottom: Examples of local box-counting slopes at different depths of the same experiment.

done by Niebling et al. [45, 53] of a similar, but smaller system they too observe an initial linear growth velocity crossing over to decay over time, however we here observe the initial growth velocity to scale with P_{in} as $v \propto P_{in}^{3/2}$ instead of $v \propto P_{in}^{1/2}$ as found in these simulations. In figure 13 (a), the log-log plot of the finger tip velocity $v(t)/(P_{in}^{3/2})$ as function of time indicates that when the finger tip velocity begins to decrease, it follows a power law equation with time, $v(t) \propto t^{-\alpha}$, where $\alpha = 2.5 \pm 0.2$.

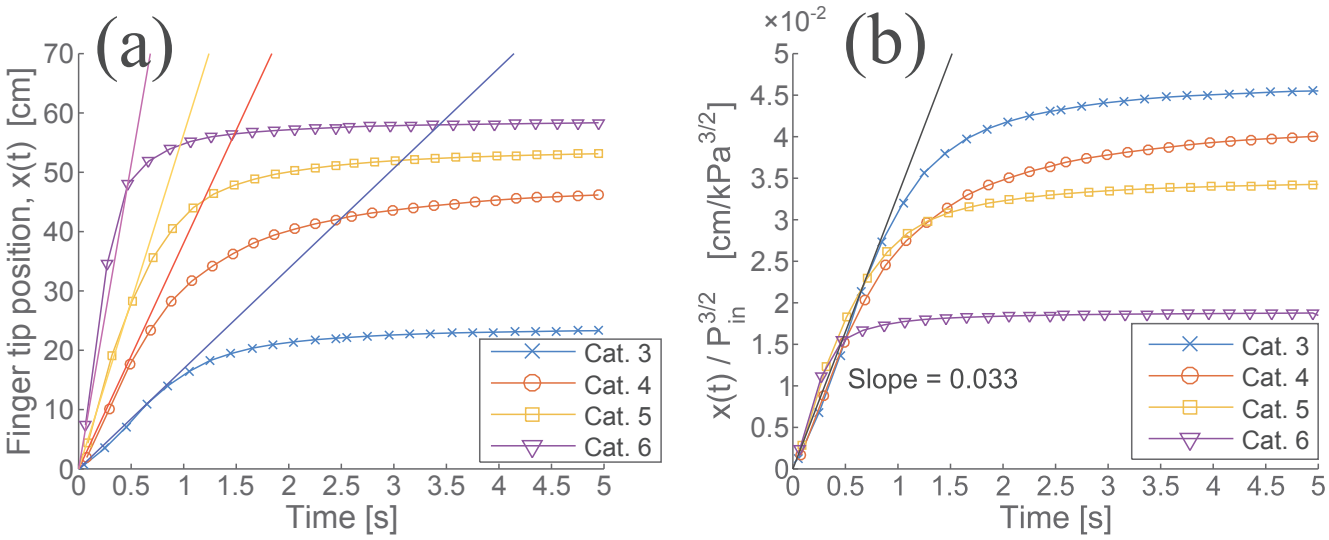

FIG. 12. (a) The finger tip position $x(t)$ as function of time, averaged for all experiments per category. The curves typically have an initial linear growth with time which crosses over to a decay with time. The patterns grow faster and longer for increasing injection pressure, and the initial linear growth is found to scale proportionally with $P_{in}^{3/2}$ as indicated by the dashed lines. (b) The finger tip positions $x(t)$ divided by $P_{in}^{\frac{3}{2}}$, showing that the initial growth fall along the same line. The injection pressures are P_{in} = 64, 110, 134 and 213 kPa, for category 3, 4, 5 and 6 respectively.

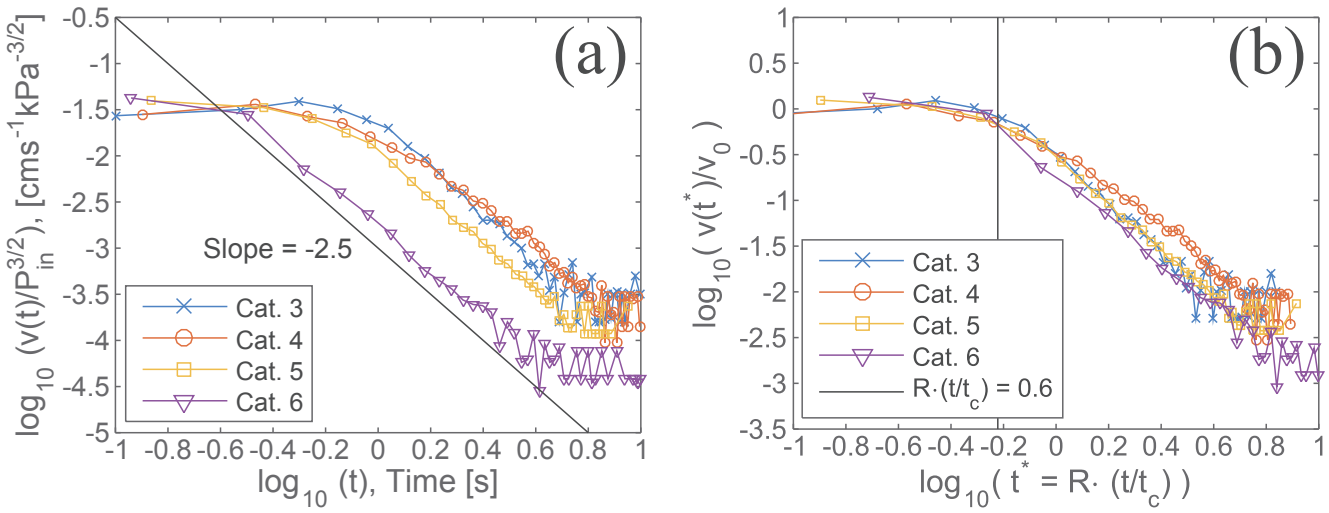

FIG. 13. (a) Log-log plot of the finger tip velocity $v(t)$ as function of time, averaged per category. The data is collapsed along the ordinate axis by dividing $v(t)$ by $P_{in}^{\frac{3}{2}}$, where P_{in} = 64, 110, 134 and 213 kPa, for category 3, 4, 5 and 6 respectively. The initial constant plateau corresponds to the period with linear growth over time, which then crosses-over to a declining slope close to -2.5 (dashed line) for all the categories. The slopes show that the decay in growth velocity follows a power law equation with time. (b) The curves of normalized finger tip velocity $v(t^*)/v_0$ are collapsed along the time axis by scaling the time as $t^* = t \cdot (v_0/x_f) = R \cdot (t/t_c)$, where x_f is the final channel length. The knee point of the curves, $R \approx 0.6$, is marked by the dashed vertical line.

E. Scaled growth model

As we have shown in figures 12 and 13, the growth of the channel length is linear with time initially until it crosses over to decay towards a final channel length. More specifically, the growth velocity is constant initially, before it crosses over to a power law decay with time. The constant initial velocity v_0 is found to scale with injection pressure P_{in} as

$$v_0 = C \cdot P_{in}^{\frac{3}{2}}, \tag{7}$$

where $C \approx 10^{-\frac{3}{2}}$ cm/(s·kPa$^{\frac{3}{2}}$) is found from the initial part of the collapsed curves $v(t)/P_{in}^{\frac{3}{2}}$ along the ordinate axis in figure 13 (a). By inserting the value for C into equation (7), we can instead collapse the curves along the ordinate axis with $v(t)/v_0$ resulting in dimensionless and normalized units for the velocity. In order to collapse the curves along the time axis, we define a critical time $t = t_c$ as the time when the growth velocity crosses over from being constant to follow a power law decay with time. At the critical time, the finger tip position can be described mathematically as

$$x_c = x(t_c) = v_0 \cdot t_c, \tag{8}$$

which gives the relation

$$t_c = \frac{x_c}{v_0} = \frac{x_c}{C \cdot P_{in}^{\frac{3}{2}}} \tag{9}$$

for the critical time.

Since we can easily measure x_f, the final length of the channel, we check if x_c can be described as a typical fraction R of x_f, such that $x_c = R \cdot x_f$, which gives

$$t_c = \frac{R \cdot x_f}{C \cdot P_{in}^{\frac{3}{2}}} = R \cdot \frac{x_f}{v_0}. \tag{10}$$

By plotting $v(t^*)/v_0$ as function of $t^* = t \cdot (v_0/x_f) = R \cdot (t/t_c)$ in a log-log plot, we do indeed find that the curves collapse along the time axis with a crossover point corresponding to $R \approx 0.6$ (read from the knee point in figure 13 (b)). Since we now have the constants C and R, we can calculate v_0 and t_c for individual experiments by inserting the respective P_{in} and x_f into equations (7) and (10). Figure 14 shows log-log plots of $v' = v(t')/v_0$ as function of $t' = t/t_c$ for individual experiments with injection pressures in the range of 50 - 250 kPa, which follow the same dimensionless curve given by the function

$$f_v(t') = \begin{cases} 1, & \text{if } t' \leq 1 \\ t'^{-\alpha}, & \text{if } t' > 1, \text{ where } \alpha = 2.5. \end{cases} \tag{11}$$

Similarly, we collapse the fingertip position $x' = x(t')/x_c$ and plot it as function of $t' = t/t_c$ for the same individual experiments, also shown in figure 14 (Note that the data is from single experiments, i.e. not the average values as in figure 13, explaining the increased amount of noise). Here, the collapsed data follow the curve given by the function

$$f_x(t') = \begin{cases} t', & \text{if } t' \leq 1 \\ \frac{1}{1-\alpha} t'^{1-\alpha} + \frac{\alpha}{\alpha-1}, & \text{if } t' > 1, \end{cases} \tag{12}$$

which is obtained by integrating each part of equation (11), requiring that $f_x(t' > 1) \to 1$ when $t' \to 1$. Further, $f_x(\infty) = \alpha/(\alpha - 1) = x_f/x_c = 1/R$, giving $R = (\alpha - 1)/\alpha = 0.6$, which fits very well with our observation in figure 13 (b). By substituting α into equation (10) we get,

$$t_c = \frac{\alpha - 1}{\alpha} \cdot \frac{x_f}{C \cdot P_{in}^{\frac{3}{2}}}. \tag{13}$$

With equations (7 - 13) we propose a description of the fundamental dynamics of the system. Since we have experimentally estimated α and equation (7) relating the initial growth velocity to injection pressure, we can estimate the evolution of the channel length during the invasion for a given injection pressure and final channel length.

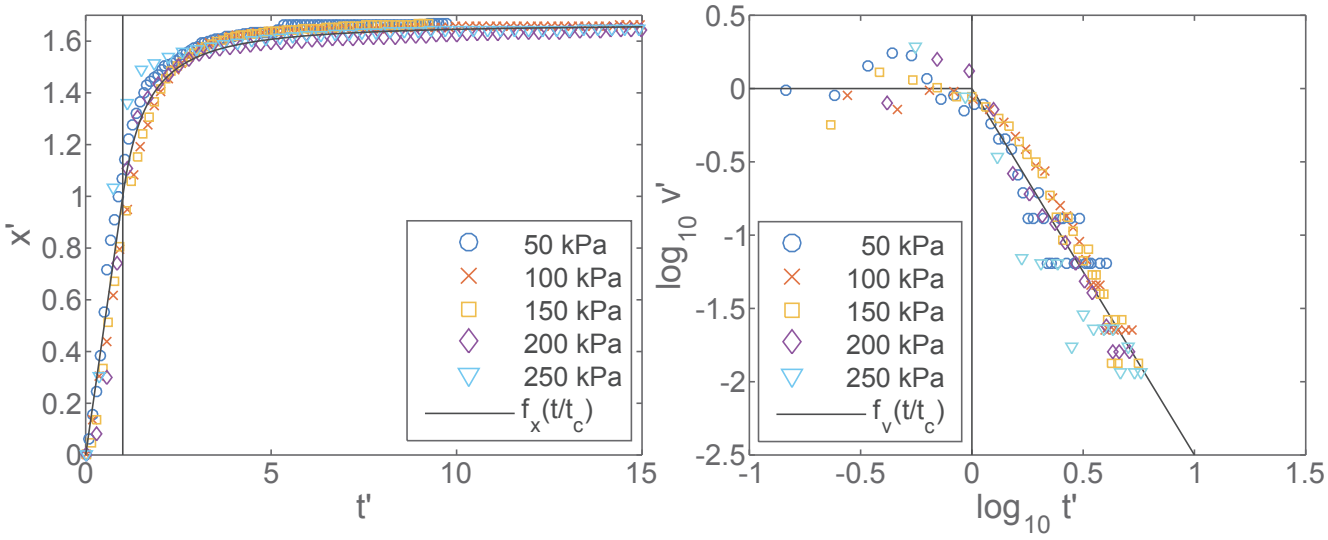

FIG. 14. Left: The collapsed finger tip positions $x' = x(t')/v_0 \cdot t_c$ as function of $t' = t/t_c$, for individual experiments with various injection pressure. The dotted vertical line indicates the cross-over at $t' = 1$, and the dashed curve shows the proposed function $f_x(t')$. Right: Log-log plot of the collapsed finger tip velocities $v' = v(t')/v_0$ as function of $t' = t/t_c$ for the same individual experiments. The dotted vertical line indicates the cross-over at $t' = 1$, and the dashed curve shows the proposed function $f_v(t')$. Recall that the parameters used for the collapse are given by the injection pressure, as $v_0 = C \cdot P_{in}^{\frac{3}{2}}$ and $t_c = ((\alpha - 1)/\alpha) \cdot (x_f/v_0(P_{in}))$, where $C = 10^{-\frac{3}{2}}$ cm/(s·kPa$^{\frac{3}{2}}$) and $\alpha = -2.5$.

IV. DISCUSSION AND CONCLUSION

The channel formations seen in our experiments result in patterns very similar to other natural patterns arising from Laplacian growth, e.g. DLA clusters, viscous fingers in empty Hele-Shaw cells, manganese dendrites, or lightning bolts. In such systems, ramified structures expand at a rate proportional to the gradient of a Laplacian ($\nabla^2\phi = 0$) potential field. This type of patterns is in the DLA universality class, where a fractal dimension of $D = 1.71$ is expected [41, 64]. However, the fractal dimensions found for our patterns mainly take values of $D \in [1.53 - 1.60]$, which is more similar to viscous fingers in porous Hele-Shaw cells. It has been established that flow in porous media is better described by another Laplacian model, i.e. the Dielectric Breakdown Model (DBM), where the interfacial growth rate is proportional to the pressure gradient of a power η higher than 1, i.e. $v \propto (\nabla P)^\eta$, where $\eta = 2$ for viscous fingers in porous media [41, 64]. In our system the potential field is the overpressure in the medium, which diffuses into the medium initially (not Laplacian). However, the diffusing pressure field quickly approaches the Laplace solution outside finger tips (after 0.4-0.5 s) and reaches a global steady state on the order of a second. In addition, we observe a feature of the channel growth which is typical for Laplacian growth systems, i.e. there is an active growth zone outside a frozen structure, due to screening of the potential gradient by the most advanced parts of the structure.

The resulting channels in our experiments are different than channels formed in similar systems having open outer boundaries, such as in [24–26]. In the open systems, the channels are generally much smoother and does not have more than 1-2 branches, while in the closed system we see ramified structures. This is thought to be a consequence of the outer boundary conditions which directly influence how the medium can be deformed. In both systems, the beads are compacted and pushed in front of the growing channel like a piston, but in the open system there is also a decompaction front moving inwards from the open outlet, easing the further displacement of beads. On the other hand, in the closed system, after the compaction front hits the outer boundary (which happens between $t = 150 - 300$ ms) further deformation is more difficult due to compaction. Thus, the local configuration of the pressure field on the tips could play a larger role on where the channels grow in this case. In addition, the overpressures imposed for channeling in our experiments (P_{in} = 40-250 kPa) are one order of magnitude larger than the ones for these open systems (P_{in} = 2-20 kPa). Although the cells in [24, 26] are smaller than ours, the one in [25] is of comparable dimensions.

For the growth dynamics, the dependency of v_0 on P_{in}, and the exponent α could be system dependent, i.e. the parameters could depend on e.g. bead size and confinement. Thus, it is of interest to investigate further how the dynamics are changing in various confined granular media, and see how the Eqs. (7 - 13) apply in those cases. The dependency of x_f on P_{in} is also of interest to investigate further, such that if system dependent parameters are known, the expected result of an air injection could be estimated by the injection pressure alone. A brief dis-

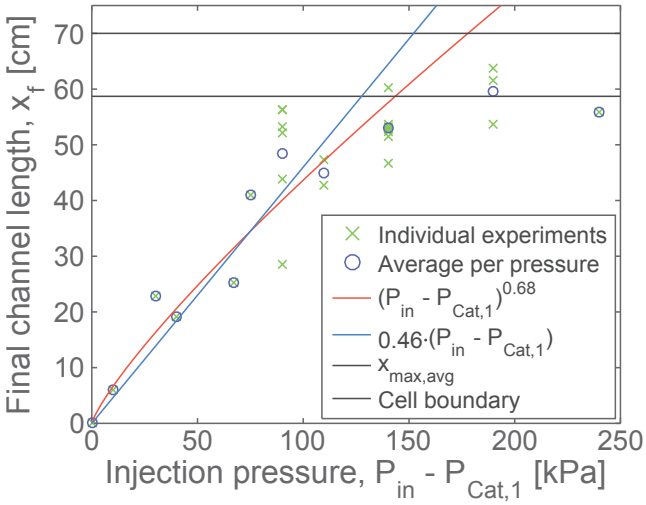

FIG. 15. The final channel length x_f is plotted as function of $P_{in} - P_{cat,1}$, where $P_{cat,1} = 9$ kPa is the average injection pressure for category 1, where $x_f = 0$. We see that there is a rather scattered (due to randomness in the initial bead configuration from experiment to experiment), but increasing trend in x_f for increasing P_{in}, but also that the final channel length for the highest injection pressures is limited by the closed outer boundary. The fit $(P_{in} - P_{cat,1})^{0.68}$ was found from the averaged x_f per pressure for $P_{in} \in [20, 150]$ kPa and suggest a power-law relationship. Alternatively, the linear fit $0.46 \cdot (P_{in} - P_{cat,1})$ fits equally well. The average limiting line $x_{max,avg}$ was found by averaging x_f over the experiments with $P_{in} \geq 200$ kPa, to indicate the influence of the cell boundary. Thus, the results from our experiments indicate that x_f increase more or less proportionally with P_{in} until a limiting length $x_{max,avg} \approx 59$ cm is reached due to the presence of the outer boundary.

cussion of what we could find from our experiments is presented in figure 15. Another interesting feature found to be common for all experiments in the system is the typical profile of the finger tips, corresponding to a growth in finger thickness w as function of distance d behind the tip as $w \propto d^{\beta}$ where $\beta = 0.68$ on average.

As shown in figure 11, the fractal dimension of the channels is found to be fairly stable along the main part of the structures, even for the thick fingers in category 6. The local box-counting method indicates that when there is little or no erosion, as is the case for categories 3 - 5, the final structures end up with typical fractal dimensions between $D = 1.53$ and 1.60. This range is similar to the one observed for viscous fingers in saturated porous media, i.e. $D = 1.53$ - 1.62, suggesting that the channels formed in our experiments are in the DBM universality class of patterns where the interface expands at a rate proportional to $(\nabla P)^2$. The thicker category 6 structures have a fractal dimension of $D = 1.76$, which is closer to DLA-patterns and viscous fingering in empty saturated Hele-Shaw cells ($D = 1.71$). However, the higher fractal dimension is probably also an effect of box-counting inside the main channel which is rather space filling compared to the system size, and this makes the box-counting slopes for category 6 more uncertain than for thinner fingers. Furthermore, the global box-counting dimensions D_B are slightly lower than the locally estimated fractal dimensions, which could be a finite size effect since less developed outer parts are also taken into account. However, for the most developed and best preserved channels (Cat. 4 and 5), we find that $D_B = 1.53$ and 1.54, which is still in good agreement with the fractal dimensions for viscous fingers in porous media. Finally, the fractal dimensions of the front is found to lie between $D_F = 1.41$ and 1.52 for all categories. This indicates that even if the structures themselves appear to change with increasing injection pressure, the roughness of the air-solid interface seems to be more or less the same.

ACKNOWLEDGMENTS

This project has received funding from the European Unions Seventh Framework Programme for research, technological development and demonstration under grant agreement no. 316889, ITN FlowTrans. We thank Alain Steyer and Miloud Talib for their technical support with experimental equipment. We would also like to thank Emily Brodsky, Daniel Koehn, Piotr Szymczak, Christine Putnis, Ulrich Kelka, Stephen Centrella, Amir Sagy, Monem Ayaz, Anke Lindner and Øistein Johnsen for nice and fruitful discussions.

[1] S. S. Suthersan. *Remediation Engineering: Design Concepts*. Boca Raton, FL: CRC Press LLC, 1999. pp. 237-54.

[2] L. L. Goodroad and J. R. Schuring. Potential of pneumatic fracturing to enhance in situ remediation technologies. *In: Waste Management 1994 Symposium. Tucson, AZ: WM SYMPOSIA, INC.*, 1994.

[3] S. Kazemian, B. B. K. Huat, A. Prasad, and M. Barghchi. A review of stabilization of soft soils by injection of chemical grouting. *Aust. J. Basic & Appl. Sci. 4(12), pp. 5862-68*, 2010.

[4] R. Z. Moayed, E. Izadi, and M. Fazlavi. In-situ stress measurements by hydraulic fracturing method at gotvand dam site, iran. *Turkish J. Eng. Env. Sci. 36, pp. 179-94*, 2012. doi:10.3906/muh-1104-9.

[5] C. T. Montgomery and M. B. Smith. Hydraulic fracturing: history of an enduring technology. *J. Pet. Technol. **62**:2632*, 2010. doi:10.2118/1210-0026-jpt.

[6] Department of Energy. Hydraulic fracturing whitepaper. *EPA 816-R-04-003, Appendix A*, 2004.

[7] G.C. Naik. Tight gas reservoirs - an unconventional natural energy source for the future. *Available online at: www.pinedaleonline.com/socioeconomic/pdfs/tight_gas.pdf (Accessed 05, 2016)*, 2003.

[8] S. M. Johnson and J. P. Morris. Hydraulic fracturing mechanisms in carbon sequestration applications. *In: 43rd U.S. Rock Mechanics Symposium and 4th U.S.-Canada Rock Mechanics Symposium. Asheville, NC: American Rock Mechanics Association*, 2009.

[9] W. H. Williamson and D. R. Wooley. *Hydraulic Fracturing to Improve the Yield of Bores in Fractured Rock*. Canberra, ACT: Australian Government Publishing Service, 1980.

[10] F. Rummel and O. Kappelmayer. The falkenberg geothermal frac-project: concepts and experimental results. *Hydraul. Fract. Geotherm. Energy **5**:5974*, 1983. doi:10.1007/978-94-009-6884-4_4.

[11] Clark L. Energy company plans to frack volcano. *In: Wired Science. Available online at: www.wired.com/wiredscience/2012/10/newberry-volcano-fracking (Accessed 05, 2016)*, 2012.

[12] A. Hurst, J. Cartwright, and Duranti D. Fluidization structures produced by upward injection of sand through a sealing lithology. *In: Van Rensbergen P., Hillis R.R., Maltman A.J. and Morley C.K., editors. Subsurface Sediment Mobilization. London: Geological Society, Special Publications 216, pp. 123-38*, 2003.

[13] H. Løseth, L. Wensaas, B. Arntsen, and M. Hovland. Gas and fluid injection triggering shallow mud mobilization in the hordaland group, north sea. *In: Van Rensbergen P., Hillis R.R., Maltman A.J. and Morley C.K., editors. Subsurface Sediment Mobilization. London: Geological Society, Special Publications 216, pp. 139-57*, 2003.

[14] P. Van Rensbergen, J. Poort, R. Kipfer, M. De Batist, M. Vanneste, J. Klerkx, and et al. Near-surface sediment mobilization and methane venting in relation to hydrate destabilization in southern lake baikal, siberia. *In: Van Rensbergen P., Hillis R.R., Maltman A.J. and Morley C.K., editors. Subsurface Sediment Mobilization. London: Geological Society, Special Publications 216, pp. 207-21*, 2003.

[15] A. R. Talukder, M. C. Comas, and J. I. Soto. Pliocene to recent mud diapirism and related mudvolcanoes in the alboran sea(western mediterrenean). *In: Van Rensbergen P., Hillis R.R., Maltman A.J. and Morley C.K., editors. Subsurface Sediment Mobilization. London: Geological Society, Special Publications 216, pp. 443-59*, 2003.

[16] N. Pralle, M. Külzer, and G. Gudehus. Experimental evidence on the role of gas in sediment liquefaction and mudvolcanism. *In: Van Rensbergen P., Hillis R.R., Maltman A.J. and Morley C.K., editors. Subsurface Sediment Mobilization. London: Geological Society, Special Publications 216, pp. 159-71*, 2003.

[17] E. Deville, A. Battani, R. Griboulard, S. Guerlais, J. P. Herbin, J. P. Houzay, and et al. The origin and processes of mudvolcanism: new insights from trinidad. *In: Van Rensbergen P., Hillis R.R., Maltman A.J. and Morley C.K., editors. Subsurface Sediment Mobilization. London: Geological Society, Special Publications 216, pp. 475-90*, 2003.

[18] R. Nuwer. Indonesias 'mud volcano' and nine years of debate about its muck. *In: NY Times. Available online at: www.nytimes.com/2015/09/22/science/9-years-of-muck-mud-and-debate-in-java.html (Accessed 10, 2016)*, 2015.

[19] A. Mazzini, H. Svensen, G. G. Akhmanov, G. Aloisi, S. Planke, A. Malthe-Sørenssen, and B. Istadi. Triggering and dynamic evolution of the lusi mud volcano, indonesia. *Earth and Planetary Sci. Lett. 261, 375-388*, 2007. doi:10.1016/j.epsl.2007.07.001.

[20] A. Mazzini, A. Nermoen, M. Krotkiewski, Y. Podladchikov, S. Planke, and H. Svensen. Strike-slip faulting as a trigger mechanism for overpressure release by piercement structures. implications for the lusi mud volcano, indonesia. *Marine and Petroleum Geology 26, 1751-1765*, 2009. doi:10.1016/j.marpetgeo.2009.03.001.

[21] A. Mazzini, G. Etiope, and H. Svensen. A new hydrothermal scenario for the 2006 lusi eruption, indonesia. insights from gas geochemistry. *Earth and Planetary Sci. Lett. 317/318, 305-318*, 2012. doi:10.1016/j.epsl.2011.11.016.

[22] M. Lupi, E. H. Saenger, F. Fuchs, and S. A. Miller. Lusi mud eruption triggered by geometric focusing of seismic waves. *Nature Geoscience 6, 642-646*, 2013. doi:10.1038/ngeo1884.

[23] M. R. P. Tingay, Rudolph M. L., M. Manga, R. J. Davies, and C. Y. Wang. Initiation of the lusi mudflow disaster. *Nature Geoscience 8, 493-494*, 2015. doi:10.1038/ngeo2472.

[24] Ø. Johnsen, R. Toussaint, K. J. Måløy, and E. G. Flekkøy. Pattern formation during air injection into granular materials confined in a circular hele-shaw cell. *Phys. Rev. **E**74, 011301*, 2006. doi:10.1103/PhysRevE.74.011301.

[25] Ø. Johnsen, R. Toussaint, K. J. Måløy, E. G. Flekkøy, and J. Schmittbuhl. Coupled air/granular flow in a linear hele-shaw cell. *Phys. Rev. **E**77, 011301*, 2008. doi:10.1103/PhysRevE.77.011301.

[26] Ø. Johnsen, C. Chevalier, A. Lindner, R. Toussaint, E. Clément, K. J. Måløy, E. G. Flekkøy, and J. Schmittbuhl. Decompaction and fluidization of a saturated and confined granular medium by injection of a vis-

cous liquid or gas. *Phys. Rev.* ***E****78, 051302*, 2008. doi:10.1103/PhysRevE.78.051302.

[27] F. K. Eriksen, R. Toussaint, A. L. Turquet, K. J. Måløy, and E. G. Flekkøy. Pressure evolution and deformation of confined granular media during pneumatic fracturing. *Phys. Rev. E, (In submission)*, 2017.

[28] X. Cheng, L. Xu, A. Patterson, H. M. Jaeger, and S. R. Nagel. Towards the zero-surface-tension limit in granular fingering instability. *Nat. Phys.* ***4****:234-7*, 2008. doi:10.1038/nphys834.

[29] P. G. Saffman and G. Taylor. The penetration of a fluid into a porous medium or hele-shaw cell containing a more viscous liquid. *Proc. R. Soc. Lond. A. Math. Phys. Sci. 245:312-29*, 1958. doi:10.1098/rspa.1958.0085.

[30] F. K. Eriksen, R. Toussaint, K. J. Måløy, and E. G. Flekkøy. Invasion patterns during two-phase flow in deformable porous media. *Front. Phys. 3:81*, 2015. doi:10.3389/fphy.2015.00081.

[31] B. Sandnes, E. G. Flekkøy, H. A. Knudsen, and K. J. Måløy. Patterns and flow in frictional fluid dynamics. *Nat. Commun.*, 2011. doi:10.1038/ncomms1289.

[32] R. Holtzman, M. L. Szulczewski, and R. Huanes. Capillary fracturing in granular media. *Phys. Rev. Lett. 108:264504*, 2012. doi:10.1103/PhysRevLett.108.264504.

[33] X. Z. Kong, W. Kinzelbach, and F. Stauffer. Morphodynamics during air injection into water-saturated movable spherical granulates. *Chem. Eng. Sci. 65:4652-60*, 2010. doi:10.1016/j.ces.2010.05.007.

[34] C. Chevalier, A. Lindner, M. Leroux, and E. Clément. Morphodynamics during air injection into a confined granular suspension. *J. Non-Newton Fluid Mech. 158:63-72*, 2008. doi:10.1016/j.jnnfm.2008.07.007.

[35] J. A. Eriksen, B. Marks, B. Sandnes, and R. Toussaint. Bubbles breaking the wall: two-dimensional stress and stability analysis. *Phys. Rev. E 91:052204*, 2015. doi:10.1103/PhysRevE.91.052204.

[36] J. A. Eriksen, R. Toussaint, K. J. Måløy, E. G. Flekkøy, and B. Sandnes. Numerical approach to frictional fingers. *Phys. Rev. E 92:032203*, 2015. doi:10.1103/PhysRevE.92.032203.

[37] B. Marks, B. Sandnes, G. Dumazer, J. A. Eriksen, and K. J. Måløy. Compaction of granular material inside confined geometries. *Front. Phys. 3:41*, 2015. doi:10.3389/fphy.2015.00041.

[38] J. A. Eriksen, R. Toussaint, K. J. Måløy, E. G. Flekkøy, and B. Sandnes. Pattern formation of frictional fingers in a gravitational potential. *arXiv:1605.07436v1 [physics.flu-dyn]*, 2016.

[39] M. Moura, E. A. Fiorentino, K. J. Måløy, G. Schäfer, and R. Toussaint. Impact of sample geometry on the measurement of pressure-saturation curves: Experiments and simulations. *Water Resour. Res. 51*, 2015. doi:10.1002/2015WR017196.

[40] D. Wilkinson and J. F. Willemsen. Invasion percolation: a new form of percolation theory. *J. Phys. A Math. Gen. 16:336576*, 1983.

[41] G. Løvoll, Y. Méheust, R. Toussaint, J. Schmittbuhl, and K. J. Måløy. Growth activity during fingering in a porous hele-shaw cell. *Phys. Rev. E 70:026301*, 2004. doi:10.1103/PhysRevE.70.026301.

[42] G. Løvoll, M. Jankov, K. J. Måløy, R. Toussaint, J. Schmittbuhl, G. Schäfer, and Y. Méheust. Influence of viscous fingering on dynamic saturationpressure curves in porous media. *Transp. Porous Med. 86: 305*, 2011. doi:10.1007/s11242-010-9622-8.

[43] K. T. Tallakstad, H. A. Knudsen, T. Ramstad, G. Løvoll, K. J. Måløy, R. Toussaint, and E. G. Flekkøy. Steady-state two-phase flow in porous media: Statistics and transport properties. *Phys. Rev. Lett. 102, 074502*, 2009. doi:10.1103/PhysRevLett.102.074502.

[44] H. Huang, F. Zhang, P. Callahan, and J. Ayoub. Granular fingering in fluid injection into dense granular media in a hele-shaw cell. *Phys. Rev. Lett. 108:258001*, 2012. doi:10.1103/PhysRevLett.108.258001.

[45] M. J. Niebling, R. Toussaint, E. G. Flekkøy, and K. J. Måløy. Dynamic aerofracture of dense granular packings. *Phys. Rev.* ***E****86, 061315*, 2012. doi:10.1103/PhysRevE.86.061315.

[46] M. J. Niebling, E. G. Flekkøy, K. J. Måløy, and R. Toussaint. Mixing of a granular layer falling through a fluid. *Phys. Rev.* ***E****82, 011301*, 2010. doi:10.1103/PhysRevE.82.011301.

[47] J. L. Vinningland, Ø. Johnsen, E. G. Flekkøy, R. Toussaint, and K. J. Måløy. Granular rayleigh-taylor instability: Experiments and simulations. *Phys. Rev. Lett.* ***99****, 048001*, 2007. doi:10.1103/PhysRevLett.99.048001.

[48] J. L. Vinningland, Ø. Johnsen, E. G. Flekkøy, R. Toussaint, and K. J. Mly, Måløy. Experiments and simulations of a gravitational granular flow instability. *Phys. Rev. E 76:051306*, 2007. doi:10.1103/PhysRevE.76.051306.

[49] J. L. Vinningland, Ø. Johnsen, E. G. Flekkøy, R. Toussaint, and K. J. Mly, Måløy. Size invariance of the granular rayleigh-taylor instability. *Phys. Rev. E 81:041308*, 2010. doi:10.1103/PhysRevE.81.041308.

[50] J. L. Vinningland, R. Toussaint, M. J. Niebling, E. G. Flekkøy, and K. J. Måløy. Family-vicsek scaling of detachment fronts in granular rayleigh-taylor instabilities during sedimentating granular/fluid flows. *Eur. Phys. J. Special Topics* ***204****, 27-40*, 2012. doi:10.1140/epjst/e2012-01550-2.

[51] C. Völtz, W. Pesch, and I. Rehberg. Rayleigh-taylor instability in a sedimenting suspension. *Phys. Rev.* ***E****65, 011404*, 2001. doi:10.1103/PhysRevE.65.011404.

[52] H. M. Jaeger, S. R. Nagel, and R. P. Behringer. Granular solids, liquids, and gases. *Rev. Mod. Phys., Vol. 68, No. 4*, 1996.

[53] M. J. Niebling, R. Toussaint, E. G. Flekkøy, and K. J. Måløy. Numerical studies of aerofractures in porous media. *Rev. Cub. Fis. 29, 1E66*, 2012.

[54] S. Turkaya, R. Toussaint, F. K. Eriksen, M. Zecevic, G. Daniel, E. G. Flekkøy, and K. J. Måløy. Bridging aerofracture evolution with the characteristics of the acoustic emissions in a porous medium. *Front. Phys. 3:70*, 2015. doi: 10.3389/fphy.2015.00070.

[55] J. Ugelstad, P. C. Mórk, K. H. Kaggerud, T. Ellingsen, and A. Berge. Swelling of oligomer-polymer particles. new methods of preparation. *Adv. Colloid Interface Sci. 13, 101*, 1980. doi:10.1016/0001-8686(80)87003-5. Produced under the trade name Dynospheres by Dyno Particles A.S., N-2001 Lillestrom, Norway.

[56] See Supplemental Material at [URL will be inserted by publisher] for the full-size figure of final structures for each category.

[57] See Supplemental Material at [URL will be inserted by publisher] for a video of a Cat. 3 channel ($P_{in} = 50$ kPa, video is 0.25 × realtime).

[58] See Supplemental Material at [URL will be inserted by publisher] for a video of a Cat. 4 channel ($P_{in} = 100$ kPa,

video is 0.25 × realtime).
[59] See Supplemental Material at [URL will be inserted by publisher] for a video of a Cat. 5 channel ($P_{in} = 150$ kPa, video is 0.25 × realtime).
[60] See Supplemental Material at [URL will be inserted by publisher] for a video of a Cat. 6 channel ($P_{in} = 250$ kPa, video is 0.05 × realtime).
[61] See Supplemental Material at [URL will be inserted by publisher] for the full-size version of figure 6, showing erosion and fingers merging in an experiment with $P_{in} = 200$ kPa.
[62] A. L. Barabási and H. E. Stanley. *Fractal Concepts in Surface Growth*. Cambridge: Cambridge University Press, 1995.
[63] J. Feder. *Fractals*. New York, NY: Plenum Press, 1988.
[64] R. Toussaint, G. Løvoll, Y. Méheust, K. J. Måløy, and J. Schmittbuhl. Influence of pore-scale disorder on viscous fingering during drainage. *Europhys Lett. 71:583*, 2005. doi:10.1209/epl/i2005-10136-9.
[65] B. B. Mandelbrot. *The fractal geometry of nature*. New York, NY: W. H. Freeman and company, 1982.
[66] K. J. Måløy, J. Feder, and T. Jøssang. Viscous fingering fractals in porous media. *Phys. Rev. L. 55:2688*, 1985.

Chapter 6

Pressure evolution and deformation of confined granular media during pneumatic fracturing

6.1 Motivation

This chapter continues with the study on flow during air injection into a confined granular medium, and now the focus turns to the evolution in the granular phase. As shown in the previous chapter, channels formed by the invading air show similar features as viscous fingers in a porous medium rather than in a Hele-Shaw cell containing just a viscous liquid. In search of explanations for these findings we were motivated to investigate the granular flow and evolution of the interstitial pressure. We wanted to evaluate how the interstitial pressure evolves during experiments, e.g. if it is far from or similar to the Laplace solution, and if there is any characteristic deformation and rheology outside the growing channels. To get answers, we obtain experimental granular displacement fields during the flow, and characterize the deformations surrounding the invading channels during different stages of the experiments. For the interstitial pressure we simulate the evolution of the pressure field numerically. Here, at each timestep, we calculate both the solution for a diffusing pressure and the Laplace solution. With the results, we check if, when and where the diffusing pressure reaches the steady-state Laplace solution. Finally, we discuss the granular rheology by correlating the diffusing pressure field with granular velocity maps from the experiments. The methods and main results in this study are presented before including a proposed scientific article, which contains more details of the work and discussion of results.

6.2 Methodology

6.2.1 Experimental setup

The experimental setup is the same as described in section 5.2.1, with a minor upgrade on the Hele-Shaw cell, i.e. the thickness of the glass plates is increased to 2.5 cm instead of 1 cm. This is done to minimize bending of the cell plates due

to the high overpressure, noting however that this did not have a significant effect on the invading air channels. The experimental frame-to-frame displacement fields are found with DIC as described in section 3.3.2, where we have used overlapping subwindows of ≈ 15 mm radius, with their centers separated by ≈ 2 mm on a square grid. The displacements are found on timesteps of 1 ms, which is between each frame of the experimental image sequences (captured at 1000 images/s).

6.2.2 Pressure simulation

For the pressure evolution in the granular medium, we solve the diffusion equation (6.1) for the pressure numerically. As mentioned in chapter 2, the air pressure evolves in the granular medium according to eq. (3.10), found from conservation of mass of the granular medium, conservation of mass for the air, and by assuming a local Darcy law [59, 77]. If the beads do not move significantly compared to the pressure diffusion, the evolution of the air pressure reduces to the diffusion equation

$$\frac{\partial P}{\partial t} = D\nabla^2 P = D\left(\frac{\partial^2 P}{\partial x^2} + \frac{\partial^2 P}{\partial y^2}\right), \tag{6.1}$$

with the diffusion constant $D = \kappa/(\beta_T \phi \mu)$, where κ is the permeability of the medium ϕ is the porosity, β_T and μ is the compressibility and viscosity of air respectively. By assuming an ideal gas, $\beta_T = 1/P_0$.

To do the simulation, we define a grid with $(I+2)\times(J+2)$ nodes having integer indices $i \in [0, I+1]$ and $j \in [0, J+1]$. By letting $\Delta x = \Delta y = 2$ mm, I and J are found from the length and width of the initial granular medium, respectively $I = 700$ mm$/\Delta x = 350$ and $J = 320$ mm$/\Delta y = 160$.

On this grid, a size-matched binary image (whose dimensions correspond to the initial granular medium) is placed such that all interior nodes with indices $i \in [1, I]$ and $j \in [1, J]$ represent points (x_i, y_j) inside the cell, where $x_i = (i - 1/2)\Delta x$ and $y_j = (j - 1/2)\Delta y$. The origin $(x = 0, y = 0)$ is at the lower left corner of the initial air-solid interface at the inlet side. By using these points, we make a discrete representation $P_{i,j} = P(x_i, y_j)$ of the pressure field.

The edge nodes, with indices $i = 0$, $j = 0$, $i = I + 1$ and/or $j = J + 1$, represent boundaries around the granular medium. Here, we set fixed boundary conditions, where the pressure at the inlet side is $P_{0,j} = P_{in}$, the pressure at the outlet side is $P_{I+1,j} = P_{out} = 0$, and the sealed sides are set to reflect the pressure just inside these boundaries; $P_{i,0} = P_{i,1}$ and $P_{i,J+1} = P_{i,J}$. In addition, the pressure inside the channel empty of beads (found from the binary frames) is held constant at the injection pressure P_{in}.

At all other positions, i.e. within the dry granular medium, the overpressure diffuses through the pore-space with a diffusion constant given by equation (3.12). However, due to compaction, the porosity and the diffusion constant evolve. The new porosity is estimated from the binary image at each timestep; by assuming a uniform solid fraction ρ_s in the medium and that the invading channel is completely empty of beads we get

$$\phi(t) = 1 - \rho_s(t) = 1 - \rho_{s,0}\frac{A_0}{A_0 - A_c(t)}, \tag{6.2}$$

where $\rho_{s,0} = 0.44$ is the initial solid fraction, A_0 is the initial area of the granular medium and $A_c(t)$ is the channel area as function of time. In our experiments, equation (6.2) gives porosities in the range $\phi \in [0.38, 0.56]$ (0.56 initially) with corresponding diffusion constants $D \in [7.4 \cdot 10^4, 3.2 \cdot 10^5]$ mm^2/s ($3.2 \cdot 10^5$ mm^2/s initially).

We solve the diffusion equation (6.1) for the pressure field numerically, during a given timestep with a given diffusion constant, by using the Crank-Nicholson scheme [84]. This is done by solving the set of linear equations for all interior points $i \in [1, I]$, $j \in [1, J]$:

$$\begin{aligned}(1+2\alpha)P_{i,j}^{n+1} - \frac{\alpha}{2}\left(P_{i-1,j}^{n+1} + P_{i+1,j}^{n+1} + P_{i,j-1}^{n+1} + P_{i,j+1}^{n+1}\right) \\ = (1-2\alpha)P_{i,j}^{n} + \frac{\alpha}{2}\left(P_{i-1,j}^{n} + P_{i+1,j}^{n} + P_{i,j-1}^{n} + P_{i,j+1}^{n}\right),\end{aligned} \tag{6.3}$$

where $\alpha = D\frac{\Delta t}{(\Delta x)^2} = 1/2$, giving $\Delta t \in [6.25 \cdot 10^{-6}, 2.70 \cdot 10^{-5}]$ s, and $n \geq 0$ is an integer time index such that $t(n) = n\Delta t$. With a nonzero granular velocity, the contribution of the second term on the right side of eq. (3.10) in eq. (6.3) would be

$$\begin{aligned}\beta_x(P_{i+1,j}^{n+1} - P_{i-1,j}^{n+1}) + \beta_y(P_{i,j+1}^{n+1} - P_{i,j-1}^{n+1}) \text{ on the left side, and} \\ -\beta_x(P_{i+1,j}^{n} - P_{i-1,j}^{n}) - \beta_y(P_{i,j+1}^{n} - P_{i,j-1}^{n}) \text{ on the right side,}\end{aligned} \tag{6.4}$$

where $\beta_x = \frac{\Delta t}{4\Delta x}(v_x)_{i,j}$ and $\beta_y = \frac{\Delta t}{4\Delta x}(v_y)_{i,j}$. A typical peak in granular velocity in our experiments is $|\vec{v}_g| = 1$ m/s, which together with the largest timestep $\Delta t = 2.70 \cdot 10^{-5}$ s gives $\beta_{x,max} = \beta_{y,max} = 3.4 \cdot 10^{-3} \ll \alpha/2$. Similarly, the contribution of the third term on the right side of eq. (3.10) in eq. (6.3) would be

$$\gamma P_{i,j}^{n+1} \text{ on the left side, and } -\gamma P_{i,j}^{n} \text{ on the right side,} \tag{6.5}$$

where $\gamma = \frac{\Delta t}{2\phi}(\dot{\varepsilon}_v)_{i,j}$, and $\dot{\varepsilon}_v = \nabla \cdot \vec{v}_g$. A typical peak in the volumetric strain rate in our experiments is $|\dot{\varepsilon}_v| = 2.5$ s^{-1}, which together with the largest timestep $\Delta t = 2.70 \cdot 10^{-5}$ s and lowest porosity $\phi = 0.38$ gives $|\gamma_{max}| = 8.9 \cdot 10^{-5}$, which is negligible. Thus, we approximate the evolution of the pressure field by solving equation (6.3), neglecting granular flow and compaction/dilation. To obtain the pressure diffusion during an experiment, we go through the sequence of binary images and let the pressure diffuse for 1 ms per frame (recalling that the framerate is 1000 images/s); when 1 ms is reached, the air cluster and related boundary condition is updated with the next image in the sequence, followed by another 1 ms of diffusion, and so on as a quasi-static evolution (The result of the previous step is used as initial pressure field for the following one).

In addition, for each frame we calculate the steady-state pressure field by solving the 2-D Laplace equation (3.9). After the pressure field reaches steady-state, it should follow the Laplace solution in circumstances where pressure diffusion is fast with respect to deformations at system scale. The Laplace equation is solved numerically by iteratively relaxing the pressure [84] at all interior points i, j:

$$P_{i,j}^{n} = \frac{P_{i-1,j}^{n-1} + P_{i+1,j}^{n-1} + P_{i,j-1}^{n-1} + P_{i,j+1}^{n-1}}{4}, \tag{6.6}$$

with the same grid and boundary conditions as above, until it converges at the criterion

$$RMSE = \sum_{i=1}^{I} \sum_{j=1}^{J} \frac{\sqrt{(P_{i,j}^{n} - P_{i,j}^{n-1})^2}}{I \cdot J} < P_{in} \cdot 10^{-8}. \tag{6.7}$$

Note that in equations (6.6) and (6.7), n is the iteration number and not a defined time index. With solutions from equations (6.3) and (6.6), we obtain the evolution of the pressure field over time, as well as steady-state solutions at each timestep.

6.3 Main results

Typically, the deformation process during the experiments can be separated into 3 stages; the initial mobilization of beads, the channel formation and compaction, and the compacted stick-slip stage. Depending on the injection pressure (e.g. for 250 and 50 kPa respectively), the first stage lasts during the initial 40 - 250 ms, the second stage in the following 250 - 1650 ms and the final stage lasts as long as particle rearrangement is possible, typically a few seconds (2 - 4). Because the system becomes jammed, little happens after 5 s.

The left plot in figure 6.1 shows typical profiles P_x of the simulated pressure field as function of depth into the granular medium, plotted at different times t after the start of injection. The figure shows profiles for both the steady-state Laplace solution and the diffusing pressure field at corresponding snapshots, where the profiles P_x are found as the average pressure across the width of the cell (perpendicular to the flow direction). Early in the experiment, just after opening the overpressure valve ($t = 1$ ms), the diffusing pressure field decays quickly as function of depth into the medium, with a range less than 10 cm, while the Laplace solution has a linear decrease of pressure from P_{in} to P_{out} across the cell length (70 cm). Thus, the two simulation methods give quite different solutions initially. Over time, both solutions of the pressure field evolve due to the opening of channels empty of beads, i.e. they move towards the cell outlet as the boundary conditions change. In addition, the profile of the diffusing pressure approaches the profile of the Laplace solution. Thus at later times, e.g. after around t = 0.8 to 1 second, the two methods give practically equal solutions for the pressure fields.

To compare the two pressure fields qualitatively, we look at the evolution of a characteristic depth s of the pressure field with time, where s is the depth from the initial air-solid interface where the pressure profile has decayed to $P_x(s) = P_{in} \cdot e^{-1}$. In the right plot in figure 6.1 the characteristic depth is plotted as function of time for both the Laplace solution and the diffusing pressure in 4 different cases $I - IV$. Case I is a reference where the granular medium is rigid with $D = 3.2 \cdot 10^5$ mm^2/s, solved analytically in 1-D with eq. (3.13). The cases II, III and IV are obtained from pressure profiles of 2-D simulations using experimental data including invasion channels as boundary conditions, with evolving diffusion constant due to porosity change. The injection pressure is $P_{in} = 100$, 150 and 200 kPa in case II, III and IV respectively. In addition, we plot the difference $s_L - s_D$ between

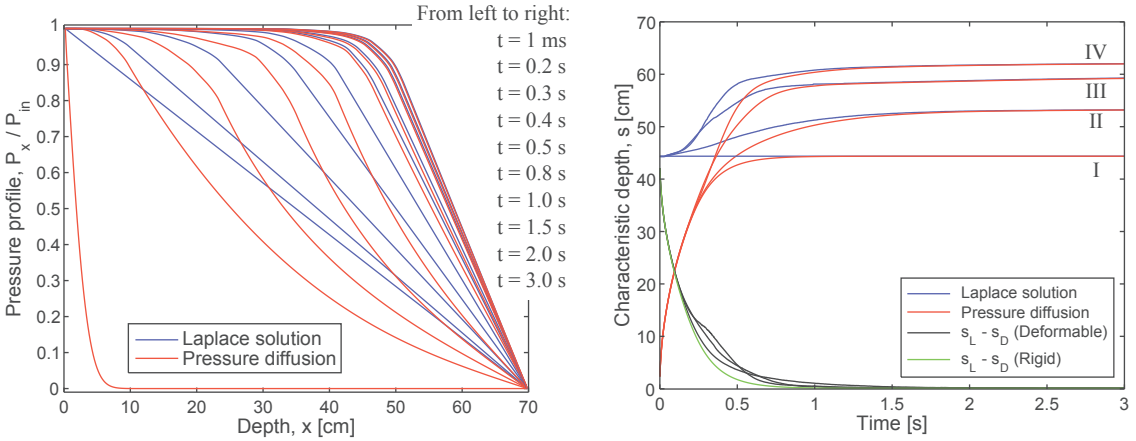

Figure 6.1: Left: Profiles of pressure fields for an experiment with $P_{in} = 200$ kPa, where the profiles show the average pressure across the cell width (perpendicular to the flow direction). The profiles are the Laplace solution (blue, solid line) and the diffusing pressure (red, dashed line). Curves from left to right for each method correspond to the times in the list. Right: Evolution of the characteristic depths s_L for the Laplace solution (blue, solid line) and s_D for the diffusing pressure (red, dashed line) as function of time for 4 different cases: I is a 1-D rigid medium reference solved analytically, II is an experiment with $P_{in} = 100$ kPa, III is an experiment with $P_{in} = 150$ kPa and IV is an experiment with $P_{in} = 200$ kPa. The difference $s_L - s_D$ for the experiments (black, dotted line) indicates that the pressures are relaxed at similar times, about 0.2 - 0.5 s after the 1-D rigid media reference indicated by the difference $s_L - s_D$ (green, dashed line).

the characteristic depth of the Laplace solution s_L and the characteristic depth of the diffusing pressure s_D. We see that for all experiments, the characteristic depth s_L for the steady-state moves towards the cell outlet due to the channels formed, further and faster with increasing overpressure. However, the difference $s_L - s_D$ decrease similarly with time for all experiments. As mentioned earlier, we also see here that the two simulation methods give practically equal solutions after around $t = 1$ s, which indicates that the diffusing pressure field is relaxed to steady-state on the order of a second, about 0.2 to 0.5 s after the 1-D rigid reference. Since the main evolution of channels and deformation usually occur within the first second of air injection, we use the diffusing pressure solution in the analysis. During channel growth (before the diffusing pressure reaches steady-state) the diffusing pressure is similar to the Laplace pressure in terms of the screening of pressure gradients behind the longest finger tips, as well as having the highest pressure gradients located on the tips of the longest fingers. In addition, during the fast channel expansion, the magnitude of pressure gradients in the diffusing pressure field seem to be up to 1.5 - 2 times higher than the Laplace solution in a region surrounding the most advanced finger tips (within 5 - 8 cm). When comparing the pressure magnitudes, the diffusing pressure behind the most advanced finger is typically ≥ 95 % of the Laplace solution, while in a region surrounding the longest finger (up to around 1.5 cm ahead) the diffusing pressure is typically ≥ 90 % of the Laplace solution.

The left part of figure 6.2 shows snapshots of the magnitude of granular velocity $|\vec{v}_g|$ during 10 ms time windows for an experiment with $P_{in} = 200$ kPa. The snapshots are centered on $t = 100$, 200, 300, 400, 500 and 600 ms, showing typical displacements during the initial mobilization and channeling stages.

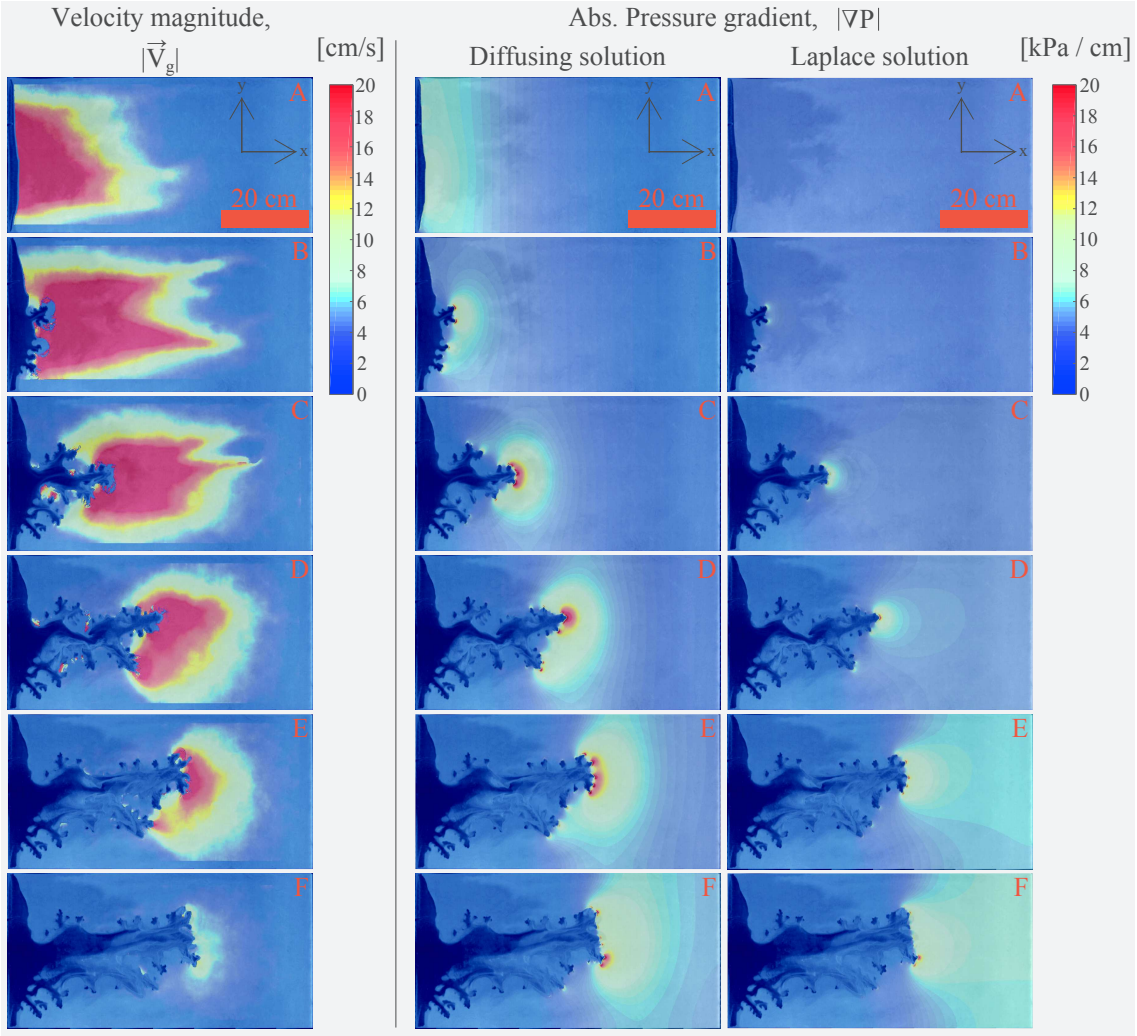

Figure 6.2: Left: Average velocity magnitude $|\vec{v}_g|$ during time windows of $\Delta t = 10$ ms, centered on $t = 100$, 200, 300, 400, 500 and 600 ms for snapshots A - F respectively. The injection pressure is $P_{in} = 200$ kPa. A zone of mobile beads builds up on the cell scale initially, and later focuses onto the most advanced fingers as the medium compacts. Beads behind the most advanced channel tips are not significantly displaced (Note that we have removed data at the channel, however noise from the erosion inside it appears in C - E). Right: The absolute pressure gradient $|\nabla P| = \sqrt{(\partial P/\partial x)^2 + (\partial P/\partial y)^2}$ for both solutions of the pressure at the snapshots A - F. The main difference between the diffusing and Laplacian pressure fields is that the diffusing one has higher pressure gradients close to the air-solid interface and finger tips, while it has lower pressure gradients near the outlet boundary. At snapshot F, the gradients start to look similar in magnitude around the channel. In both solutions, the pressure gradient is screened behind the longest fingers, and the highest magnitudes are on the longest finger tips.

The first snapshot, at $t = 100$ ms is in the later part of the initial mobilization stage. There is still no channel formed, just a slightly curved air-solid interface with a zone of mobilized beads in front of it, spanning about half of the cell. The displacement is mainly in the flow direction, and is higher along the center of the cell and closer to the air-solid interface. The rest of the snapshots, $t = 200 - 600$ ms, are taken during the instability and compaction stage. During this stage, fingers open up and form an invasion channel over time. The initially large and spread zone of mobilized beads ahead of the air-solid interface shrinks in size and magnitude over time, focusing onto the tips of the longest fingers. The displacements are largest close to and out from the longest fingers, while there is very little displacement behind the longest fingers.

The right part of figure 6.2 shows the absolute values of the pressure gradient $|\nabla P|$ for both the diffusing and Laplacian pressure fields, at the same snapshots as discussed above. Apart from diffusing or being at steady-state, both pressure fields have pressure gradients which are highest on the tips of longest fingers, and has a decreasing magnitude but more evenly distributed across the cell width with distance in front of the longest channel. The pressure gradients are screened behind the most advanced fingers. We see that the most displaced regions in the medium coincide well with the highest pressure gradients, while $|\nabla P|$ and $|\vec{v}_g|$ goes towards 0 behind the longest fingers. This becomes more evident at later stages when the displacements are more local, as higher pressure gradients are needed to deform the compacted medium further. In figure 6.2 B and C for the granular velocity, the mobilized zones have irregular shapes on the front with relatively large variations in velocity magnitude compared to the corresponding pressure gradients in these regions. This suggests that displacements in the compacted zone is not only subject to the local pore pressure gradient, but also to solid stresses, i.e. forces related to momentum transfer through bead contacts, as well as local variations in packing density.

However, the direction against the pressure gradient vectors $(-\nabla P)$ is found to correlate well with the direction of granular displacement vectors $\vec{u}_g$. We calculate the normalized correlation coefficient C_{dir} for the direction of two vectors $\vec{a}$ and $\vec{b}$ as

$$C_{dir} = \frac{\vec{a} \cdot \vec{b}}{|\vec{a}||\vec{b}|} = \cos\theta, \tag{6.8}$$

which is the normalized dot-product of the vectors. The value of $C_{dir} \in [-1, 1]$ gives the cosine of the angle θ between the vectors, where $C_{dir} = 1$ means that they are perfectly aligned, $C_{dir} = 0$ that they are perpendicular, and $C_{dir} = -1$ that they have opposite directions. For displacements above the noise threshold of 0.1 pixel size, we find that the correlation is near 1 at all locations and snapshots ($\Delta t = 1$ ms), suggesting that the beads more or less always move in the direction of $-\nabla P$.

The compacted zones are found from the total displacement fields as the zone where beads have been displaced more than one tenth of a pixel (70 µm), i.e. beads that have been displaced from the initial configuration. For all experiments, it seems to be a common initial behavior for the expansion of the compacted zone; After the start of air injection there is typically a delay of around 10 ms before any visible displacement occurs. Then, over the first 20 to 30 cm into the medium

the propagation is typically a bit faster, at a rate of 8 - 10 m/s, before crossing over to a slower growth rate typically between 1.5 to 3 m/s. After crossing over to a slower rate, the compacted zone in the 50 kPa experiment expand at a more or less constant rate fluctuating around 1.5 m/s until it reaches the outlet side. Similarly, the compacted zone in the 250 kPa experiment expands at a more or less constant rate, but at a higher rate around 3 m/s. In the 100, 150 and 200 kPa experiments, the compacted zones has an expansion rate similar to the 250 kPa experiment until reaching a depth of $x = 50$ - 60 cm into the medium, where they slow down to about 1.5 m/s, probably due to jamming and increased friction. The compacted zones expand in the direction from the inlet towards the outlet, and in all our experiments they reach the outlet boundary shortly after the start of injection, typically after $t = 170$ to 250 ms (380 ms for the 50 kPa experiment).

The strain rates in figure 6.3, again for the same snapshots A - F as in figure 6.2, shows that there is a compressive strain rate across the compacted zones (plots on the top), indicating that the beads are moving faster in the flow direction closer to the invading channel, while the shear rates in the same figure (plots on the bottom) indicate a shear flow with faster displacement in the flow direction along the fracture planes of the channels. Rate of compaction of the medium during experiments is quantified by evaluating the incremental volumetric strain, which is the sum of the normal strains $\varepsilon_v = \varepsilon_{xx} + \varepsilon_{yy}$ estimated with DIC (we assume a 2-D geometry such that $\varepsilon_{zz} = 0$ due to the rigid cell plates). The volumetric strain rate $\dot{\varepsilon}_v$ (or divergence of the granular velocity $\nabla \cdot \vec{v}_g$) is found by $\varepsilon_v / \Delta t$. Similarly, the shear rate $\dot{\gamma}_{xy}$ during the flow is found from incremental shear as $\gamma_{xy}/\Delta t$. Typically during channel growth, most of the compaction of the medium occurs in front of the channel. Before the compacted zone hits the outlet side (in snapshots A and B), the strain rate seems similar in the compacting areas, while in snapshots C and D it seems to be higher closer to the channel tip. As the channel growth stops during snapshots E and F, the compaction rate decrease. There are also some small zones of decompaction close to the air-solid interface associated with the opening of finger tips, where beads may be pushed away from each other. The shear flow coincides with the compacting zone, and suggest that the displacements are highest along the axis of the growing channels and decrease with perpendicular distance away, similar to laminar flow in a pipe where the displacement is highest along the center. This shows that the medium in front of the growing channel is sheared in addition to compacted. During the invasion, we observe that local deformations outside separate branches have the same behavior as the cell scale deformation around the main channel.

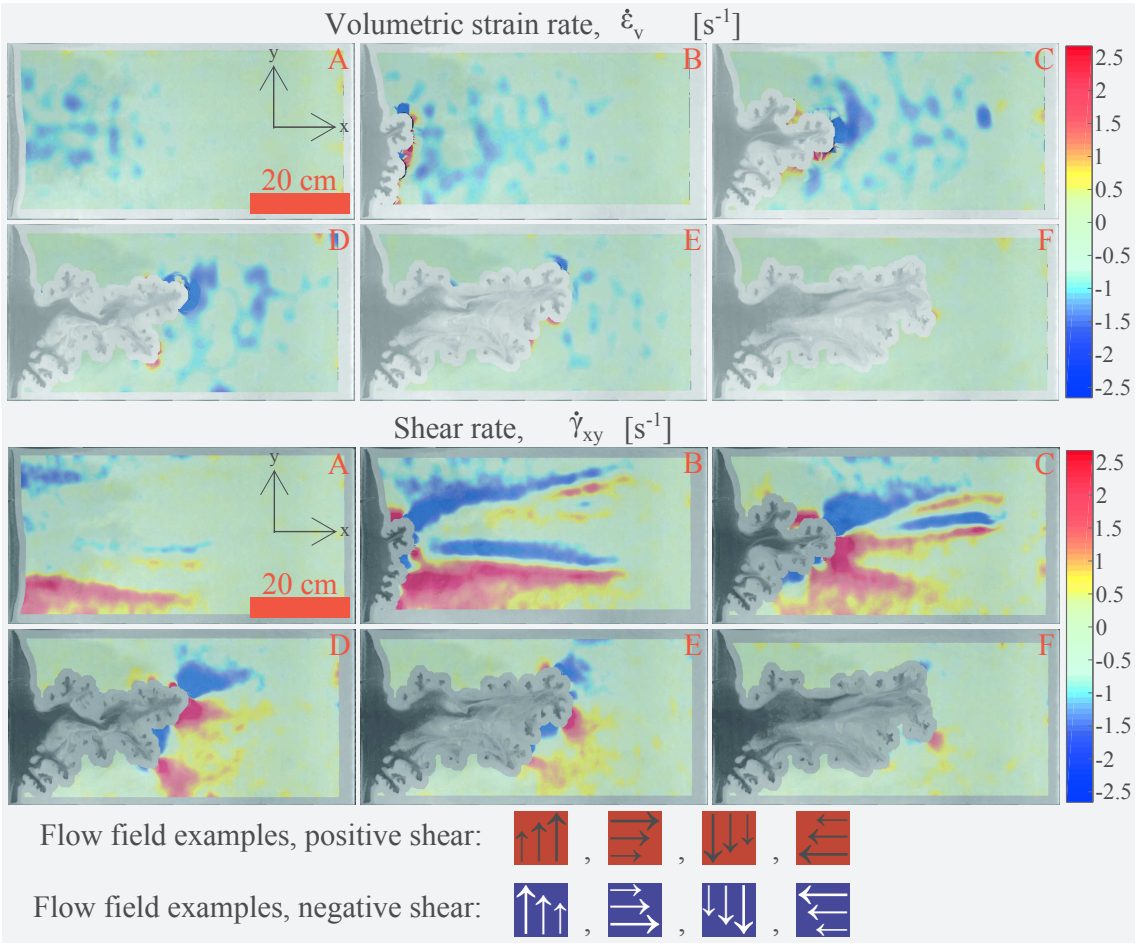

Figure 6.3: Top: Volumetric strain rate $\dot{\varepsilon}_v = \nabla \cdot \vec{v}_g$ in snapshots centered at $t = 100$, 200, 300, 400, 500 and 600 ms for snapshots A - F respectively, for an experiment with $P_{in} = 200$ kPa. Most of the compaction (negative $\dot{\varepsilon}_v$) occurs in front of the main channel, but some compaction at a lower rate happens on the sides of it. Bottom: Shear rate $\dot{\gamma}_{xy}$ during the snapshots A - F. The sheared regions coincide with the compacting regions, while there is little shear strain behind the longest fingers. We see lines out from the most advanced channel tips separating regions where the shear has opposite signs. These lines can be interpreted as follows; if the shear changes sign from positive to negative across a line (going in the positive y-direction), it means that the displacement is higher along the line than the surrounding medium. If the change is from negative to positive, the medium is displaced less along the line than the surrounding medium. The legend on the bottom relates flow behavior with the colors in the deformation map (the shear strain seen here is due to flow from left to right in front of the channel, or up/down on the sides of the main channel).

From average measurements in the zone ahead of the growing channel, we typically find that before the compaction front hits the outlet, the velocity in the growth direction v_x increases with time, also for an increasing range, and that the velocity has a roughly linear decreasing trend with distance ahead of the channel. This suggests that, on average, the compacting strain rate (divergence of v_x) is roughly constant with x in the bulk of the compaction zone. The profiles change character after the compaction front has hit the outlet; we now find the velocity in front of the fingers to decrease with time, and that the divergence of velocity is more like an exponential decay with distance ahead of the channel, suggesting that compactions are highest closer to the channel. In addition, we find that beads move away perpendicularly to the flow direction in front of the most advanced channel tip, with initial decompaction in the $y-$direction close to the tip, crossing over to compaction further away. The magnitude of v_y decreases with time as the medium compacts.

The final stage begins when the system is more or less jammed on cell scale. At this point, the fingers grow slowly and do not deform the medium on a global scale anymore. However, we observe random and sudden jumps of channel growth at the most advanced tips, probably due to particle rearrangements in the vicinity of the finger tips. A stick-slip event in these experiments usually lasts for 5 - 10 ms and the channel tips propagate 3 - 5 mm during this time. The typical steps of a stick-slip event are summarized as follows; Initially, there is very little displacement since we are in the compacted stage. Suddenly an area at a distance ahead of the channel compacts due to rearrangement of beads, causing an area closer to the channel tips to decompact. The decompacted area quickly re-compacts, and a decompaction-compaction wave moves from the initially rearranged area towards the channel. The fingers expand quickly when the decompaction-compaction front reaches them, and since the front moves towards the channel, the closest fingers expand before the ones further behind. After the stick-slip event has occurred, the system is back to a jammed state. In addition, similar to the fast channel growth, we find that the medium is slightly sheared just in front of the channel, and that the displacements are in the direction against the pressure gradient. The events are thought to be triggered due to the diffusing pressure, such that when the pressure gradient exceeds a threshold formed by solid stress, beads may rearrange.

The velocity magnitude in the region in front of the growing channel is found to have a scattered, but more or less linear relationship with the pressure gradient on average. The coefficient α from linear fits

$$|\vec{v}_g| = \alpha|\nabla P| + c \tag{6.9}$$

describing the average increase of velocity due to an increase of ∇P is plotted as function of time for the experiments with $P_{in} = 150$, 200 and 250 kPa in the left plot in figure 6.4. To collapse the data along the time axis, we use the normalized time $t' = t/t_c$ where t_c is the time when the compacted zone reach the outlet side for the respective experiments. We see for all experiments that for times before the compacted zone hits the outlet ($t' < 1$), α increases linearly with time. Then, after the compaction front has reached the outlet side ($t' > 1$), α seems to have an exponential decay with time. The inset in the left plot in figure 6.4 shows that there is a cutoff threshold ∇P_c such that $|\vec{v}_g| = 0$ if $\nabla P < \nabla P_c$. The cutoff threshold is

linked to equation (6.9) by writing $|\vec{v}_g| = \alpha(\nabla P - \nabla P_c)$, where $\nabla P_c = -c/\alpha$. The thresholds ∇P_c does not come from forces exerted by the air, but from solid friction along the plates, which depends on the normal solid stress and grain configurations, as well as the in-plane solid stress. Hence, it is essentially a manifestation of the solid stress between the grains, and grain/plates, which we do not model, but that we indirectly measure overall as ∇P_c. The forces displacing beads in the granular medium are related to the pore pressure gradient $-\nabla P$, as well as normal and shear solid stresses at contacts between beads and the cell plates. We do not resolve the solid stresses from the experiments, but if the main force felt by the medium is due to $-\nabla P$, it suggests a non-Newtonian rheology for the granular medium between the plates. Assuming a Bingham type rheology where

$$\vec{v}_g = -\frac{h^2}{\mu_B}(\nabla P - \nabla P_c), \tag{6.10}$$

and h is the cell gap, the granular paste has an effective viscosity $\mu_B \propto 1/\alpha$. Equation (6.10) is found by assuming a shear rate proportional to shear stress $\dot{\gamma} = (\sigma - \sigma_{yield})/\mu_B$, flow rate proportional to shear rate $|\vec{v}_g| \propto h\dot{\gamma}$ and shear stress proportional to the pressure gradient $\sigma \propto -h\nabla P$. If the main force felt by the medium is due to $-\nabla P$, our results suggest that $\mu_B \propto t^{-1}$ before the compacted zone reaches the outlet boundary, and an effective viscosity increasing as $\mu_B \propto e^{\beta t}$ after the compacted zone has reached the outlet boundary. Thus $|\vec{v}_g| \to 0$ for $t \gg t_c$, and similarly $|\vec{v}_g| = 0$ for small times $t \to 0$, i.e. the medium is solid-like at these times. The threshold ∇P_c evolves during experiments as shown in the right plot in figure 6.4 for the experiments with $P_{in} = 150$, 200 and 250 kPa. Again, the data has been collapsed along the time axis by the time the compacted zone reaches the outlet side. We see that the average thresholds ∇P_c decrease similarly before the compacted zone reaches the outlet boundary, decreasing from ∇P_c between 10 and 15 kPa/cm initially, down to a minimum around 1 - 2 kPa/cm at around the time the compacted zone reaches the outlet boundary. The decrease in ∇P_c with time seems to fluctuate around the fit

$$\nabla P_c = \frac{\nabla P_{c,min}}{\sqrt{t}}\sqrt{t_c} \tag{6.11}$$

as indicated in the plot for $t \leq t_c$. After the compacted zone has hit the outlet boundary, the thresholds begin to increase, faster with higher injection pressure. This probably depends on the injection pressure and the speed of the invading channel, i.e. the compaction rate and the forces available to compact the medium further. As the increase in ∇P_c slows down (at t/t_c around 2.5 - 3), the thresholds are approaching the pressure gradient in the zone surrounding the longest fingers. Thus, the medium is becoming solid-like and we cross over to the compacted regime. However, the pressure gradients are still 2 - 3 times higher than the thresholds just outside the tips of the most advanced channels, so they propagate slowly. In addition, during the fast channel growth, we can assume that ∇P_c is small compared to the pressure gradients on the most advanced finger tips, where e.g. ∇P can be around 40 to 60 kPa/cm for the 250 kPa experiment.

Thus, in the growing zone where the granular medium is displaced in front of the channel, we have that $v_g \propto (\nabla P - \nabla P_c)$ on average. This is a Laplacian growth

($v \propto \nabla P$) if ∇P_c is small, and if the Laplacian field and diffusing field are close to each other locally. It should result in a fractal dimension around 1.71 for the growing channel, similar to DLA clusters. However, as shown in chapter 5, we find fractal dimensions for the invasion patterns to be around 1.5 to 1.6, which is similar to viscous fingers in porous media [85]. It has been derived for viscous fingers in porous media that the growth should go like $v \propto (\nabla P - \nabla P_c)$, where the thresholds are capillary pressures at the fluid-fluid interface [2, 40]. With noise in the thresholds (as for disordered porous media) they found fractal dimensions of the patterns around 1.5 - 1.6, and that the growth is better described by the Dielectric Breakdown Model (DBM), where $v \propto (\nabla P)^\eta$ with $\eta = 2$, rather than DLA. Considering that we see a Bingham type rheology in our experiments, this could, with noise in the thresholds, be responsible for the channel growth being in another universality class than DLA and therefore would be better described by DBM with $\eta = 2$.

A more detailed presentation of the methods and results in this study is given in the related article over the following pages. The article is a proposed paper, planned to be submitted to Physical Review E in the near future.

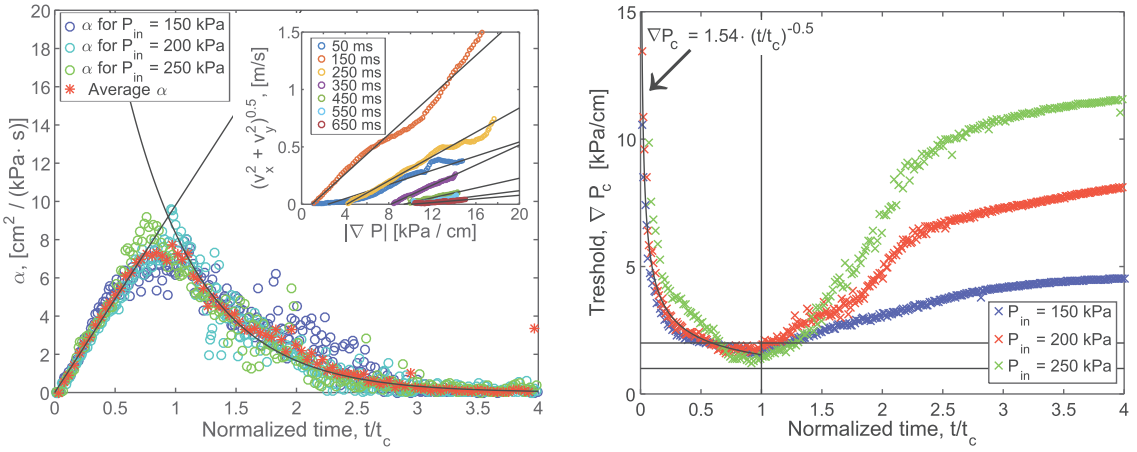

Figure 6.4: Left: Evolution of the linear fit parameter α with time, describing the average relationship $|\vec{v}_g| \approx \alpha \cdot |\nabla P| + c$ between the velocity magnitude $|\vec{v}_g|$ and the pressure gradient magnitude $|\nabla P|$. The plots of α are for the experiments with P_{in} = 150, 200 and 250 kPa, where the data is collapsed along the time axis by t_c, the time when the compacted zone reaches the outlet boundary. Before the compaction front reaches the outlet boundary ($t < t_c$), α increase linearly with time (linear fit = $9.8 \cdot (t/t_c)$), while for $t > t_c$, α has an exponential decay with time (exponential fit = $41.68 \cdot e^{-1.61(t/t_c)}$). In the inset: Examples of linear fits to the average velocity magnitude as function of pressure gradient. Note that over time there is an increasing offset from the ordinate axis, corresponding to the threshold $\nabla P_c = -c/\alpha$. For the experiments with P_{in} = 150, 200 and 250 kPa, the value of t_c is 240, 250 and 170 ms respectively. Right: Evolution of the thresholds ∇P_c as function of normalized time t/t_c for the experiments with P_{in} = 150, 200 and 250 kPa, where t_c = 240, 250 and 170 ms respectively. For $t/t_c \leq 1$, the thresholds decrease from 10 - 15 kPa/cm initially to between 1 and 2 kPa/cm (indicated by the horizontal lines) at $t/t_c = 1$. The power law fit (solid black curve) suggests that the decrease in ∇P_c is inversely proportional to the square root of time. After the compacted zone has reached the outlet boundary, for $t/t_c > 1$, ∇P_c begins to increase with time, faster for higher injection pressure. Then, at t/t_c around 2.5 - 3, the increase of the threshold with time slows down. At this point, ∇P_c is approaching the pressure gradient values $|\nabla P|$ in the zone surrounding the longest fingers.

PAPER 3

Pressure evolution and deformation of confined granular media during pneumatic fracturing

Fredrik K. Eriksen,* Renaud Toussaint, and Antoine Léo Turquet
Institut de Physique du Globe de Strasbourg,
Université de Strasbourg/EOST,
Centre National de la Recherche Scientifique, Strasbourg, France

Knut J. Måløy and Eirik G. Flekkøy
Department of Physics, University of Oslo, Oslo, Norway

(Dated: March 20, 2017)

By means of digital image correlation, we experimentally characterize the deformation of a dry granular medium confined inside a Hele-Shaw cell due to air injection at a constant overpressure high enough to deform it (from 50 to 250 kPa). Air injection at these overpressures leads to the formation of so called pneumatic fractures, i.e. channels empty of beads, and we discuss the typical deformations of the medium surrounding these structures. In addition we simulate the diffusion of the fluid overpressure into the medium, comparing it with the Laplacian solution over time, and relating pressure gradients with corresponding granular displacements. In the compacting medium we find that the diffusing pressure field becomes similar to the Laplace solution on the order of a second. However, before the diffusing pressure approaches the Laplacian solution, we find that it resembles the Laplacian field with the highest pressure gradients on the most advanced finger tips, and with the pressure gradient screened behind them. We show that the granular displacements more or less always move in the direction against the local pressure gradients, and when comparing granular velocities with pressure gradients in the zone ahead of channels, we observe a Bingham type of rheology for the granular paste (the mix of air and beads), with an effective viscosity μ_B and thresholds ∇P_c evolving during mobilization and compaction of the medium. Such a rheology, with noise in the thresholds could be responsible for placing the pattern growth in a universality class like viscous fingers in porous media, i.e. the Dielectric Breakdown Model with $\eta = 2$, where fractal dimensions are found between 1.5 and 1.6 for the patterns.

PACS numbers: 83.60.Wc, 81.05.Rm, 47.20.Ma

I. INTRODUCTION

Several processes in engineering, industry and earth sciences involve pneumatic (gas) or hydraulic (liquid) fracturing of the soil, which occurs when fluids in the ground are driven to high enough pressures to deform, fracture and generate porosity in the surrounding soil or rock. For example in environmental engineering, pneumatic or hydraulic fracturing is done to enhance the removal of hazardous contaminants in the vadose zone (soil remediation) [1, 2], for soil stabilization injection to ensure a solid foundation for structures [3], or in packer tests for project planning, risk assessment and safe construction of dams and tunnels [4]. In industry, hydraulic fracturing is done to enhance oil and gas recovery [5–7], CO_2 sequestration [8], water well- and geothermal energy production [9–11]. The evolution of faults and fractures at crustal scale can also be affected by fluid flow [12–14] as well as the rheology of fluid saturated faults [15–17]. Related natural processes such as subsurface sediment mobilization are studied in earth sciences, where seepage channels initiate due to erosion of granular soils by the fluid seeping through [18], leading later to channel and river network formations [19] - physicists are interested in the interplay between fluid flow evolution and erosion patterns [20]. Also, sand injectites, mud diapirs and mud volcanoes are formed due to pore-fluid overpressure [21–26]. For example, the Lusi mud volcano in Indonesia is the biggest and most damaging mud volcano in the world [27], having displaced 40 000 people from their homes, and has been active since May 2006. There is an ongoing debate about how it was triggered, i.e. whether it formed naturally by an earthquake or geothermal process [28–31], or that it is a man-made consequence of a nearby drilling operation by a company probing for natural gas [32].

Fluid injections into granular media has been extensively studied in laboratory experiments and simulations, where a common method to simplify the problem is to confine the experiment within a quasi-2-dimensional geometry, i.e. a Hele-Shaw cell. In [33, 34], the decompaction, fluidization regimes, and coupling between air and granular flow was studied in dry granular media in open circular and rectangular cells during air injection at different overpressures. Similar behavior was seen for the injection of liquid into a granular material initially

* Also at Department of Physics, University of Oslo, Oslo, Norway; Correspondence: eriksen@unistra.fr

saturated with the same liquid [35], so it is reasonable to assume that studies of pneumatic fracturing also has applications in hydraulic fracturing. The patterns formed during fluid injection into a granular medium, and evolution of the fluid-solid interface, have been found to resemble Diffusion Limited Aggregation patterns (DLA) and viscous fingering [36], a fingering instability that occurs when a less viscous liquid is injected into a porous medium containing a more viscous liquid with which it cannot mix [37]. As mentioned in [34], the main difference between the viscous- and granular fingering instabilities is the absence of interfacial tension in the granular case. For example, the stabilizing forces in viscous fingering are surface forces, while in granular fingering it is the build-up of friction between particles and against the confinement. However, both instabilities are driven by the pressure gradient across the defending medium, which is largest on the longest finger tips, making more advanced fingers grow on expense of the less advanced ones. A notable difference between air injection into a dry granular medium and a saturated one is that the overpressure initially diffuses into the packing in the dry (saturated with compressible air) case, while it is already a steady-state Laplace field over the defending liquid in the saturated case.

Further, during air injection into liquid saturated granular media and suspensions, the characteristics of emerging patterns and behavior of the media depend on injection rate, and the competition between mobilized friction and surface forces [38–51]. For example, one observes flow regimes such as two phase flow in rigid porous media [47–51], capillary fracturing, stick-slip bubbles and labyrinth patterns [38–46]. In the opposite case, during liquid injection into dry granular media [52], the flow behavior goes from stable invasion towards viscous fingering for increasing flow rate and viscosity of the invading fluid. At intermediate conditions, fractures open up inside the invaded region. The same trend is shown in numerical studies for gas injection into granular media containing the same gas [53].

Typically, in all processes involving fluid injection into granular media, there are flow regimes where the medium has either solid-like behavior or fluid-like behavior. This is one of the special properties of granular media, which also have gas-like behavior in some cases [54].

In this paper, we present an experimental study on deformations and evolution of pressure fields during air injection into confined granular media. More specifically, we inject air at constant overpressure into a dry granular medium inside a Hele-Shaw cell, where air escapes at the outlet while beads cannot. The motivation of this setup is to characterize the evolution of the interstitial pressure as well as deformations surrounding pneumatic fractures in compacting granular media, and the coupling between compaction and flow. As opposed to similar experiments with open outer boundary conditions [33–35], here, after the flow compacts the medium there is no decompaction. We thus observe the material behavior (at high enough overpressure to displace beads) to have a transition from fluid-like to solid-like during experiments, and that eventual invasion patterns will initially resemble viscous fingering in the fluid-like regime, crossing over to stick-slip fracture propagation as the medium becomes more solid-like, until it reaches a final structure as the compacted medium has reached a completely solid-like behavior. A similar, but smaller system has been studied in numerical simulations by Niebling et al. [53, 55]. By varying the interstitial fluid viscosity, two flow regimes were identified; one with finely dispersing bubbles and large scale collective motion of particles, the other one with build-up of a compaction front and fracturing. These flow regimes depend, respectively, on whether the particles are primarily accelerated by the imposed pressure gradient in the fluid, or interactions through particle contacts. This in turn depends on the diffusivity of the interstitial fluid pressure in the granular medium. Due to the confined nature of our experiment, it is thought to be a laboratory analog to pneumatic and hydraulic fracturing of tight rock reservoirs where the free boundary at the surface is very distant from the injection zone. In other words, in a situation where the fractures stop before reaching a free surface such that the surrounding medium is not decompacted. Therefore, new insight into this problem may have industrial applications in addition to increase the understanding of flow and transformations in porous media.

It is also worth to mention a closely related project [56], where acoustic emissions recorded during the experiments are analyzed. There, it is shown that different stages of the invasion process can be identified acoustically in terms of characteristic frequencies and distinct microseismic events. In this paper we characterize the deformations that are the source of these emissions.

II. METHODS

A. Experimental setup

The experimental setup is a linear Hele-Shaw cell, partially filled with Ugelstad spheres [57], i.e. dry, non-expanded polystyrene beads with a diameter of 80 µm ± 1 %. The cell is made out of two rectangular glass plates (80×40×2.5 cm in length, width and thickness respectively) clamped together on top of each other with an aluminum spacer controlled separation of 1 mm. A cell volume (76×32×0.1 cm) is formed between the plates by an impermeable sealing tape as shown in figure 1, with one of the short sides left open (outlet). Next, beads are filled into the cell by pouring them through the open side until the packing occupies about 90 % of the cell volume, followed by closing the open side with a semi-permeable filter (a 50 µm steel mesh) to keep beads inside the cell while allowing air to escape. The cell is then flipped vertically to place the granular medium against the semi-permeable outlet by using gravity, resulting in a volume

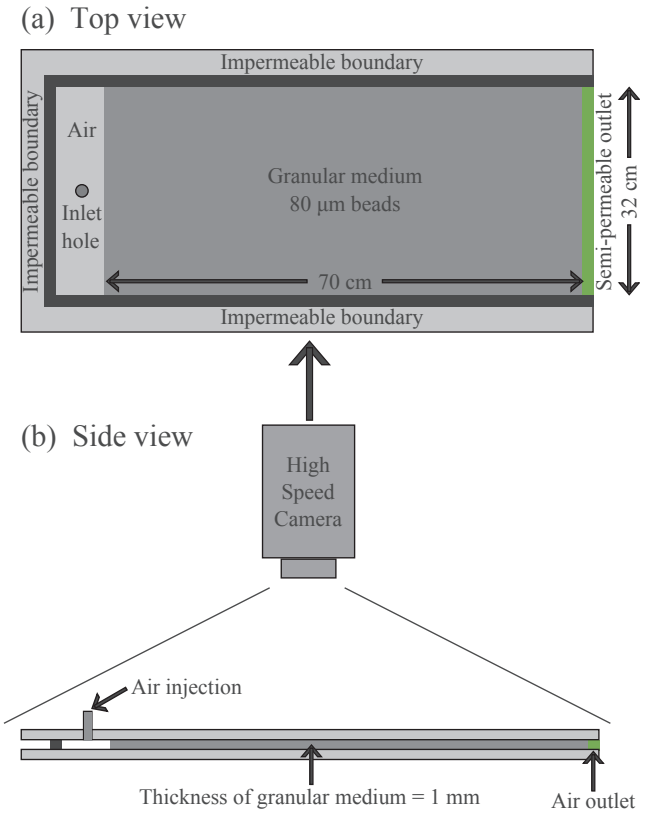

FIG. 1. Sketch of the experimental setup. (a) Top-down view of the prepared cell: The granular medium is confined inside the cell by three impermeable boundaries and an air-permeable boundary on the outlet side. The granular medium is placed against the outlet boundary such that it has a linear interface against a region empty of beads on the sealed inlet side, where pressurized air can be injected. (b) Side view of the setup showing the high speed camera placed above. The glass plates are clamped together with aluminum framing while the cell gap is controlled with 1 mm thick spacers, which are not shown here.

packing fraction of approximately $\rho_s = 0.44 \pm 0.04$, assumed to be more or less uniform across the medium. This leaves a volume empty of beads on the sealed side of the cell, opposite to the semi-permeable outlet, with a linear air-solid interface. An inlet hole on the sealed side of the cell is connected to a pressurized air tank which lets us inject air at a constant and maintained overpressure, $P_{in} = P_{abs,in} - P_0$ (absolute pressure - atmospheric pressure), ranging from 5 to 250 kPa. This will force air to move through the granular medium, towards the semi-permeable outlet, where $P_{abs,out} = P_0 = 100$ kPa, or in terms of overpressure above the atmospheric one, $P_{out} = 0$.

During experiments, the prepared cell is positioned horizontally. A selected overpressure is set at the pressure tank outlet and verified by a Honeywell pressure sensor with an accuracy of ±4 kPa. The tubing between the pressure tank and the cell inlet is equipped with an electronic valve such that the air injection is started with a digital trigger signal. Positioned above, with a top-down view of the cell, a Photron SA5 high speed camera is started with the same trigger signal, recording the air invasion at a framerate of 1000 images/s and a resolution of 1024×1024 pixels (1 pixel ≈ 0.7 mm in the cell). Light from a 400 W Dedolight studio lamp provides uniform and flicker-free illumination onto the white beads of the medium. A small fraction of the beads (< 10 %) are dyed black with ink to create tracer particles that are used for tracking frame-to-frame deformations in the granular medium. The experiments are run for 10 s, but typically the fracturing and/or compaction of the granular medium takes less than 5 s.

B. Image processing

In analysis of the images from the high speed camera, we investigate the deformation of the granular medium surrounding the channels formed. We perform image processing with Matlab to obtain quantitatively the information contained in the images.

The invading structure used as a boundary condition in the pressure simulations is segmented out by converting the grayscale raw data into binary images, where the pixels with value = 1 represent the channel and the pixels with value = 0 represent the granular medium. This is achieved by thresholding each frame in the image sequence with the initial image as reference, such that the pixels having a value less than 30% of the corresponding initial value are set to 1 (white) and the rest are set to 0 (black), as shown in figure 2 (c).

The frame-to-frame displacement fields are obtained with Ncorr, a Matlab based Digital Image Correlation (DIC) software [58, 59]. The basic principle of Ncorr is to cross-correlate subwindows of one image with an image taken at a later time to obtain displacement vectors $\vec{U}(x,y) = u(x,y)\vec{i} + v(x,y)\vec{j}$ located at (x,y) positions in the first image, indicating the displacement of the subwindows between the images. In steps, the principle of the Ncorr algorithm is as follows:

1. A subwindow at a selected position in the first image is cross-correlated with the succeeding image. This is done by multiplying the 2D Fourier transform of the subwindow with the 2D Fourier transform of the succeeding image, where the inverse Fourier transform of the result gives the convolution of the two images. The pixel with the highest value in the convolution yields the displacement with integer pixel accuracy, i.e. the initial guess.

2. To estimate the displacement with sub-pixel accuracy, a quintic B-spline interpolation of the graymap is calculated in the vicinity of the initial guess. This permits image correlation to be evaluated with sub-pixel displacements in this area.

3. In the interpolated area, the subwindow is iteratively translated and deformed in small steps to find a best match with the succeeding image. The location of the best match gives the displacement with sub-pixel accuracy.

4. The full image displacement field is found by the Reliability Guided DIC method; the remaining subwindows are analyzed in queue, one after the other, by using the obtained displacement of a nearest neighbor as initial guess. Thus, only steps 2 - 3 are repeated for the remaining subwindows. The queue of subwindows is updated at each iteration, such that the algorithm always analyzes the one with the best correlation at its initial guess.

Furthermore, Green-Lagrangian strains are calculated from spatial derivatives of the incremental displacement field as:

$$
\begin{aligned}
E_{xx} &= \frac{1}{2}\left(2\frac{\partial u}{\partial x} + \left(\frac{\partial u}{\partial x}\right)^2 + \left(\frac{\partial v}{\partial x}\right)^2\right) \\
E_{yy} &= \frac{1}{2}\left(2\frac{\partial v}{\partial y} + \left(\frac{\partial u}{\partial y}\right)^2 + \left(\frac{\partial v}{\partial y}\right)^2\right) \\
E_{xy} &= \frac{1}{2}\left(\frac{\partial u}{\partial y} + \frac{\partial v}{\partial x} + \frac{\partial u}{\partial x}\frac{\partial u}{\partial y} + \frac{\partial v}{\partial x}\frac{\partial v}{\partial y}\right),
\end{aligned}
\tag{1}
$$

which for small deformations are similar to small strains: $E_{xx} = \varepsilon_{xx} = \partial u/\partial x$, $E_{yy} = \varepsilon_{yy} = \partial v/\partial y$, and $E_{xy} = \gamma_{xy} = 0.5 \cdot (\partial u/\partial y + \partial v/\partial x)$, i.e. when the quadratic terms can be neglected. Ncorr also includes an algorithm for obtaining the total Lagrangian displacement from the incremental displacement fields. See the article by the developers of Ncorr [58], or the web page [59], for an in-depth explanation of the software.

In our analysis, we use subwindows with 20 pixels radius ($\approx$ 14 mm), with their centers separated by a distance of 3 pixels ($\approx$ 2 mm) on a square grid. We use a timestep of 1 ms between successive images, thus obtaining incremental displacements on the smallest timestep possible with our setup. We use the total Lagrangian displacements to identify the compacted zone as a region where the total displacement is above a threshold of one tenth of the pixel size. Examples of a compacted zone and displacement field are shown in figure 2 (d) and (e).

C. Numerical simulations

We use numerical simulations to estimate the evolution of local overpressure values $P(x, y) = P_{abs}(x, y) - P_0$ in the granular medium during experiments. To do this we define a grid with $(I + 2) \times (J + 2)$ nodes having integer indices $i \in [0, I + 1]$ and $j \in [0, J + 1]$. By adopting lattice grid step size $\Delta x = \Delta y = 2$ mm, I and J are determined from the length and width of the initial

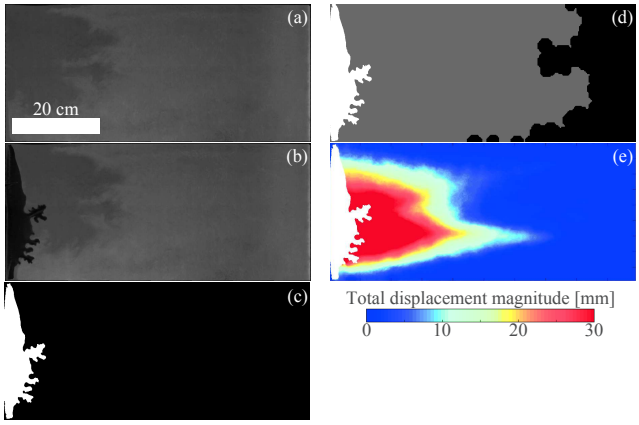

FIG. 2. Image processing examples for a snapshot in an experiment with injection pressure $P_{in} = 200$ kPa. (a) Shows the grayscale snapshot of the initial granular medium ($t = 0$), (b) is a grayscale snapshot of the deformed granular medium at the beginning of channel formation ($t = 200$ ms), where a region is emptied of beads (black), (c) shows the corresponding binary image where the emptied structure is shown in white, (d) indicates the compacted zone in gray, and (e) is the total magnitude of bead displacement as found with DIC.

granular medium, respectively $I = 700$ mm$/\Delta x = 350$ and $J = 320$ mm$/\Delta y = 160$.

On this grid, a size-matched binary image (whose dimensions correspond to the initial granular medium) is placed such that all interior nodes with indices $i \in [1, I]$ and $j \in [1, J]$ represent points (x_i, y_j) inside the cell, where $x_i = (i - 1/2)\Delta x$ and $y_j = (j - 1/2)\Delta y$. The origin $(x = 0, y = 0)$ is at the lower left corner of the initial air-solid interface at the inlet side. By using these points, we make a discrete representation $P_{i,j} = P(x_i, y_j)$ of the pressure field.

The edge nodes, with indices $i = 0$, $j = 0$, $i = I + 1$ and/or $j = J + 1$, represent boundaries around the granular medium. Here, we set fixed boundary conditions, where the pressure at the inlet side is $P_{0,j} = P_{in}$, the pressure at the outlet side is $P_{I+1,j} = P_{out} = 0$, and the sealed sides are set to reflect the pressure just inside these boundaries; $P_{i,0} = P_{i,1}$ and $P_{i,J+1} = P_{i,J}$. In addition, the pressure inside the channel empty of beads (found from the binary frames) is held constant at the injection pressure P_{in}.

At all other positions, i.e. within the dry granular medium, the overpressure diffuses through the pore-space with a diffusion constant given by

$$
D = \frac{\kappa P_0}{\phi\mu} = \frac{d^2\phi^2 P_0}{180(1-\phi)^2\mu},
\tag{2}
$$

assuming the Carman-Kozeny expression is valid for the permeability κ [53, 56]. In equation (2), $d = 80$ µm is the bead diameter, $\mu = 1.81 \cdot 10^{-5}$ Pa·s is the viscosity of air, and $P_0 = 100$ kPa. Due to deformation, the porosity

ϕ is estimated from the binary image at each timestep; by approximating the solid fraction ρ_s as uniform in the medium for the estimation of the permeability, and assuming that the invading channel is completely empty of beads we get

$$\phi(t) = 1 - \rho_s(t) = 1 - \rho_{s,0}\frac{A_0}{A_0 - A_c(t)}, \tag{3}$$

where $\rho_{s,0} = 0.44$ is the initial solid fraction, A_0 is the initial area of the granular medium and $A_c(t)$ is the channel area as function of time. In our experiments, equation (3) gives porosities in the range $\phi \in [0.38, 0.56]$ (0.56 initially) with corresponding diffusion constants $D \in [7.4 \cdot 10^4, 3.2 \cdot 10^5]$ mm^2/s ($3.2 \cdot 10^5$ mm^2/s initially). The evolution of air pressure P in the granular medium is given by the equation [53, 60]

$$\frac{\partial P}{\partial t} = D\nabla^2 P - \vec{v}_g \cdot \nabla P - \frac{P}{\phi}\nabla \cdot \vec{v}_g, \tag{4}$$

where $\vec{v}_g = v_x\vec{i} + v_y\vec{j}$ is the granular velocity. By neglecting the source terms corresponding to the internal deformations (this is discussed in the appendix paragraph), i.e. $\vec{v}_g = \vec{0}$, we solve the diffusion equation for the pressure field

$$\frac{\partial P}{\partial t} = D\left(\frac{\partial^2 P}{\partial x^2} + \frac{\partial^2 P}{\partial y^2}\right) \tag{5}$$

numerically during a given timestep with a given diffusion constant by using the Crank-Nicholson scheme [61]. This is done by solving the set of linear equations for all interior points $i \in [1, I]$, $j \in [1, J]$:

$$\begin{aligned} &(1+2\alpha)P_{i,j}^{n+1} \\ &- \frac{\alpha}{2}\left(P_{i-1,j}^{n+1} + P_{i+1,j}^{n+1} + P_{i,j-1}^{n+1} + P_{i,j+1}^{n+1}\right) \\ &= (1-2\alpha)P_{i,j}^{n} \\ &+ \frac{\alpha}{2}\left(P_{i-1,j}^{n} + P_{i+1,j}^{n} + P_{i,j-1}^{n} + P_{i,j+1}^{n}\right), \end{aligned} \tag{6}$$

where $\alpha = D\frac{\Delta t}{(\Delta x)^2} = 1/2$, giving $\Delta t \in [6.25 \cdot 10^{-6}, 2.70 \cdot 10^{-5}]$ s, and $n \geq 0$ is an integer time index such that $t(n) = n\Delta t$. To obtain the pressure diffusion during an experiment, we go through the sequence of binary images and let the pressure diffuse for 1 ms per frame (recalling that the framerate is 1000 images/s); when 1 ms is reached, the air cluster and related boundary condition is updated with the next image in the sequence, followed by another 1 ms of diffusion, and so on as a quasi-static evolution (The result of the previous step is used as initial pressure field for the following one).

In addition, for each frame we calculate the steady-state pressure field by solving the 2-D Laplace equation

$$\frac{\partial^2 P}{\partial x^2} + \frac{\partial^2 P}{\partial y^2} = 0. \tag{7}$$

This is done by iteratively relaxing the pressure [61] at all interior points i, j:

$$P_{i,j}^{n} = \frac{P_{i-1,j}^{n-1} + P_{i+1,j}^{n-1} + P_{i,j-1}^{n-1} + P_{i,j+1}^{n-1}}{4}, \tag{8}$$

with the same grid and boundary conditions as above, until it converges at the criterion

$$RMSE = \sum_{i=1}^{I}\sum_{j=1}^{J}\frac{\sqrt{(P_{i,j}^{n} - P_{i,j}^{n-1})^2}}{I \cdot J} < P_{in} \cdot 10^{-8}. \tag{9}$$

Note that in equations (8) and (9), n is the iteration number and not a defined time index.

With solutions from equations (6) and (8), we obtain the evolution of the pressure field over time, as well as steady-state solutions (solutions of the Laplace equation) at each timestep. The diffusion equation is more accurate to represent the physical pore pressure field in the experiments than the Laplace one initially, but the idea is to compute the Laplace solution to compare if, when and where, and with what accuracy the growth can be compared to a Laplacian growth process.

III. RESULTS

As expected, we find the granular medium to exhibit either a solid-like or fluid-like behavior. In the fluid-like regime we observe significant deformation, where beads are displaced by amounts of multiple bead sizes, and that the granular medium has a behavior much like a viscous liquid being invaded by air. For example, the air opens up channels in the medium, and we observe a granular Saffman-Taylor like instability [37]. However, due to the boundary conditions we always end up with a solid-like medium at the end of an experiment, where there is no apparent deformation or bead displacements, and the air is reaching the cell outlet by seeping through the pore-space. Typically, the deformation process during the experiments can be separated into 3 stages; the initial mobilization of beads without significant channel formation, the channel formation and compaction, and the compacted stick-slip stage. Depending on the injection pressure (e.g. for 250 and 50 kPa respectively), the first stage lasts during the initial 40 - 250 ms, the second stage in the following 250 - 1650 ms and the final stage lasts as long as particle rearrangement is possible, typically a few seconds (2 - 4). Because the system becomes jammed, little happens after 5 s.

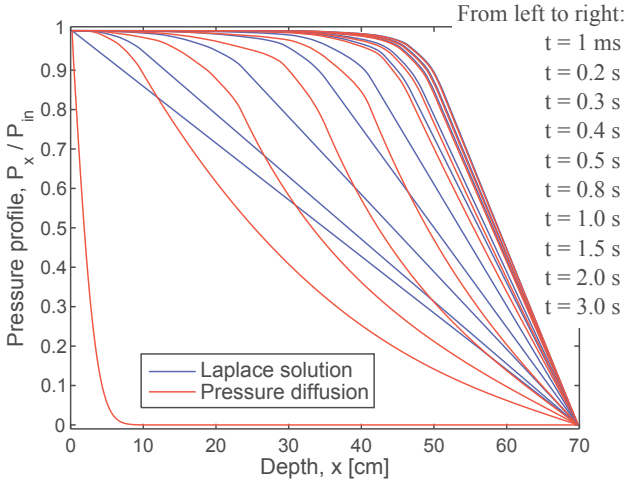

FIG. 3. Profiles of pressure fields for an experiment with $P_{in} = 200$ kPa, where the profiles show the average pressure across the cell width (perpendicular to the flow direction). The profiles are the Laplace solution (blue, solid line) and the diffusing pressure (red, dashed line), curves from left to right for each method correspond to the times in the list.

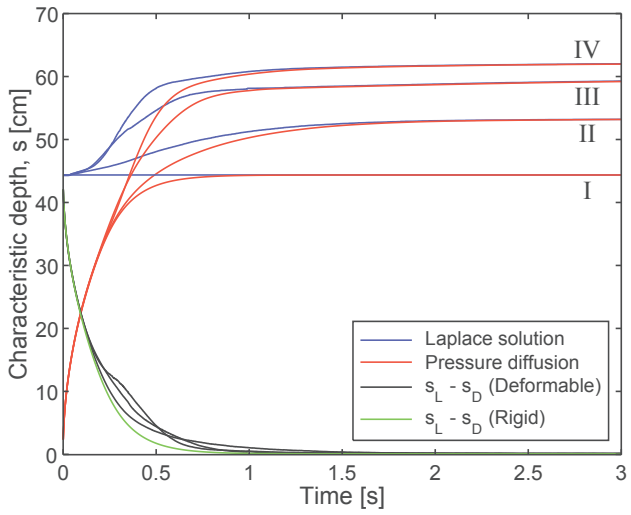

FIG. 4. Evolution of the characteristic depths s_L for the Laplace solution (blue, solid line) and s_D for the diffusing pressure (red, dashed line) as function of time for 4 different cases: I is a 1-D rigid medium reference solved analytically, II is an experiment with $P_{in} = 100$ kPa, III is an experiment with $P_{in} = 150$ kPa and IV is an experiment with $P_{in} = 200$ kPa. The difference $s_L - s_D$ for the experiments (black, dotted line) all seem to follow the difference $s_L - s_D$ for the 1-D rigid media reference (green, dashed line).

A. Pressure evolution

Figure 3 shows typical profiles P_x of the simulated pressure field as function of depth into the granular medium, plotted at different times t after the start of injection. The figure shows profiles for both the steady-state Laplace solution and the diffusing pressure field at corresponding snapshots, where the profiles P_x are found as the average pressure across the width of the cell (perpendicular to the flow direction). Early in the experiment, just after opening the overpressure valve ($t = 1$ ms), the diffusing pressure field decays quickly as function of depth into the medium, with a range less than 10 cm, while the Laplace solution has a linear decrease of pressure from P_{in} to P_{out} across the cell length (70 cm). Thus, the two simulation methods give quite different solutions initially. Over time, both solutions of the pressure field evolve due to the opening of channels empty of beads, i.e. they move towards the cell outlet as the boundary conditions change. In addition, the profile of the diffusing pressure approaches the profile of the Laplace solution. Thus at later times, e.g. after around t = 0.8 to 1 second, the two methods give practically equal solutions for the pressure fields.

To compare the two pressure fields qualitatively, we look at the evolution of a characteristic depth s of the pressure field with time, where s is the depth into the medium where the pressure profile has decayed to $P_x(s) = P_{in} \cdot e^{-1}$. In figure 4 the characteristic depth is plotted as function of time for both the Laplace solution and the diffusing pressure in 4 different cases $I - IV$. Case I is a reference where the granular medium is rigid with $D = 3.2 \cdot 10^5$ mm^2/s, solved analytically in 1-D. The cases II, III and IV are obtained from pressure profiles of 2-D simulations using experimental data including invasion channels as boundary conditions, with evolving diffusion constant due to porosity change. The analytical solution for the 1-D diffusing pressure is

$$P(x,t) = P_{in}\left(1 - \frac{x}{L}\right) - \sum_{n=1}^{\infty} \frac{2P_{in}}{\pi n} \sin\left(\frac{n\pi x}{L}\right) e^{-\frac{n^2\pi^2}{L^2}Dt}, \quad (10)$$

where $L = 70$ cm is the system length. We see in eq. (10) that for increasing time t, the diffusing pressure goes towards the steady-state Laplace solution $P(x) = P_{in}\left(1 - \frac{x}{L}\right)$. The injection pressure is $P_{in} = 100$, 150 and 200 kPa in case II, III and IV respectively. In addition, in figure 4 we plot the difference $s_L - s_D$ between the characteristic depth of the Laplace solution s_L and the characteristic depth of the diffusing pressure s_D. We see that for all experiments, the characteristic depth s_L for the steady-state moves towards the cell outlet due to the channels formed, further and faster with increasing overpressure. However, the difference $s_L - s_D$ decrease similarly with time for all experiments. As mentioned earlier, we also see here that the two simulation methods give practically equal solutions after around $t = 1$ s, which indicates that the diffusing pressure field is relaxed to steady-state on the order of a second, about 0.2 to 0.5 s after the 1-D rigid reference. Since the main evolution of

channels and deformation usually occur within the first second of air injection, we use the diffusing pressure solution for the discussions in this article. However, before the diffusing pressure reaches steady-state, the pressure behind the most advanced channel tip is similar to the Laplace solution such that the pressure gradient is more or less screened here, suggesting that Laplacian growth dynamics of the channel could be a fair assumption.

B. Initial mobilization and channel formation stages

The left part of figure 5 shows snapshots of the magnitude of granular velocity $|\vec{v}_g|$ during 10 ms time windows for an experiment with $P_{in} = 200$ kPa. The snapshots are centered on $t = 100$, 200, 300, 400, 500 and 600 ms, showing typical displacements during the initial mobilization and channeling stages. The first snapshot, at $t = 100$ ms is in the later part of the initial mobilization stage. There is still no channels formed, just a slightly curved air-solid interface with a zone of mobilized beads in front of it, spanning about half of the cell. The displacement is mainly in the flow direction, and is higher along the center of the cell and closer to the air-solid interface. The rest of the snapshots, $t = 200 - 600$ ms, are taken during the instability and compaction stage. During this stage, fingers open up and form an invasion channel over time. The initially large and spread zone of mobilized beads ahead of the air-solid interface shrinks in size and magnitude over time, focusing onto the tips of the longest fingers. The displacements are largest close to and out from the longest fingers, while there is very little displacement behind the longest fingers.

The right part of figure 5 shows the absolute values of the pressure gradient $|\nabla P|$ for both the diffusing and Laplacian pressure fields, at the same snapshots as discussed above. Apart from diffusing or being at steady-state, both pressure fields have pressure gradients which are highest on the tips of longest fingers, and has a decreasing magnitude but more evenly distributed across the cell width with distance in front of the longest channel. The pressure gradients are screened behind the most advanced fingers. We see that the most displaced regions in the medium coincide well with the highest pressure gradients, while ∇P and $|\vec{v}_g|$ goes towards 0 behind the longest fingers. This becomes more evident at later stages when the displacements are more local, as higher pressure gradients are needed to deform the compacted medium further. In figure 5 (b) and (c) for the granular velocity, the mobilized zones have irregular shapes on the front with relatively large variations in displacement magnitude compared to the corresponding pressure gradients in these regions. This suggests that the displacements in the compacted zone is not only subject to the local pore pressure gradient, but also to solid stresses, i.e. forces related to momentum transfer through bead contacts, as well as local variations in packing density. In [62], numerical simulations include solid stresses and air vibrations to evaluate the total stress state inside the cell.

To investigate directional correlation between the driving force ($-\nabla P$) and the bead displacements ($\vec{u}_g$), we calculate the normalized correlation coefficient for the directions of the vectors. The normalized correlation coefficient C_{dir} for the direction of two vectors $\vec{a}$ and $\vec{b}$ is obtained by

$$C_{dir} = \frac{\vec{a} \cdot \vec{b}}{|\vec{a}||\vec{b}|} = \cos\theta, \tag{11}$$

which is the normalized dot-product of the vectors. The value of $C_{dir} \in [-1, 1]$ gives the cosine of the angle θ between the vectors, where $C_{dir} = 1$ means that they are perfectly aligned, $C_{dir} = 0$ that they are perpendicular, and $C_{dir} = -1$ that they have opposite directions. In figure 6 (a)-(d) we have used equation (11) to correlate the directions of $-\nabla P$ and $\vec{u}_g$ at each grid point where $|\vec{u}_g| >$ 70 µm (one tenth of a pixel size) on intervals of 1 ms at different stages during the deformation. We see that the correlation is near 1 at all locations and snapshots, suggesting that the beads more or less always move in the direction of $-\nabla P$. To show this fact for all experiments, the bottom part of figure 6 includes a plot of the average C_{dir} (taken over the zones where $|\vec{u}_g|$ is larger than one tenth of the pixel size) as function of time calculated for intervals where the channel length grows by 2.5 % increments of the final channel length.

Figure 7 shows the evolution of the compacted zones with time for experiments with different P_{in}. The compacted zones are obtained by thresholding the total displacement fields (from DIC) with a displacement threshold of 70 µm, i.e. one tenth of a pixel size. The result gives a binary image with white pixels where beads have been significantly displaced from the initial configuration and black pixels otherwise. Then, to reduce noise from the displacement data, the binary images are morphologically closed to connect nearby clusters of white pixels. Here, morphological closing is done as follows: first, all pixels within a distance corresponding to 1 cm from any white pixel is made white (dilation). Next, in the dilated image, all pixels within a distance of 1 cm from any black pixel is made black (erosion). After morphological closing, we keep only the largest cluster of white pixels and consider this as the compacted zone. The top plot shows the depth x into the medium of the most advanced part of the compacted zones as function of time. For all experiments, it seems to be a common initial behavior for the expansion of the compacted zone: After the start of air injection there is typically a delay of around 10 ms before any visible displacement occurs. Then, over the first 20 to 30 cm into the medium the propagation is typically a bit faster, at a rate of 8 - 10 m/s, before crossing over to a slower growth rate typically between 1.5 to 3 m/s. After crossing over to a slower rate, the compacted zone in the 50 kPa experiment expand at a more or less constant rate fluctuating around 1.5 m/s

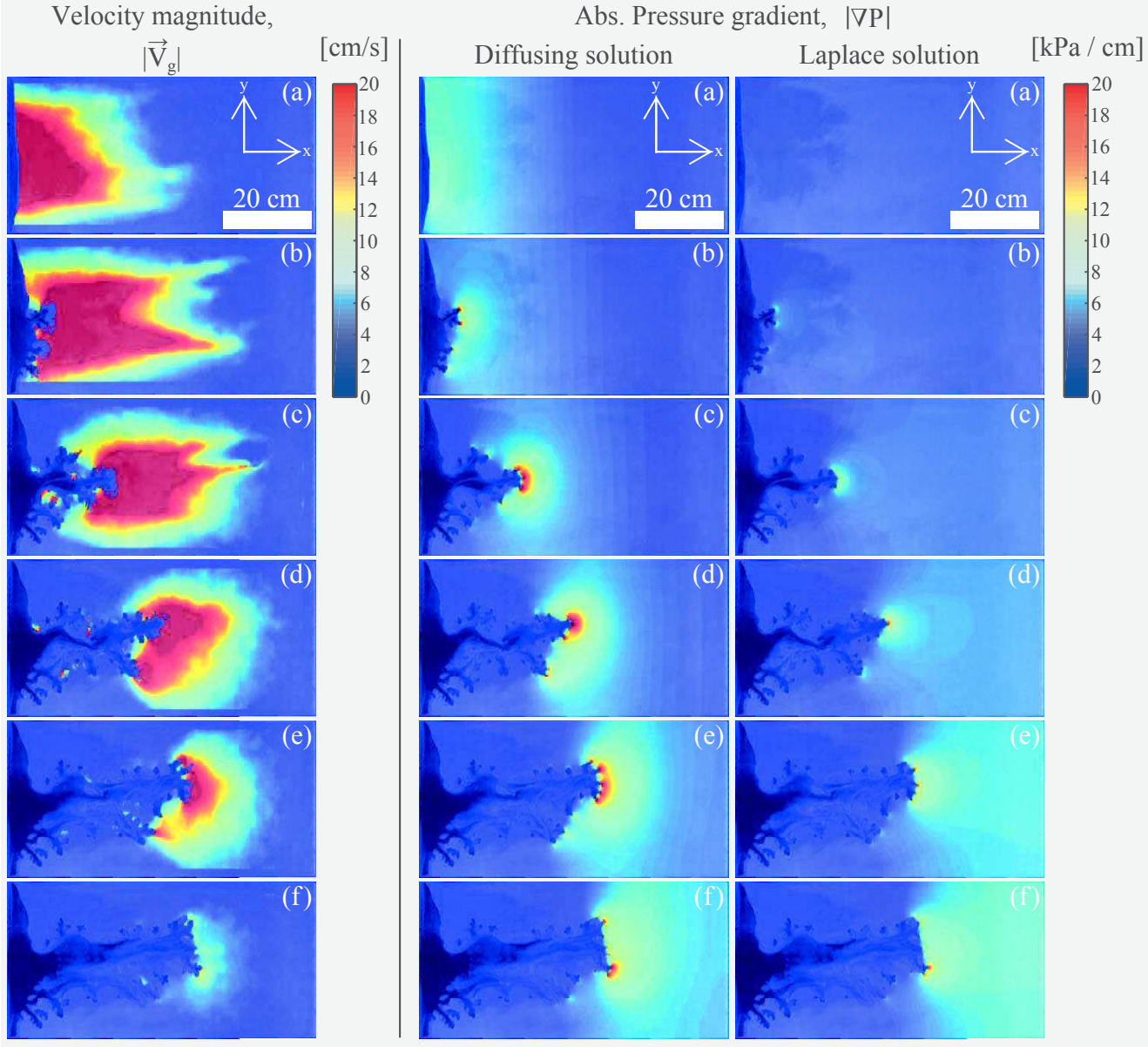

FIG. 5. Left: Average velocity magnitude $|\vec{v}_g|$ during time windows of $\Delta t = 10$ ms, centered on $t = 100$, 200, 300, 400, 500 and 600 ms for snapshots (a) - (f) respectively. The injection pressure is $P_{in} = 200$ kPa. A zone of mobile beads builds up on the cell scale initially, and later focuses onto the most advanced fingers as the medium compacts. Beads behind the most advanced channel tips are not significantly displaced (Note that we have removed data at the channel, however noise from the erosion inside it appears in (c) - (e)). Right: The absolute pressure gradient $|\nabla P| = \sqrt{(\partial P/\partial x)^2 + (\partial P/\partial y)^2}$ for both solutions of the pressure at the snapshots (a) - (f). The main difference between the diffusing and Laplacian pressure fields is that the diffusing one has higher pressure gradients close to the air-solid interface and finger tips, while it has lower pressure gradients near the outlet boundary. At snapshot (f), the gradients start to look similar in magnitude around the channel. In both solutions, the pressure gradient is screened behind the longest fingers, and the highest magnitudes are on the longest finger tips.

until it reaches the outlet side. Similarly, the compacted zone in the 250 kPa experiment expands at a more or less constant rate, but at a higher rate around 3 m/s. In the 100, 150 and 200 kPa experiments, the compacted zones has an expansion rate similar to the 250 kPa experiment until they reach a depth of $x = 50$ - 60 cm into the medium, where they slow down to about 1.5 m/s, probably due to jamming and increased friction. The bottom part of figure 7 shows a visual representation of the compacted zones over time. The front of the compacted zones seems to be fairly stable, preserving more or less its initial translational symmetry and an approxi-

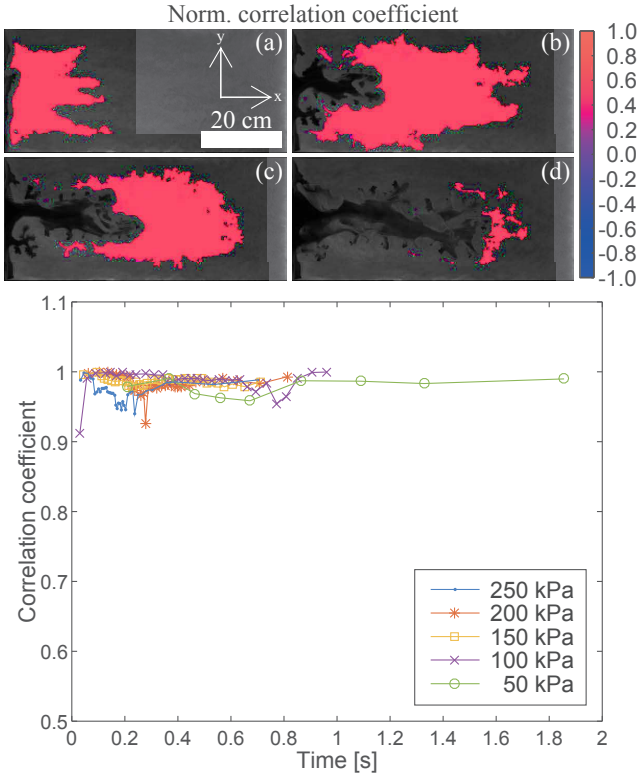

FIG. 6. Top: Normalized correlation between the vector fields of the negative pressure gradient $-\nabla P$ and granular displacements $\vec{u}_g$ for snapshots separated by 1 ms at different stages of the deformation during an experiment with $P_{in} = 250$ kPa; (a) is during the initial mobilization, (b) is during the instability stage just after the compaction front has reached the outer boundary, (c) is during the instability stage with a more compacted medium, and (d) is in the compacted stage. The correlation coefficient is the cosine of the angle between vectors, and is close to 1 in all snapshots, meaning that the beads are generally displaced in the direction against the pressure gradient, i.e. in the direction of the driving force. Displacement magnitudes less than one tenth of a pixel size ($\approx$ 70 µm) are considered noise and not included (gray). Bottom: The average correlation coefficient in areas with displacement magnitude above the noise level is plotted as function of time for the experiments analyzed, showing that the normalized correlation coefficient between $-\nabla P$ and $\vec{u}_g$ is close to 1 over time in all cases.

mately linear shape, for the lower injection pressures (50 - 150 kPa), while initially for 200 and 250 kPa the fronts are more rough. This initial roughness could be due to granular stress reaching further than the influence of the pore pressure gradient, since the pore pressure gradient diffuses and promotes a stable front (see interpretation in [53]). At longer times, the presence of the straight outer boundary increases granular friction, and could influence the diffusing field, which leads again to a straighter front.

The rate of compaction of the medium during experiments is quantified by evaluating the incremental volumetric strain, which is the sum of the incremental normal

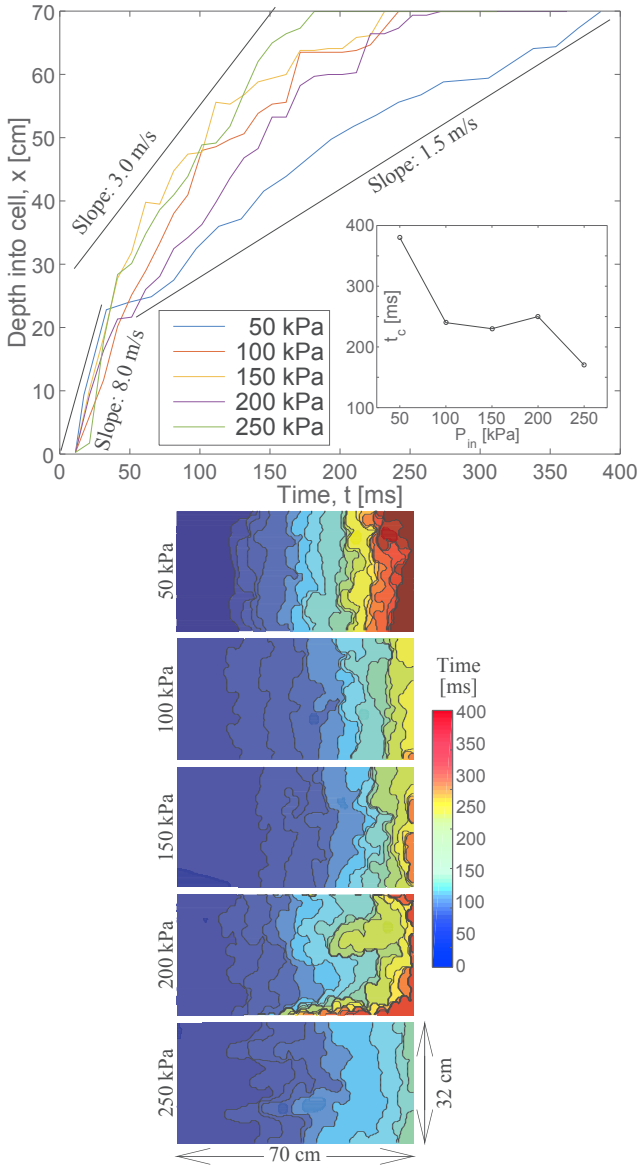

FIG. 7. Top: Depth of the compacted zones into the medium plotted as function of time for experiments with different injection pressure. The inserted slopes (dashed lines) indicate velocities for reference. Typically, the compacted zone reaches the outer boundary between $t = 150$ and 250 ms after the start of injection, however for the lowest pressure it takes around 380 ms. The propagation of the compacted front has a common behavior for all experiments initially. First there is a 10 ms delay after the start of injection until any visible deformation is observed, then the expansion is typically faster ($\approx$ 8 m/s) over the first 20 to 30 cm before crossing over to a slower growth rate. The compacted zone in the 50 kPa experiment expand at a rate averaging around 1.5 m/s, while in the 250 kPa experiment the rate fluctuates around 3 m/s. In the 100, 150 and 200 kPa experiments the compacted zones expand at a rate similar to the 250 kPa experiment until a depth of $x = 50$ to 60 cm, where they slow down, probably due to jamming of the system, but continue to propagate at an average rate around 1.5 m/s as the pressure gradients increase. Inset: Time t_c when the front hits the outlet as function of P_{in}. Bottom: Visual representation of the evolution of the compaction zones where the color code represents the time of the snapshot.

strains $\varepsilon_v = \varepsilon_{xx} + \varepsilon_{yy}$ estimated with DIC (we assume a 2-D geometry such that $\varepsilon_{zz} = 0$ due to the rigid cell plates). The volumetric strain rate $\dot{\varepsilon}_v$ (or divergence of the granular velocity $\nabla \cdot \vec{v}_g$) is found from incremental volumetric strain as $\varepsilon_v/\Delta t$. Snapshots of the volumetric strain rates in the medium are shown on the top in figure 8, again for the same snapshots (a) - (f) as in figure 5. The compacting zone (negative $\dot{\varepsilon}_v$), expands in the flow direction from the cell inlet towards the outlet side. Typically during channel growth, most of the compaction of the medium occurs in front of the channel. Before the compacted zone hits the outlet side (in (a) and (b)), the strain rate seems similar in the compacting areas, while in (c) and (d) it seems to be higher closer to the channel tip. As the channel growth stops during (e) and (f), the compaction rate decreases. There is also some small zones of decompaction close to the air-solid interface associated with the opening of finger tips, where beads may be pushed away from each other.

The bottom of figure 8 shows snapshots of the shear rate $\dot{\gamma}_{xy}$ during the flow, found from incremental shear as $\gamma_{xy}/\Delta t$. The snapshots suggest that the displacements are highest in front of the growing channels and decrease with perpendicular distance away, similar to laminar flow in a pipe where the displacement is highest along the center. This shows that the beads in front of the growing channel are sheared in addition to compacted. During the invasion, we observe that local deformations outside separate branches have the same behavior as the cell scale deformation around the main channel.

C. Compacted stick-slip stage (source shape for acoustic emissions)

The final stage begins when the system is more or less jammed at the cell scale. At this point, the fingers grow slowly and do not deform the medium on a global scale anymore. However, we also observe random and sudden jumps of channel growth, probably due to particle rearrangements in the vicinity of the finger tips. Figure 9 shows a more detailed analysis of the deformations during a stick-slip event in the compacted stage, where 6 successive snapshots of 1 ms intervals display the volumetric strain, displacement magnitude, shear strain, and the correlation between the directions of displacement and opposite pressure gradient during each snapshot. A stick-slip event in this system usually lasts for 5 - 10 ms and the channel tips can propagate up to 3 - 5 mm during this time. The typical steps of a stick-slip event are summarized in the figure: Initially, there is very little displacement since we are in the compacted stage. Suddenly an area ahead of the channel compacts due to rearrangement of beads, causing an area just in front of the channel tips to decompact. The decompacted area re-compacts as a decompaction-compaction front moves from the initially rearranged area towards the channel. The channel tips expand quickly when the decompaction-compaction front reaches them, and since the front moves towards the channel, the channel tip closest to the rearranged beads expands before the ones further behind. After the stick-slip event has occurred, the system is back to a jammed state. In addition, we see that the medium is slightly sheared just in front of the channel, and that the displacements are in the direction against the pressure gradient also during stick-slip. This type of event generates intermittent acoustic emissions, as reported in [56]. This spatio-temporal source shape is characteristic of a seismic pulse [63]. Acoustic localization of such events is discussed in [64].

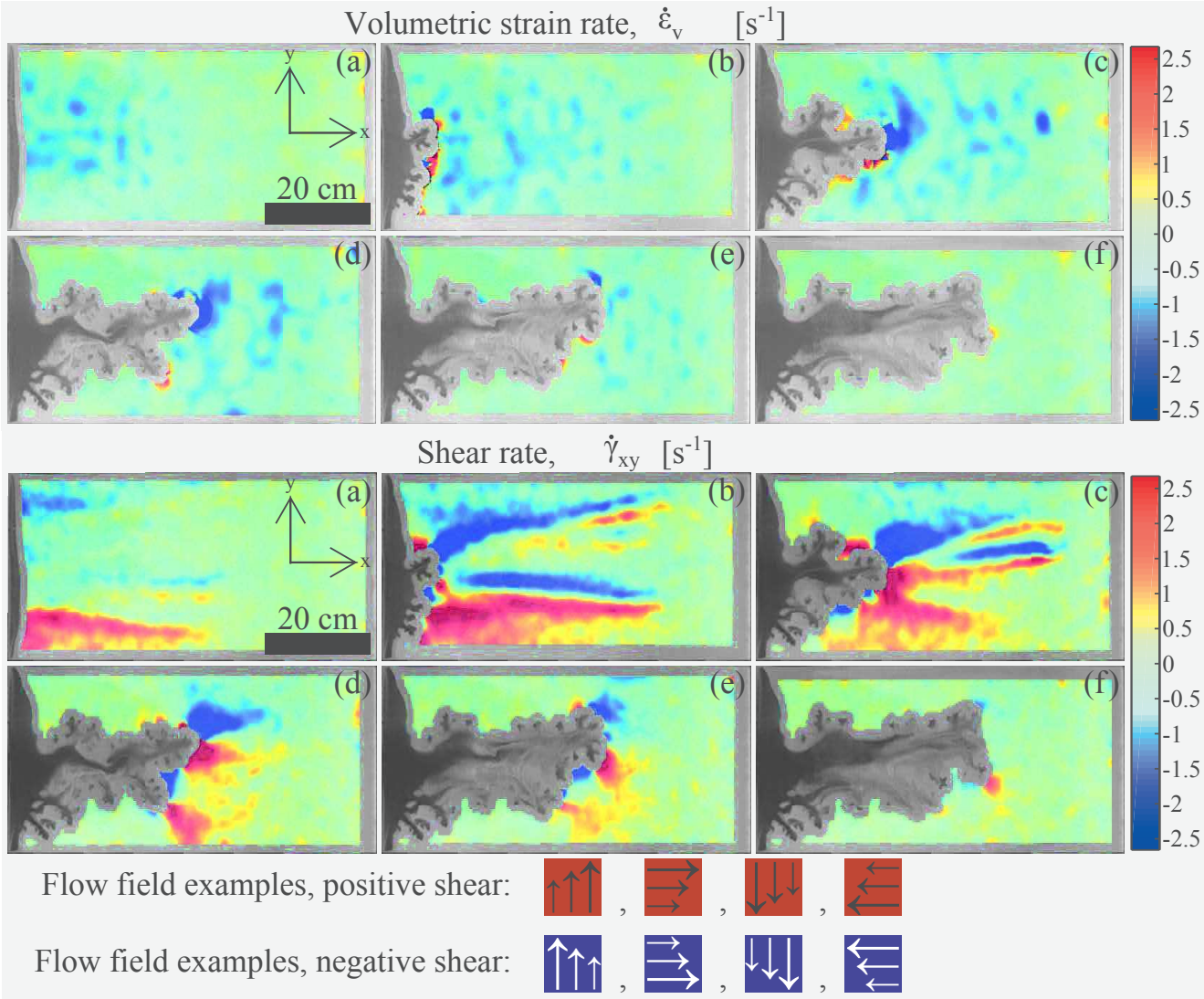

FIG. 8. Top: Volumetric strain rate $\dot{\varepsilon}_v = \nabla \cdot \vec{v}_g$ in snapshots centered at $t = 100$, 200, 300, 400, 500 and 600 ms for snapshots (a) - (f) respectively, for an experiment with $P_{in} = 200$ kPa. Most of the compaction (negative $\dot{\varepsilon}_v$) occurs in front of the main channel, but some compaction at a lower rate happens on the sides of it. Bottom: Shear rate $\dot{\gamma}_{xy}$ during the snapshots (a) - (f). The sheared regions coincide with the compacting regions, while there is little shear strain behind the longest fingers. We see lines out from the most advanced channel tips separating regions where the shear has opposite signs. These lines can be interpreted as follows; if the shear changes sign from positive to negative across a line (going in the positive y-direction), it means that the displacement is higher along the line than the surrounding medium. If the change is from negative to positive, the medium is displaced less along the line than the surrounding medium. The legend on the bottom relates flow behavior with the colors in the deformation map (the shear strain seen here is due to flow from left to right in front of the channel, or up/down on the sides of the main channel).

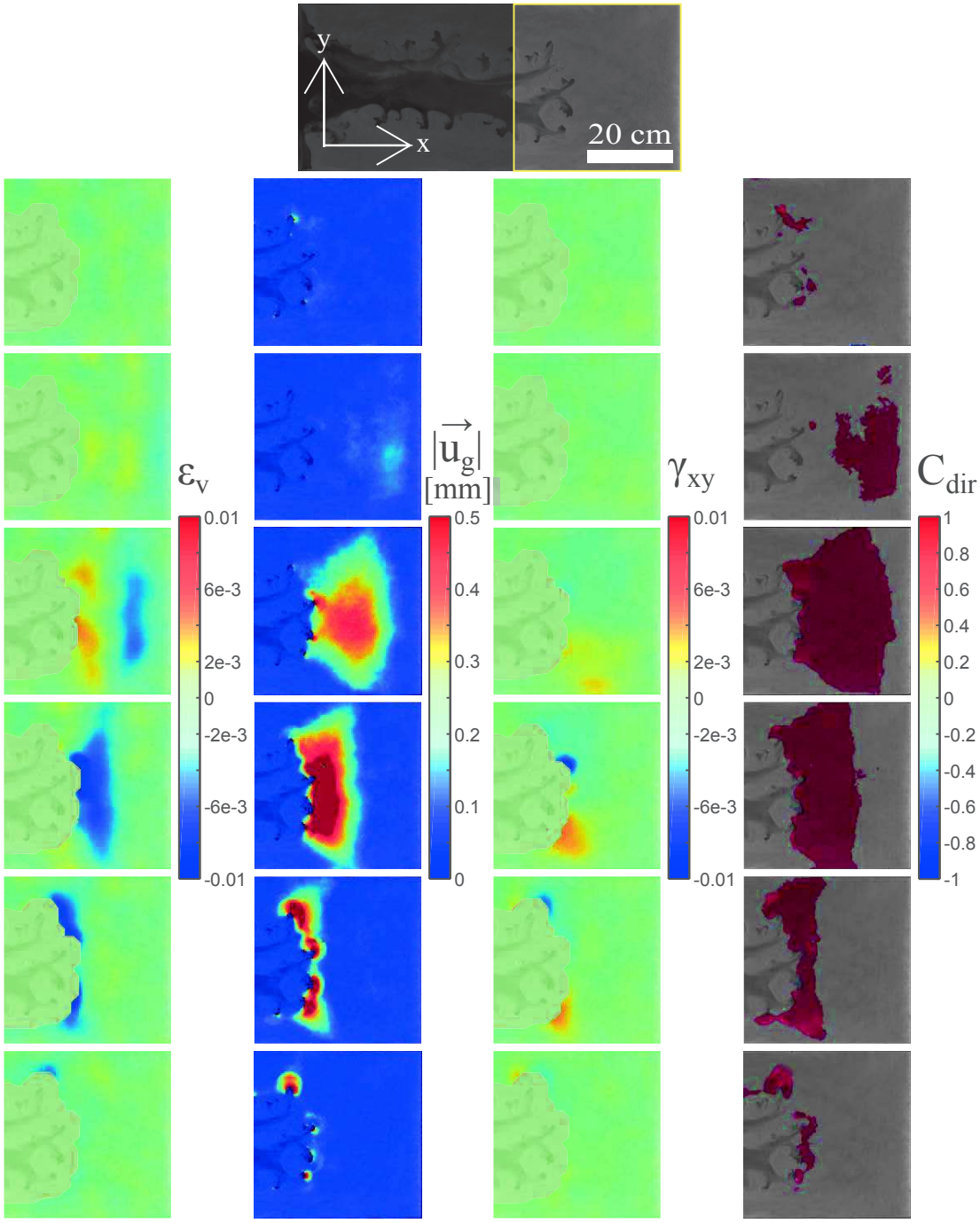

FIG. 9. Deformations during a stick-slip event in an experiment with $P_{in} = 250$ kPa. The snapshots show deformations in a zoomed in region on successive 1 ms intervals, where the time increases from top to bottom. The columns from left to right show: volumetric strain ε_v, displacement magnitude $|\vec{u}_g|$, shear strain γ_{xy}, and C_{dir}, the normalized correlation coefficient between displacements and negative pressure gradient $\vec{u}_g$ and $-\nabla P$. The thumbnail on the top indicates the location of the zoomed in region. A stick-slip event typically lasts between 5 to 10 ms, and the finger tips may expand up to 3 - 5 mm. The deformations shown in the snapshots are typical: Initially there is little deformation (compacted stage) until beads in a region in front of the channel rearrange and compact. Consequently, beads in a zone adjacent to the finger tips de-compact and the fingers propagate as this zone re-compacts, i.e. a de-compaction/compaction front moves from the initially rearranged zone towards the channel and the fingers expand as the front reaches them, such that the closest fingers expand first. The displacements are in the direction of $-\nabla P$, and the medium is also sheared slightly in front of the channel.

D. Flow in front of channels

In this section, we present some measurements on the average flow ahead of the growing main channel in an experiment with $P_{in} = 250$ kPa, i.e. in a region of interest only covering the length between the channel tip and the outlet side, as well as spanning the central half width of the cell. The average velocity profiles v_x in the flow direction are shown as function of distance ahead of the channel tip for different snapshots in figure 10. The profiles are found as the average u-displacement across the width of the region during time windows of $\Delta t = 10$ ms, divided by the duration of the time window. The left plot in the figure shows $v_x(x)$ at selected snapshots before the compaction front has reached the outlet side, and the right plot shows $v_x(x)$ at times after the compaction front has reached the outlet side. We see that before the compaction front hits the outlet, the velocity in front of the channel increases with time, also for an increasing range, and that the velocity has a roughly linear decreasing trend with distance ahead of the channel along the first ≈ 20 cm of the compaction zone. This suggests that, on average, the compacting strain rate (divergence of v_x) is roughly constant with x in the bulk of the compaction zone. The profiles change character after the compaction front has hit the outlet; we now find the velocity in front of the fingers to decrease with time, and that the velocity decreases like an exponential decay with distance ahead of the channel, suggesting that the compaction rate is higher closer to the channel.

The profiles for the velocity v_y perpendicular to the $x-$direction are plotted in figure 11 for selected snapshots during channel growth. The profiles show the average velocity along the cell width, in a narrow region of 2.5 cm thickness located ≈ 1.5 cm ahead of the growing channel. The plot indicates that beads move perpendicularly away from a position close to the most advanced channel tip, with initially increasing velocity as function of distance away from it, indicating decompaction in the $y-$direction close to the tip. Then at positions further away, the medium is compacted. The magnitude of v_y decreases with time as the medium compacts.

The velocity magnitude in the considered region of interest (rectangular area between the channel tip and the outlet side spanning the central half width of the cell) is found to have a scattered, but more or less linear relationship with the pressure gradient on average. The coefficient α from linear fits (shown in the inset of figure 12)

$$|\vec{v}_g| = \alpha|\nabla P| + c \tag{12}$$

describing the average increase of velocity due do an increase of ∇P is plotted as function of time for the experiments with $P_{in} = 150$, 200 and 250 kPa in figure 12. To collapse the data along the time axis, we use the normalized time $t' = t/t_c$ where t_c is the time when the compacted zone reach the outlet side for the respective experiments (found from figure 7). Respectively, for $P_{in} = 50$, 100, 150, 200 and 250 kPa, $t_c = 380$, 240, 230, 250 and 170 ms. We see for all experiments that for times before the compacted zone hits the outlet ($t' < 1$), α increases linearly with time. Then, after the compaction front has reached the outlet side ($t' > 1$), α seems to have an exponential decay with time. The inset in figure 12 shows that there is a cutoff threshold ∇P_c such that $|\vec{v}_g| = 0$ if $\nabla P < \nabla P_c$. The cutoff threshold can be found by rewriting equation (12) to $|\vec{v}_g| = \alpha(\nabla P - \nabla P_c)$, giving $\nabla P_c = -c/\alpha$. The forces displacing beads in the granular medium are related to the pore pressure gradient $-\nabla P$, as well as normal and shear solid stresses at contacts between beads. We do not resolve the solid stresses from the experiments (it is however evaluated in [62]), but if the main force felt by the medium is due to $-\nabla P$, it suggests a non-Newtonian rheology for the granular medium between the plates. Assuming a Bingham type rheology where

$$\vec{v}_g = -\frac{h^2}{\mu_B}(\nabla P - \nabla P_c), \tag{13}$$

and h is the cell gap, the granular paste has an effective viscosity $\mu_B = h^2/\alpha$. Then, our results in figure 12 suggest that

$$\begin{aligned}\mu_B = \frac{h^2}{\alpha} &= \frac{10^{-6}\ \text{m}^2}{9.8\ (\text{cm}^2/\text{kPa}\cdot\text{s})}\frac{t_c}{t} \\ &= \frac{10^{-6}\ \text{m}^2}{9.8\cdot 10^{-7}\ (\text{m}^2/\text{Pa}\cdot\text{s})}\frac{t_c}{t} \\ &\sim \frac{t_c}{t}\ \text{Pa}\cdot\text{s}\end{aligned} \tag{14}$$

before the compacted zone reaches the outlet boundary, where $t_c = 380$, 240, 230, 250 and 170 ms for $P_{in} = 50$, 100, 150, 200 and 250 kPa respectively (from the inset in figure 7). After the compacted zone has reached the outlet boundary, the effective viscosity increases as

$$\begin{aligned}\mu_B = \frac{h^2}{\alpha} &= \frac{10^{-6}\ \text{m}^2}{41.68\ (\text{cm}^2/\text{kPa}\cdot\text{s})}e^{\beta(t/t_c)} \\ &= \frac{10^{-6}\ \text{m}^2}{41.68\cdot 10^{-7}\ (\text{m}^2/\text{Pa}\cdot\text{s})}e^{\beta(t/t_c)} \\ &\sim (0.24\ \text{Pa}\cdot\text{s})\cdot e^{\beta(t/t_c)},\end{aligned} \tag{15}$$

with $\beta = 1.61$ (from figure 12), and t_c from the inset in figure 7. Thus $|\vec{v}_g| \to 0$ for $t \gg t_c$, and similarly $|\vec{v}_g| = 0$ for small times $t \to 0$, i.e. the medium is solid-like at these times. The threshold ∇P_c evolves during experiments as shown in figure 13 for the experiments with $P_{in} = 150$, 200 and 250 kPa. The data has been collapsed along the time axis as in figure 12. We see that the average thresholds ∇P_c decrease similarly before the compacted zone reaches the outlet boundary, decreasing

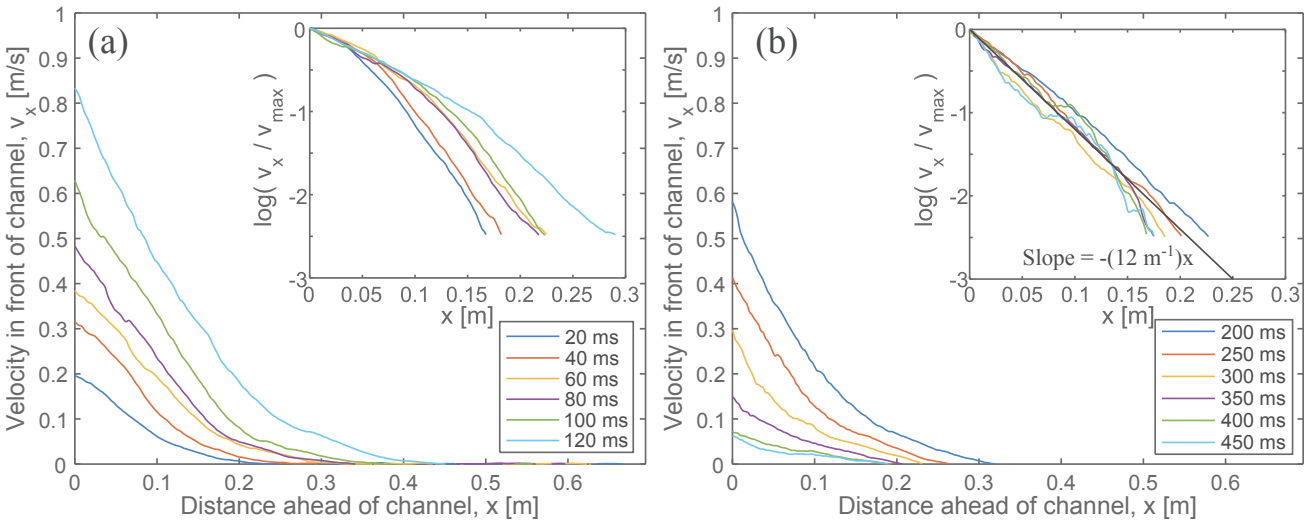

FIG. 10. Average velocity profiles v_x plotted as function of distance ahead of the channel for different snapshots, where (a) is before the compaction zone reaches the outlet boundary and (b) is after. The insets show the corresponding profiles in semi-log plots. In (a) the decay of v_x with increasing x is more or less linear in the bulk of the compaction zone, while in (b) v_x seems to have an exponential decay.

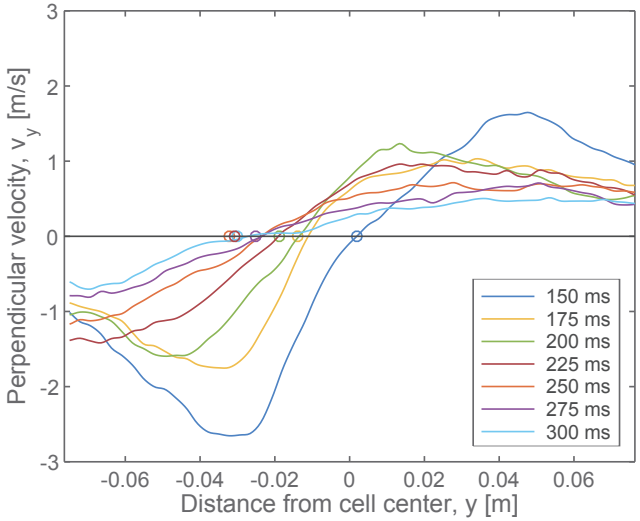

FIG. 11. Average velocity profiles v_y at 1.5 cm ahead of the channel tip are plotted as function of distance from the center line of the cell, for snapshots during channel growth. The magnitude of the velocity decays with time, but the profiles show that the medium flows away from the channel tip, with positions indicated by open circles.

from ∇P_c between 10 and 15 kPa/cm initially, down to a minimum around 1 - 2 kPa/cm at around the time the compacted zone reaches the outlet boundary. The decrease in ∇P_c with time seems to fluctuate around the fit

$$\nabla P_c = \frac{\nabla P_{c,min}}{\sqrt{t}}\sqrt{t_c} \qquad (16)$$

as indicated in figure 13 for $t \leq t_c$, where $\nabla P_{c,min}$ is around 1.5 kPa/cm. After the compacted zone has hit the outlet boundary, the thresholds begin to increase, faster with higher injection pressure. This probably depends on the injection pressure and the speed of the invading channel, i.e. the compaction rate and the forces available to compact the medium further. As the increase in ∇P_c slows down (at t/t_c around 2.5 - 3), the thresholds are approaching the pressure gradient in the zone surrounding the most advanced finger tips. Thus, the medium is becoming solid-like and we cross over to the compacted regime. However, the pressure gradients are still 2 - 3 times higher than the thresholds just outside the tips of the most advanced channels, so they propagate slowly. In addition, during the fast channel growth, we can assume that ∇P_c is small compared to the pressure gradients on the most advanced finger tips, where e.g. ∇P can be around 40 to 60 kPa/cm for the 250 kPa experiment.

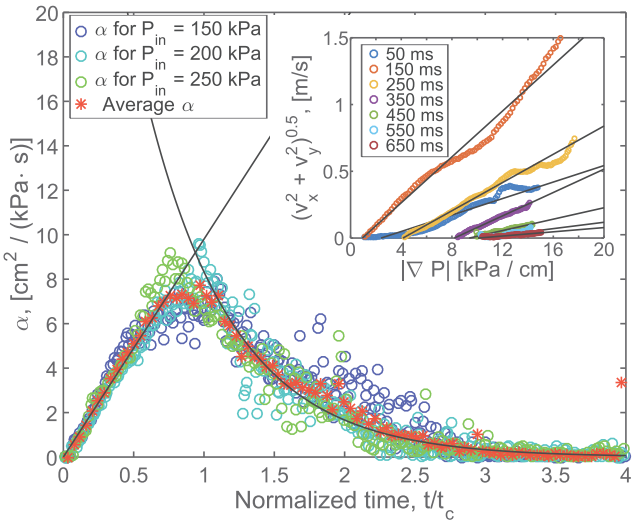

FIG. 12. Evolution with time of the fit parameter α, proportional to the inverse of Bingham effective viscosity of the granular medium, describing the average relationship $|\vec{v}_g| \approx \alpha \cdot |\nabla P| + c$ between the velocity magnitude $|\vec{v}_g|$ and the pressure gradient magnitude $|\nabla P|$. The plots of α are for the experiments with $P_{in} = 150$, 200 and 250 kPa, where the data is collapsed along the time axis by t_c, the time when the compacted zone reaches the outlet boundary. Before the compaction front reaches the outlet boundary ($t < t_c$), α increase linearly with time (linear fit $= 9.8 \cdot (t/t_c)$ cm^2/(kPa·s)), while for $t > t_c$, α has an exponential decay with time (exponential fit $= 41.68 \cdot e^{-1.61(t/t_c)}$ cm^2/(kPa·s)). In the inset: Examples of linear fits to the average velocity magnitude as function of pressure gradient. Note that over time there is an increasing offset from the ordinate axis, corresponding to the threshold $\nabla P_c = -c/\alpha$. For the experiments with $P_{in} = 150$, 200 and 250 kPa, the value of t_c is 230, 250 and 170 ms respectively.

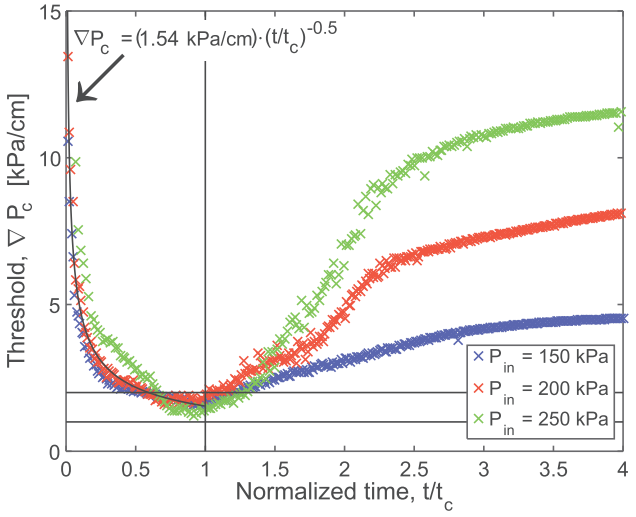

FIG. 13. Evolution of the thresholds ∇P_c as function of normalized time t/t_c for the experiments with $P_{in} = 150$, 200 and 250 kPa, where $t_c = 230$, 250 and 170 ms respectively. For $t/t_c \leq 1$, the thresholds decrease from 10 - 15 kPa/cm initially to between 1 and 2 kPa/cm (indicated by the horizontal lines) at $t/t_c = 1$. The power law fit (solid black curve) suggests that the decrease in ∇P_c is inversely proportional to the square root of time. After the compacted zone has reached the outlet boundary, for $t/t_c > 1$, ∇P_c begins to increase with time, faster for higher injection pressure. Then, at t/t_c around 2.5 - 3, the increase of the threshold with time slows down. At this point, ∇P_c is approaching the pressure gradient values $|\nabla P|$ in the zone surrounding the most advanced finger tips.

IV. DISCUSSION AND CONCLUSION

In the comparison of the steady-state pressure field with the diffusing pressure field, we found that the diffusing pressure reaches the steady-state Laplacian solution after around 1 s, which is after the main growth of the channels stops. For reference, in the analytical rigid 1-D medium with the same porosity as the initial granular medium, the diffusing pressure reached steady-state after around 0.7 s. During channel growth, the diffusing pressure is similar to the Laplacian pressure in terms of the screening of pressure gradients behind the longest finger tips, as well as having the highest pressure gradients located on the tips of the longest fingers. However, during the fast channel expansion, the magnitude of pressure gradients ($|\nabla P|$) in the diffusing pressure field may be up to 1.5 - 2 times higher than in the Laplace solution in a region close to the most advanced finger tips. When comparing the pressure magnitudes (P), the diffusing pressure behind the most advanced finger tips is typically $\geq$ 95 % of the Laplace solution (not exceeding 100 %), while in a region surrounding the most advanced finger tips (up to about 1.5 cm ahead) the diffusing pressure is typically $\geq$ 90 % of the Laplace solution (not exceeding 100 %).

The compacting part of the medium, as shown in figure 7 initially expand in the direction from the inlet towards the outlet, and in all our experiments they reach the outlet boundary shortly after the start of injection, typically after t = 170 to 250 ms (380 ms for the 50 kPa experiment). The strain rates in figure 8 shows that there is a compacting strain rate across the medium, indicating that the beads are moving faster in the flow direction closer to the invading channel, while the shear rates in the same figure indicate a shear flow where the fastest displacements occur in front of the finger tips, aligned in the growth direction of the fingers. When the compacted zone hits the outlet boundary, the medium more or less instantly becomes harder to displace; The medium exhibits a Bingham like rheology, and before the compaction front hits the outlet, the pressure gradient ∇P_c needed to displace beads appears to decrease with time as the medium mobilizes, while after the compacted zone hits the outlet ∇P_c crosses over to increase with time. Similarly, if $-\nabla P$ is the main driving force, an effective viscosity μ_B of the medium is suggested to decrease inversely with time before the compacting zone reaches the outlet. After that, it increases exponentially with time due to jamming of the confined system.

In terms of fracture dynamics for the opening of channels, the deformation shown in figure 8 suggests that the channel propagates by mode II fracturing with out of plane shear, i.e. shear planes along the confining plates, plus some in plane shear along the sides of directions emanating from the most advanced fingers empty of beads. In other words, the channel is pushing the material in front of it to propagate. At the same time, the typical displacements outside channel tips shown in figure 11 indicate a mode I fracture opening, as beads are pushed out to the sides in front of finger tips. Therefore, we suggest that the channels propagate with a mixed mode I/II opening at the tips. This is consistent with the pressure gradients which are pointing radially inwards to the finger tips, and is also supported by findings in [64] where the mechanics leading to acoustic emissions are observed (based on the polarisation on the sensors) to have two different types; compaction/relaxation or shearing. From the correlation between displacement vectors and the pressure gradient in figure 6 we find that all bead displacements occur in the direction against the pressure gradients, even in sudden stick-slip deformations (figure 9) where one could assume that some beads could be forced in random directions by contact forces in the compacted medium. Of course, this may happen inside the medium where we do not have any way of tracking beads, however it did not seem to happen in the visible top-layer.

As we showed in figure 9, it is possible to detect and track the evolution in space and time of the slip velocity field in zones of rearranging beads during stick-slip events lasting less than 10 ms by using DIC. This could prove as a useful tool in the development of acoustic localization techniques by experiments assisted with optical data, where energy release from distinct events of shearing and compacting media can be used to estimate a location for the source region as in [65]. In such setups it is an advantage to know the kinds of deformations happening, and where they happen, in order to validate measurements and methods. In addition to localization, deformation data can be an aid in discovering mechanisms of characteristic acoustic emissions during channel formation, such as discussed in [56]. For example, we have observed that the channel propagation typically features small stick-slip events rather than propagating in a smooth movement, especially towards the later part of the compaction stage. Perhaps this can be detected as distinct acoustic events, and even be used for localizing the channel tip during growth.

In the growing zone, where the granular medium is displaced in front of the channel, we found that $v_g \propto (\nabla P - \nabla P_c)$ on average. This is a Laplacian growth ($v \propto \nabla P$) if ∇P_c is small, and if the Laplacian field and diffusing field are close to each other locally. It should result in a fractal dimension around 1.71 for the growing channel, similar to DLA clusters [66] and viscous fingers in empty Hele-Shaw cells [37]. However, we find fractal dimensions for the invasion patterns to be around 1.5 to 1.6, which is similar to viscous fingers in porous media [67]. It has been derived for viscous fingers in porous media that the growth should go like $v \propto (\nabla P - \nabla P_c)$, where the thresholds are capillary pressures at the fluid-fluid interface [49, 68]. With noise in the thresholds (as for disordered porous media) they found fractal dimensions of the patterns around 1.5 - 1.6, and that the growth is better described by the Dielectric Breakdown Model (DBM), where $v \propto (\nabla P)^\eta$ with $\eta = 2$, rather than DLA. Considering that we see a Bingham type rheology in our

experiments, this could, with noise in the thresholds, be responsible for the channel growth being in another universality class than DLA and therefore would be better described by DBM with $\eta = 2$.

ACKNOWLEDGMENTS

This project has received funding from the European Unions Seventh Framework Programme for research, technological development and demonstration under grant agreement no. 316889, ITN FlowTrans. We thank Alain Steyer and Miloud Talib for their technical support with experimental equipment.

APPENDIX

Here is a discussion of why we neglect the granular displacements in the simulations of the pore pressure diffusion. When including the granular velocity, the contribution of the second term on the right side of eq. (4) in eq. (6) would be

$$\begin{gathered}\beta_x(P^{n+1}_{i+1,j} - P^{n+1}_{i-1,j}) + \beta_y(P^{n+1}_{i,j+1} - P^{n+1}_{i,j-1}) \\ \text{on the left side and} \\ -\beta_x(P^{n}_{i+1,j} - P^{n}_{i-1,j}) - \beta_y(P^{n}_{i,j+1} - P^{n}_{i,j-1}) \\ \text{on the right side,}\end{gathered} \tag{17}$$

where $\beta_x = \frac{\Delta t}{4\Delta x}(v_x)_{i,j}$ and $\beta_y = \frac{\Delta t}{4\Delta x}(v_y)_{i,j}$. A typical peak in granular velocity in our experiments is $|\vec{v}_g| = 1$ m/s, which together with the largest timestep in the simulations $\Delta t = 2.70 \cdot 10^{-5}$ s gives $\beta_{x,max} = \beta_{y,max} = 3.4 \cdot 10^{-3} \ll \alpha/2$. Similarly, the contribution of the third term on the right side of eq. (4) in eq. (6) would be

$$\begin{gathered}\gamma P^{n+1}_{i,j} \text{ on the left side and} \\ -\gamma P^{n}_{i,j} \text{ on the right side,}\end{gathered} \tag{18}$$

where $\gamma = \frac{\Delta t}{2\phi}(\dot{\varepsilon}_v)_{i,j}$, and $\dot{\varepsilon}_v = \nabla \cdot \vec{v}_g$. A typical peak in the volumetric strain rate in our experiments is $|\dot{\varepsilon}_v| = 2.5$ s^{-1}, which together with the largest timestep in the simulations $\Delta t = 2.70 \cdot 10^{-5}$ s and lowest porosity $\phi = 0.38$ gives $|\gamma_{max}| = 8.9 \cdot 10^{-5}$, which is also negligible. Thus, we approximate the evolution of the pressure field by solving equation (6), neglecting granular flow and compaction/dilation.

[1] S. S. Suthersan. *Remediation Engineering: Design Concepts*. Boca Raton, FL: CRC Press LLC, 1999. pp. 237-54.

[2] L. L. Goodroad and J. R. Schuring. Potential of pneumatic fracturing to enhance in situ remediation technologies. *In: Waste Management 1994 Symposium. Tucson, AZ: WM SYMPOSIA, INC.*, 1994.

[3] S. Kazemian, B. B. K. Huat, A. Prasad, and M. Barghchi. A review of stabilization of soft soils by injection of chemical grouting. *Aust. J. Basic & Appl. Sci. 4(12), pp. 5862-68*, 2010.

[4] R. Z. Moayed, E. Izadi, and M. Fazlavi. In-situ stress measurements by hydraulic fracturing method at gotvand dam site, iran. *Turkish J. Eng. Env. Sci. 36, pp. 179-94*, 2012. doi:10.3906/muh-1104-9.

[5] C. T. Montgomery and M. B. Smith. Hydraulic fracturing: history of an enduring technology. *J. Pet. Technol.* ***62****:2632*, 2010. doi:10.2118/1210-0026-jpt.

[6] Department of Energy. Hydraulic fracturing whitepaper. *EPA 816-R-04-003, Appendix A*, 2004.

[7] G.C. Naik. Tight gas reservoirs - an unconventional natural energy source for the future. *Available online at: www.pinedaleonline.com/socioeconomic/pdfs/tight_gas.pdf (Accessed 05, 2016)*, 2003.

[8] S. M. Johnson and J. P. Morris. Hydraulic fracturing mechanisms in carbon sequestration applications. *In: 43rd U.S. Rock Mechanics Symposium and 4th U.S.-Canada Rock Mechanics Symposium. Asheville, NC: American Rock Mechanics Association*, 2009.

[9] W. H. Williamson and D. R. Wooley. *Hydraulic Fracturing to Improve the Yield of Bores in Fractured Rock.* Canberra, ACT: Australian Government Publishing Service, 1980.

[10] F. Rummel and O. Kappelmayer. The falkenberg geothermal frac-project: concepts and experimental results. *Hydraul. Fract. Geotherm. Energy* ***5****:5974*, 1983. doi:10.1007/978-94-009-6884-4_4.

[11] Clark L. Energy company plans to frack volcano. *In: Wired Science. Available online at: www.wired.com/wiredscience/2012/10/newberry-volcano-fracking (Accessed 05, 2016)*, 2012.

[12] I. Ghani, D. Koehn, R. Toussaint, and C. W. Passchier. Dynamic development of hydrofracture. *Pure Appl. Geophys. 170 (11), 1685-1703*, 2013. doi:10.1007/s00024-

012-0637-7.

[13] A. Vass, D. Koehn, R. Toussaint, I. Ghani, and S. Piazolo. The importance of fracture-healing on the deformation of fluid-filled layered systems. *Journal of Structural Geology 67, 94-106*, 2014. doi:10.1016/j.jsg.2014.07.007.

[14] I. Ghani, D. Koehn, R. Toussaint, and C. W. Passchier. Dynamics of hydrofracturing and permeability evolution in layered reservoirs. *Frontiers in Physics 3, 67*, 2015. doi:10.3389/fphy.2015.00067.

[15] L. Goren, E. Aharonov, D. Sparks, and R. Toussaint. Pore pressure evolution in deforming granular material: A general formulation and the infinitely stiff approximation. *Journal of Geophysical Research: Solid Earth 115 (B9)*, 2010. doi:10.1029/2009JB007191.

[16] L. Goren, E. Aharonov, D. Sparks, and R. Toussaint. The mechanical coupling of fluid-filled granular material under shear. *Pure Appl. Geophys. 168 (12), 2289-2323*, 2013. doi:10.1007/s00024-011-0320-4.

[17] H. Aochi, B. Poisson, R. Toussaint, X. Rachez, and J. Schmittbuhl. Self-induced seismicity due to fluid circulation along faults. *Geophys. J. Int. 196 (3), 1544-1563*, 2013. doi:10.1093/gji/ggt356.

[18] M. Berhanu, A. Petroff, O. Devauchelle, A. Kudrolli, and D. H. Rothman. Shape and dynamics of seepage erosion in a horizontal granular bed. *Phys. Rev. E 86, 041304*, 2012. doi:10.1103/PhysRevE.86.041304.

[19] D. M. Abrams, A. E. Lobkovsky, A. P. Petroff, K. M. Straub, B. McElroy, D. C. Mohrig, A. Kudrolli, and D. H. Rothman. Growth laws for channel networks incised by groundwater flow. *Nature Geoscience 28, 193*, 2009. doi:10.1038/NGEO432.

[20] A. Kudrolli and X. Clotet. Evolution of porosity and channelization of an erosive medium driven by fluid flow. *Phys. Rev. Lett. 117, 028001*, 2016. doi:10.1103/PhysRevLett.117.028001.

[21] A. Hurst, J. Cartwright, and Duranti D. Fluidization structures produced by upward injection of sand through a sealing lithology. *In: Van Rensbergen P., Hillis R.R., Maltman A.J. and Morley C.K., editors. Subsurface Sediment Mobilization. London: Geological Society, Special Publications 216, pp. 123-38*, 2003.

[22] H. Løseth, L. Wensaas, B. Arntsen, and M. Hovland. Gas and fluid injection triggering shallow mud mobilization in the hordaland group, north sea. *In: Van Rensbergen P., Hillis R.R., Maltman A.J. and Morley C.K., editors. Subsurface Sediment Mobilization. London: Geological Society, Special Publications 216, pp. 139-57*, 2003.

[23] P. Van Rensbergen, J. Poort, R. Kipfer, M. De Batist, M. Vanneste, J. Klerkx, and et al. Near-surface sediment mobilization and methane venting in relation to hydrate destabilization in southern lake baikal, siberia. *In: Van Rensbergen P., Hillis R.R., Maltman A.J. and Morley C.K., editors. Subsurface Sediment Mobilization. London: Geological Society, Special Publications 216, pp. 207-21*, 2003.

[24] A. R. Talukder, M. C. Comas, and J. I. Soto. Pliocene to recent mud diapirism and related mudvolcanoes in the alboran sea(western mediterrenean). *In: Van Rensbergen P., Hillis R.R., Maltman A.J. and Morley C.K., editors. Subsurface Sediment Mobilization. London: Geological Society, Special Publications 216, pp. 443-59*, 2003.

[25] N. Pralle, M. Külzer, and G. Gudehus. Experimental evidence on the role of gas in sediment liquefaction and mudvolcanism. *In: Van Rensbergen P., Hillis R.R., Maltman A.J. and Morley C.K., editors. Subsurface Sediment Mobilization. London: Geological Society, Special Publications 216, pp. 159-71*, 2003.

[26] E. Deville, A. Battani, R. Griboulard, S. Guerlais, J. P. Herbin, J. P. Houzay, and et al. The origin and processes of mudvolcanism: new insights from trinidad. *In: Van Rensbergen P., Hillis R.R., Maltman A.J. and Morley C.K., editors. Subsurface Sediment Mobilization. London: Geological Society, Special Publications 216, pp. 475-90*, 2003.

[27] R. Nuwer. Indonesias 'mud volcano' and nine years of debate about its muck. *In: NY Times. Available online at: www.nytimes.com/2015/09/22/science/9-years-of-muck-mud-and-debate-in-java.html (Accessed 10, 2016)*, 2015.

[28] A. Mazzini, H. Svensen, G. G. Akhmanov, G. Aloisi, S. Planke, A. Malthe-Sørenssen, and B. Istadi. Triggering and dynamic evolution of the lusi mud volcano, indonesia. *Earth and Planetary Sci. Lett. 261, 375-388*, 2007. doi:10.1016/j.epsl.2007.07.001.

[29] A. Mazzini, A. Nermoen, M. Krotkiewski, Y. Podladchikov, S. Planke, and H. Svensen. Strike-slip faulting as a trigger mechanism for overpressure release by piercement structures. implications for the lusi mud volcano, indonesia. *Marine and Petroleum Geology 26, 1751-1765*, 2009. doi:10.1016/j.marpetgeo.2009.03.001.

[30] A. Mazzini, G. Etiope, and H. Svensen. A new hydrothermal scenario for the 2006 lusi eruption, indonesia. insights from gas geochemistry. *Earth and Planetary Sci. Lett. 317/318, 305-318*, 2012. doi:10.1016/j.epsl.2011.11.016.

[31] M. Lupi, E. H. Saenger, F. Fuchs, and S. A. Miller. Lusi mud eruption triggered by geometric focusing of seismic waves. *Nature Geoscience 6, 642-646*, 2013. doi:10.1038/ngeo1884.

[32] M. R. P. Tingay, Rudolph M. L., M. Manga, R. J. Davies, and C. Y. Wang. Initiation of the lusi mudflow disaster. *Nature Geoscience 8, 493-494*, 2015. doi:10.1038/ngeo2472.

[33] Ø. Johnsen, R. Toussaint, K. J. Måløy, and E. G. Flekkøy. Pattern formation during air injection into granular materials confined in a circular hele-shaw cell. *Phys. Rev. **E**74, 011301*, 2006. doi:10.1103/PhysRevE.74.011301.

[34] Ø. Johnsen, R. Toussaint, K. J. Måløy, E. G. Flekkøy, and J. Schmittbuhl. Coupled air/granular flow in a linear hele-shaw cell. *Phys. Rev. **E**77, 011301*, 2008. doi:10.1103/PhysRevE.77.011301.

[35] Ø. Johnsen, C. Chevalier, A. Lindner, R. Toussaint, E. Clément, K. J. Måløy, E. G. Flekkøy, and J. Schmittbuhl. Decompaction and fluidization of a saturated and confined granular medium by injection of a viscous liquid or gas. *Phys. Rev. **E**78, 051302*, 2008. doi:10.1103/PhysRevE.78.051302.

[36] X. Cheng, L. Xu, A. Patterson, H. M. Jaeger, and S. R. Nagel. Towards the zero-surface-tension limit in granular fingering instability. *Nat. Phys. **4**:234-7*, 2008. doi:10.1038/nphys834.

[37] P. G. Saffman and G. Taylor. The penetration of a fluid into a porous medium or hele-shaw cell containing a more viscous liquid. *Proc. R. Soc. Lond. A. Math. Phys. Sci. 245:312-29*, 1958. doi:10.1098/rspa.1958.0085.

[38] F. K. Eriksen, R. Toussaint, K. J. Måløy, and E. G. Flekkøy. Invasion patterns during two-phase flow in

deformable porous media. *Front. Phys. 3:81*, 2015. doi:10.3389/fphy.2015.00081.

[39] B. Sandnes, E. G. Flekkøy, H. A. Knudsen, and K. J. Måløy. Patterns and flow in frictional fluid dynamics. *Nat. Commun.*, 2011. doi:10.1038/ncomms1289.

[40] R. Holtzman, M. L. Szulczewski, and R. Huanes. Capillary fracturing in granular media. *Phys. Rev. Lett. 108:264504*, 2012. doi:10.1103/PhysRevLett.108.264504.

[41] X. Z. Kong, W. Kinzelbach, and F. Stauffer. Morphodynamics during air injection into water-saturated movable spherical granulates. *Chem. Eng. Sci. 65:4652-60*, 2010. doi:10.1016/j.ces.2010.05.007.

[42] C. Chevalier, A. Lindner, M. Leroux, and E. Clément. Morphodynamics during air injection into a confined granular suspension. *J. Non-Newton Fluid Mech. 158:63-72*, 2008. doi:10.1016/j.jnnfm.2008.07.007.

[43] J. A. Eriksen, B. Marks, B. Sandnes, and R. Toussaint. Bubbles breaking the wall: two-dimensional stress and stability analysis. *Phys. Rev. E 91:052204*, 2015. doi:10.1103/PhysRevE.91.052204.

[44] J. A. Eriksen, R. Toussaint, K. J. Måløy, E. G. Flekkøy, and B. Sandnes. Numerical approach to frictional fingers. *Phys. Rev. E 92:032203*, 2015. doi:10.1103/PhysRevE.92.032203.

[45] B. Marks, B. Sandnes, G. Dumazer, J. A. Eriksen, and K. J. Måløy. Compaction of granular material inside confined geometries. *Front. Phys. 3:41*, 2015. doi:10.3389/fphy.2015.00041.

[46] J. A. Eriksen, R. Toussaint, K. J. Måløy, E. G. Flekkøy, and B. Sandnes. Pattern formation of frictional fingers in a gravitational potential. *arXiv:1605.07436v1 [physics.flu-dyn]*, 2016.

[47] M. Moura, E. A. Fiorentino, K. J. Måløy, G. Schäfer, and R. Toussaint. Impact of sample geometry on the measurement of pressure-saturation curves: Experiments and simulations. *Water Resour. Res. 51*, 2015. doi:10.1002/2015WR017196.

[48] D. Wilkinson and J. F. Willemsen. Invasion percolation: a new form of percolation theory. *J. Phys. A Math. Gen. 16:336576*, 1983.

[49] G. Løvoll, Y. Méheust, R. Toussaint, J. Schmittbuhl, and K. J. Måløy. Growth activity during fingering in a porous hele-shaw cell. *Phys. Rev. E 70:026301*, 2004. doi:10.1103/PhysRevE.70.026301.

[50] G. Løvoll, M. Jankov, K. J. Måløy, R. Toussaint, J. Schmittbuhl, G. Schäfer, and Y. Méheust. Influence of viscous fingering on dynamic saturationpressure curves in porous media. *Transp. Porous Med. 86: 305*, 2011. doi:10.1007/s11242-010-9622-8.

[51] K. T. Tallakstad, H. A. Knudsen, T. Ramstad, G. Løvoll, K. J. Måløy, R. Toussaint, and E. G. Flekkøy. Steady-state two-phase flow in porous media: Statistics and transport properties. *Phys. Rev. Lett. 102, 074502*, 2009. doi:10.1103/PhysRevLett.102.074502.

[52] H. Huang, F. Zhang, P. Callahan, and J. Ayoub. Granular fingering in fluid injection into dense granular media in a hele-shaw cell. *Phys. Rev. Lett. 108:258001*, 2012. doi:10.1103/PhysRevLett.108.258001.

[53] M. J. Niebling, R. Toussaint, E. G. Flekkøy, and K. J. Måløy. Dynamic aerofracture of dense granular packings. *Phys. Rev.* ***E****86, 061315*, 2012. doi:10.1103/PhysRevE.86.061315.

[54] H. M. Jaeger, S. R. Nagel, and R. P. Behringer. Granular solids, liquids, and gases. *Rev. Mod. Phys., Vol. 68, No. 4*, 1996.

[55] M. J. Niebling, R. Toussaint, E. G. Flekkøy, and K. J. Måløy. Numerical studies of aerofractures in porous media. *Rev. Cub. Fis. 29, 1E66*, 2012.

[56] S. Turkaya, R. Toussaint, F. K. Eriksen, M. Zecevic, G. Daniel, E. G. Flekkøy, and K. J. Måløy. Bridging aerofracture evolution with the characteristics of the acoustic emissions in a porous medium. *Front. Phys. 3:70*, 2015. doi: 10.3389/fphy.2015.00070.

[57] J. Ugelstad, P. C. Mórk, K. H. Kaggerud, T. Ellingsen, and A. Berge. Swelling of oligomer-polymer particles. new methods of preparation. *Adv. Colloid Interface Sci. 13, 101*, 1980. doi:10.1016/0001-8686(80)87003-5. Produced under the trade name Dynospheres by Dyno Particles A.S., N-2001 Lillestrom, Norway.

[58] J. Blaber, B. Adair, and A. Antoniou. Ncorr: Open-source 2d digital image correlation matlab software. *Exp. Mech.*, 2015. doi:10.1007/s11340-015-0009-1.

[59] J. Blaber. Ncorr - open source 2d digital image correlation matlab software. *Available online at: http://www.ncorr.com/ (Accessed 10, 2016).*

[60] S. McNamara, E. G. Flekkøy, and K. J. Måløy. Grains and gas flow: Molecular dynamics with hydrodynamic interactions. *Phys. Rev. E 61, 4054*, 2000. doi:10.1103/PhysRevE.61.4054.

[61] W. H. Press, S. A. Teukolsky, W. T Vetterling, and B. P. Flannery. *Numerical recipies in Fortran 77, 2nd ed.: The art of scientific computing*. Cambridge: Cambridge University Press, 2001.

[62] A. L. Turquet, R. Toussaint, F. K. Eriksen, G. Daniel, D. Koehn, E. G. Flekkøy, and K. J. Måløy. Numerical studies of the acoustic emissions during pneumatic fracturing. *J. Geophys. Res. Solid Earth (In Submission)*, 2017.

[63] J.-P. Ampuero and Y. Ben-Zion. Cracks, pulses and macroscopic asymmetry of dynamic rupture on a bimaterial interface with velocity-weakening friction. *Geophys. J. Int. 173, 674692*, 2008. doi:10.1111/j.1365-246X.2008.03736.x.

[64] A. L. Turquet, R. Toussaint, F. K. Eriksen, O. Lengliné, G. Daniel, E. G. Flekkøy, and K. J. Måløy. Source localization of acoustic emissions during pneumatic fracturing. *Geophys. Res. Lett. (In Submission)*, 2017.

[65] S. Turkaya, R. Toussaint, F. K. Eriksen, O. Lengliné, D. Guillaume, E. G. Flekkøy, and K. J. Måløy. Note: Localization based on estimated source energy homogeneity. *Rev. Sci. Instrum. 87, 096101*, 2016. doi:10.1063/1.4962407.

[66] T. A. Jr. Witten and L. M. Sander. Diffusion-limited aggregation, a kinetic critical phenomenon. *Phys. Rev. Lett. 47, 1400-1403*, 1981. doi:10.1103/PhysRevLett.47.1400.

[67] F. K. Eriksen, R. Toussaint, S. Turkaya, K. J. Måløy, and E. G. Flekkøy. Pneumatic fractures in confined granular media. *(Submitted)*, 2016.

[68] R. Toussaint, G. Løvoll, Y. Méheust, K. J. Måløy, and J. Schmittbuhl. Influence of pore-scale disorder on viscous fingering during drainage. *Europhys Lett. 71:583*, 2005. doi:10.1209/epl/i2005-10136-9.

Chapter 7

Reactive flow in fractured chalk

7.1 Motivation

In addition to the experiments discussed in chapters 3 - 5, we began a preliminary experimental study on the slow transformation process of chemically evolving fractures in carbonate reservoir rock. We wanted to characterize the local evolution of fracture surfaces subject to different durations of reactive flooding with the same flow rate, to look for typical behaviors. For example, we were interested in the amount of dissolution/precipitation as function of the initial fracture aperture, impact of flow direction, and evolution of fracture surface roughness for different durations of reactive flooding. In addition, we wanted to develop experimental methods for further experiments such as measuring the impact of the reaction on the surrounding stresses in the rock. In this chapter, the current methods and results are presented.

7.2 Methodology

7.2.1 Samples and sample preparation

The samples are cylindrical core samples of "Limit Obourg Nouvelles" chalk from the CBR Harmignies quarry in the Mons basin in Belgium, i.e. upper cretaceous chalk retrieved from around 30 meters depth. Chemically speaking, it is a form of limestone composed of calcite ($CaCO_3$). The samples have a diameter of 38.1 mm and are cut into pieces with lengths varying between 17 and 26 mm. The average porosity of the chalk is 0.43, found by measuring the weight difference of samples when they are dry and saturated with water.

In these experiments, we want to investigate the evolution of fractures during reactive flow, so in the sample preparation we break the samples into two pieces through the diametrical plane. This is achieved in a Brazilian test cell as shown in figure 7.1. The breaking process is done as follows; first, the sample is fitted with a protective plastic jacket to limit the damage where the stress is applied. Then it is placed in the brazilian test cell, where a normal stress is applied across the diametrical plane of the sample. The load is applied on the cell plates holding the sample by a hydraulic piston, with an increasing force at a rate of 100 N per minute. The loading is continued until the sample fails and has a fracture opening across

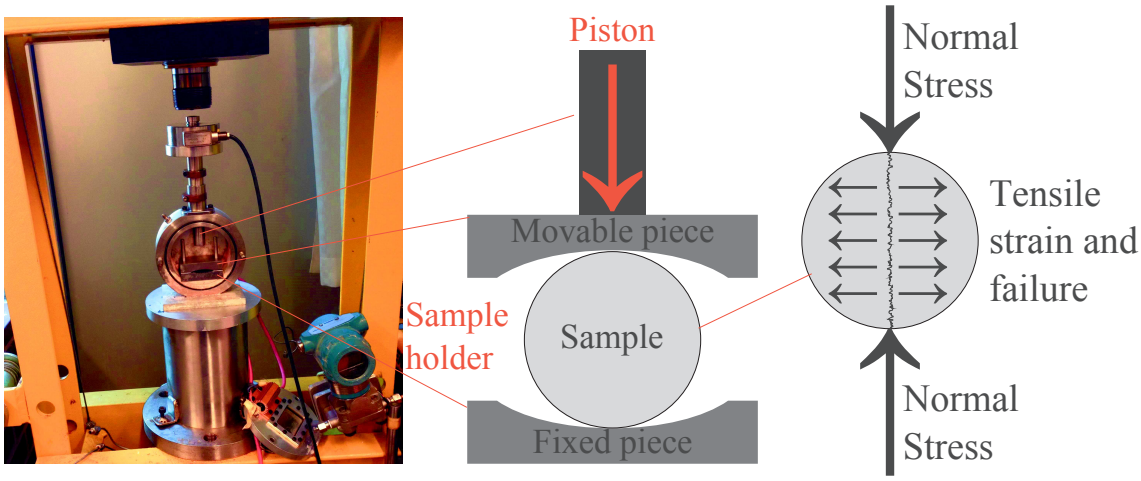

Figure 7.1: The Brazilian test cell. Left: Photo of the rig and test cell. Middle: A sketch of the cell; the sample is held between two rounded plates, where the bottom plate is fixed and the top plate can move vertically. During the Brazilian test, a piston applies a downward force on the top plate. The piston moves downwards in a smooth movement, increasing the force on the top plate at a rate of 100 N per minute. This continues until the sample fractures. Right: Sketch of the stress and deformation of the sample; normal stress from the cell plates leads to tensile strain in the diametrical plane of the sample. When the yield strength of the sample is reached, a tensile fracture opens and goes through the diametrical plane, splitting the sample in half.

the diametrical plane due to tensile strain. With this method, we always observed the fracture to go across the sample in one quick event. The samples have a tensile strength between 0.4 and 0.7 MPa, corresponding to a load of around 1 to 1.3 kN from the piston. The brazilian tests take from 3 to 5 minutes when starting with a load of 0.8 kN (applied with a manual lever when inserting the sample).

7.2.2 Reactive flooding

For the reactive flooding experiments, the samples are put back together and inserted into a rubber jacket with an inner diameter similar to the sample diameter. To secure the sample, excess space in the rubber jacket is occupied by a spacer, i.e. a metal cylinder with the same diameter as the sample and a 1 cm hole through the principal axis. Then, the assembled sample is put inside a Hassler cell as shown in figure 7.2. The Hassler cell is a cylindrically confined flow cell, where the confinement is provided by a pressurized fluid outside the rubber jacket, isolated from a fluid inlet and outlet to the sample inside the rubber jacket. We used a 700 kPa confining pressure provided by pressurized nitrogen, found to be sufficient for the conditions in our experiments as well as very clean and easy to use (instead of e.g. oil).

A Quizix QX pump system connected to the cell inlet enables precise control of the flow rate, which we set to 0.1 ml/min for all the experiments, as well as the possibility for changing between distilled water (measured pH = 6.1, due to absorbed atmospheric CO_2) and chalk saturated water (measured pH = 9.9).

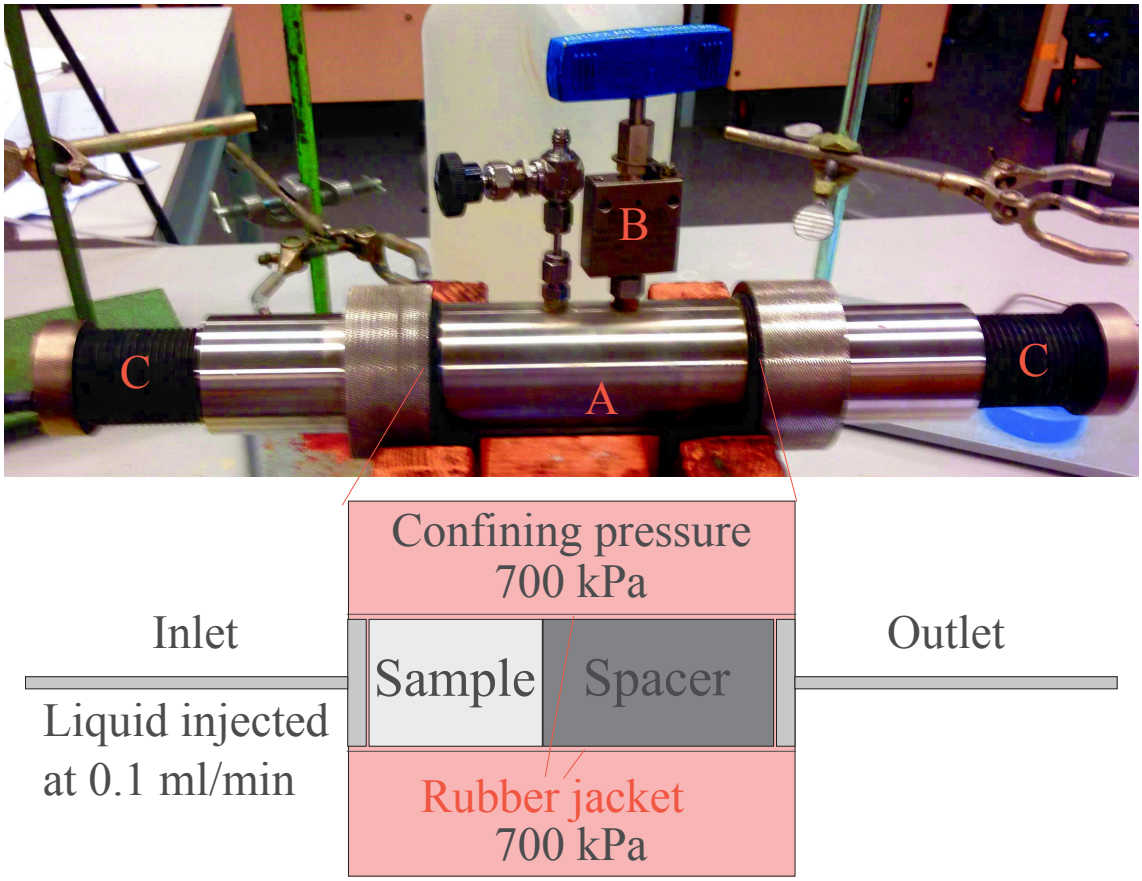

Figure 7.2: The Hassler cell. Top: The assembled Hassler cell; A indicates the sample chamber, B indicates the confining pressure inlet/outlet valve, and C indicates the inlet and outlet caps. Tubing allowing fluids into or out of the sample is connected through these caps. Bottom: Sketch of the interior of the sample chamber; The sample and spacer are confined inside the rubber jacket under a confining pressure of 700 kPa (Nitrogen gas). The inlet and outlet tubing permits fluid flow through the confined sample, where distilled water is injected at 0.1 ml/min during experiments. The inlet/outlet caps shown in the top photo are used to clamp the inlet plate, sample, spacer and outlet plate together, while the rubber jacket isolates the flooding experiment from the pressurized confining gas.

The saturated water is prepared by putting some chalk samples and distilled water in a container, and let the water saturate for about 24 hours. Before use, possible particles are filtered out of the water by a 20 micron filter. The saturated water is used in the beginning of the experiment to flood the system, i.e. saturated water is pumped into the initially dry system, and when saturated water is coming out at the outlet side the injected fluid is switched to distilled water. Due to the volume of tubing on the inlet side, the reactive flow reaches the sample after about 45 minutes. So the start of reactive flow experiment is considered to begin 45 minutes after changing to distilled water. The reactive flooding experiments were performed for different durations ranging from 4 hours to 41 hours.

7.2.3 Obtaining local surface profiles

We use a Wyko NT1100 White Light Interferometer (WLI) microscope in Vertical Scanning mode (VSI) to obtain local 3-D profiles of the fracture surfaces. The method is based on the short coherence length of white light, and that the interference fringes have peak intensity when the test beam (reflecting off the sample) has the same optical path length as the reference beam (fixed length). The layout of the interferometer is shown in figure 7.3. The objective is moved vertically while tracking its vertical offset with a piezo-electric translation stage. The reflected beam forming an image on the CCD screen is a combination of the reference beam and the test beam (re-combined at the beam splitter), which will have peak intensity if the two beams have travelled the same optical length. As the objective is moved, the CCD image is recorded at each step. An algorithm finds the vertical position with highest intensity for each pixel and makes a 3-D profile of the scanned surface with this information. In a WLI setup with a broadband light source, we will only see interference fringes in the short range of the coherence length, where the wavelengths in the reflected beam have almost the same phase conditions as the light source. Outside the range of the coherence length, the phases and interferences are randomly distributed, and no interference fringes are observed.

The dependence of the correlogram width on the coherence length and central wavelength is briefly explained by assuming a Gaussian spectrum for the emitted light [86]. The normalized spectral density function is defined according to

$$S(\nu) = \frac{1}{\sqrt{\pi}\Delta\nu} e^{-\frac{\nu-\nu_0}{\Delta\nu}}, \tag{7.1}$$

where $\Delta\nu$ is the effective $1/e$-bandwidth and ν_0 is the mean frequency. The autocorrelation function of the light field, which is measured at the CCD screen for each pixel, is given by the Fourier transform of eq. (7.1) as

$$k(\tau) = \int_{-\infty}^{\infty} S(\nu) e^{-i2\pi\nu\tau} d\nu = e^{-(\pi\tau\Delta\nu)^2} \cdot e^{-i2\pi\nu_0\tau}. \tag{7.2}$$

By rewriting eq. (7.2) with $\nu_0 = c/\lambda_0$, $L_c = c/(\pi\Delta\nu)$, and $\tau = 2(z - z_0)/c$, we can describe the intensity measured at the CCD plate as function of z, the distance from the sample to the beam splitter. Here, c is the speed of light, λ_0 is the central wavelength, L_c is the correlation length, and $2(z - z_0)$ is the optical path difference

where z_0 is the distance of the reference mirror from the beam splitter. By assuming that the reference and test beams have the same intensity I_0, the intensity measured at a pixel in the CCD screen is given by

$$I(z) = I_0 \Re\{1 + k(z)\} = I_0 \left(1 + e^{-4\left(\frac{z-z_0}{L_c}\right)^2} \cdot \cos\left(4\pi \frac{(z - z_0)}{\lambda_0}\right)\right). \qquad (7.3)$$

Equation (7.3) shows that the intensity distribution is formed by a Gaussian envelope, and a periodic modulation of period $\lambda_0/2$. While a real correlogram is more distorted than this ideal case, it shows the strong dependence of the correlogram on the central wavelength λ_0 (in the range of 400 - 700 nm for visible light) and coherence length L_c of the light source (usually on the order of microns). This shows that we will only observe an interference pattern for a small range of $(z - z_0)$, and will be focused on different elevations of the sample during scanning.

The output data from the interferometer is an image of width W and height H where the pixels contain elevation values $h(x, y)$ at each pixel position in the measured area (1 pixel size ≈ 2 µm). The fracture surfaces are profiled on both pieces of the sample, before and after the flooding experiments. Since the surface profiles are local (areas between 4×5 mm and 8×8 mm), we drill 1.5 mm benchmark holes in the samples to measure roughly similar areas in the succeeding measurements. Resulting 3-D profiles for similar areas on the opposing fracture surfaces of a sample (side A and side B) are shown in figure 7.4. During data processing, tilt of the profiles is removed by subtracting a linear plane fitted to the profile data. To align surface profiles before and after experiments (same piece of the sample, e.g. side A with side A), the profiles are cross-correlated during translational and rotational displacements, such that they are best aligned at the highest correlation coefficient. Aligning profiles of opposing fracture surfaces of the same sample (side A with side B) is done in the same fashion, but first the side B profile is been multiplied with -1 and flipped along the x-axis. This is done to represent the surface elevation h_B in the same direction as h_A, and to account for the mirroring of the fracture surfaces (it corresponds to rotating the profile 180 degrees about the y-axis). An example of aligned profiles from opposing surfaces is shown in figure 7.5.

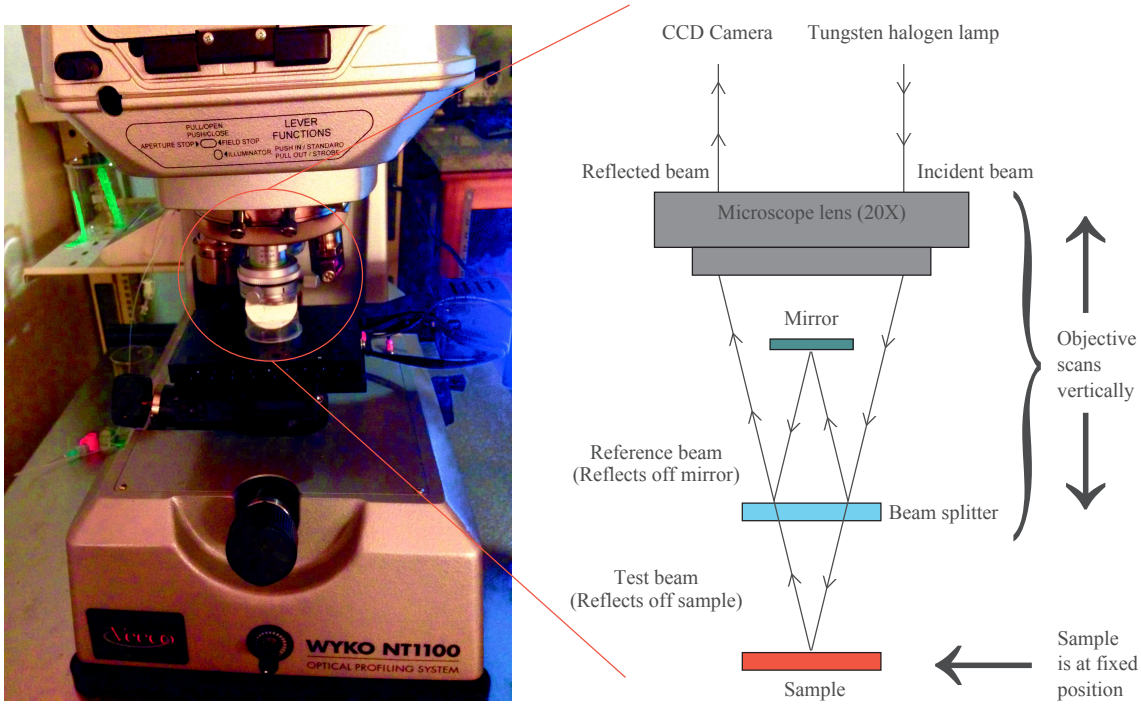

Figure 7.3: The Wyko NT1100 optical profiling system. Left: Photo of the equipment with the sample under the microscope objective (inside red circle). Right: Principle of the Mirau interferometer; Incident white light goes through the microscope lens and hits a beam splitter plate (semi-transparent mirror), splitting the beam into a reference beam and a test beam. The reference beam reflects off a mirror at a fixed position in the objective, while the test beam reflects off the sample. Then the two beams combine at the beam splitter plate, and goes back through the microscope lens to a CCD camera which records the beam intensity at each pixel. Due to constructive interference, the beam intensity is highest when the optical path of the test beam is equal to the optical path of the reference beam. By scanning the objective vertically (relative to the sample), and by recording the vertical position of the objective, an algorithm finds the vertical position at each pixel where the beam intensity is highest, and with this information a surface profile is made.

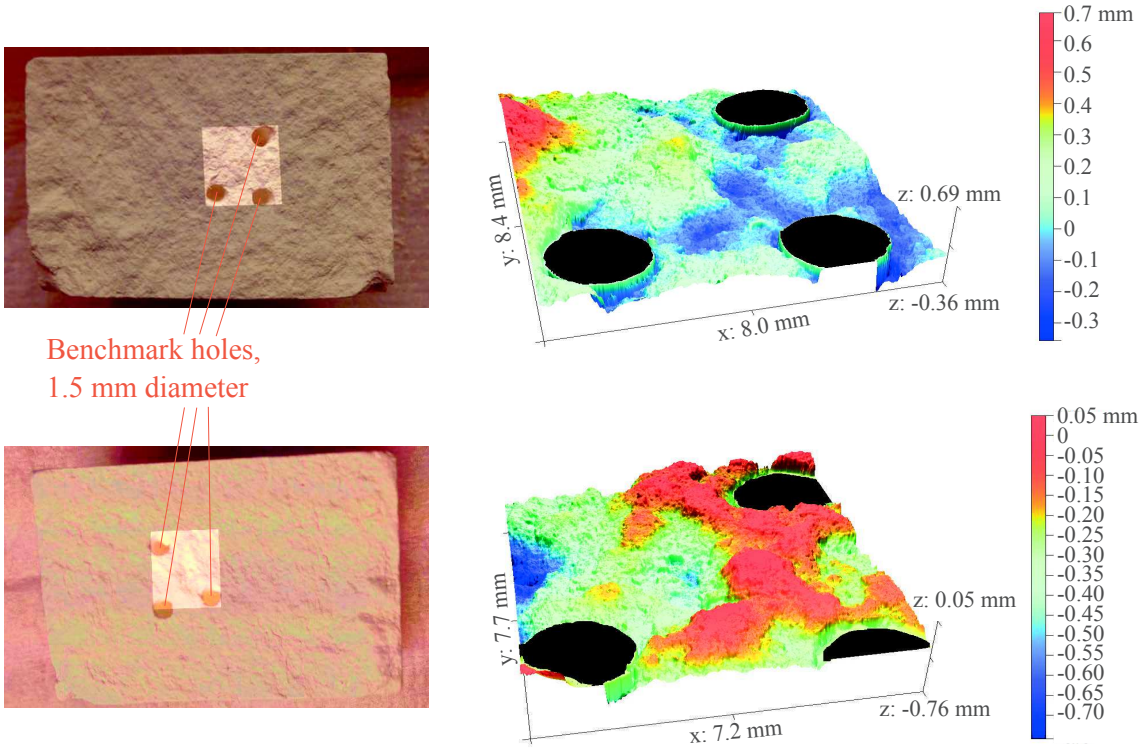

Figure 7.4: Examples of 3-D profiles before reactive flooding. Left: The measured fracture surfaces, where the pieces shown are the opposite sides of the same fractured sample. The brighter areas indicate the profiled regions. Right: The resulting 3-D profiles as found with WLI. We see that details in the profiles match: valleys in the top profile matches peaks in the bottom profile and vice-versa. Note that in this figure, the tilt of the sample is not subtracted, and the profile on the bottom is flipped but not multiplied by -1.

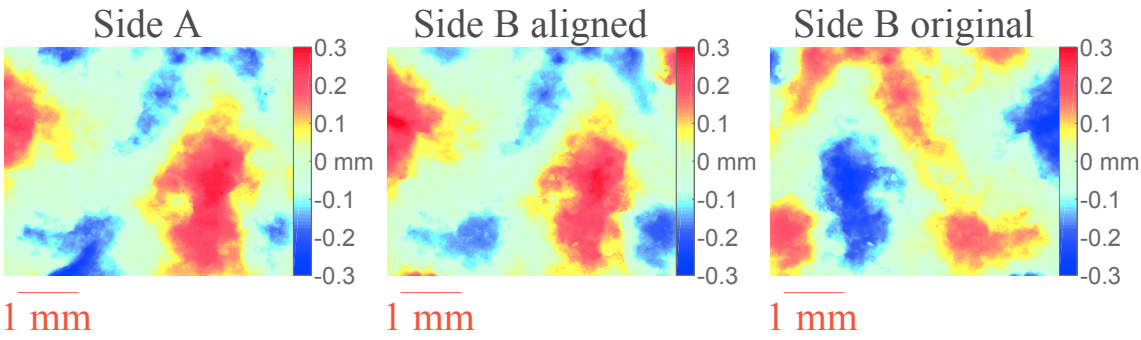

Figure 7.5: Examples of aligned profiles. Left: Side A is the profile to be matched by side B. Middle: Side B has been flipped horizontally and aligned with side A. Right: The original side B profile before it is flipped along the x-axis and multiplied by -1.

7.3 Analysis and results

We performed 5 experiments of reactive flooding with distilled water at a flow rate of 0.1 ml/min, with various durations in the range of 4 to 41 hours. However, only 3 of the experiments had good positional match between the measured surface profiles $h_{A,before}$, $h_{A,after}$, $h_{B,before}$ and $h_{B,after}$. In return, these surface profiles are from experiments spread across the range of flow durations; 4, 22.5 and 41 hours. We analyze these three sets of surface profiles.

The surface roughness is characterized by calculating the elevation fluctuations as function of displacement d, i.e. calculating the structure function [87, 88] for the profiles. We find the 2nd order structure function along the x-direction as

$$C_2(d) = \langle (h(x+d,y) - h(x,y))^2 \rangle^{\frac{1}{2}}, \tag{7.4}$$

for $d = 1$ to $W/2$, and along the y-direction as

$$C_2(d) = \langle (h(x,y+d) - h(x,y))^2 \rangle^{\frac{1}{2}}, \tag{7.5}$$

for $d = 1$ to $H/2$, where the angle brackets denote the spatial average. The roughness exponent ζ of a fracture surface is evaluated by plotting C_2 as function of d in a log-log plot. If the structure function follows a power law

$$C_2(d) \sim d^{\zeta}, \tag{7.6}$$

the surface is self-affine over a range of scales with an associated roughness exponent.

The structure functions were calculated for the fracture surfaces before and after reactive flooding, and for both sides A and B. Log-log plots of the results are shown in figure 7.6. The structure functions plotted here are the averages of equations (7.4) and (7.5). We see that all the considered fracture surfaces have self-affine properties, with a roughness exponent of $\zeta \approx 0.7$. This roughness exponent was measured over the range of scales $d = 10^{-2}$ mm to 1 mm for the samples used in the experiments with 22.5 and 41 hours of reactive flow, while for the sample used in the 4 hour experiment the range is $d = 10^{-2}$ mm to 0.16 mm. For scales above $d = 0.16$ mm, the fracture surfaces on this sample are less rough with ζ around 0.3. In addition, the surface roughness was not observed to change after any of the durations of reactive flooding done here.

Figure 7.7 shows estimated fracture apertures $a = h_B - h_A$ between the aligned profiles before and after flooding, the change in fracture aperture $r = a_{after} - a_{before}$, and the initial mid-fracture elevation $\overline{h} = (h_A + h_B)/2$. Since the surface profiles are locally and individually measured, it is not trivial to determine the real fracture aperture in the assembled samples. As a crude approach here, the fracture surfaces h_A and h_B are forced to be in contact but not intersect, such that the apertures are adjusted to $a' = a - \min(a)$. By looking at figure 7.7, we observe some features to investigate; There is a slight pattern in the estimated dissolution for the 4 hour experiment, where there are some distinct lines going roughly in the flow direction. This is not seen in the experiments with longer flow durations. However, for the experiments with 22.5 and 41 hours of flow time, it looks like regions with small initial fracture aperture have more dissolution, while regions with larger initial

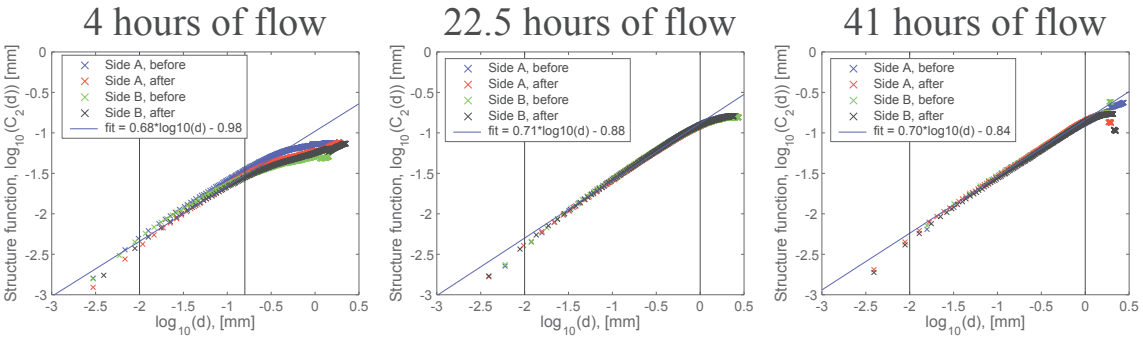

Figure 7.6: Log-log plots of the structure function C_2 as function of spacing d for the different fracture surfaces. A roughness exponent $\zeta \approx 0.7$ is found to be typical, both before and after the reactive flooding.

fracture opening have more precipitation. We investigate the changes in fracture aperture by spatial autocorrelation, and cross-correlation with the initial aperture and mid-plane.

We calculate the cross-correlation of two data sets X and Y for relative displacements Δy in the flow direction as

$$C_{XY}(\Delta y) = \frac{\langle (X(x,y) - \overline{X})(Y(x, y+\Delta y) - \overline{Y})\rangle}{\sigma_X \sigma_Y}, \tag{7.7}$$

and relative displacements Δx perpendicular to the flow direction as

$$C_{XY}(\Delta x) = \frac{\langle (X(x,y) - \overline{X})(Y(x+\Delta x, y) - \overline{Y})\rangle}{\sigma_X \sigma_Y}, \tag{7.8}$$

where σ_X and σ_Y are the standard deviations of X and Y, and the angle brackets denote spatial average. The autocorrelation of a data set is done by correlating it with itself in equations (7.7) and (7.8).

The autocorrelation of the change r in fracture aperture is shown in figure 7.8 A) as function of relative displacements perpendicular to the flow direction (Δx) and relative displacements parallel with the flow direction (Δy). After 4 hours of reactive flow, the changes in fracture aperture correlate only locally; for relative displacements perpendicular to the flow direction, the correlation coefficient drops below 0.5 for displacements larger than $\pm$ 0.05 mm, and in the direction parallel with the flow direction, it drops below 0.5 at displacements of $\pm$ 0.07 mm. In addition, there are some periodic fluctuations in the correlation function for relative displacements perpendicular to the flow direction, with peaks at relative displacements $\pm$0.3, $\pm$0.5, $\pm$1 and $\pm$1.3 mm. These small fluctuations could be a response to the linear shapes observed in figure 7.7. For the experiment with flow duration of 22.5 hours, we see that the correlation length for r is increased both parallel with and perpendicular to the flow direction, with correlation coefficients above 0.5 for all the relative displacements measured in the flow direction $\pm$2 mm, and within $\pm$ 1.2 mm perpendicular to the flow direction. For the experiment with 41 hours of reactive flow, the autocorrelation of r in the flow direction remain above 0.5 within the relative displacements of $\pm$ 1.5 mm measured. For displacements in the perpendicular direction, it remains above 0.45 within the measured displacements $\pm$

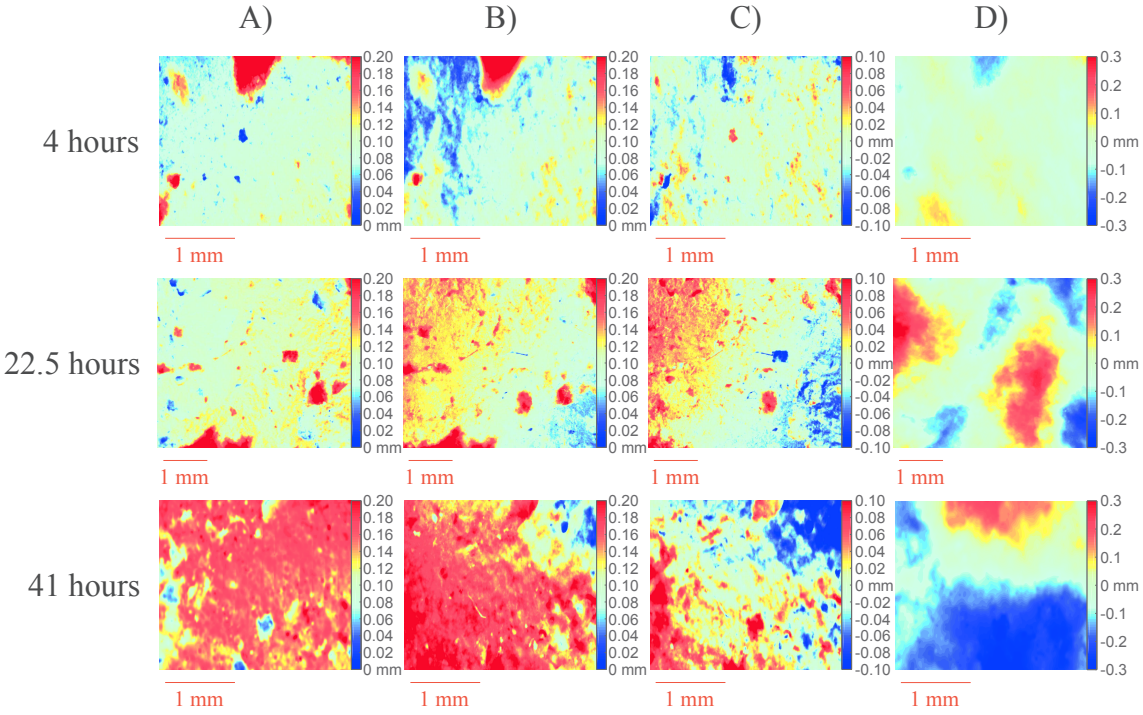

Figure 7.7: Fracture profiles for the different samples analyzed. A) Fracture aperture a' before reactive flooding, B) Fracture aperture a' after reactive flooding, C) Change r in fracture aperture after reactive flooding, and D) The initial mid-fracture elevation $\overline{h}$ before reactive flooding. The flow direction is from the top towards the bottom.

1.5 mm. In general, the spatial correlation of the changes in fracture aperture tend to increase with increased flow duration, first along the flow direction, then also perpendicular to it. Figure 7.8 B) shows the cross-correlation between the change r in fracture aperture and the initial fracture aperture a'_{before}, for relative displacements along the flow direction and perpendicular to it. There is a general trend of stronger anticorrelation between r and a'_{before} with increasing flow duration. For the 4 h experiment, the correlation is low for all relative displacements measured. For the 22.5 hours experiment, the zero-displacement anticorrelation is moderate with a correlation coefficient at -0.5, as well as a weak anticorrelation (between -0.3 and -0.4) with the upstream initial aperture (seen as positive displacement in the flow direction). For the experiment with 41 hours of reactive flow, the zero-displacement anticorrelation is high, with a correlation coefficient at -0.7. The correlation function also shows weak anticorrelation (from -0.2 to -0.4) of r with the surrounding regions in the initial aperture. Figure 7.8 C) shows the cross-correlations of the change r in fracture opening with the initial mid-plane $\overline{h}$. For the 4 hour experiment the correlation is low, with correlation coefficients within $\pm$ 0.2. For the 22.5 hour experiment, the correlation coefficient is low for perpendicular displacements and the zero-displacement, more or less within $\pm$ 0.2. There is an increase from weak to moderate (0.2 to 0.5) positive correlation with the upstream mid-plane (positive displacements in the flow direction). For the 41 hours experiment, there is a weak anticorrelation for displacements perpendicular to the flow direction (-0.3 to -0.4)

and for the zero-displacement (-0.3), and a moderate positive correlation (0.4 - 0.5) with the mid-plane at 1 to 1.5 mm downstream. With these results we do not find a general trend between the mid-plane and the change in fracture aperture.

Figure 7.9 shows the binned average relationship between the change in fracture aperture r and initial fracture aperture a'_{before}, and the binned average of the relationship between the change in fracture aperture r and initial mid-plane $\overline{h}$. For all samples, we see an average decrease in dissolution with increasing initial fracture aperture, and a cross-over to precipitation for the largest initial fracture apertures, which is consistent with the anticorrelation found for this relationship. For the average of the relationship between the fracture gap and the initial mid-fracture elevation, we do not see a typical trend. For the 4 hour experiment the relationship looks uncorrelated. For the 22.5 hour experiment there is more precipitation at the lowest point, no correlation between -0.15 and 0.15 mm, and increasing dissolution at the highest points. For the 41 hour experiment, it is more dissolution at the lowest point, and more precipitation at the highest points. As mentioned, the zero-displacement correlation coefficients between r and $\overline{h}$ are low or weak (0.2 to - 0.3) for all samples.

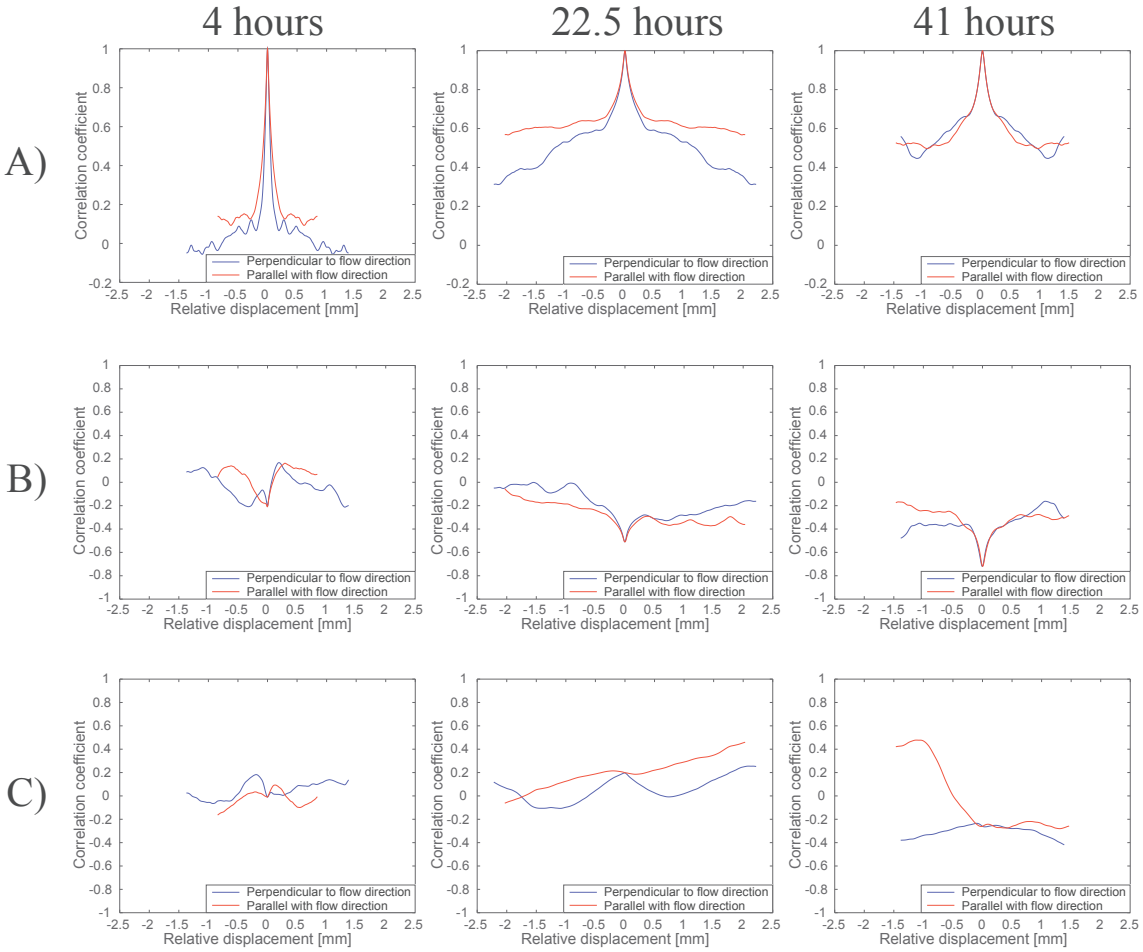

Figure 7.8: Correlation functions as function of relative displacement. A) is the autocorrelation of r, the change in fracture aperture, B) is the cross-correlation between r and the initial fracture aperture a'_{before}, and C) is the cross-correlation between r and the initial mid-plane $\overline{h}$

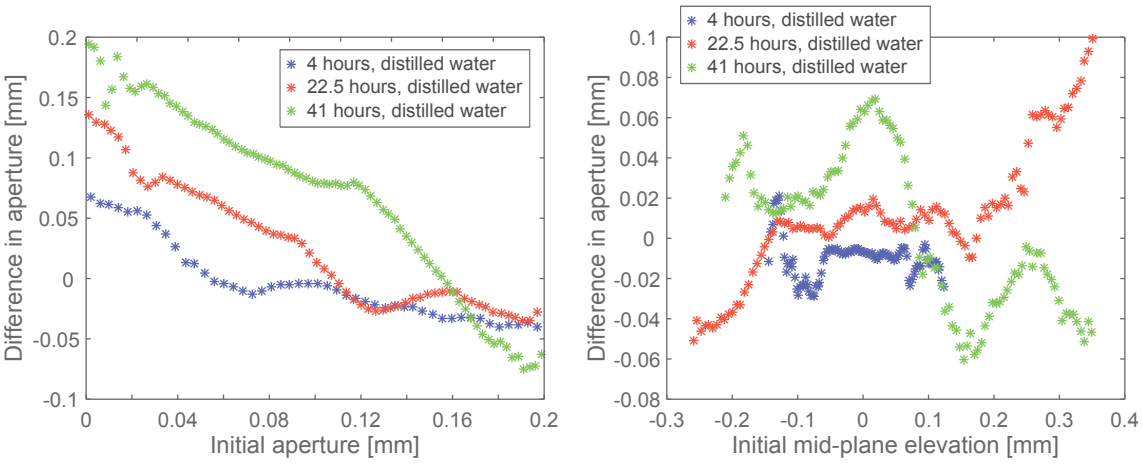

Figure 7.9: Binned average values of the change in fracture opening as function of initial fracture opening (left) and initial mid-fracture elevation (right)

7.4 Conclusion

In this preliminary study, we measured the roughness exponent for the fracture surfaces to be $\zeta \sim 0.7$, which is consistent with the morphology of fractures in materials with a disordered distribution of breaking strength [79]. Furthermore, the surface roughness was not observed to change after the durations of reactive flooding done in the experiments here (up to 41 hours). When investigating the evolution of the fracture apertures, we found that the regions with smaller initial apertures dissolved the most, while the regions with larger initial apertures had the most precipitation. This could perhaps be linked to the local flow velocity, which at a constant flux would be higher in the smaller apertures, providing more fresh water for reactions, while in the larger apertures the water would stay longer and deposit more chalk to the surface than is dissolved. For the shortest experiment (4 h), a pattern of dissolved lines along the flow direction was observed. The spatial correlation of reactions were found to increase with flow duration, first along the flow direction and later also in the perpendicular direction. We did not find a typical relationship between the change in fracture aperture and initial mid-plane.

Chapter 8

Conclusion and perspectives

This chapter is a summary of key findings together with some perspectives of future research.

For the invasion patterns during two-phase flow, we studied the typical patterns formed and characterized the surrounding deformations in the medium. The patterns are found to have similar fractal dimensions, around 1.5 and 1.6 for all boundary conditions, though the patterns show local differences depending on boundary conditions, where the invasion patterns in the open deformable medium changes the most as function of radius. For these invasion patterns, there is a transition with radius, with locally defined fractal dimensions, crossing over from around 1.7 - 1.8 initially, to 1.6 at an intermediate range and down towards 1.4 for the outer radii. The low outer fractal dimension indicates that the fingers cross over to a new instability, where 1 or 2 fingers come within a range from the outlet where beads become easier to displace, and grow on expense of the other fingers. This instability could be studied closer, e.g. evaluate how and where it begins as function of injection pressure, how fast the radial finger growth is, and if the behavior changes with constant injection rate rather than injection pressure.

The area of the two-phase flow patterns is found to follow a Family-Vicsek scaling with time and radius, where the scaling exponent for the area as function of time is higher for more deformable systems, i.e. $\alpha = 1.45$, 1.58 and 1.73 for the rigid, confined deformable and open deformable medium respectively. This indicates that the area of the invading clusters changes at a faster rate for more deformable media. This, to our knowledge, newly measured exponent for viscous fingers in deformable porous media, calls for theoretical evaluation.

During experiments, the displacements outside the invasion patterns are directed radially outwards due to a viscous pressure gradient in the saturating liquid, while the displacements are directed perpendicularly away from the air-liquid interface close to the longest fingers. In the confined deformable system the viscous pressure gradient leads to a compaction of the medium until it becomes rigid, while in the open deformable medium we observe an initial compaction of the medium followed by decompaction. Further analysis on the deformations would be to compute the Laplace solution for the pressure field in the liquid, and characterize the granular rheology by comparing the pressure gradient with displacements. The correlation between the directions of displacement and the negative pressure gradient could be

evaluated to investigate to what degree and where the displacements are directed against the pressure gradient. Results from the confined deformable and open deformable experiments could be compared to further investigate their differences and similarities.

In the study of air injection into dry dense granular media we have investigated both the patterns formed and the surrounding deformations together with simulated pressure fields. We found that the fractal dimensions for the developed channels in a confined dry granular medium was around 1.5 to 1.6, for injection pressures where the patterns were not too eroded by air flow. This is similar to the established fractal dimensions for viscous fingers in porous media, where randomly distributed capillary thresholds at the invasion front are responsible for the patterns being in a universality class modeled by the Dielectric Breakdown Model with $\eta = 2$ [2]. When investigating the deformations of the medium and simulated pressure fields, we found that the beads had a non-Newtonian, Bingham type rheology between the cell plates, which with noise in the thresholds can be responsible of placing the pattern growth into the same universality class as viscous fingers in porous media. The influence of these thresholds on the patterns formed is of interest to investigate further, for example, will the patterns look more like viscous fingers in an empty Hele-Shaw cell if the thresholds are very low compared to the pressure gradient, i.e. a rheology more like a Newtonian fluid? Will the patterns be rougher like viscous fingers in porous media if the thresholds are more significant and more disordered? This could be tested by varying the properties of the cell, beads or interstitial fluid. To lower the influence of the thresholds, maybe water could be injected into a water saturated medium instead of air into a dry one. Increased disorder in the thresholds for bead motion could be achieved by using fine grained sand instead of beads, or adding some roughness to the bottom plate of the cell, like a sandblasted plexiglass plate or a layer of sandpaper. In addition, simulations could be done where the beads and plates are frictionless, or where disordered friction could be added. Experiments can also be done to investigate how the patterns formed in a cell with open outer boundary and a rough bottom plate would change from the patterns formed in regular open cells.

The growth of the channel length with time was found to scale with injection pressure, and the growth can be modeled over time if the final length x_f is known. Before a critical time, the growth velocity is constant and scales with the injection pressure as $P_{in}^{3/2}$. After the critical time, the growth velocity follows a characteristic power law decay with time, $v(t) \sim t^{\alpha}$ with $\alpha = -2.5$. The critical time is found to depend on the final channel length in addition to the injection pressure. To be able to describe the channel growth by the injection pressure alone, it is necessary to investigate how the final length x_f depends on injection pressure and boundary conditions. In principle, a lot of data could be obtained quickly in repeated experiments where only the final length of the channel and the injection pressure is recorded. In addition, it is of interest to evaluate how the model for the channel growth proposed here would fit with experiments in other confined cells with e.g. different cell gap, fluids, bead size, and cell dimensions. Perhaps, if the behavior described by this model can be fitted to a given system, it could be developed and upscaled for field applications.

In the late compacted stage of the experiments, we observed intermittent growth of the channel tips due to sudden bead rearrangements ahead of the channel. It is believed that the pressure gradient of the diffusing field suddenly overcomes the granular stress of jammed beads such that they rearrange. When this happens, the rearranging zone is compacted by the pressure gradient such that a zone closer to the channel is decompacted. As these beads compact, the channel expands a few mm. These stick-slip events could be investigated more in detail by first forming a developed channel at a lower pressure, start recording images at a zoomed in region around the most advanced channel, and then increase the injection pressure to induce further bead rearrangements. Together with the recording of acoustic emissions, this could be a nice experiment for the development of localization techniques and identification of characteristic emissions. Related work with acoustics is presented in the co-authored papers in the next chapter.

The results in the preliminary study of reactive flow in fractured chalk indicate that more dissolution occurs in initially narrow fracture apertures, while less dissolution, or precipitation, occurs in initially larger fracture apertures. The correlation coefficient between initial fracture aperture and change in the fracture aperture was found to be -0.5 and -0.7 for experiments with 22.5 and 41 hours of reactive flow respectively. For the short 4 hour experiment, we observed a dissolution pattern of lines going roughly in the flow direction, not seen for the experiments which lasted longer. These are behaviors that should be investigated in further experiments, where various flow durations and flow rates should be tested. For example, preferably with a microscope that can efficiently profile the full fracture surfaces, experiments could be done where the fracture is profiled, flooded for some time, profiled, flooded again, and so on to make time lapse data. Full surface profiles could in addition make it easier to evaluate the fracture apertures, and enable correlations with larger offsets. The surface roughness exponent was not observed to change significantly for the durations of reactive flow we did (up to 41 hours), but it could be investigated as function of time in further experiments with longer durations. In addition, we designed a flow cell (not yet built) where the sample can be loaded parallel with, and perpendicular to the fracture plane in the diametrical direction, while the applied load is measured by force sensors. In future experiments, this cell could be used to characterize the effect of reactions on the solid stresses surrounding the evolving fractures.

Chapter 9

Co-authored papers

This chapter includes articles I have contributed to as a co-author during the work of this thesis, in particular contributing to the work with experiments and discussions.

9.1 Paper 4: Bridging aero-fracture evolution with the characteristics of the acoustic emissions in a porous medium

In this article, acoustic emissions during the same type of experiments as in chapters 5 and 6 are recorded and analyzed together with optical data from the high speed camera. The acoustic signals are recorded by piezoelectric sensors and shock accelerometers placed on the bottom plate of the cell. During experiments, air/solid interactions inside the cell create acoustic signals which are transmitted through the beads and excite the cell plates where the signals are recorded. Signature acoustic events are characterized in the Fourier spectrum and discussed together with the optical data to identify various sources, such as compaction of the medium, channel formation and distinct events due to particle rearrangements in the compacted state. It is found that there is typically a transition between Type 1 and Type 2 events during the experiments, where Type 1 events are non-impulsive low frequency signals associated with channel formation and compaction of the medium, and Type 2 events are impulsive signals with energies spread over a wide range of frequencies, associated with sudden particle rearrangements in the compacted stage. Furthermore, the Type 1 events are found to evolve during the channel growth with increasing mean frequency, and when the channel is developed there is a cross over to Type 2 events. The accumulated number of Type 2 events after the cross-over are found to follow a modified Omori law, similar to the stick-slip relaxation events which follows a big earthquake at real scale. The paper was published in Frontiers in Physics in September 2015.

PAPER 4

frontiers in Physics

ORIGINAL RESEARCH
published: 08 September 2015
doi: 10.3389/fphy.2015.00070

Bridging aero-fracture evolution with the characteristics of the acoustic emissions in a porous medium

Semih Turkaya[1], Renaud Toussaint[1], Fredrik K. Eriksen[1,2], Megan Zecevic[3], Guillaume Daniel[3], Eirik G. Flekkøy[2] and Knut J. Måløy[2]*

[1] Centre National de la Recherche Scientifique, Institut de Physique du Globe de Strasbourg, Université de Strasbourg, Strasbourg, France, [2] Department of Physics, University of Oslo, Oslo, Norway, [3] Magnitude, Sainte Tulle, France

The characterization and understanding of rock deformation processes due to fluid flow is a challenging problem with numerous applications. The signature of this problem can be found in Earth Science and Physics, notably with applications in natural hazard understanding, mitigation or forecast (e.g., earthquakes, landslides with hydrological control, volcanic eruptions), or in industrial applications such as hydraulic-fracturing, steam-assisted gravity drainage, CO_2 sequestration operations or soil remediation. Here, we investigate the link between the visual deformation and the mechanical wave signals generated due to fluid injection into porous medium. In a rectangular Hele-Shaw Cell, side air injection causes burst movement and compaction of grains along with channeling (creation of high permeability channels empty of grains). During the initial compaction and emergence of the main channel, the hydraulic fracturing in the medium generates a large non-impulsive low frequency signal in the frequency range 100 Hz–10 kHz. When the channel network is established, the relaxation of the surrounding medium causes impulsive aftershock-like events, with high frequency (above 10 kHz) acoustic emissions, the rate of which follows an Omori Law. These signals and observations are comparable to seismicity induced by fluid injection. Compared to the data obtained during hydraulic fracturing operations, low frequency seismicity with evolving spectral characteristics have also been observed. An Omori-like decay of microearthquake rates is also often observed after injection shut-in, with a similar exponent $p \approx 0.5$ as observed here, where the decay rate of aftershock follows a scaling law $dN/dt \propto (t - t_0)^{-p}$. The physical basis for this modified Omori law is explained by pore pressure diffusion affecting the stress relaxation.

Keywords: fracturing, lamb waves, acoustic emissions, power spectral evolution, Hele-Shaw cell

OPEN ACCESS

Edited by:
Ferenc Kun,
University of Debrecen, Hungary

Reviewed by:
Takahiro Hatano,
The University of Tokyo, Japan
Loic Vanel,
Université Claude Bernard Lyon 1, France

****Correspondence:***
Semih Turkaya,
Centre National de la Recherche Scientifique UMR 7516, Institut de Physique du Globe de Strasbourg, Université de Strasbourg, 5 Rue Rene Descartes, 67084 Strasbourg, France
turkaya@unistra.fr

Specialty section:
This article was submitted to Interdisciplinary Physics, a section of the journal Frontiers in Physics

Received: *29 June 2015*
Accepted: *21 August 2015*
Published: *08 September 2015*

Citation:
Turkaya S, Toussaint R, Eriksen FK, Zecevic M, Daniel G, Flekkøy EG and Måløy KJ (2015) Bridging aero-fracture evolution with the characteristics of the acoustic emissions in a porous medium. Front. Phys. 3:70. doi: 10.3389/fphy.2015.00070

1. Introduction

Fluid flow [1, 2], rock deformation [3] and granular dynamics [4] by themselves are very large scientific domains to investigate individually [5]. However, the idea of putting them together via a system of deformable porous medium with a fluid flow makes the phenomena even harder to understand. Rapid changes in the porosity of the medium due to fluid flow, channeling and fracturing via momentum exchange with the flow make understanding the mechanics of the system a challenge [6–9]. Hydraulic fracturing of the ground is a good example for this coupled behavior of solid and fluid phases. First, the pressure of the flow creates fissures and cracks which

changes the permeability of the initial rock. Then, a flowing mixture of fine sand and chemicals helps maintain this cracked state by penetrating the newly opened areas. By jamming and/or cementing the newly-formed channels and cracks, possible relaxation after injection is prevented. Thus, a more permeable state of the rock is preserved after injection for various types of industrial applications. Recently, various well-stimulation projects have attempted to use pressurized gas (N_2, CO_2), instead of water, to trigger fracturing within reservoirs for several reasons (e.g., to avoid wasting water, to sequestrate CO_2, environmental risks due to chemicals etc.) [10–12]. In this study, contrary to conventional fracturing methods, the fractures are induced using air injection.

Monitoring, predicting and controlling fracture evolution during hydraulic-fracturing, steam-assisted gravity drainage, or CO_2 sequestration operations is a key goal [13–16]. One possibility for monitoring is to use generated acoustic emissions during those operations. In the hydraulic fracturing industry, the typical monitoring devices consist of geophones and seismometers. However, the interpretation of the signals during fast deformations of porous media due to fast fluid flow is not simple. Particularly, the measurements of deformations are usually difficult to achieve in an opaque medium, and the source of the seismic waves and acoustic emissions can be complex. The study of microseismicity during well operations is routinely done in the industry, but its interpretation is often delicate [17–19].

In this paper, we present an experimental study using a purpose-built setup allowing channeling and fracturing due to fluid flow, where we can observe the deformations optically using a fast camera and transparent setup, and simultaneously record the mechanical waves emitted by the complex channels and fractures created. Both signals, optical and acoustic/microseismic, are then analyzed. They display a complex evolution of the source geometry, and of the spectral characteristics. The experimental setup designed to achieve this consists of a rectangular Hele-Shaw cell filled with 80 microns diameter grains, mixed with fluid (air). The linear cell has three lateral sealed boundaries and a semi-permeable one enabling fluid (but not solid) flow. During the experiments, air is injected into the system from the side opposite to the semi-permeable boundary so that the air penetrates into the solid and at high injection pressures makes a way to the semi-permeable boundary via the creation of channels and fractures - or at low injection pressures, directly using the pore network.

For a similar system of aerofractures in a Hele-Shaw cell, a numerical model was conducted by Niebling et al. [20]. These models were also compared with experiments for further development and validation [20–24]. Same kind of experiments—but without acoustic monitoring—with a Hele-Shaw cell have also been conducted. Johnsen et al. worked on the coupled behavior by air injection into the porous material both in fluid saturated and non-saturated cases to study multiphase flow numerically and experimentally [23, 25, 26]. Aero-granular coupling in a free falling porous medium in a vertical Hele-Shaw cell was studied numerically and experimentally by Vinningland et al. [27–29]. Varas et al. conducted experiments of air injection into the saturated porous media in a Hele-Shaw cell [30, 31] and in a cylinder box [32]. Eriksen et al. and McMinn et al. worked on injecting gas into a saturated deformable porous medium [Eriksen et al., submitted; 33]. Sandnes et al. classified different regimes of fingering of porous media in a Hele-Shaw cell [34]. Rust et al. developed a closed-system degassing model using volcanic eruption data [35]. Holtzman et al. also studied air induced fracturing where they identified different invasion regimes [36]. Furthermore, a recent study was conducted by Eriksen et al. where the air injection causes bubbles in a fluid-grain mixture [37].

The equivalent of microseismicity monitoring in the lab is the tracking of acoustic events. Hall et al. compared recorded acoustic emissions with the digital image correlation to track crack propagation in the rock samples [38]. Valès et al. used acoustic emissions to track strain heterogeneities in Argilite rocks [39]. Some studies have started to look at sources directly, both optically and acoustically, in various problems to characterize the different source mechanisms [40–44]. Farin et al. conducted some experimental studies on rockfalls and avalanches where he monitors those phenomena using acoustic emissions [45]. Stojanova et al. worked on fracture of paper using acoustic emissions created during crack propagation [46–48]. During the current experiments, acoustic signals are recorded using different sensors (shock accelerometers and piezoelectric sensors). Those signals are compared and investigated further in both time and frequency domains. Furthermore, during the experiments, photos of the Hele-Shaw cell are taken using a high speed camera. Thus, it is possible to visualize the complex branched patterns arising due to the solid-fluid interaction and to process images to gather information about the strain and strain rates, and investigate the mechanical properties of the solid partition.

2. Experimental Setup

A Hele-Shaw cell is made of two glass plates (80×40 cm) placed on top of the other, separated by 1.5 mm distance. The plates are separated via aluminum spacers placed close to the edges to provide equidistant spacing across the cell. For the experiments particular to this study, we completely sealed three boundaries of the Hele-Shaw cell and made one semi-permeable boundary using 50 μm steel mesh which allows fluid to exit the system but keeps the solid grains inside the cell. One of the plates has an inlet, which is used for injection of pressurized air, located at the bottom end of the plate, midway from the long edges 3 cm inside from one of the clamps close to the shorter edge (**Figure 1A**). The cell is filled with non-expanded polystyrene grains (80 μm diameter $\pm$1%) called Ugelstad spheres (see details in Toussaint et al. [49]). The density of the spheres is 1.005 g/cm^3. A mass of 170 g of grains is required to fill the cell, corresponding to an initial solid fraction of 52 ± 5% which is close to the 57% random loose pack for monodispersed grains [50]. Solid fraction of the grains in similar systems was investigated thoroughly by Johnsen et al. and found to be as low as 44% [23]. The difference between our experimental value and the theoretical value for an infinite box could be due to finite size of the cell which causes steric effect between the grains and the flat boundaries of the container, making the solid fraction 10–15% less [51]. Additionally, the

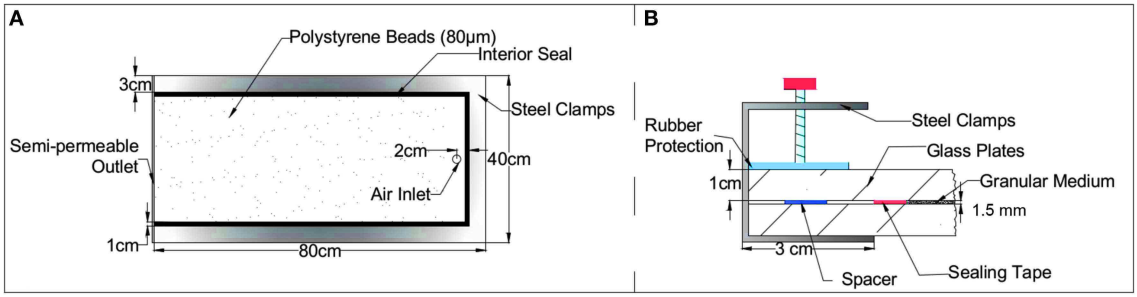

FIGURE 1 | Schematic diagram of the Hele-Shaw cell including the dimensions. (A) Top view of the Hele-Shaw cell including its dimensions. The cell is made of two glass plates which are placed on top of the other with 1.5 mm spacing between them. A porous medium is placed inside the cell. Three sides of the cell are sealed and the 4th boundary is sealed with a semi-permeable filter. **(B)** Side view of the Hele-Shaw cell showing clamp details. To protect the glass plates from point loading, a rubber sheet is placed in between the screw and the plate. Aluminum spacers are placed in between the plates to provide equivalent spacing everywhere in the cell.

measurement of 1.5 mm plate separation is subject to an error of 10% which has a direct effect on the solid fraction error bar. Electrostatic forces and humidity are also effective for real experimental beads and not for theoretical hard spheres, which can lower the solid fraction.

Some of the grains are colored with Indian ink to provide markers and texture, allowing a better resolution of the displacement measurements based on optical data. Images taken via high speed camera are used for digital image correlation to have full field measurements of displacement, velocity, strain rate etc. [21, 52–54]. The solid-air interface is placed 1-2 cm away from the inlet to avoid pressure localization close to the inlet. A schematic diagram of the Hele-Shaw cell is shown in **Figure 1**. The sides of the Hele-Shaw cell are clamped using steel clamps after sealing with double-sided rubber sealing tape. To protect the glass plates from stress focus on the clamping points, rubber sheets are placed between the clamp screws and the glass plates. Before placing the semi-permeable boundary, the cell is placed vertically and grains are poured inside. Following this, a semi-permeable filter is placed on the 4th edge. Then, the Hele-Shaw cell is positioned vertically, in a way that the semi-permeable boundary stays at the bottom side to decompact grains and homogenize the solid fraction through the cell. Another important goal of this rotation process is to provide a small rectangular buffer empty of grains around the air injection inlet to avoid having point injection force over the medium. After the filling phase, the Hele-Shaw cell is placed horizontally.

Air injection is started and ceased via an electrovalve placed on the pipe very close to the air inlet, (**Figure 2**). This air pressure is provided via a pressurized air tank. Injection pressure over time is constant. It starts like a step function and is monitored using a pressure sensor placed on the air inlet allowing to check if the real injection pressure is within 5% of the value required during the experiment.

During the experiments, acoustic signals are recorded using different sensors. The data recorded on the piezoelectric sensors which are mostly sensitive in the range (200–900 kHz) are amplified with a Signal Preamplifier. The data recorded on the shock accelerometers which are mostly sensitive in the range (1 Hz–26 kHz) are amplified with a Brüel and Kjaer Nexus Charge Amplifier—Type 2692-A. The amplified/conditioned signal is transmitted to the computer via a Ni-DAQ mx PCI-6133 acquisition card with multiple channels at 1 MHz sampling rate (**Figure 2**). In addition, synchronized with the acoustical data, images of the Hele-Shaw cell are taken via a Photron SA5 high speed camera transferred and stored numerically. A TTL signal is used as a trigger to initiate the injection and the data acquisition via the camera and the acoustic sensors, thus, enabling time synchronization between the apparatus. Ambient lab noise is also recorded for reference and investigated using camera and accelerometer recordings prior to air injection. After recording, the signals are corrected by using the response function of the accelerometers provided by the manufacturer and cross-checked at the lab.

3. Experimental Observations

At large enough injection pressures, the fluid makes its way by creating channels and fractures toward the semi-permeable boundary as seen in **Figure 3**. In the beginning, the solid-air interface of the porous medium (closest to the injection point) moves more or less homogeneously, with the appearance of only large scale curvature of the interface (**Figure 3B**). Then after roughly 150 ms, some thin finger-like carved formations of thickness around 2 mm start to appear at several points (marked with yellow circles in **Figure 3C**). As injection continues, those fingers penetrate further in the medium. They get larger and wider with the help of the air pressure (**Figure 3D**). In addition to that enlargement, fingers branch out into thinner fingers. In the end, a tree-like branched channel network is created inside the porous medium. As a result of those fractures and channels, the surrounding material is displaced and the porous medium is compacted. Fracturing, channeling and fluid interaction inside the porous medium has its effects on the granular part of the medium. These interactions also result in granular transportation and compaction which involves inter-granular interactions as well as interactions of the solid grains with the confining glass plates. Initially the solid fraction is homogenous inside the plate.

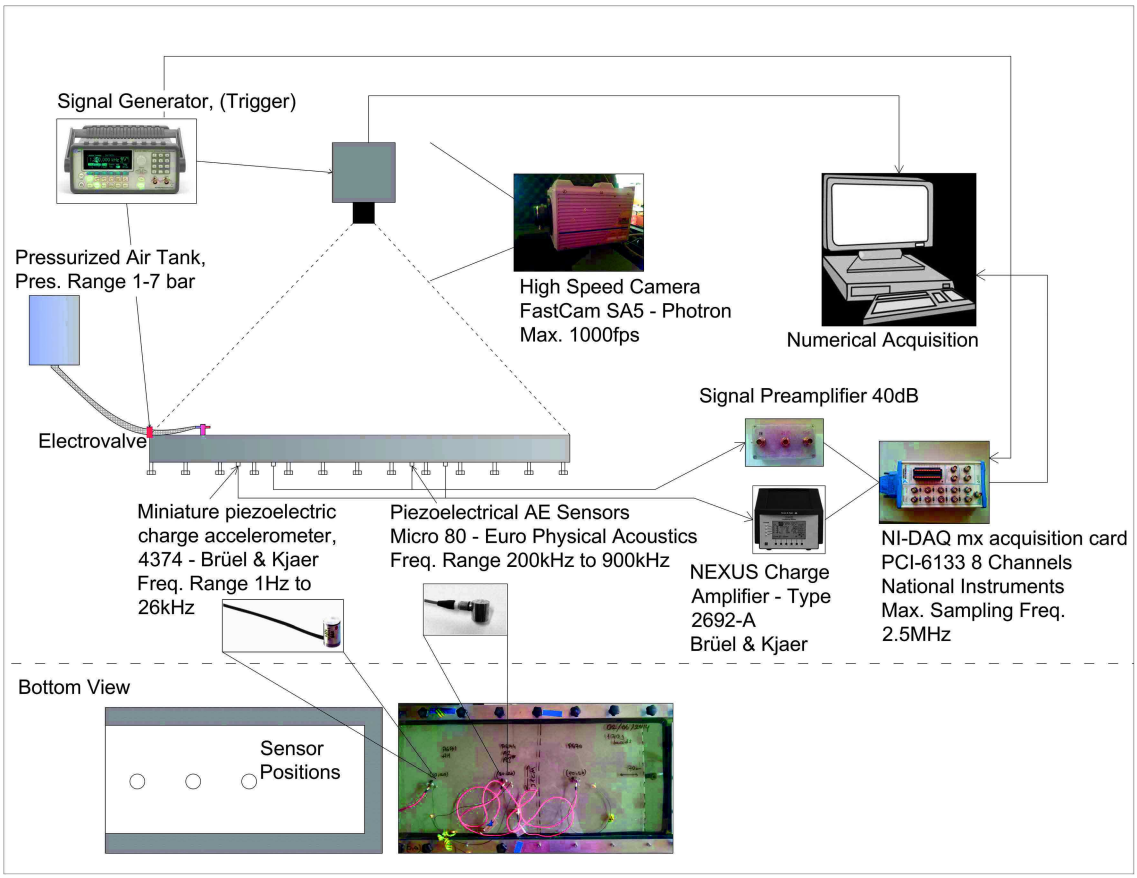

FIGURE 2 | The acquisition chain of the aero-fracturing experiments with a Hele-Shaw cell. The signal acquisition card, camera and the electrovalve connected to the air pump are triggered at the same time via a TTL sent from the signal generator to have synchronized optical and acoustic data. The sensors are placed on the bottom glass plate of the Hele-Shaw cell.

However, during the experiment the solid fraction of the grains increases in the close vicinity of the channels and fractures (up to the maximum possible solid fraction up to 63% for loose packed medium [50]. As observed in numerical models of such system in Niebling et al. [24], this solid fraction may decrease with distance from the fingers. After the experiment, depending on the pressure duration, initial solid fraction, and overpressure, some parts of the medium may have remained at the initial solid fraction, in other words may not have been compacted at all.

The acoustic events recorded during the experiments arise presumably due to sources of various types. While some vibrations are happening solely due to the air pressure fluctuation inside the channels, some others are generated by the stress increases on the plates due to granular compaction, intra-porous air pressure vibrations, granular shocks and variation of the friction forces. These sources excite the confining plates, transporting mechanical waves to the sensors, i.e., the source types that are convoluted with the response of the Hele Shaw cell structure. Eventually, what is recorded is not just a signal created by a simple source, but a systemic response (i.e., signals interacting with plates and clamps, reflecting from edges, refracting through interfaces and eventually having different characteristic properties) to the many individual processes happening inside the plate during the whole period of the experiment. Signature of the signals recorded during experiments did not depend significantly of the sensor type and location.

Even though many individual acoustic events are superposed in time in the recorded signals, and are influenced by a systemic response, this does not mean that their specific signature is lost. Superposed signals may hide their signatures in the time domain, however their influence in the power spectrum may still be noticeable. In the following section, the evolution of the power spectral signature with varying solid-fluid interactions (e.g., compaction of the solid with fluid pressure, channeling, diffusion of the overpressure of the injected fluid through the pore spaces etc.) is shown. First, the power spectrum of several snapshots in time (i.e., Fast Fourier Transform, FFT), taken from different experimental stages, are presented. Then, they are analyzed and compared with each other. The flowchart in **Figure 4** describes the analysis procedure.

4. Results

4.1. Power Spectral Evolution

The first time window analyzed, occurred prior to injection (i.e., at a state of rest). **Figure 3** shows an image of the Hele-Shaw cell,

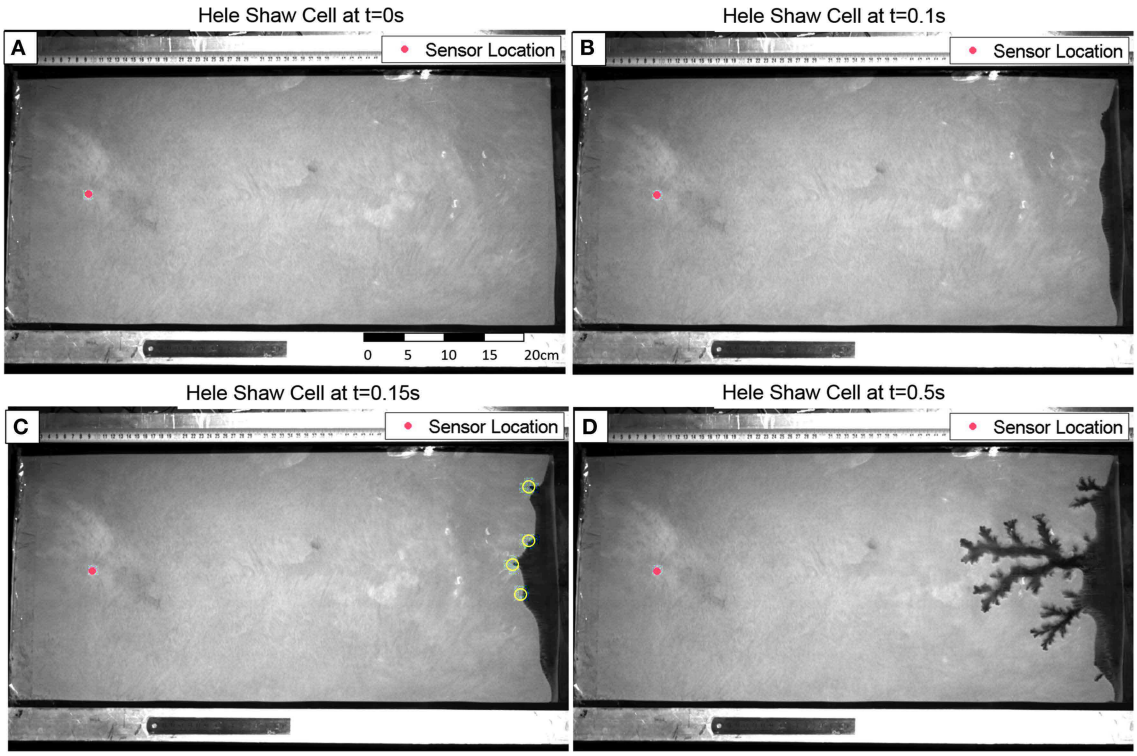

FIGURE 3 | Image of the Hele-Shaw Cell prior to injection (A), during quasi-homogenous compaction (B) and during channeling (C–D). Red dot shows the position of the acoustic sensor (accelerometer). Yellow circles in **(C)** represent the locations of the first finger-like carved formations.

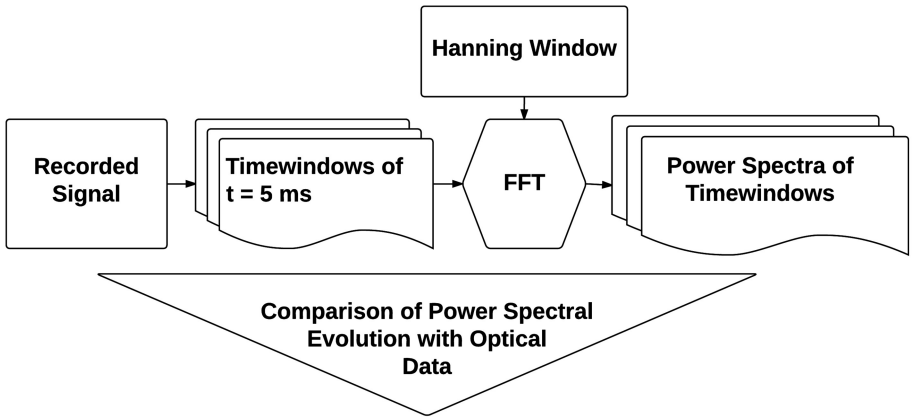

FIGURE 4 | Flowchart showing the acoustic-emission analysis procedure. Snapshots of the experimental signal is taken. Then, they are first converted to the fourier domain to obtain the power spectra. Afterwards, power spectra are compared with each other to understand differences.

acquired via the fast speed camera. The acoustic recordings at the same time step are shown in **Figure 5**. The air injection starts at $t = 0$ s.

Before injection, only ambient electrical noise in the recording system is present. Its power spectrum is flat (**Figure 5**, Right, Blue Curve). After correction with the sensor response the mechanical response (**Figure 5**, Right, Red Curve) is obtained. This noise represents the minimum mechanical vibration level which can be captured by the sensors without being hidden by the electrical noise. Aside from the ambient noise within the lab, no other signal is present. The red strip (time window of 0.005 s) on the experimental signal (**Figure 5**, Top-Left) shows the time window of signal when the picture in **Figure 3A** is taken. The FFT is applied to this time window to obtain the power spectrum which is presented in the right panel of **Figure 5**.

Compaction starts when the fluid (air) pressure is sufficiently large to move the solid grains. In **Figure 6A**, 150 ms after the

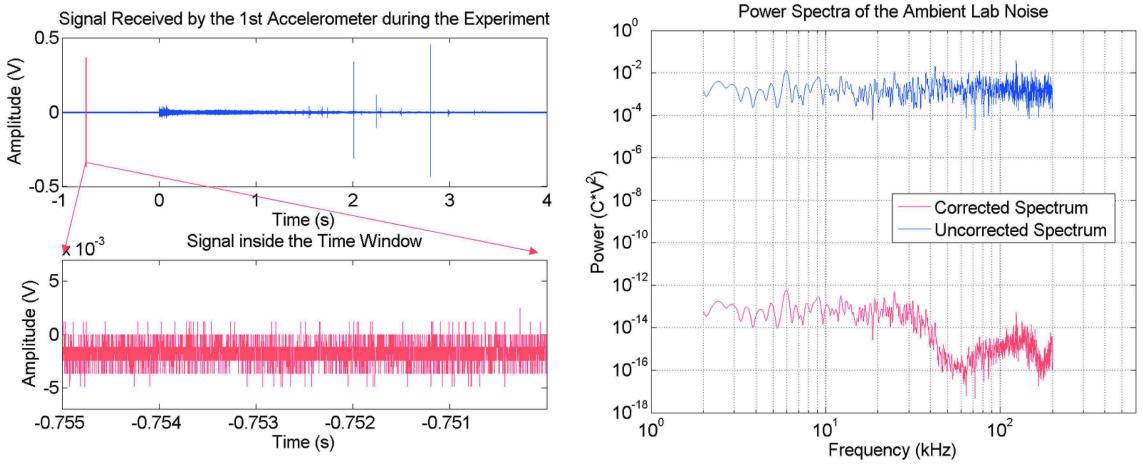

FIGURE 5 | Ambient Lab Noise recorded prior to experiment. The red strip in the top left panel (time window of 0.005 s) and its zoomed version **(Bottom left panel)** corresponds to the snapshot that the power spectra **(Right)** occurred at. **Right panel:** The uncorrected (blue) and corrected with sensor response (red) power spectra of the ambient lab noise.

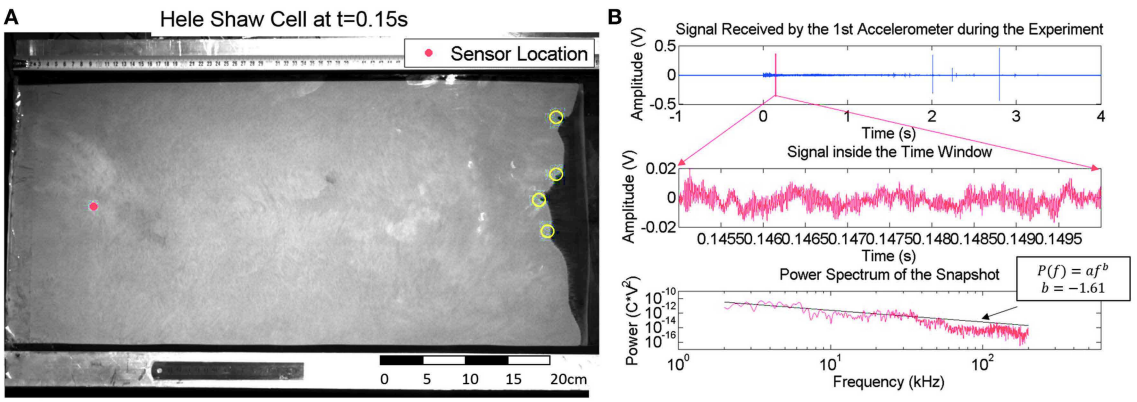

FIGURE 6 | Optical (A) and acoustic (B) experimental recordings just before channeling. Yellow circles on the left image shows the initiation points of the channeling. The red dot on the left image illustrates the sensor location where the signal on the right is recorded. Top Right panel: Acoustic signal recorded throughout the entire experiment. The red strip (time window of 0.005 s) corresponds to the snapshot that the image **(A)** and power spectrum (Bottom Right) occurred at.

start of the injection, channel initiation can be observed at several points, as highlighted by the yellow circles. Due to the interaction between the solid and fluid phases inside the Hele-Shaw cell, some mechanical signals are generated. The power spectrum of the signal recorded during this snapshot is presented in the bottom right panel of **Figure 6**. As channeling continues, the bulk movement of the grains takes place together with fluid motion. This causes emergent acoustic emissions which are predominantly in the low frequency range (less than 10 kHz). Vibration of the plates, granular friction and stress differences on the plates due to compaction create waves that are also in the power spectrum. All those contributions from different source mechanics gives a shape to the presented power spectra, similar to a power law decay having an exponent $b = -1.61$.

In addition to this slope, it is possible to find the mean frequency of the power spectra using Equation (1).

$$\langle f \rangle = \frac{\int f|a(f)|^2 df}{\int |a(f)|^2 df} \tag{1}$$

This will show the dominant frequency range within the signal. In the following **Figure 7**, it can be seen that the mean frequency starts very low and then increases with increasing energy in the high frequency range. As the channel network develops, we see that the mean frequency reaches to its maximum value. Using cubic fitting, this mean frequency curve is estimated and compared with the optically obtained curves. An inflection point of the fitted curve is observed around time $t_0 = 1.49$ s after injection. This corresponds to the point where the finger

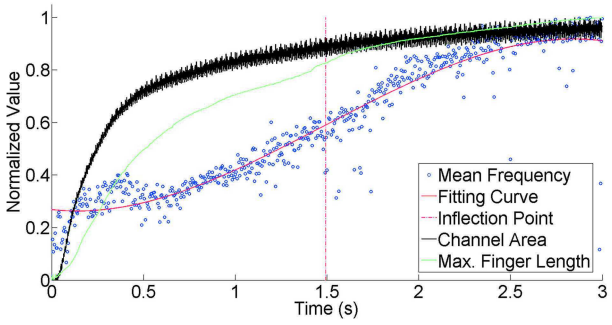

FIGURE 7 | Mean frequency evolution (normalized with the maximum value 200 kHz) during injection. As the channel network develops progressively the energy percentage in the low frequency range $f < 10$ kHz diminishes, and the mean frequency gets higher. A cubic polynomial curve (red) is fitted to the mean frequency data to simplify the comparison and discussions. The location of the inflection point of this curve is indicated by the (red) dash dot strip ($t_0 = 1.49$ s). In this curve the normalized maximum finger length (green, maximum value is approximately 35 cm) and the carved area (black, maximum value is approximately 270 cm^2) is also presented.The area saturates to a maximum at a time close to t_0. The length still increases slightly after t_0, in particular, a small step in finger length (high slope of the length curve, corresponding to a large stick slip event connected to the finger) can be noticed around t_0.

development stops and the regime inside the Hele-Shaw cell changes to a slow relaxation stage with slow fluid overpressure diffusion detailed in the discussion section.

4.2. Acoustic Events

It is possible to link the information received from the small scale lab experiments with large scale data, and vice-versa. In the experiments, we noted that the number of acoustic events occurring inside the Hele-Shaw cell is related to the empty channel area. However, after the fractured area reaches the final channel network shape, stress relaxation events are observed. These events are investigated further using event counting methods based on the ratio of Short Term Average over Long Term Average (STA/LTA) for event detection and compared with the evolution of the channel area inside the Hele-Shaw cell.

4.2.1. Event Detection

Detecting the number of events occurring during fracturing is a good indicator of the compaction level within the material. As long as there is motion of granular particles with the fast fluid flow it is very probable to detect some acoustic events in the experimental recording. However, it is very important to analyze and understand which part of the recording can be labeled an event and which part can not. STA/LTA threshold method is commonly used in seismic data interpretation [55–58]. If the parameters are selected carefully, it is very easy to use and is very robust [59]. While LTA considers the average temporal noise to have an idea of the general behavior of the site, STA looks for intense changes in the signal in a small time window to detect acoustic events. Thus, it makes the ratio of those two parameters sensitive to the more complex events as well. When this STA/LTA ratio passes a pre-defined threshold, it is considered as an event (**Figure 8**), and the event counter is incremented. As long as the ratio stays above the threshold, it does not trigger again. Right after the ratio goes below the threshold, the algorithm can be triggered again for the next event to be counted. This algorithm (for one time window) can be generalized as follows:

$$\frac{(STA)}{(LTA)} = \frac{\frac{1}{N_s}\sum_i^{i+N_s}(s(i)^2)}{\frac{1}{N_l}\sum_i^{i+N_l}(s(i)^2)} \tag{2}$$

$$\Psi = \frac{(STA)}{(LTA)} \rightarrow \Psi > T \rightarrow Event \tag{3}$$

where $s(i)^2$ is the squared raw signal in the time domain (if necessary, a filtered signal $s'(i)^2$ can be used for different characteristic events), N_s and N_l are the length of the short (0.05 ms) and long time (1 ms) windows respectively and T is the predefined threshold for an event. The threshold to detect events may change between different datasets or different types of acoustic events.

4.2.2. Event Classification

One important thing that should be mentioned about the STA/LTA counting method is the frequency range used. After detailed analysis, it has become apparent that two different types of events exist within the experimental dataset. The first type of events are the non-impulsive low frequency (less than 10 kHz, similar to **Figure 6**) events (Type 1) which are related to the fluid flow and to the fluid-grain interactions rearranging the grains and producing major deformations and channeling. These events begin at the moment when the air injection starts and continue until a fully developed channel network is reached. It is possible to determine accurately this period from the optically acquired data, simply by calculating the area of the channel (estimated via the number of dark pixels in a binarized image) that saturates to a maximum value before the end of the acoustic emissions. Interestingly, in our findings, the number of Type 1 acoustic events follows a similar trend in time as the evolving emptied channel area within the Hele-Shaw cell (**Figure 9**). To enable the detection algorithm to distinguish between the different types of events, frequency filters are applied. To detect Type 1 events, a butterworth bandpass filter with corner frequencies 100 Hz and 10 kHz is applied to the raw signal $s(i)$ before the STA/LTA event detection is applied.

The second type is the aftershock-like events, Type 2. Unlike the Type 1 events, in power spectrum their energy is spread over a wide frequency range similar to the one presented in **Figure 10**. These events are similar to the stick-slip relaxation events following a big earthquake in real scale. Compacted grains are rearranging their positions to have a more compacted state due to continuous air injection which results in some of their energy being released as acoustic emissions. To detect Type 2 events, a highpass filter for frequencies higher than 100 kHz is applied to the raw signal $s(i)$ before the STA/LTA event detection is applied. In **Figure 11** the evolution in the power spectrum with time is presented. In the figure, a Type 2 event occurred at $t = 2.8$ s is also presented.

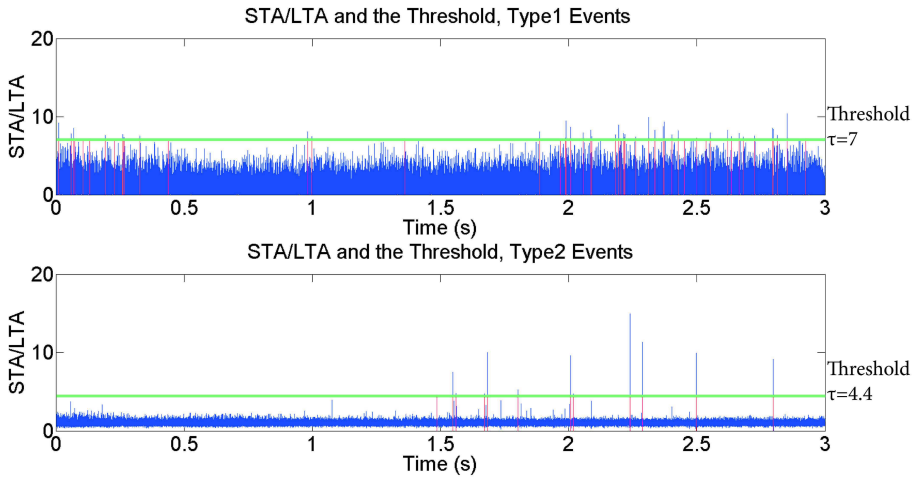

FIGURE 8 | STA/LTA detection plots for Type 1 (upper figure) and Type 2 (lower figure) events. Top: The raw signal is filtered by using a butterworth bandpass filter with corner frequencies 100 Hz and 10 kHz before computation. **Bottom:** The raw signal is filtered by using a highpass filter for frequencies higher than 100 kHz before computation. We found that some of the Type 2 events can be classified as Type 1 events since they have energy in the low frequency higher than the threshold.

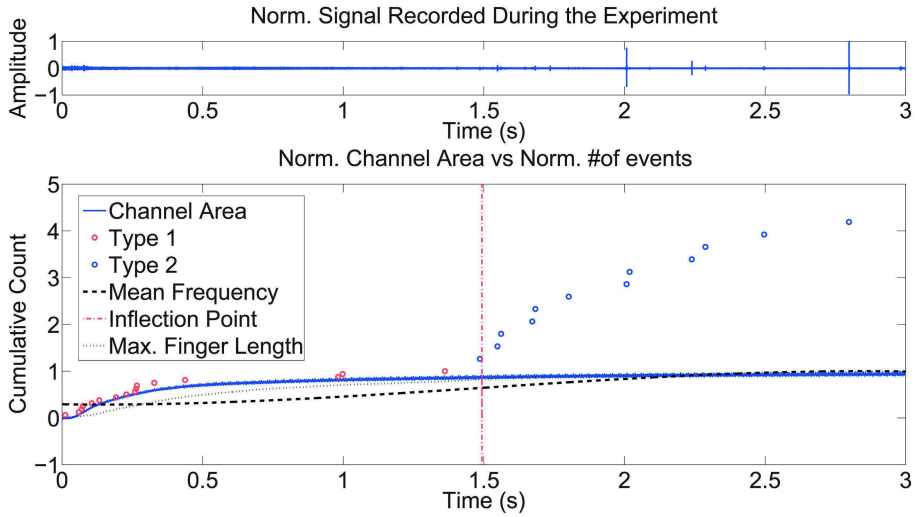

FIGURE 9 | Top: Signal recorded during the experiment. **Bottom:** Blue curve shows dark pixel counting over the image to compare compacted area with the number of different acoustic events occurred. Circles represent cumulative number of events normalized with maximum number of Type 1 events (i.e., 17 events). Cumulative number of Type 1 events (red points) are fitting well to the normalized channel area with time presented in the lower plot. First Type 2 (blue) event occurs very close to the inflection point of the mean frequency curve. Type 2 events are very impulsive and noticeable in the top panel as well.

After investigating further, we also noticed that the occurrence frequency of these events decay with time, similar to the Omori Law [60, 61]. In the following section, curve fitting to the number of Type 2 acoustic emissions assuming an Omori Law decay (**Figure 12**) will be discussed.

4.2.3. Omori Law

Omori [60, 61] worked on the half-day and monthly frequencies of aftershocks of the 1891 Nobi earthquake in Japan [60, 61] . He found that the frequency of aftershocks $n(t')$ at time t' can be expressed as:

$$n(t') = K(t' + c)^{-1} \tag{4}$$

and the same equation for the cumulative number of aftershocks is given as

$$N(t') = \int_0^{t'} n(s)ds = Kln(t'/c + 1), \tag{5}$$

where c is a characteristic time, small and positive, K is the slope of the fit in the semi-logarithmic domain and $N(t')$ is the number of cumulative aftershocks up to time t'. Following

Omori, Utsu (1957) emphasized that the real aftershock activity decays with time differently than the originally derived Omori Law and proposed the equation for the frequency of aftershocks, with another fitting exponent p, as Utsu [62, 63]:

$$n(t') = K'(t' + c')^{-p} \tag{6}$$

and called this the Modified Omori Law (MOL). The corresponding equation for the cumulative number of aftershocks is given as:

$$N(t') = \frac{K'}{(p-1)}\left(c'^{1-p} - (t' + c')^{1-p}\right) \tag{7}$$

where c' is a characteristic time and K' is the slope having the dimension of time$^{(p-1)}$.

Using these approaches Omori Parameters K, c and p are estimated on our experimental catalog of Type 2 events, using time $t' = t - t_0$, where t_0 is the time defined in Section 4.1, that corresponds to the end of the channel formation and to the inflection point of the mean frequency recorded (**Figure 12**). A bin size to find frequency of occurrence of the events is selected as 0.2 s. However, it is more robust to use cumulative number of aftershocks (Equations 5 and 7) to avoid choosing an additional parameter for binning which can vary. Fitting is computed with 95% confidence bounds (i.e., two standard deviations away from the mean of the estimated value) to show the quality of fitting. Fitting parameters are calculated by a linear regression in the semi-logarithmic space of the cumulative number of events as $K = 4.89 \pm 1.33$ and $c = 0.13 \pm 0.8$ s. The Root Mean Square Error (RMSE) - average of the residual of the fit - is calculated to be 0.57 in this particular fit using the Equation (5).

Using the Modified Omori Law (i.e., Equation 7) fitting parameters are found as $K' = 5.34 \pm 1.52$ s$^{-0.45}$, $c' = 0.0066 \pm 0.55$ s, $p = 0.55 \pm 0.38$ and RMSE is calculated to be 0.53 and the error bar is evaluated as the standard error [64]. The dashed lines in the **Figure 12** represents two RMSE from the fitted curves.

5. Discussion

5.1. Discussion of the Experimental Results

The power spectrum of the mechanical signal at the different time windows show that the interactions inside the Hele-Shaw cell are evolving with continuous injection. In the beginning, there is a bulk movement of the grains due to the compaction caused by air injection. In **Figure 6B** it can be seen that the power spectrum follows a power law trend with an

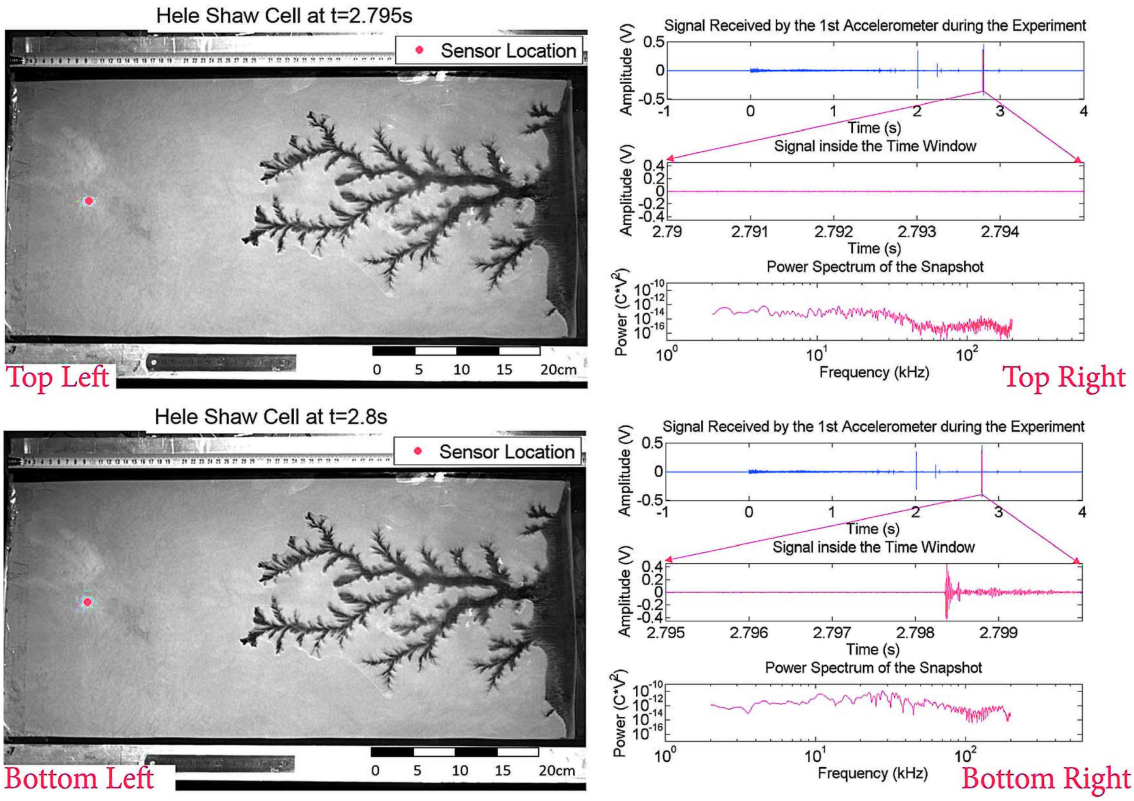

FIGURE 10 | Optical (Left) and acoustic (Right) experimental recordings just before (Top) and during (Bottom) an aftershock like event. The red dot on the left image illustrates the sensor location where the signal on the right is recorded. **Top Right:** Acoustic signal recorded throughout the entire experiment. The red strip (time window of 0.005 s) corresponds to the snapshot that the image **(Left)** and power spectrum **(Right)** occurred at.

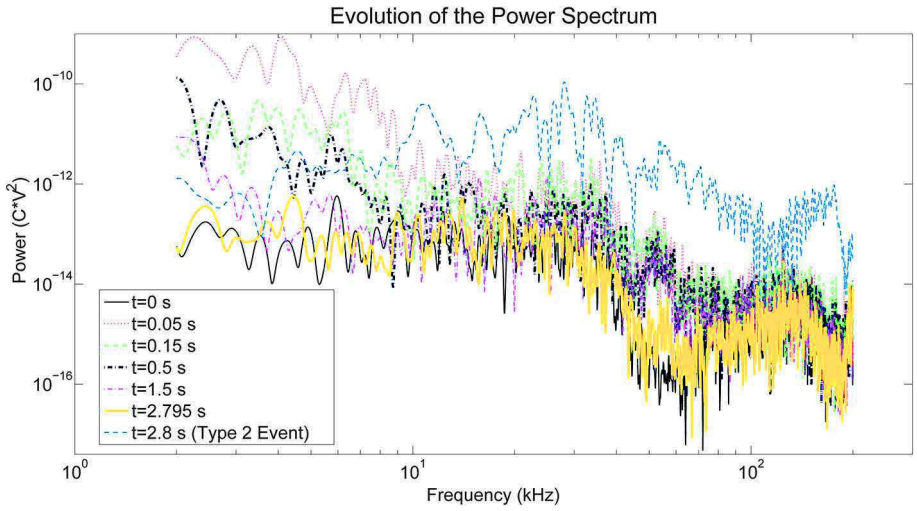

FIGURE 11 | The evolution of power spectrum over different time windows are presented. With time, the power is decreasing until finally reaching back to the initial level. However, during Type 2 events the spectrum has a completely different signature.

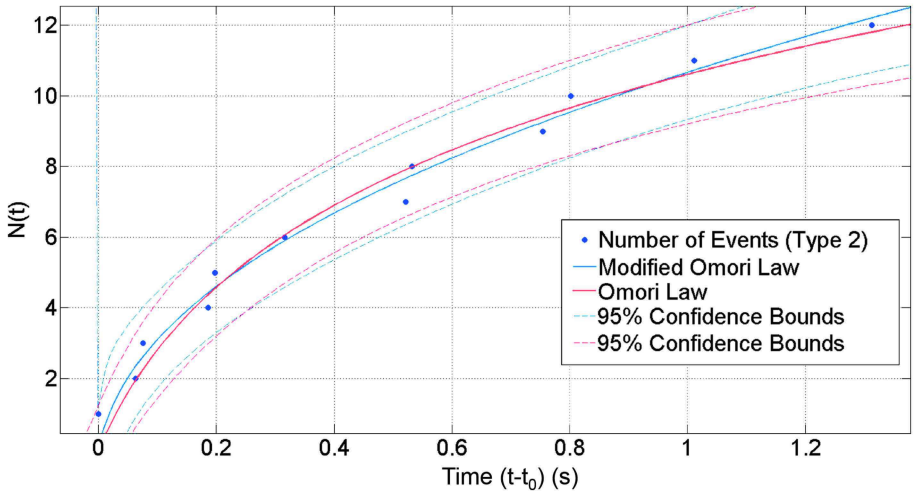

FIGURE 12 | Conventional and Modified Omori Law Fits of the cumulative number of events. The circles represent the cumulative number of events and the solid lines represent the fitting curves given by the Equations (5) and (7). $t' = 0$ in this representation corresponds to time $t_0 = 1.49$ s after the start of the air injection.

exponent equal to −1.61 without any major peak. This indicates, although there are many different phenomena with various characteristic frequencies happening at the same time (e.g., bulk compaction, interactions between solid and fluid phase, stress redistribution among the medium etc.), that a scale-free mechanical phenomenon—probably related to the developing branching pattern—is dominating the emissions. Since the low frequency has higher energy, it can be seen that the mean frequency of the initial part $t < 1.5$ s is low as well (**Figure 7**). As the channeling and fingering starts, the mean frequency is shifting from lower frequencies $f < 10$ kHz to the higher frequencies. Moreover, this evolution can be seen in **Figure 11**. Rising mean frequency is also seen in the signals recorded during some volcanic processes, as e.g., the 2004 eruption process of the Arenal volcano, Costa Rica, and was interpreted as related to the stress increase with time due to the fluid pressure [65]. Additionally, the rate of this increase decreases as the channel network establishes. The trend which represents the channel area and also increasing permeability due to fracturing, is given in **Figure 9** by checking the dark pixels in the images through time. Occurrence frequency of low frequency earthquake-like events (described as Type 1) decreases with increased permeability due to fingering and fracturing indicated in the work of Frank et al. about real scale events seen in Mexico [66].

The inflection point (**Figure 7** red dash dot line) of the mean frequency curve ($t_0 = 1.49$ s) shows the point where the power spectra evolves from a power law trend (**Figure 6B**) to stick-slip aftershock like events (**Figure 10**, Bottom Right) whose

power spectra consists of several peaks in the frequencies higher than 10 kHz (**Figure 11**) which causes the increase in the mean frequency. This inflection point occurs almost at the same time as the small step in the maximum finger length curve (high slope of the length curve, **Figure 7** green) can be noticed around t_0. This small step shows a stick slip motion in the most advanced finger tip. The inflection point also corresponds to the start of occurrence of the first Type 2 event which is presented in **Figure 9**. We can thus attribute it to a change in dynamics of the pneumatic fracture process: the main tree of channels stabilizes, and a slower stress relaxation process starts in the bulk around the channels, which leads to different type of acoustic event signatures, associated to the appearance of the impulsive Type 2 events.

The presence of this inflection point in the average frequency of the power spectrum, and the appearance of impulsive events (Type 2), can be suggested as the interesting signatures of the stabilization of the main channel during the monitoring of field scale hydrofracture or pneumatic fracture: these clear signatures can be detectable even in opaque field scale microseismic monitoring studies. This change of event types can also be seen in **Figure 9** which shows the event detection using STA/LTA event detection procedure. As presented in the bottom panel of **Figure 8**, Type 2 events are detected starting from the inflection point of the mean frequency curve ($t_0 = 1.49$ s). Furthermore, we noticed that the cumulative number of Type 2 events are following an Omori Law trend which is shown in the **Figure 12**. This is due to the similarity between the aftershocks which is observed in real life and the Type 2 events in the medium which are due to the local stress relaxations. $K = 4.89 \pm 1.33$ and $c = 0.13 \pm 0.8$ s for the Omori Law and $K' = 5.34 \pm 1.52$ $s^{-0.45}$, $c' = 0.0066 \pm 0.55$ s, $p = 0.55 \pm 0.38$ for the Modified Omori Law are computed as fitting parameters. It can be said that the Modified Omori Law—Equation (7)—gives slightly better fitting results to this dataset (RMSE is 0.57 for Omori Law and 0.53 for Modified Omori Law) due to the application of another parameter which is making the fitting procedure more sensitive.

The obtained p-value in this study ($p = 0.55$) corresponds to the p-value range for earthquakes studied by different scientists (i.e., 0.6–1.6 [63], or 0.3–2.0 [67]). There are several studies for different types of earthquake mechanisms with varying p-values. Utsu [63] presented some of them: $p = 0.9 \pm 0.1$ is found for the 1962 Westport earthquake in New Zealand, $p = 1.4$ is found for the 1965 Hindu Kush intermediate-depth ($h = 214$ km) earthquake, and $p = 0.84$ is found for the aftershocks following a rock fracture event in a mine causing a low magnitude earthquake ($M = -2$). This variability has been attributed to the variations in the state of stress, temperature, structural heterogeneities, material parameters, etc., in different tectonic regimes. However, a single, dominant factor controlling this parameter has not yet been identified [68].

In different examples, post-injection fluid-induced seismic events at various injection sites such as Fenton Hill, USA, and Soultz-sous-Forêts, France, appear to decay with an Omori-like fashion [69]. The rate of the post-injection seismic events in these cases has not been analyzed using the conventional MOL, thus a direct comparison between the obtained p-values cannot be carried out. In other examples, Nur and Booker [70] found that the decay of earthquakes following a step in the pore fluid pressure obeys a Modified Omori Law (MOL) with $p = 0.5$, which was consistent with a pore fluid diffusion law. Similarly, Yamashita worked on a model linking the fault slip and fluid flow in a system preloaded in shear. He found that the p-value is 0.48 for an early time period in a sequence of induced secondary aftershocks [71]. This link was also derived by Shapiro et al. [72–74] and Rozhko et al. [75] for the events related to pressure changes in operation wells. Their formulation relates the rate of acoustic events to the temporal change in pore pressure. This is very similar to the p-value obtained by fitting the MOL to our experimental results.

5.2. Physical Explanation of the Experiments

The observed p-value in our experiments is also consistent with the derivations and approximations carried out in the models derived by Niebling et al. [20, 24] or Johnsen et al. [25] for systems related to the one currently studied. The exponent of this Modified Omori Law and its prefactor can be directly related to the stress relaxation due to the diffusion of fluid pressure with the following approximations - that will be validated a posteriori by the agreement between the exponent and prefactor derived and the one that can be measured directly.

After the initial fast stage where the large empty channel is created, the compressibility of the fluid induces a slower seepage into the surrounding material. The boundary conditions can be considered as fixed for the granular material along the channel: owing to the large permeability of the channel, the boundary condition along the channel corresponds to an approximately homogeneous fluid pressure equal to the imposed inlet pressure, which also corresponds to the total stress since no grains are present in the channel, and the total pressure and pore pressure correspond on this boundary. The outlet boundary conditions can be considered as fixed pore pressure equal to the atmospheric one, and fixed displacement due to the semipermeable grid. The boundary conditions along the plates correspond to no flux for the fluid, and no normal displacement for the particles.

Since no large motion occurs in the following relaxation stage, the total stress field in the medium can be approximated as constant. This total stress $\sigma^{\mathbf{T}}$ is the sum of the solid stress $\sigma^{\mathbf{s}}$ arising from the forces transmitted in the grain-grain and grain-plate contacts, and the pore pressure $\mathbf{p}$:

$$\sigma^{\mathbf{T}} = \sigma^{\mathbf{s}} + \mathbf{pId}, \tag{8}$$

where $\mathbf{Id}$ is the identity matrix. This general formulation of summing the solid-bearing and fluid-bearing parts of the stress is for example demonstrated by Jackson [76], and is valid as long as the large scale shear stress due to fluid-solid momentum exchange is negligible. It was shown to hold, for example, in sheared saturated granular layers [77].

The total stress being fixed with fixed boundary conditions, the balance between solid-bearing and fluid-bearing stress changes as the fluid seeps in due to pore pressure relaxation. For every grain-grain contact and grain-plate contact, the stick/slip

criterion can be described using a Coulomb friction criterion according to which slip occurs when the equality is reached:

$$\sigma_s^s \geq \mu \sigma_n^s, \tag{9}$$

where σ_n^s and σ_s^s are respectively the norms of the normal and shear (frictional) solid stress transmitted by the contact considered, and μ is the friction coefficient depending on the characteristics of the contacting elements (grains and plates).

The fluid can be explicitly considered by expressing this law in terms of total stress and fluid pressure, using Equations (8, 9) which leads to a formulation corresponding to Terzaghi's 1936 effective stress formulation [77, 78]:

$$\sigma_s^T \geq \mu(\sigma_n^T - p), \tag{10}$$

where p is the pore fluid pressure. With fixed total stress, Equation (10) can be reformulated in terms of fluid pressure required for the grain pairs to slide:

$$p > \sigma_n^T - \frac{\sigma_s^T}{\mu}. \tag{11}$$

We assume a random distribution for the local total stress values, σ_s^T and σ_n^T, and call ξ the density of contacts per unit surface of the plates that will break with an acoustic emission due to sufficiently high pore fluid pressure. According to the above criterion, when p rises from the initial value to the final one a slip, during which micro acoustic events are produced, happens. The rate of events can be derived as follows: the system is considered to have a quasi one dimensional geometry where the grains ahead of the channel in the average flow direction correspond to $x > 0$. The initial value of the overpressure (i.e., pressure above the atmospheric pressure) is approximated as $P = P_{max}$ for $x < 0$ and $P = 0$ for $x > 0$. This holds if the initial channel creation was fast compared to pressure diffusion, so that the pressure skin depth stayed small with respect to the system size during channel creation, which was verified numerically by Niebling et al. [20].

The variation of the pore pressure over time is thus the key factor in this system to change stability of the porous medium. This pore pressure can be expressed using the fluid pressure diffusion into the porous medium. Considering that the grains are not moving, the pore velocity v_d of the fluid (local velocity in the pores) and the Darcy velocity v_D, can be computed from Darcy's law. As presented e.g., in Niebling's work [22] or Johnsen's [26]:

$$v_d = \frac{v_D}{\phi} = -\frac{\kappa}{\phi\mu}\nabla P \tag{12}$$

where κ is the local permeability, ϕ is the local porosity of the granular medium, μ is the fluid viscosity and P is the pressure gradient driving the flow. Implementing this equation into conservation of mass we have:

$$\partial_t(\phi\rho(P)) + \nabla(\phi\rho(P)v_d) = 0 \tag{13}$$

where $\rho(P)$ is the updated mass density of air, obtained assuming the state equation of a perfect gas which is following the relation $\rho(P) = \rho_0 \frac{P}{P_0}$ which is valid for this type of setups since the pressure is not varying by orders of magnitude with no strong density changes over the cell. When the pressure dependence of the density is included in the analysis which is indeed more correct, the diffusion equation becomes nonlinear. It can be treated numerically, Niebling et al. [20]. As shown by Niebling et al., no qualitative changes are noted in this kind of regime though and the same kind of scaling law for the growth of the skin depth is observed. In this equation, ρ_0 is the density of air and P_0 is the atmospheric pressure. This puts Equation (13) into the form:

$$\frac{\rho_0}{P_0}\partial_t(\phi P) - \nabla(\rho_0 \frac{\kappa}{\mu}\nabla P) = 0. \tag{14}$$

Considering that porosity ($\phi = \phi_0$) and local permeability ($\kappa = \kappa_0$) does not change with time, after some simplification Equation (14) will become:

$$\frac{\phi_0}{P_0}\partial_t(P) - \frac{\kappa_0}{\mu}\nabla^2 P = 0. \tag{15}$$

Then, from Equation (15) we can derive the diffusion equation as:

$$\partial_t(P) = \frac{\kappa_0 P_0}{\phi_0 \mu}\nabla^2 P \tag{16}$$

where the part before the pressure gradient of Equation (16) can be described as diffusivity constant of overpressure in a porous medium, corresponding to the slow Biot wave [79]:

$$D = \frac{\kappa_0 P_0}{\phi_0 \mu}. \tag{17}$$

The local permeability κ_0 can be computed using Carman-Kozeny equation [22]:

$$\kappa_0 = \frac{d^2}{180}\frac{\phi^3}{(1-\phi)^2} \tag{18}$$

where $d = 80\,\mu$m is the diameter of the grains and ϕ, the porosity of the medium, is around 48% which is typical for this kind of preparation. The results of Niebling et al. [20] show that in this kind of system, fast forming aerofractures are formed, followed by a slow diffusion of overpressure away from the large channels - our slow relaxation stage.

He modeled the behavior of the aerofractures with two different stages, with initially a fast channel formation in the beginning due to the high fluid pressure and following, close to the injection point, a thick compaction front which satisfies Equation (11).

As the overpressure diffuses in the medium, the grains can slip and rearrange, possibly giving rise to the acoustic events. The fundamental solution of Equation (16) is derived with an approximated 1D boundary condition, having an initial condition $P = 0$ at $t = t_1$ describing the finger tip as a flat boundary at $x = 0$, and the space ahead of it as $x > 0$. Then, the initial condition for the overpressure is $\Delta P = 0$ for $x > 0$ and $t = t_1$ (when the finger stops and the overpressure has not

yet penetrated far from the boundary). Furthermore, boundary conditions corresponding to the imposed overpressure are $\Delta P = P_{max}$ at $x = 0$ (the finger boundary), and $\Delta P = 0$ at $x \to +\infty$ (far ahead of the finger). The solution of the diffusion Equation (16) gives the overpressure at distance x ahead of the tip of the empty channel, and at time $t > t1$, after the end of the channel formation [25]:

$$\begin{aligned}\Delta P(x,t) &= P_{max}\mathrm{erfc}\left(\frac{x}{2\sqrt{D(t-t_1)}}\right)\\ &= P_{max}\frac{2}{\sqrt{\pi}}\int_{x/2\sqrt{D(t-t_1)}}^{\infty} e^{-y^2}dy \end{aligned} \quad (19)$$

where t_1 is the time when the end of channel growth stops, P_{max} is the saturation level of pressure. As it is described in Equation (11) fluid pressure is directly effective on the number of failing contacts.

This exponentially decreasing pressure field, for order of magnitude estimates, can be approximated as a zone of (skin) depth $2\sqrt{D(t-t_1)}$ ahead of the finger tip experimenting a significant overpressure rise close to the maximum overpressure P_{max}, and a negligible overpressure in the zone ahead of it. Since ξ contacts break—with an acoustic emission—per unit area when the overpressure rises from 0 to P_{max}, the cumulative number of contacts failing (i.e., the cumulative number of acoustic emissions) can be approximated via the equation below:

$$N(t) = 2L\xi\sqrt{D(t-t_1)} = \sqrt{(t-t_1)/\tau} \quad (20)$$

where L is the width of the cell. Furthermore, there is a characteristic time related to the pore pressure diffusion and density of contacts breaking due to this pore pressure increase,

$$\tau = 1/(4DL^2\xi^2). \quad (21)$$

This time τ is different from the other characteristic time t_1, that corresponds to the start of the diffusive behavior for the pore pressure.

Equating Equations (7) and (20) (and recalling that the time t' is measured with respect to t_0 in this last equation), we obtain the prediction:

$$((t-t_1)/\tau)^{0.5} = \frac{K'}{1-p}((t'+c')^{(1-p)} - c'^{(1-p)}), \quad (22)$$

which predicts that $1-p = 0.5$, i.e., $p = 0.5$, $t - t_1 = t' + c'$, $c' = 0$ which leads to $t - t_1 = t'$. Considering $t' = t - t_0$, this becomes $t_1 = t_0$ and finally Equation (22) turns into $K'/(1-p) = \tau^{-(1-p)}$.

This is indeed the case up to the error bars: $t_1 = t_0 - c'$, with $c' = 0.0066 \pm 0.55$ s, i.e., the start of the diffusive regime $t = t_1$ corresponds to the end of the growth of the finger $t = t_0$ up to the error bar, and p is found to be $p = 0.55 \pm 0.38$, equal to 0.5 up to the error bar. The prefactor of the MOL, found with the central p-value of 0.55 to be $K' = 5.34 \pm 1.52\ \mathrm{s}^{-0.45}$, allows to evaluate the characteristic diffusion time

$$\tau = (K'/(1-p))^{1/(p-1)} = (5.34/0.45)^{(-1/0.45)} = 0.004\ \mathrm{s}. \quad (23)$$

The frequency of occurrence of events is the time derivative:

$$\frac{dN}{dt} = \frac{1}{2\sqrt{\tau(t-t_1)}}. \quad (24)$$

The present study thus suggests that $p = 0.5$ in the Modified Omori Law is the signature of the slow stress relaxation due to the diffusion of the overpressure in the medium surrounding the cavities.Presumably, this p-value may decrease if the fluid injected slowly enough so that the diffusion skin depth becomes large with respect to the channel width during the injection, which is a contrary to the situation depicted here [20]. Also, large injection pressure may lead to subcritical crack growth and change p-value [40, 42, 80].

The prefactor of this law, corresponding to the characteristic time $\tau = 0.004$ s for this diffusion, can thus be related to the porosity and permeability of the medium around the channels, the viscosity and compressibility of the fluid, and the density of failing sites leading to events.

Putting τ back into the Equation (21) it is possible to calculate ξ via the following equation:

$$\xi = \frac{1}{2L\sqrt{D\tau}} \quad (25)$$

Recalling the expressions Equations (17) and (18), we obtain for this medium a diffusivity

$$D = \frac{d^2\phi^2 P_0}{180(1-\phi)^2\mu} = 0.20\ \mathrm{m}^2/\mathrm{s} \quad (26)$$

where we have used the air viscosity, $\mu = 1.810^{-5}$ Pa s, and the atmospheric pressure value $P_0 = 10^5$ Pa.

These two last equations, Equations (25) and (26), allow to express the density of the triggered seismogenic contacts, with $L = 0.4$ m, as:

$$\xi = \frac{1}{2L\sqrt{D\tau}} \simeq 45/\mathrm{m}^2 \quad (27)$$

for this presented experimental setup. This indicates that around 45 contacts per square meter can give rise to strong events due to overpressure rise (which is far lower than the total number of contacts $\approx 2.3 \times 10^{10}$ for the grains and cell thickness considered). This shows that just a small subfraction of contacts give rise to strong events.

It is also very consistent within the order of magnitude with the fact that 12 events of Type 2 were observed during this relaxation in the system of size around 50 cm ahead of the main finger by 40 cm width, i.e., of size 0.2 m^2 corresponding to a density around 50 m^{-2} microseismogenic events happening during this stress relaxation.

6. Conclusion

A purpose-built Hele-Shaw cell experiment was designed to enable both optical and acoustic recordings associated with controlled fracturing of a porous medium via air injection.

The optical and acoustic recordings are analyzed together to obtain a further understanding of the type of deformation occurring within the cell. Based on the evolution of the power spectrum and mean frequency of the acoustic data with time, together with the growing channel network, it can be determined that the low frequency content $f < 10$ kHz of the acoustic emissions is directly related to the permeability state of the medium. Low frequencies dominate the power spectrum as long as the medium has not reached its final fractured state. After this state is reached, aftershock-like events seem to release the stress from the medium in the post-fractured phase. These aftershock-like events have a broadband spectrum where the energy is not focused on the low frequency but spread on a wide span of frequencies. These events occur right after reaching the final fractured state and their frequency of occurrence decays with time. Both power spectra evolution and diminishing frequency of occurrence are present in real scale microseismic data. In addition, it is possible to estimate the number of aftershocks by using Modified Omori Law in experimental and microseismic data. These signatures, inflection point in the average frequency, appearance of impulsive events of high frequency, and starting point of an Omori Law, can be used straightforwardly in large scale microseismic monitoring of fluid injection and well stimulation. The permeability of the medium can also be directly estimated from the prefactor of the Omori Law.

Acknowledgments

We would like to thank Alain Steyer and Miloud Talib for their technical support during experimental campaigns. We would also like to thank Maxime Farin for stimulating discussions during this work. This project has received funding from the European Union's Seventh Framework Programme for research, technological development and demonstration under grant agreement no 316889, from the REALISE program of the Alsatian research network, from the Universities of Oslo and Strasbourg via a gjesteforsker program and an IDEX Espoirs award.

References

1. Guyon E, Hulin JP, Petit L. *Hydrodynamique Physique.* Savoirs Actuels, EDP Sciences (2001). Available online at: http://books.google.fr/books?id=ma8Me9pe1-MC
2. Spurk JH. *Fluid Mechanics. Problems and Solutions.* Springer Verlag (1997).
3. Craig RF. *Craig's Soil Mechanics, 7th Edn.* Taylor & Francis (2004). Available online at: http://books.google.fr/books?id=pfK66ZiuWMcC
4. Duran J, Reisinger A, de Gennes PG. *Sands, Powders, and Grains: An Introduction to the Physics of Granular Materials.* Partially Ordered Systems. New York, NY: Springer (2012). Available online at: https://books.google.no/books?id=x9TiBwAAQBAJ
5. Herrmann HJ, Hovi JP, Luding S. *Physics of Dry Granular Media.* NATO Advanced Science Institutes Series. Series E, Applied Sciences. Springer (1998). Available online at: http://books.google.fr/books?id=TZyOKD8bJRgC
6. Gidaspow D. *Multiphase Flow and Fluidization: Continuum and Kinetic Theory Descriptions.* Academic Press (1994). Available online at: http://books.google.fr/books?id=vYVexK0-tooC
7. Kunii D, Levenspiel O. *Fluidization Engineering. Butterworth-Heinemann Series in Chemical Engineering.* Butterworth-Heinemann (1991). Available online at: http://books.google.fr/books?id=ZVnb17qRz8QC
8. Goren L, Aharonov E, Sparks D, Toussaint R. Pore pressure evolution in deforming granular material: a general formulation and the infinitely stiff approximation. *J Geophys Res Solid Earth* (2010) **115**:B09216. doi: 10.1029/2009JB007191
9. Goren L, Aharonov E, Sparks D, Toussaint R. The mechanical coupling of fluid-filled granular material under shear. *Pure Appl Geophys.* (2011) **168**:2289–323. doi: 10.1007/s00024-011-0320-4
10. Schuring JR, Kosson DS, Fitzgerald CD, Venkatraman S. *Pneumatic Fracturing and Multicomponent Injection Enhancement of in Situ Bioremediation.* U.S. Patent No. 5,560,737. Google Patents. (1996) Available online at: http://www.google.com/patents/US5560737
11. US. Environmental Protection Agency. *Accutech Pneumatic Fracturing Extraction and Hot Gas Injection, Phase One: Applications Analysis Report.* Cincinnati, OH: DIANE Publishing Company (1994).
12. Gao F, Xie H, Zhou F, Ju Y, Xie L, Liu Y, et al. *Pneumatic Fracturing Method and System for Exploiting Shale Gas.* U.S. Patent App. 14/335,935. Google Patents (2014). Available online at: https://www.google.com/patents/US20140326450
13. Charléty J, Cuenot N, Dorbath L, Dorbath C, Haessler H, Frogneux M. Large earthquakes during hydraulic stimulations at the geothermal site of Soultz-sous-Forłts. *Int J Rock Mech Mining Sci.* (2007) **44**:1091–105. doi: 10.1016/j.ijrmms.2007.06.003
14. Cuenot N, Dorbath C, Dorbath L. Analysis of the microseismicity induced by fluid injections at the EGS site of soultz-sous-forłts (Alsace, France): implications for the characterization of the geothermal reservoir properties. *Pure Appl Geophys.* (2008) **165**:797–828. doi: 10.1007/s00024-008-0335-7
15. Dorbath L, Cuenot N, Genter A, Frogneux M. Seismic response of the fractured and faulted granite of Soultz-sous-Forłts (France) to 5 km deep massive water injections. *Geophys J Int.* (2009) **177**:653–75. doi: 10.1111/j.1365-246X.2009.04030.x
16. Aochi H, Poisson B, Toussaint R, Schmittbuhl J. Induced seismicity along a fault due to fluid circulation: conception and application. In: *Japan Geoscience Union Meeting 2011.* Chiba (2011).
17. Valkó P, Economides MJ. *Hydraulic Fracture Mechanics.* Wiley (1995). Available online at: https://books.google.com.tr/books?id=zcFTAAAAMAAJ
18. Cornet F, Helm J, Poitrenaud H, Etchecopar A. Seismic and aseismic slips induced by large-scale fluid injections. In: *Seismicity Associated with Mines, Reservoirs and Fluid Injections.* Basel: Springer (1998). p. 563–83.
19. Cornet FH. *Elements of Crustal Geomechanics.* Cambridge University Press (2015). Available online at: https://books.google.fr/books?id=GdXeBgAAQBAJ
20. Niebling MJ, Toussaint R, Flekkøy EG, Måløy KJ. Dynamic aerofracture of dense granular packings. *Phys Rev E* (2012) **86**:061315. doi: 10.1103/physreve.86.061315
21. Niebling MJ, Flekkøy EG, Måløy KJ, Toussaint R. Mixing of a granular layer falling through a fluid. *Phys Rev E* (2010) **82**:011301. doi: 10.1103/physreve.82.011301
22. Niebling MJ, Flekkøy EG, Måløy KJ, Toussaint R. Sedimentation instabilities: impact of the fluid compressibility and viscosity. *Phys Rev E* (2010) **82**:051302. doi: 10.1103/PhysRevE.82.051302
23. Johnsen Ø, Toussaint R, Måløy KJ, Flekkøy EG. Pattern formation during air injection into granular materials confined in a circular hele-shaw cell. *Phys Rev E* (2006) **74**:011301. doi: 10.1103/physreve.74.011301
24. Niebling MJ, Toussaint R, Flekkøy EG, Måløy KJ. Numerical studies of aerofractures in porous media. *Rev Cubana Fis.* (2012) **29**:1E66–70. Available online at: http://www.fisica.uh.cu/biblioteca/revcubfis/files/Archivos/2012/Vol29-No1E/RCF-29-1E-66.pdf
25. Johnsen Ø, Toussaint R, Måløy KJ, Flekkøy EG, Schmittbuhl J. Coupled air/granular flow in a linear hele-shaw cell. *Phys Rev E* (2008) **77**:011301. doi: 10.1103/PhysRevE.77.011301
26. Johnsen Ø, Chevalier C, Lindner A, Toussaint R, Clément E, Måløy KJ, et al. Decompaction and fluidization of a saturated and confined granular medium by injection of a viscous liquid or gas. *Phys Rev E* (2008) **78**:051302. doi: 10.1103/physreve.78.051302

27. Vinningland JL, Johnsen Ø, Flekkøy EG, Toussaint R, Måløy KJ. Granular rayleigh-taylor instability: experiments and simulations. *Phys Rev E* (2007) **99**:048001. doi: 10.1103/PhysRevLett.99.048001
28. Vinningland JL, Johnsen Ø, Flekkøy EG, Toussaint R, Måløy KJ. Experiments and simulations of a gravitational granular flow instability. *Phys Rev E* (2007) **76**:051306. doi: 10.1103/physreve.76.051306
29. Vinningland JL, Johnsen Ø, Flekkøy EG, Toussaint R, Måløy KJ. Size invariance of the granular rayleigh-taylor instability. *Phys Rev E* (2010) **81**:041308. doi: 10.1103/physreve.81.041308
30. Varas G, Vidal V, Géminard JC. Dynamics of crater formations in immersed granular materials. *Phys Rev E* (2009) **79**:021301. doi: 10.1103/PhysRevE.79.021301
31. Varas G, Géminard JC, Vidal V. Air invasion in a granular layer immersed in a fluid: morphology and dynamics. *Granular Matter* (2013) **15**:801–10. doi: 10.1007/s10035-013-0435-7
32. Varas G, Vidal V, Géminard JC. Venting dynamics of an immersed granular layer. *Phys Rev E* (2011) **83**:011302. doi: 10.1103/PhysRevE.83.011302
33. MacMinn CW, Dufresne ER, Wettlaufer JS. Fluid-driven deformation of a soft granular material. *Phys Rev X* (2015) **5**:011020. doi: 10.1103/PhysRevX.5.011020
34. Sandnes B, Flekkøy E, Knudsen H, Måløy K, See H. Patterns and flow in frictional fluid dynamics. *Nat Commun.* (2011) **2**:288. doi: 10.1038/ncomms1289
35. Rust A, Cashman K, Wallace P. Magma degassing buffered by vapor flow through brecciated conduit margins. *Geology* (2004) **32**:349–52. doi: 10.1130/G20388.2
36. Holtzman R, Szulczewski ML, Juanes R. Capillary fracturing in granular media. *Phys Rev Lett.* (2012) **108**:264504. doi: 10.1103/PhysRevLett.108.264504
37. Eriksen JA, Marks B, Sandnes B, Toussaint R. Bubbles breaking the wall: two-dimensional stress and stability analysis. *Phys Rev E* (2015) **91**:052204. doi: 10.1103/PhysRevE.91.052204
38. Hall SA, de Sanctis F, Viggiani G. Monitoring fracture propagation in a soft rock (Neapolitan Tuff) using acoustic emissions and digital images. *Pure Appl Geophys.* (2006) **163**:2171–204. doi: 10.1007/s00024-006-0117-z
39. Valès F, Bornert M, Gharbi H, Nguyen M, Eytard JC. Micromechanical investigations of the hydro-mechanical behaviour of argillite rocks, by means of optical full field strain measurement and acoustic emission techniques. In: *Proc. Int. Soc. Rock Mechanics.* Lisbon (2007).
40. Grob M, Schmittbuhl J, Toussaint R, Rivera L, Santucci S, Måløy K. Quake catalogs from an optical monitoring of an interfacial crack propagation. *Pure Appl Geophys.* (2009) **166**:777–99. doi: 10.1007/s00024-004-0496-z
41. Grob M, van der Baan M. Inferring *in-situ* stress changes by statistical analysis of microseismic event characteristics. *Leading Edge* (2011) **30**:1296–301. doi: 10.1190/1.3663403
42. Lengliné O, Toussaint R, Schmittbuhl J, Elkhoury JE, Ampuero J, Tallakstad KT, et al. Average crack-front velocity during subcritical fracture propagation in a heterogeneous medium. *Phys Rev E* (2011) **84**:036104. doi: 10.1103/PhysRevE.84.036104
43. Lengliné O, Schmittbuhl J, Elkhoury J, Ampuero JP, Toussaint R, Måløy KJ. Downscaling of fracture energy during brittle creep experiments. *J Geophys Res Solid Earth* (2011) **116**. doi: 10.1029/2010jb008059
44. Lengliné O, Elkhoury J, Daniel G, Schmittbuhl J, Toussaint R, Ampuero JP, et al. Interplay of seismic and aseismic deformations during earthquake swarms: an experimental approach. *Earth Planet Sci Lett.* (2012) **331**:215–23. doi: 10.1016/j.epsl.2012.03.022
45. Farin M, Mangeney A, Roche O. Fundamental changes of granular flow dynamics, deposition, and erosion processes at high slope angles: insights from laboratory experiments. *J Geophys Res Earth Surf.* (2014) **119**:504–32. doi: 10.1002/2013JF002750
46. Stojanova M, Santucci S. Acoustic emissions in fracturing paper. In: *ICF13.* Beijing (2013).
47. Stojanova M, Santucci S, Vanel L, Ramos O. The effects of time correlations in subcritical fracture. An acoustic analysis. In: *21ème Congrès Français de Mécanique, 26 au 30 août 2013.* Bordeaux (2013).
48. Stojanova M, Santucci S, Vanel L, Ramos O. High frequency monitoring reveals aftershocks in subcritical crack growth. *Phys Rev Lett.* (2014) **112**:115502. doi: 10.1103/PhysRevLett.112.115502
49. Toussaint R, Flekkøy EG, Helgesen G. The memory of fluctuating brownian dipolar chains. *Phys Rev E* (2006) **74**:051405. doi: 10.1103/PhysRevE.74.051405
50. Scott GD. Packing of spheres: packing of equal spheres. *Nature* (1960) **188**:908–9. doi: 10.1038/188908a0
51. Ciamarra MP, Coniglio A, de Candia A. Disordered jammed packings of frictionless spheres. *Soft Matter* (2010) **6**:2975–81. doi: 10.1039/c001904f
52. Hild F, Roux S. Digital image correlation: from displacement measurement to identification of elastic properties a review. *Strain* (2006) **42**:69–80. doi: 10.1111/j.1475-1305.2006.00258.x
53. Viggiani G, Hall SA. Full-field measurements, a new tool for laboratory experimental geomechanics. In: *Fourth Symposium on Deformation Characteristics of Geomaterials,* Vol. 1. Amsterdam: IOS Press (2008). p. 3–26.
54. Travelletti J, Delacourt C, Allemand P, Malet JP, Schmittbuhl J, Toussaint R, et al. Correlation of multi-temporal ground-based optical images for landslide monitoring: application, potential and limitations. *ISPRS J Photogramm Remote Sens.* (2012) **70**:39–55. doi: 10.1016/j.isprsjprs.2012.03.007
55. Allen RV. Automatic earthquake recognition and timing from single traces. *Bull Seismol Soc Am.* (1978) **68**:1521–32.
56. Baer M, Kradolfer U. An automatic phase picker for local and teleseismic events. *Bull Seismol Soc Am.* (1987) **77**:1437–45.
57. Earle PS, Shearer PM. Characterization of global seismograms using an automatic-picking algorithm. *Bull Seismol Soc Am.* (1994) **84**:366–76.
58. Wong J, Han L, Bancroft J, Stewart R. Automatic time-picking of first arrivals on noisy microseismic data. *CSEG* (2009) **1**:1–4.
59. Trnkoczy A. Understanding & setting sta/lta trigger algorithm parameters for the k2. *Appl Note* (1998) **41**:16–20.
60. Omori F. On after-shocks. *Rep Imp Earthq Inv Corn.* (1894) **2**:103–38.
61. Omori F. On after-shocks of earthquakes. *J Coll Sci Imp Univ Tokyo* (1894) **7**:111–200.
62. Utsu T. Magnitudes of earthquakes and occurrence of their aftershocks. *Zisin* (1957) **2**:35–45.
63. Utsu T, Ogata Y, Matsu'ura RS. The centenary of the Omori formula for a decay law of aftershock activity. *J Phys Earth* (1995) **43**:1–33. doi: 10.4294/jpe1952.43.1
64. Press WH, Teukolsky SA, Vetterling WT, Flannery BP. *Numerical Recipes 3rd Edition: The Art of Scientific Computing, 3rd Edn.* New York, NY: Cambridge University Press (2007).
65. Almendros J, Abella R, Mora MM, Lesage P. Array analysis of the seismic wavefield of longperiod events and volcanic tremor at arenal volcano, Costa Rica. *J Geophys Res Solid Earth* (2014) **119**:5536–59. doi: 10.1002/2013JB010628
66. Frank WB, Shapiro NM, Husker AL, Kostoglodov V, Bhat HS, Campillo M. Along-fault pore-pressure evolution during a slow-slip event in Guerrero, Mexico. *Earth Planet Sci Lett.* (2015) **413**:135–43. doi: 10.1016/j.epsl.2014.12.051
67. Helmstetter A, Sornette D. Diffusion of epicenters of earthquake aftershocks, Omori's law, and generalized continuous-time random walk models. *Phys Rev E* (2002) **66**:061104. doi: 10.1103/PhysRevE.66.061104
68. Lindman M, Lund B, Roberts R, Jonsdottir K. Physics of the Omori law: inferences from interevent time distributions and pore pressure diffusion modeling. *Tectonophysics* (2006) **424**:209–22. doi: 10.1016/j.tecto.2006.03.045
69. Langenbruch C, Shapiro SA. Decay rate of fluid-induced seismicity after termination of reservoir stimulations. *Geophysics* (2010) **75**:MA53–62. doi: 10.1190/1.3506005
70. Nur A, Booker JR. Aftershocks caused by pore fluid flow? *Science* (1972) **175**:885–7. doi: 10.1126/science.175.4024.885
71. Yamashita T. Regularity and complexity of aftershock occurrence due to mechanical interactions between fault slip and fluid flow. *Geophys J Int.* (2003) **152**:20–33. doi: 10.1046/j.1365-246X.2003.01790.x
72. Shapiro SA, Huenges E, Borm G. Estimating the crust permeability from fluid-injection-induced seismic emission at the KTB site. *Geophys J Int.* (1997) **131**:F15–8. doi: 10.1111/j.1365-246X.1997.tb01215.x

73. Shapiro SA, Audigane P, Royer JJ. Large-scale *in situ* permeability tensor of rocks from induced microseismicity. *Geophys J Int.* (1999) **137**:207–13. doi: 10.1046/j.1365-246x.1999.00781.x
74. Shapiro SA, Rothert E, Rath V, Rindschwentner J. Characterization of fluid transport properties of reservoirs using induced microseismicity. *Geophysics* (2002) **67**:212–20. doi: 10.1190/1.1451597
75. Rozhko AY, Podladchikov YY, Renard F. Failure patterns caused by localized rise in pore-fluid overpressure and effective strength of rocks. *Geophys Res Lett.* (2007) **34**:L22304. doi: 10.1029/2007GL031696
76. Jackson R. *The Dynamics of Fluidized Particles. Cambridge Monographs on Mechanics.* Cambridge University Press (2000). Available online at: https://books.google.fr/books?id=wV9ekwf-fA8C
77. Goren L, Toussaint R, Aharonov E, Sparks DW, Flekkøy EG. A general criterion for liquefaction in granular layers with heterogeneous pore pressure. *Poromechanics V.* (2013) 415–424. doi: 10.1061/9780784412992.049
78. Terzaghi VK. The shearing resistance of saturated soils and the angle between the planes of shear. In: *Proceedings of the 1st International Conference on Soil Mechanics and Foundation Engineering,* Vol. 1. Cambridge, MA: Harvard University Press (1936). p. 54–6.
79. Masson YJ, Pride SR, Nihei KT. Finite difference modeling of Biot's poroelastic equations at seismic frequencies. *J Geophys Res Solid Earth* (2006) **111**:B10305. doi: 10.1029/2006JB004366
80. Santucci S, Vanel L, Ciliberto S. Slow crack growth: models and experiments. *Eur Phys J Spec Top.* (2007) **146**:341–56. doi: 10.1140/epjst/e2007-00192-9

Conflict of Interest Statement: The authors declare that the research was conducted in the absence of any commercial or financial relationships that could be construed as a potential conflict of interest.

9.2 Paper 5: NOTE: Localization Based On Estimated Source Energy Homogeneity

Following the previous article, it was of interest to investigate methods for localizing sources of the signals received. In this paper, a new localization method for signals on a thin plate is proposed, based on the attenuation of energy and inverted source amplitude comparison. The method is developed and tested on both synthetic numerically simulated signals, as well as experimental signals originating from known sources and locations (e.g. steel pellet dropped on the plate at a given location). The localization method is tested against many existing methods, and found to be very versatile and works better than the conventional techniques considering computational cost and accuracy. The principle of the technique is as follows; with multiple sensors (here, 4) at different locations, the energy of the source signal is estimated as function of distance from the receiver, i.e. inversion taking account of the attenuation by travel distance of the wave. The source is then localized at the position where these estimated energies have the best match with each other. The accuracy of the method is discussed for various sampling rates, for non-dispersive and dispersive waves in systems with and without reflection. The expansion of the method into 3-D is also considered possible. This article was published in Review of Scientific Instruments in September 2016.

PAPER 5

REVIEW OF SCIENTIFIC INSTRUMENTS **87**, 096101 (2016)

Note: Localization based on estimated source energy homogeneity

Semih Turkaya,[1,a)] Renaud Toussaint,[1] Fredrik Kvalheim Eriksen,[1,2] Olivier Lengliné,[1] Guillaume Daniel,[3] Eirik G. Flekkøy,[2] and Knut Jørgen Måløy[2]
[1]*IPG Strasbourg, CNRS, Université de Strasbourg, Strasbourg, France*
[2]*Department of Physics, University of Oslo, Oslo, Norway*
[3]*Magnitude, Sainte Tulle, France*

(Received 7 June 2016; accepted 25 August 2016; published online 8 September 2016)

Acoustic signal localization is a complex problem with a wide range of industrial and academic applications. Herein, we propose a localization method based on energy attenuation and inverted source amplitude comparison (termed estimated source energy homogeneity, or ESEH). This inversion is tested on both synthetic (numerical) data using a Lamb wave propagation model and experimental 2D plate data (recorded with 4 accelerometers sensitive up to 26 kHz). We compare the performance of this technique with classic source localization algorithms: arrival time localization, time reversal localization, and localization based on energy amplitude. Our technique is highly versatile and out-performs the conventional techniques in terms of error minimization and cost (both computational and financial). *Published by AIP Publishing.* [http://dx.doi.org/10.1063/1.4962407]

Source localization of acoustic signals is fundamental for a broad range of academic and industrial applications, from robotics to medicine and from telecommunications to geoscience.[1–7] Even though it is trivial to locate impulsive, non-dispersive signals without any reflections,[8] as the signal and propagating medium get more complex this task becomes more difficult. In this paper, a new approach of localization based on the signal energy is presented. It is possible to implement this estimated source energy homogeneity (ESEH) method into the authors' previous work[9] to localize microseismic events in aero-fracturing of a porous medium in a Hele-Shaw Cell,[10] or other types of 2D experiments such as fracture propagation experiments in plexiglass[11] or crack propagation in paper.[12] Furthermore, it is possible to implement this method into a 3D medium at a larger scale which then can be used in the industrial applications such as geothermal activities,[13–15] well stimulation,[16] etc.

We here present a set of experimental and numerical results that compare different methods of localization: Arrival Time Delay Localization (ATL),[17–19] Energy Based Localization (EBL),[20,21] Time Reversal Localization (TRL)[7,22] (see S1, the supplementary material), and ESEH.

A glass (or plexiglass) plate having dimensions 80 cm × 40 cm × 1 cm is used for experiments. A 4.5 mm diameter steel ball is dropped from 2–3 cm height above the plate on different locations. The signal generated by the impact is recorded with a set of 4 miniature piezoelectric accelerometers (Brüel and Kjaer - 4374) with an optimal sensitivity in the (1 Hz–26 kHz) frequency range. The recorded signal is amplified and conditioned using a Brüel and Kjaer Nexus Charge Amplifier—Type 2692-A. Then, the signals are transmitted to the computer using a Ni-DAQ mx PCI-6133 acquisition card.

This new method relies on the principle that the source energy, after correction from travel path-related attenuation, should be equal (or almost equal) at every sensor location. The energy spreading due to distance for plates of thickness h can be expressed, from energy conservation and isotropy along the plates, as $E_m = \frac{E_s}{2\pi Rh}$ where E_s is the total emitted source energy and E_m is the energy density integrated over time and plate thickness, on a receiver m at a distant R. An additional attenuation factor due to the viscosity of the plate material can be incorporated as $E_m = \frac{E_s}{2\pi Rh} e^{-\alpha R_m}$, where α is a damping factor of dimension of inverse length (when this one is lowly or non-dependent of frequency). The source energy can thus be expressed from the energy received at m as

$$E_s = 2\pi RhE_m e^{-\alpha R_m}. \quad (1)$$

Modifying this Eq. (1) for localization we have[23,24]

$$E_s(\mathbf{r_s}, \mathbf{r_n}) = \int_0^{\omega_{Nyq}} 2\pi R(n)\rho hc(\omega)\frac{|a(\omega)|^2}{\omega^2} e^{\alpha(\omega)R(n)} d\omega, \quad (2)$$

where $E_s(\mathbf{r_s}, \mathbf{r_n})$ is the source energy seen from the sensor number n at position $\mathbf{r_n}$, the source is at position $\mathbf{r_s}$, ρ is the mass density of the plate, $c(\omega)$ is the group velocity over different ω (angular frequency) at which the energy is traveling,[24] $a(\omega)$ is the acceleration of the plate after Fourier transform, $R(n) = \|\mathbf{r_n} - \mathbf{r_s}\|$ is the distance between the source and the receiver n, and ω_{Nyq} is the Nyquist frequency ($\omega_{Nyq} = \frac{\pi}{dt}$ where dt is a discrete time step). The part $e^{\alpha(\omega)R}$ represents correction due to the material based attenuation which is equal to 1 in the case of glass plate.[24] For plexiglass plate for the frequencies lower than the cutoff frequency $\omega_c = \omega(1/h)$, this attenuation coefficient is equal to $\alpha(\omega) = 1\ \mathrm{m}^{-1}$, and for the frequencies higher than cutoff frequency it is $\alpha(\omega) = 7.64 \times 10^{-4}\omega^{2/3}\ \mathrm{m}^{-1}$.[24] Defining an average operator as $\langle A \rangle = \frac{1}{N}\sum_{n'=1}^{N} A(n')$ and using the normalized source energy $\Psi_s(\mathbf{r_s}, \mathbf{r_n}) = E_s(\mathbf{r_s}, \mathbf{r_n})/\max(E_s(\mathbf{r_s}, \mathbf{r_n}))$ where $\max(E_s(\mathbf{r_s}, \mathbf{r_n}))$ is the maximum over the N sensors, we can formulate the standard deviation of the energy recorded at N different sensors as $\sigma(\mathbf{r_s}) = \sqrt{\frac{1}{N}\sum_{n=1}^{N}(\Psi_s(\mathbf{r_s}, \mathbf{r_n}) - \langle\Psi_s(\mathbf{r_s}, \mathbf{r_n})\rangle)^2}$. The minimum of this standard deviation, $\sigma(\mathbf{r_s})$ over the plate will

a)Electronic mail: turkaya@unistra.fr

indicate the position of the source. This method is based on the direct wave (signal without the arrival of reflected waves from the sides). Therefore, it is necessary to carefully define the time window prior to the arrival of reflection so as to achieve high quality estimates of the source position. We define a direct wave window ranging from the impact duration of the source by using Hertzian mechanics (30 μs and 96 μs for the glass and plexiglass plates, respectively)[25,26] up to the time of arrival of the reflected wave, i.e., $\tau_{source} < L/V_R$, where L is the length of the raypath of the closest reflected wave (97 μs and 375 μs for the glass and plexiglass plates, respectively). We used window sizes 50 μs on glass and 200 μs on plexiglass for the experimental cases. The Rayleigh wave velocity is $V_{R_{glass}} \approx 3100$ m/s and $V_{R_{plexi}} \approx 800$ m/s on glass and plexiglass plates.[24]

Tests on synthetic data using hertzian contact load during shocks[25,26] are conducted to check different methods (ATL, TRL, EBL, and ESEH) in different conditions before testing in physical experiments (see S2, the supplementary material). During the localization estimations, we used Rayleigh wave velocity V_R as the wave velocity. However, it is possible to implement different group velocities for different frequencies in ESEH which decreases the error around ≈10 mm. In Table I, the average error of the different cases of signal generation is presented in this order: infinite and non-dispersive plate, infinite and dispersive plate by taking into account different velocities over the frequency spectrum, finite and non-dispersive plate by taking into account the reflected waves from the boundaries, and finite and dispersive plate by taking into account both. Signals for 18 various source locations are generated and localized using different methods. From Table I, it can be seen that the effect of uncertainty due to the estimation of the source energy in the conventional method leads to some estimation error even in the simplest case. In the infinite cases where the reflections are not included, energy based methods are more precise. A clear definition of the primary signal means that ESEH performs well in all circumstances. ATL is comparable to ESEH when the medium is non-dispersive; however, with increased dispersivity the performance of ATL decreases due to the attendant uncertainty in the wave velocity.

TABLE I. Table showing the average distance between the real source position and the estimated position (i.e., error) in mm for different cases in the signal generation.

Mean error, glass plate (mm)	ATL	TRL	EBL	ESEH
Infinite, non-dispersive	0	0	7	0
Infinite, dispersive	45	26	35	4
Finite, non-dispersive	2	2	20	5
Finite, dispersive	35	27	50	36
Experimental	21	29	48	33
Mean error, plexiglass plate (mm)	**ATL**	**TRL**	**EBL**	**ESEH**
Infinite, non-dispersive	0	0	7	0
Infinite, dispersive	30	61	27	11
Finite, non-dispersive	0	0	21	3
Finite, dispersive	36	37	48	40
Experimental	48	34	34	30

TABLE II. Table showing the computational time in milliseconds for different cases.

Mean computational cost (ms)	ATL	TRL	EBL	ESEH
Infinite, non-dispersive	6	31	5567	125
Infinite, dispersive	6	31	5567	125
Finite, non-dispersive	6	43	6983	257
Finite, dispersive	6	22	4760	90

In Table II, it is possible to compare computational costs for each method in every signal generation context.

This table is obtained by measuring the time spent during the estimation process with different methods. The window size of the signal is optimized for the cases to better include the direct wave. As a result, some of the less complex cases have longer signals and thus take more time to estimate. From Table II, it can be seen that ATL is the cheapest method while EBL is the most expensive.

We tested experimentally the effect of the ball size (1 mm, 5 mm, and 10 mm) and stiffness of the plate (polyamide, glass, and steel) of the signals. We observed that these properties do not affect localization results significantly. The average estimation error for different sampling rates for a set of experiments using a 5 mm steel ball hitting on a plexiglass plate is presented in Figure 1.

On the other hand, due to the lower Rayleigh wave velocity (≈800 m/s) in plexiglass, direct wave is clearer. This allows energy based methods to work in this case with a resolution ≈3.3 ± 1.0 cm, which is calculated by averaging the difference between the real and estimated source position for all the experiments (including the human error on targeting the predefined source position). Analysis of the experiments with different spatial resolution (by changing the grid from 1 cm to 1 mm) has a minor effect on the resolution of the data, but it increases the computational cost 70 times (see S3, the supplementary material). The conventional energy based localization method can be optimized by having a linearly spaced grid of 10 points between the maximum and the minimum possible source energy (see S4, the supplementary material).

The sampling rate of the signal has a significant effect on the estimation process; the smaller the sampling rate, the

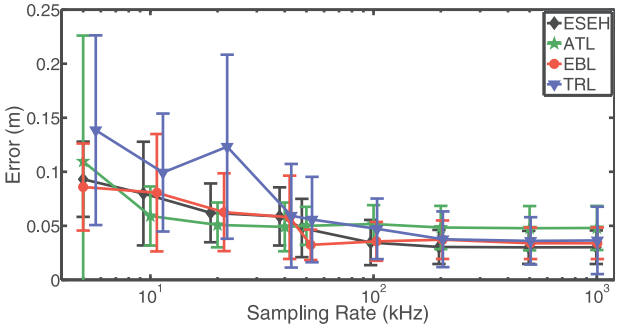

FIG. 1. Figure showing the decay of the average error on plexiglass plate with different sampling rates in different methods. Signals with lower sampling rates are obtained by decimating the experimentally recorded signal with 1 MHz sampling rate.

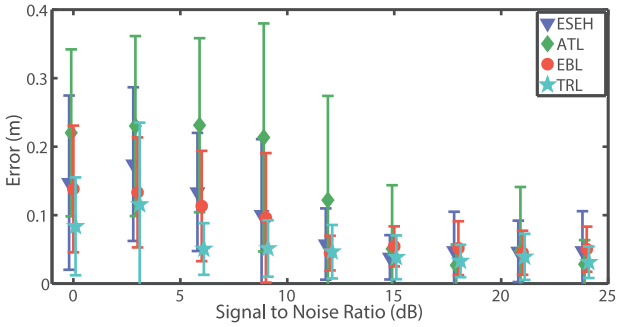

FIG. 2. Figure showing the effect of the SNR (added artificially) of the signal over the estimation quality in different methods on glass plate.

higher the error on localization. However, EBL and ESEH are the most stable techniques and provide better results over the range of sampling rates tested.

To see the effect of signal to noise ratio (SNR) in localization, Gaussian white noise with different amplitude is added to the input data. In Figure 2, it can be seen that the average error from ATL is the largest when the signal quality is poor. Here, ESEH and EBL have very similar responses. Moreover, no dependence on the propagation medium (i.e., glass or plexiglass) has been observed for the decay of the localization error with respect to the SNR (see S5, the supplementary material).

To see the effect of array geometry on the resolution, we placed the sensors in different positions over the plate in the simulations. Based on our investigations, we found out that a "T" shaped sensor placement gives the best results (≈10% better estimation) (see S6, the supplementary material).

The theoretical formulation of ESEH can be used in 3D media by changing the cylindrical energy spreading (with a decay of the energy in $1/R$) in Eq. (1) to spherical spreading and modifying the material based viscosity α for the selected 3D medium. Thus, we have for deep sources: $E_m = \frac{E}{\frac{4}{3}\pi R^2} e^{-\alpha R_m}$ and for superficial sources: $E_m = \frac{E}{\frac{2}{3}\pi R^2} e^{-\alpha R_m}$. The two main advantages of employing a 3D medium are that (1) the signals reflected from the sides are generally clearly distinguishable (or not existing at all when boundaries are sufficiently distant) and (2) the waves are body waves, meaning that the medium is non-dispersive. We thus, anticipate improved resolution in a 3D medium compared to a system of plates.

The proposed method, ESEH, appears to be the best compromise with respect to location accuracy and computational cost among the set of methods tested in this study. Particularly, if the primary signal can clearly be defined, ESEH is very convenient to use. Despite being slower than ATL and TRL, it is more robust when the signal is noisy, dispersive, or fast propagating. This method can be easily applied in 2D environments such as touchscreens, or membranes,[12,27] or in 3D in the petroleum industry, seismology, or medicine.

See the supplementary material S1 for the explanation of the different localization methods used in this study, S2 for detailed information about the numerical simulation, S3 for the details of spatial resolution of EBL, S4 for the optimization of the source energy grid in EBL, S5 for details of the SNR comparison, and S6 for the details of the different array geometries compared.

We thank A. Steyer and M. Talib for the technical support and M. Farin for discussions during this work. This project has received funding from the EU's 7th Framework Programme for research under Grant Agreement No. 316889, from the REALISE program of the Alsatian research network, from the Universities of Oslo and Strasbourg via a gjesteforsker program, and an IDEX Espoirs award. We also thank J. Farquharson for his help in language to make the article easier to understand.

[1]A. Gershman, V. Turchin, and V. Zverev, IEEE Trans. Signal Process. **43**, 2249 (1995).
[2]J. Valin, F. Michaud, J. Rouat, and D. Letourneau, in *IROS 2003. Proceedings. IEEE/RSJ* (IEEE, 2003), Vol. 2, pp. 1228–1233.
[3]E. Elnahrawy, X. Li, and R. Martin, in *Sensor and Ad Hoc Communications and Networks* (IEEE, 2004), pp. 406–414.
[4]D. Malioutov, M. Cetin, and A. Willsky, IEEE Trans. Signal Process. **53**, 3010 (2005).
[5]Q. Zhu, S. Tannenbaum, and S. H. Kurtzman, Surg. Oncol. Clin. North Am. **16**, 307 (2007), Pre and Postoperative Cancer Imaging: Practical and Innovative Approaches.
[6]M. Fink, AIP Conf. Proc. **1650**, 13 (2015).
[7]J. Garnier and M. Fink, Wave Motion **53**, 80 (2015).
[8]K. Aki and P. Richards, *Quantitative Seismology*, 2nd ed. (University Science Books, 2002).
[9]S. Turkaya, R. Toussaint, F. Eriksen, M. Zecevic, G. Daniel, E. Flekkøy, and K. Måløy, Front. Phys. **3**, 70 (2015).
[10]M. J. Niebling, R. Toussaint, E. Flekkøy, and K. Måløy, Revista Cubana de Fisica **29**, 1E66 (2012).
[11]O. Lengliné, R. Toussaint, J. Schmittbuhl, J. Elkhoury, J. Ampuero, K. Tallakstad, S. Santucci, and K. Måløy, Phys. Rev. E **84**, 036104 (2011).
[12]M. Stojanova, S. Santucci, L. Vanel, and O. Ramos, Phys. Rev. Lett. **112**, 115502 (2014).
[13]F. Cornet, J. Helm, H. Poitrenaud, and A. Etchecopar, *Seismicity Associated with Mines, Reservoirs and Fluid Injections* (Springer, 1998), pp. 563–583.
[14]K. Evans, F. Cornet, T. Hashida, K. Hayashi, T. Ito, K. Matsuki, and T. Wallroth, Geothermics **28**, 455 (1999).
[15]J. Šílenỳ, Z. Jechumtálová, and C. Dorbath, Pure Appl. Geophys. **171**, 2783 (2014).
[16]N. Belayouni, A. Gesret, G. Daniel, and M. Noble, Geophysics **80**, WC133 (2015).
[17]G. Carter, IEEE Trans. Acoust., Speech, Signal Process. **29**, 461 (1981).
[18]J. Smith and J. Abel, IEEE Trans. Acoust., Speech, Signal Process. **35**, 1661 (1987).
[19]M. Brandstein, J. Adcock, and H. Silverman, IEEE Speech Audio Process. **5**, 45 (1997).
[20]Y. Hu and D. Li, in *Multimedia Signal Processing* (IEEE, 2002), pp. 371–375.
[21]X. Sheng and Y.-H. Hu, in *Information Processing in Sensor Networks*, edited by F. Zhao and L. Guibas, Lecture Notes in Computer Science Vol. 2634 (Springer, Berlin, Heidelberg, 2003), pp. 285–300.
[22]M. Fink, IEEE Trans. Ultrason. Eng. **39**, 555 (1992).
[23]C. Hibert, A. Mangeney, G. Grandjean, and N. M. Shapiro, J. Geophys. Res. Earth Surf. **116**, f04032, doi:10.1029/2011JF002038 (2011).
[24]M. Farin, A. Mangeney, J. De Rosny, R. Toussaint, J. Sainte-Marie, and N. Shapiro, J. Sound Vib. **362**, 176 (2016).
[25]K. L. Johnson, *Contact Mechanics* (Cambridge University Press, 1985).
[26]M. Farin, A. Mangeney, R. Toussaint, J. de Rosny, N. Shapiro, T. Dewez, C. Hibert, C. Mathon, O. Sedan, and F. Berger, J. Geophys. Res. Solid Earth **120**, 7102, doi:10.1002/2015JB012331 (2015).
[27]R. Toussaint, O. Lengline, S. Santucci, T. Vincent-Dospital, M. Naert-Guillot, and K. J. Maloy, Soft Matter **12**, 5563 (2016).

Bibliography

[1] K. J. Måløy, J. Feder, and T. Jøssang. Viscous fingering fractals in porous media. *Phys. Rev. L. 55:2688*, 1985.

[2] R. Toussaint, G. Løvoll, Y. Méheust, K. J. Måløy, and J. Schmittbuhl. Influence of pore-scale disorder on viscous fingering during drainage. *Europhys Lett. 71:583*, 2005. doi:10.1209/epl/i2005-10136-9.

[3] E. Lemaire, P. Levitz, G. Daccord, and H. Van Damme. From viscous fingering to viscoelastic fracturing in colloidal fluids. *Phys. Rev. Lett. 67, 2009*, 1991. doi:10.1103/PhysRevLett.67.2009.

[4] P. G. Saffman and G. Taylor. The penetration of a fluid into a porous medium or hele-shaw cell containing a more viscous liquid. *Proc. R. Soc. Lond. A. Math. Phys. Sci. 245:312-29*, 1958. doi:10.1098/rspa.1958.0085.

[5] F. K. Eriksen, R. Toussaint, K. J. Måløy, and E. G. Flekkøy. Invasion patterns during two-phase flow in deformable porous media. *Front. Phys. 3:81*, 2015. doi:10.3389/fphy.2015.00081.

[6] E. Sharon, M. G. Moore, W. D. McCormick, and H. L. Swinney. Coarsening of viscous fingering patterns. *Phys. Rev. Lett. 91, 205504*, 2003. doi:10.1103/PhysRevLett.91.205504.

[7] B. Davidovitch, A. Levermann, and I. Procaccia. Convergent calculation of the asymptotic dimension of diffusion limited aggregates: Scaling and renormalization of small clusters. *Phys. Rev. E 62, R5919-R5922*, 2000. doi:10.1103/PhysRevE.62.R5919.

[8] H. M. Jaeger, S. R. Nagel, and R. P. Behringer. Granular solids, liquids, and gases. *Rev. Mod. Phys., Vol. 68, No. 4*, 1996.

[9] GDR MiDi. On dense granular flows. *Eur. Phys. J. E 14: 341*, 2004. doi:10.1140/epje/i2003-10153-0.

[10] S. S. Suthersan. *Remediation Engineering: Design Concepts*. Boca Raton, FL: CRC Press LLC, 1999. pp. 237-54.

[11] L. L. Goodroad and J. R. Schuring. Potential of pneumatic fracturing to enhance in situ remediation technologies. *In: Waste Management 1994 Symposium. Tucson, AZ: WM SYMPOSIA, INC.*, 1994.

[12] S. Kazemian, B. B. K. Huat, A. Prasad, and M. Barghchi. A review of stabilization of soft soils by injection of chemical grouting. *Aust. J. Basic & Appl. Sci. 4(12), pp. 5862-68*, 2010.

[13] R. Z. Moayed, E. Izadi, and M. Fazlavi. In-situ stress measurements by hydraulic fracturing method at gotvand dam site, iran. *Turkish J. Eng. Env. Sci. 36, pp. 179-94*, 2012. doi:10.3906/muh-1104-9.

[14] C. T. Montgomery and M. B. Smith. Hydraulic fracturing: history of an enduring technology. *J. Pet. Technol.* ***62****:2632*, 2010. doi:10.2118/1210-0026-jpt.

[15] Department of Energy. Hydraulic fracturing whitepaper. *EPA 816-R-04-003, Appendix A*, 2004.

[16] G.C. Naik. Tight gas reservoirs - an unconventional natural energy source for the future. *Available online at: www.pinedaleonline.com/socioeconomic/pdfs/tight_gas.pdf (Accessed 05, 2016)*, 2003.

[17] S. M. Johnson and J. P. Morris. Hydraulic fracturing mechanisms in carbon sequestration applications. *In: 43rd U.S. Rock Mechanics Symposium and 4th U.S.-Canada Rock Mechanics Symposium. Asheville, NC: American Rock Mechanics Association*, 2009.

[18] W. H. Williamson and D. R. Wooley. *Hydraulic Fracturing to Improve the Yield of Bores in Fractured Rock*. Canberra, ACT: Australian Government Publishing Service, 1980.

[19] F. Rummel and O. Kappelmayer. The falkenberg geothermal frac-project: concepts and experimental results. *Hydraul. Fract. Geotherm. Energy* ***5****:5974*, 1983. doi:10.1007/978-94-009-6884-4_4.

[20] Clark L. Energy company plans to frack volcano. *In: Wired Science. Available online at: www.wired.com/wiredscience/2012/10/newberry-volcano-fracking (Accessed 05, 2016)*, 2012.

[21] A. Hurst, J. Cartwright, and Duranti D. Fluidization structures produced by upward injection of sand through a sealing lithology. *In: Van Rensbergen P., Hillis R.R., Maltman A.J. and Morley C.K., editors. Subsurface Sediment Mobilization. London: Geological Society, Special Publications 216, pp. 123-38*, 2003.

[22] H. Løseth, L. Wensaas, B. Arntsen, and M. Hovland. Gas and fluid injection triggering shallow mud mobilization in the hordaland group, north sea. *In: Van Rensbergen P., Hillis R.R., Maltman A.J. and Morley C.K., editors. Subsurface Sediment Mobilization. London: Geological Society, Special Publications 216, pp. 139-57*, 2003.

[23] P. Van Rensbergen, J. Poort, R. Kipfer, M. De Batist, M. Vanneste, J. Klerkx, and et al. Near-surface sediment mobilization and methane venting in relation

to hydrate destabilization in southern lake baikal, siberia. *In: Van Rensbergen P., Hillis R.R., Maltman A.J. and Morley C.K., editors. Subsurface Sediment Mobilization. London: Geological Society, Special Publications 216, pp. 207-21*, 2003.

[24] A. R. Talukder, M. C. Comas, and J. I. Soto. Pliocene to recent mud diapirism and related mudvolcanoes in the alboran sea(western mediterrenean). *In: Van Rensbergen P., Hillis R.R., Maltman A.J. and Morley C.K., editors. Subsurface Sediment Mobilization. London: Geological Society, Special Publications 216, pp. 443-59*, 2003.

[25] N. Pralle, M. Külzer, and G. Gudehus. Experimental evidence on the role of gas in sediment liquefaction and mudvolcanism. *In: Van Rensbergen P., Hillis R.R., Maltman A.J. and Morley C.K., editors. Subsurface Sediment Mobilization. London: Geological Society, Special Publications 216, pp. 159-71*, 2003.

[26] E. Deville, A. Battani, R. Griboulard, S. Guerlais, J. P. Herbin, J. P. Houzay, and et al. The origin and processes of mudvolcanism: new insights from trinidad. *In: Van Rensbergen P., Hillis R.R., Maltman A.J. and Morley C.K., editors. Subsurface Sediment Mobilization. London: Geological Society, Special Publications 216, pp. 475-90*, 2003.

[27] R. Nuwer. Indonesias 'mud volcano' and nine years of debate about its muck. *In: NY Times. Available online at: www.nytimes.com/2015/09/22/science/9-years-of-muck-mud-and-debate-in-java.html (Accessed 10, 2016)*, 2015.

[28] A. Mazzini, H. Svensen, G. G. Akhmanov, G. Aloisi, S. Planke, A. Malthe-Sørenssen, and B. Istadi. Triggering and dynamic evolution of the lusi mud volcano, indonesia. *Earth and Planetary Sci. Lett. 261, 375-388*, 2007. doi:10.1016/j.epsl.2007.07.001.

[29] A. Mazzini, A. Nermoen, M. Krotkiewski, Y. Podladchikov, S. Planke, and H. Svensen. Strike-slip faulting as a trigger mechanism for overpressure release by piercement structures. implications for the lusi mud volcano, indonesia. *Marine and Petroleum Geology 26, 1751-1765*, 2009. doi:10.1016/j.marpetgeo.2009.03.001.

[30] A. Mazzini, G. Etiope, and H. Svensen. A new hydrothermal scenario for the 2006 lusi eruption, indonesia. insights from gas geochemistry. *Earth and Planetary Sci. Lett. 317/318, 305-318*, 2012. doi:10.1016/j.epsl.2011.11.016.

[31] M. Lupi, E. H. Saenger, F. Fuchs, and S. A. Miller. Lusi mud eruption triggered by geometric focusing of seismic waves. *Nature Geoscience 6, 642-646*, 2013. doi:10.1038/ngeo1884.

[32] M. R. P. Tingay, Rudolph M. L., M. Manga, R. J. Davies, and C. Y. Wang. Initiation of the lusi mudflow disaster. *Nature Geoscience 8, 493-494*, 2015. doi:10.1038/ngeo2472.

[33] I. Ghani, D. Koehn, R. Toussaint, and C. W. Passchier. Dynamic development of hydrofracture. *Pure Appl. Geophys. 170 (11), 1685-1703*, 2013. doi:10.1007/s00024-012-0637-7.

[34] A. Vass, D. Koehn, R. Toussaint, I. Ghani, and S. Piazolo. The importance of fracture-healing on the deformation of fluid-filled layered systems. *Journal of Structural Geology 67, 94-106*, 2014. doi:10.1016/j.jsg.2014.07.007.

[35] I. Ghani, D. Koehn, R. Toussaint, and C. W. Passchier. Dynamics of hydrofracturing and permeability evolution in layered reservoirs. *Frontiers in Physics 3, 67*, 2015. doi:10.3389/fphy.2015.00067.

[36] L. Goren, E. Aharonov, D. Sparks, and R. Toussaint. Pore pressure evolution in deforming granular material: A general formulation and the infinitely stiff approximation. *Journal of Geophysical Research: Solid Earth 115 (B9)*, 2010. doi:10.1029/2009JB007191.

[37] L. Goren, E. Aharonov, D. Sparks, and R. Toussaint. The mechanical coupling of fluid-filled granular material under shear. *Pure Appl. Geophys. 168 (12), 2289-2323*, 2013. doi:10.1007/s00024-011-0320-4.

[38] H. Aochi, B. Poisson, R. Toussaint, X. Rachez, and J. Schmittbuhl. Self-induced seismicity due to fluid circulation along faults. *Geophys. J. Int. 196 (3), 1544-1563*, 2013. doi:10.1093/gji/ggt356.

[39] R. Lenormand. Pattern growth and fluid displacements through porous media. *Physica 140A, 114-123*, 1986.

[40] G. Løvoll, Y. Méheust, R. Toussaint, J. Schmittbuhl, and K. J. Måløy. Growth activity during fingering in a porous hele-shaw cell. *Phys. Rev. E 70:026301*, 2004. doi:10.1103/PhysRevE.70.026301.

[41] R. Toussaint, K. J. Måløy, Y. Méheust, G. Løvoll, M. Jankov, G. Schäfer, and J. Schmittbuhl. Two-phase flow: structure, upscaling, and consequences for macrosopic transport properties. *Vadoze Zone Journal 11 3*, 2012. doi:10.2136/vzj2011.0123.

[42] H. Huang, F. Zhang, P. Callahan, and J. Ayoub. Granular fingering in fluid injection into dense granular media in a hele-shaw cell. *Phys. Rev. Lett. 108:258001*, 2012. doi:10.1103/PhysRevLett.108.258001.

[43] X. Z. Kong, W. Kinzelbach, and F. Stauffer. Morphodynamics during air injection into water-saturated movable spherical granulates. *Chem. Eng. Sci. 65:4652-60*, 2010. doi:10.1016/j.ces.2010.05.007.

[44] G. Varas, V. Vidal, and Géminard J. C. Morphology of air invasion in an immersed granular layer. *Phys. Rev. E 83, 061302*, 2011. doi:10.1103/PhysRevE.83.061302.

[45] J. L. Vinningland, Ø. Johnsen, E. G. Flekkøy, R. Toussaint, and K. J. Måløy. Granular rayleigh-taylor instability: Experiments and simulations. *Phys. Rev. Lett.* ***99****, 048001*, 2007. doi:10.1103/PhysRevLett.99.048001.

[46] V. Frette, J. Feder, T. Jøssang, and Meakin P. Buoyancy-driven fluid migration in porous media. *Phys. Rev. Lett. 68, 3164*, 1992. doi:10.1103/PhysRevLett.68.3164.

[47] C. Völtz, W. Pesch, and I. Rehberg. Rayleigh-taylor instability in a sedimenting suspension. *Phys. Rev.* ***E****65, 011404*, 2001. doi:10.1103/PhysRevE.65.011404.

[48] M. J. Niebling, E. G. Flekkøy, K. J. Måløy, and R. Toussaint. Mixing of a granular layer falling through a fluid. *Phys. Rev.* ***E****82, 011301*, 2010. doi:10.1103/PhysRevE.82.011301.

[49] A. Birovljev, L. Furuberg, J. Feder, T. Jøssang, K. J. Måløy, and A. Aharony. Gravity invasion percolation in two dimensions: Experiment and simulation. *Phys. Rev. Lett. 67, 584*, 1991. doi:10.1103/PhysRevLett.67.584.

[50] Y. Méheust, G. Løvoll, K. J. Måløy, and J. Schmittbuhl. Interface scaling in a two-dimensional porous medium under combined viscous, gravity, and capillary effects. *Phys. Rev. E 66, 051603*, 2002. doi:10.1103/PhysRevE.66.051603.

[51] D. Wilkinson and J. F. Willemsen. Invasion percolation: a new form of percolation theory. *J. Phys. A Math. Gen. 16:336576*, 1983.

[52] R. Chandler, J. Koplik, K. Lerman, and J. F. Willemsen. Capillary displacement and percolation in porous media. *J. Fluid Mech. vol. 119, 249-267*, 1982.

[53] R. Lenormand and C. Zarcone. Capillary fingering: Percolation and fractal dimension. *Transport in Porous Media 4, 599-612*, 1989.

[54] L. Paterson. Diffusion-limited aggregation and two-fluid displacements in porous media. *Phys. Rev. Lett. vol. 52, issue 18, 1621-1624*, 1984. doi:10.1103/PhysRevLett.52.1621.

[55] E. Lemaire, Y. O. M. Abdelhaye, J. Larue, Benoit R., P. Levitz, and H. Van Damme. Pattern formation in noncohesive and cohesive granular media. *Fractals 1, 968-976*, 1993. doi:10.1142/S0218348X93001040.

[56] Ø. Johnsen, R. Toussaint, K. J. Måløy, and E. G. Flekkøy. Pattern formation during air injection into granular materials confined in a circular hele-shaw cell. *Phys. Rev.* ***E****74, 011301*, 2006. doi:10.1103/PhysRevE.74.011301.

[57] X. Cheng, L. Xu, A. Patterson, H. M. Jaeger, and S. R. Nagel. Towards the zero-surface-tension limit in granular fingering instability. *Nat. Phys.* ***4****:234-7*, 2008. doi:10.1038/nphys834.

[58] Ø. Johnsen, R. Toussaint, K. J. Måløy, E. G. Flekkøy, and J. Schmittbuhl. Coupled air/granular flow in a linear hele-shaw cell. *Phys. Rev.* ***E****77, 011301*, 2008. doi:10.1103/PhysRevE.77.011301.

[59] M. J. Niebling, R. Toussaint, E. G. Flekkøy, and K. J. Måløy. Dynamic aerofracture of dense granular packings. *Phys. Rev.* ***E****86, 061315*, 2012. doi:10.1103/PhysRevE.86.061315.

[60] Ø. Johnsen, C. Chevalier, A. Lindner, R. Toussaint, E. Clément, K. J. Måløy, E. G. Flekkøy, and J. Schmittbuhl. Decompaction and fluidization of a saturated and confined granular medium by injection of a viscous liquid or gas. *Phys. Rev.* ***E****78, 051302*, 2008. doi:10.1103/PhysRevE.78.051302.

[61] M. J. Niebling, R. Toussaint, E. G. Flekkøy, and K. J. Måløy. Numerical studies of aerofractures in porous media. *Rev. Cub. Fis. 29, 1E66*, 2012.

[62] B. Sandnes, E. G. Flekkøy, H. A. Knudsen, and K. J. Måløy. Patterns and flow in frictional fluid dynamics. *Nat. Commun.*, 2011. doi:10.1038/ncomms1289.

[63] R. Holtzman, M. L. Szulczewski, and R. Huanes. Capillary fracturing in granular media. *Phys. Rev. Lett. 108:264504*, 2012. doi:10.1103/PhysRevLett.108.264504.

[64] C. Chevalier, A. Lindner, M. Leroux, and E. Clément. Morphodynamics during air injection into a confined granular suspension. *J. Non-Newton Fluid Mech. 158:63-72*, 2008. doi:10.1016/j.jnnfm.2008.07.007.

[65] J. A. Eriksen, B. Marks, B. Sandnes, and R. Toussaint. Bubbles breaking the wall: two-dimensional stress and stability analysis. *Phys. Rev. E 91:052204*, 2015. doi:10.1103/PhysRevE.91.052204.

[66] J. A. Eriksen, R. Toussaint, K. J. Måløy, E. G. Flekkøy, and B. Sandnes. Numerical approach to frictional fingers. *Phys. Rev. E 92:032203*, 2015. doi:10.1103/PhysRevE.92.032203.

[67] B. Marks, B. Sandnes, G. Dumazer, J. A. Eriksen, and K. J. Måløy. Compaction of granular material inside confined geometries. *Front. Phys. 3:41*, 2015. doi:10.3389/fphy.2015.00041.

[68] J. A. Eriksen, R. Toussaint, K. J. Måløy, E. G. Flekkøy, and B. Sandnes. Pattern formation of frictional fingers in a gravitational potential. *arXiv:1605.07436v1 [physics.flu-dyn]*, 2016.

[69] M. Moura, E. A. Fiorentino, K. J. Måløy, G. Schäfer, and R. Toussaint. Impact of sample geometry on the measurement of pressure-saturation curves: Experiments and simulations. *Water Resour. Res. 51*, 2015. doi:10.1002/2015WR017196.

[70] G. Løvoll, M. Jankov, K. J. Måløy, R. Toussaint, J. Schmittbuhl, G. Schäfer, and Y. Méheust. Influence of viscous fingering on dynamic saturationpressure curves in porous media. *Transp. Porous Med. 86: 305*, 2011. doi:10.1007/s11242-010-9622-8.

[71] K. T. Tallakstad, H. A. Knudsen, T. Ramstad, G. Løvoll, K. J. Måløy, R. Toussaint, and E. G. Flekkøy. Steady-state two-phase flow in porous media: Statistics and transport properties. *Phys. Rev. Lett. 102, 074502*, 2009. doi:10.1103/PhysRevLett.102.074502.

[72] J. L. Vinningland, Ø. Johnsen, E. G. Flekkøy, R. Toussaint, and K. J. Mly, Måløy. Experiments and simulations of a gravitational granular flow instability. *Phys. Rev. E 76:051306*, 2007. doi:10.1103/PhysRevE.76.051306.

[73] J. L. Vinningland, Ø. Johnsen, E. G. Flekkøy, R. Toussaint, and K. J. Mly, Måløy. Size invariance of the granular rayleigh-taylor instability. *Phys. Rev. E 81:041308*, 2010. doi:10.1103/PhysRevE.81.041308.

[74] J. L. Vinningland, R. Toussaint, M. J. Niebling, E. G. Flekkøy, and K. J. Måløy. Family-vicsek scaling of detachment fronts in granular rayleigh-taylor instabilities during sedimentating granular/fluid flows. *Eur. Phys. J. Special Topics **204**, 27-40*, 2012. doi:10.1140/epjst/e2012-01550-2.

[75] S. Turkaya, R. Toussaint, F. K. Eriksen, M. Zecevic, G. Daniel, E. G. Flekkøy, and K. J. Måløy. Bridging aero-fracture evolution with the characteristics of the acoustic emissions in a porous medium. *Front. Phys. 3:70*, 2015. doi: 10.3389/fphy.2015.00070.

[76] S. Turkaya, R. Toussaint, F. K. Eriksen, O. Lengliné, D. Guillaume, E. G. Flekkøy, and K. J. Måløy. Note: Localization based on estimated source energy homogeneity. *Rev. Sci. Instrum. 87, 096101*, 2016. doi:10.1063/1.4962407.

[77] S. McNamara, E. G. Flekkøy, and K. J. Måløy. Grains and gas flow: Molecular dynamics with hydrodynamic interactions. *Phys. Rev. E 61, 4054*, 2000. doi:10.1103/PhysRevE.61.4054.

[78] J. Feder. *Fractals*. New York, NY: Plenum Press, 1988.

[79] A. L. Barabási and H. E. Stanley. *Fractal Concepts in Surface Growth*. Cambridge: Cambridge University Press, 1995.

[80] B. B. Mandelbrot. *The fractal geometry of nature*. New York, NY: W. H. Freeman and company, 1982.

[81] J. Blaber, B. Adair, and A. Antoniou. Ncorr: Open-source 2d digital image correlation matlab software. *Exp. Mech.*, 2015. doi:10.1007/s11340-015-0009-1.

[82] J. Blaber. Ncorr - open source 2d digital image correlation matlab software. *Available online at: http://www.ncorr.com/ (Accessed 10, 2016)*.

[83] J. Ugelstad, P. C. Mórk, K. H. Kaggerud, T. Ellingsen, and A. Berge. Swelling of oligomer-polymer particles. new methods of preparation. *Adv. Colloid Interface Sci. 13, 101*, 1980. doi:10.1016/0001-8686(80)87003-5. Produced under the trade name Dynospheres by Dyno Particles A.S., N-2001 Lillestrom, Norway.

[84] W. H. Press, S. A. Teukolsky, W. T Vetterling, and B. P. Flannery. *Numerical recipies in Fortran 77, 2nd ed.: The art of scientific computing*. Cambridge: Cambridge University Press, 2001.

[85] F. K. Eriksen, R. Toussaint, S. Turkaya, K. J. Måløy, and E. G. Flekkøy. Pneumatic fractures in confined granular media. *(Submitted)*, 2016.

[86] W. Bauer, M. Weber, and S. Chanbai. White light interferometry. *In: Q.J. Wang, Y.-W. Chung, editors. Encyclopedia of Tribology. New York: Springer Science+Business Media, pp. 4115-26*, 2013. doi:10.1007/978-0-387-92897-5.

[87] S. Santucci, M. Grob, R. Toussaint, J. Schmittbuhl, A. Hansen, and K. J. Måløy. Fracture roughness scaling: A case study on planar cracks. *EPL, 92 44001*, 2010. doi:10.1209/0295-5075/92/44001.

[88] A. Neuville, R. Toussaint, J. Schmittbuhl, D. Koehn, and J. O. Schwarz. Characterization of major discontinuities from borehole cores of the black consolidated marl formation of draix (french alps). *Hydrol. Process. 26, 20852094*, 2012. doi:10.1002/hyp.7984.

Fredrik ERIKSEN

Écoulements dans des fractures et milieux poreux en évolution

Résumé

Mots-clés : Milieux granuleux et poreux, instabilités, transformation mécanique et chimique, diffusion de la pression interstitielle

Cette thèse est une étude expérimentale de la transformation lente et rapide d'un milieu poreux sous l'action de l'écoulement d'un fluide. Le processus rapide est une déformation mécanique avec formation de canaux en raison de la forte pression du fluide, alors que le processus lent correspond à l'évolution chimique des fractures. L'étude de la déformation rapide est effectuée grâce à l'injection d'air à pression constante dans un milieu granulaire sec ou saturé. Par des techniques d'imagerie nous avons pu caractériser l'invasion par des motifs de Saffman-Taylor ; la déformation du milieu ; ainsi que les régimes d'écoulement et la dynamique de croissance des canaux. La pression interstitielle est évaluée numériquement et utilisée pour caractériser la rhéologie. L'étude de la transformation lente repose sur des expériences où de l'eau distillée est injecté à débit constant à travers un échantillon de calcaire fracturé. En comparant l'ouverture des fractures mesurées avant et après l'écoulement, nous avons caractérisé l'évolution des fractures pour différentes durées d'écoulement réactif.

Résumé en anglais

Keywords: Granular and porous media, flow instabilities, mechanical and chemical transformation, pore pressure diffusion

This thesis is an experimental study of flow and transformation of porous media, where we study both fast and slow transformation of the media due to fluid flow. The fast process is mechanical deformation and channel formation due to high fluid pressure, and the slow process is chemical evolution of fractures. In the study of fast deformation, we perform experiments where air is injected at a constant overpressure into a saturated or dry granular medium. From recorded images, we characterize Saffman-Taylor like invasion patterns, surrounding deformation of the medium, flow regimes, and channel growth dynamics. Pore pressure is evaluated numerically, and used to characterize the rheology. In the study of slow transformation, we perform experiments where distilled water is injected at a constant flow rate through a fractured chalk sample. By comparing fracture apertures measured before and after experiments, we study the evolution of fractures for different durations of reactive flow.